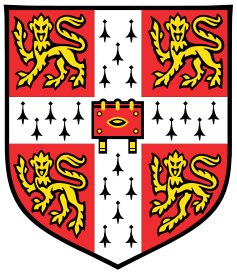
Finite Element Modelling and Experimental Characterisation of Auricle Mechanics for Earable Design



Yunpeng Li

Supervisor: Prof. Michael Sutcliffe
Prof. Manohar Bance

Advisor: Dr. Shery Huang

Department of Engineering
University of Cambridge

This thesis is submitted for the degree of
Doctor of Philosophy

Hughes Hall October 2025

Declaration

This thesis is the result of my own work and includes nothing which is the outcome of work done in collaboration except as declared in the preface and specified in the text. It is not substantially the same as any work that has already been submitted, or is being concurrently submitted, for any degree, diploma or other qualification at the University of Cambridge or any other University or similar institution except as declared in the preface and specified in the text. It does not exceed the prescribed word limit for the relevant Degree Committee.

Yunpeng Li
October 2025

Abstract

Wearable devices are rapidly evolving into the next generation of smart technologies with the potential to transform daily life. Among these, auricle-mounted "earables" are emerging as a promising platform for neural interfaces, leveraging the ear's anatomical accessibility, social acceptability, and structural stability. The auricle provides a natural site for integrating miniaturised EEG electrodes and sensors, but its compliant, anisotropic mechanics and susceptibility to deformation under motion pose significant challenges for device stability, comfort, and signal fidelity.

This thesis develops a systematic framework for characterising auricle biomechanics and translating these insights into earable design. A multi-stage methodology was implemented, combining physical phantoms, volunteer experiments, and finite element (FE) simulations. First, simplified and anatomically refined auricle phantoms were constructed to develop controlled experiment methods under static and dynamic loading, from which stiffness, deformation angle, and natural frequency were quantified. In vivo experiments with 31 volunteers validated these findings, revealing gender and morphology dependent variations in auricle mechanics. Dynamic analysis further established resonance frequencies in the 20–30 Hz range, critical for understanding gait and motion induced artefacts.

A FE model was then developed and validated against phantom and volunteer data. The nonlinear tissue behaviour of the auricle was captured by hyperelastic material model, while parametric studies demonstrated the influence of geometry, material parameters, and boundary constraints on auricle response. Finally, prototype earable devices were simulated and tested to assess contact pressure, impedance, and decoupling behaviour under locomotion. Results showed that device mass distribution and interface geometry critically affect both comfort and motion robustness.

Together, this work establishes an experimentally validated computational platform for earable design. By linking auricle mechanics to electrode stability and motion artefact susceptibility, it fills a key gap in wearable neural interface research and provides practical guidance for future earable development.

I would like to dedicate this thesis to my loving families . . .

Acknowledgements

First, I would like to express my sincere gratitude to Prof Michael Sutcliffe and Prof Manohar Bance for their continuous support and guidance throughout the four years of my doctoral studies. With their assistance, I learned to become a better scientist, and their encouragement ensured that I never had to despair.

I would also like to extend my sincere thanks to Dr Iwan Robert and Dr Filip Hrncirik. Without their generous help and technical expertise, I would have spent countless additional years struggling with 3D printing, medical image processing, and the operation and calibration of essential experimental instruments. Their practical advice and willingness to share knowledge were invaluable to the progress of this work.

I am deeply grateful for the support provided by the Department of Engineering, particularly Stefan Savage, Simon Marshall, Graham Smith, and R. James Macleod. They were consistently kind and supportive in assisting with my experimental requirements. Special thanks go to Simon for spending many days in the laboratory helping me set up and troubleshoot the Instron machine, and to Graham for his invaluable help with volunteer recruitment.

Finally, I would like to thank my family and the many friends I made along this journey. Their unwavering support, encouragement, and companionship made the doctoral process far more enjoyable and far less daunting than it might otherwise have been. During a particularly difficult period for my family, their understanding, patience, and unconditional love provided me with immense strength and reassurance.

Thank you, Shirui. This journey we shared was a gift from the very beginning of my PhD, and you were there for me when I needed support the most. Through every hardship and moment of doubt we faced together, you were always by my side. Wherever life takes us, please know that I will always be there for you.

Table of contents

List of figures **xiv**

List of tables **xviii**

Nomenclature **xix**

1 Introduction **1**

1.1 What Is an Earable Device 1

1.2 Why Study Auricle Mechanics 2

1.3 Scope of This Thesis 2

1.4 Outline of This Thesis 3

2 Literature review **5**

2.1 Neural Interfaces: Development and Applications 5

2.1.1 Neural Signal Background 6

2.1.2 Wearable NI 9

2.2 Ear as NI device carrier 11

2.2.1 Ear anatomy 11

2.2.2 On-Ear device design 12

2.2.3 Ear for neural signal collection 15

2.2.4 Comfort Considerations for Ear-Based Devices 16

2.3 Biomechanical Analysis 17

2.3.1 Structural Analysis 17
2.3.2 Ear Material Analysis 19
2.3.3 Finite Element Analysis 20
2.4 Contact Considerations for Wearable Devices 21
2.4.1 Pressure Distribution 21
2.4.2 Robustness Under Motion 22
2.4.3 Material for Wearable Devices 23
2.5 Summary of Literature and Research Gap 23

3 Mechanical Study with Auricle Phantom Model 25
3.1 Introduction 25
3.2 Phantom Model Construction 26
3.2.1 Medical Image Processing 27
3.2.2 Phantom Manufacture 28
3.3 Static Loading Response 34
3.3.1 Experiment Method 34
3.3.2 Result And Discussion 37
3.4 Dynamic Loading Response 41
3.4.1 Experiment Method 42
3.4.2 Result Of Load Release Test 42
3.4.3 Result Of Vibration Response Test 47
3.5 Digital Simulation Approaches 49
3.5.1 FE Simulation Of Mechanical tests 50
3.5.2 Simulation Setup 51
3.5.3 Simulation Result And Comparison 53
3.6 Improved Phantom Model and Experimental Refinement 56
3.6.1 Improved Construction Process 56
3.6.2 Experimental Refinement 58

3.6.3 Static and Dynamic Results 59
3.6.4 Summary of improvements 60
3.7 Conclusions 61

4 Human Auricle Study and Biomechanical Modelling 63
4.1 Introduction 63
4.2 Human Subject Experiment Design 64
4.2.1 Method development 64
4.2.2 Beam Model Consideration 64
4.2.3 Experimental Setup 66
4.3 Static Loading Response 70
4.3.1 Data Collection Procedure 70
4.3.2 Data Processing and Analysis 71
4.3.3 Statistic Summary and Discussions 73
4.4 Dynamic Loading Response 74
4.4.1 Dynamic Data Collection 75
4.4.2 Data Processing and Modelling 75
4.5 Analysis Of Auricle Mechanics 77
4.5.1 Correlation with Geometric Properties 77
4.5.2 Beam Model Analysis 79
4.6 Conclusions 82

5 Auricle Computational Modelling and Geometric Matching 84
5.1 Introduction 84
5.2 Auricle Model Construction 85
5.2.1 Auricle Mesh Generation 85
5.2.2 Auricle Simulation Demonstration 89
5.2.3 Auricle Mesh Verification 93

5.3 Parameter Study 95
5.3.1 Linear Material Study 95
5.3.2 Hyperelastic Material Study — Ogden Model 97
5.3.3 Geometric Variation and Morphological Impact 104
5.4 Auricle Model Verification 106
5.4.1 System Vibration Study 106
5.4.2 Earable Interaction 109
5.4.3 Simulation Results for Earable Interaction 111
5.5 Discussion and Conclusion 113

6 Earable Prototype Evaluation and Device Decoupling Analysis 115
6.1 Introduction 115
6.2 Device Coupling and Pressure Distribution under Controlled Vibration . . . 116
6.2.1 Objective 116
6.2.2 Static FE Analysis 117
6.2.3 Dynamic FE Sinusoidal Vibration Analysis 118
6.3 *In Vivo* Gait Analysis and FE Validation 123
6.3.1 Objective 123
6.3.2 Experimental System Setup 123
6.3.3 Protocol and Data Acquisition 124
6.3.4 FE Simulation with IMU-derived Boundary Conditions 125
6.3.5 Results and Key Findings 128
6.4 Earable Electrode Study 128
6.4.1 Introduction 128
6.4.2 Contact Characterisation of Soft Electrodes 128
6.4.3 Skin Impedance Measurement and Pressure Dependence 133
6.4.4 Estimating Contact Radius and Interface Modelling 134
6.5 Results and Discussion 138

7 Conclusion **140**

7.1 Summary of Key Findings 140

7.2 Limitations 141

7.3 Future Work 142

7.4 Concluding Remarks 143

References **145**

Appendix A Fabrication Detail of Realistic Auricle Phantom **155**

Appendix B Beam Bending Model for Auricular Deformation **158**

Appendix C Volunteer Experiment Materials **161**

Appendix D Auricle Model Presentation **174**

Appendix E Detail FEA Report **180**

List of figures

2.1 Classification of EEG Frequency Bands 7
2.2 Block Diagram of a Standard EEG Monitoring System 8
2.3 Over scalp EEG recording system 9
2.4 Anatomy of the human auricle 12
2.5 Standard Anatomical Reference Frames and Planes 13
2.6 Ear based devices 14
2.7 Conventional earphone design 14
2.8 Ear structure study 18

3.1 Auricle model acquisition from CT and segmentation 27
3.2 Phantom model illustration 28
3.3 Model comparison of auricle cartilage thickness 29
3.4 Combined method result of phantom fabrication 31
3.5 Auricle Phantom Material Test 32
3.6 Static loading 35
3.7 Image processing workflow 36
3.8 String modulus 37
3.9 Static Loading Tracking 38
3.10 Angle Illustration 39
3.11 Angle and force relationship 40
3.12 Displacement Illustration 40

3.13 Displacement and force relationship 41
3.14 Step Response Figure 43
3.15 Dynamic loading 44
3.16 Step Response Result Figure 45
3.17 Impulse test analysis 46
3.18 Gain and phase 47
3.19 Frequency test analysis 48
3.20 Abaqus Setup 53
3.21 Abaqus Result – Static Load Simulation 54
3.22 Impulse Response Figure 55
3.23 New Phantom Construction 57
3.24 Phantom Construction Process 58
3.25 Realistic phantom experiment setup 59
3.26 Realistic phantom test results 60

4.1 Effect of pulling angle on beam deformation 67
4.2 Volunteer test configuration 68
4.3 Experiment equipment 69
4.4 Photometric measurement of auricle dimensions 70
4.5 Volunteer static test result 73
4.6 Volunteer dynamic result 77
4.7 Measured effective stiffness with width and length 78
4.8 Measured natural frequency with width and length 79
4.9 Relationship between stiffness and natural frequency 82

5.1 CT-derived auricle mesh 86
5.2 Anatomical validation of the layered auricle model 87
5.3 Comparison of auricle model dimensions with volunteer data 90

5.4 Demonstration simulation of auricle deformation 92
5.5 Mesh convergence analysis of the auricle finite element model 95
5.6 Contour plots of linear elastic material model 96
5.7 Simulation result with volunteer data 97
5.8 Comparison of Ogden and linear material responses 99
5.9 Effect of bulk 100
5.10 Contour plots of skin hyperelastic material model 102
5.11 Contour plots of cartilage hyperelastic material model 103
5.12 Comparison of Ogden model with volunteer data 104
5.13 Mechanical response of auricle models with varied geometries 105
5.14 System vibration characterisation of the auricle model 108
5.15 Earable prototype fitted to auricle 110
5.16 Von Mises stress map of the auricle with earable 112
5.17 Quantitative comparison of auricle loading under different mass distributions 113

6.1 Simulation model display 117
6.2 FE static analysis of auricle–device interaction 119
6.3 Vibration trajectories of auricle and devices 120
6.4 Simulation results of contact pressure response 121
6.5 Earphone model decoupling from the ear 122
6.6 Schematic of the gait analysis setup 124
6.7 Time-domain comparison of acceleration data 126
6.8 Gait-driven FE simulation results for the earable prototype 127
6.9 Electrode contact test schematic 129
6.10 Electrode contact experiment results 130
6.11 Characterisation of the eutectogel electrode 130
6.12 Experimental setup for electrode–skin impedance measurement 134

6.13 Electrode–skin impedance at 50 Hz as a function of measured applied normal force 135

6.14 FE analysis of an electrode in contact with a skin 136

6.15 FE result of electrode contact with soft skin layers of varying thickness . . . 137

6.16 Electrode–skin impedance at 50 Hz with contact radius 138

A.1 Assembly of the initial mould box for the simplified auricle phantom. . . . 156

A.2 Transparent mould box used for improved visual control of silicone filling. . 156

A.3 Demonstration of failed mould box and ruptured phantoms, with attempts using both Ecoflex^{TM} 00-30 and Mold Max^{TM} 10 157

B.1 A straight beam subjected to end loading. 158

D.1 The CT-scanned auricle model outlook. 174

D.2 The CT-scanned auricle model cross section on transverse plane. 175

D.3 The database SHORT auricle model outlook. 175

D.4 The database SHORT auricle model cross section on transverse plane. . . . 176

D.5 The database THICK auricle model outlook. 176

D.6 The database THICK auricle model cross section on transverse plane. . . . 177

D.7 The database LONG auricle model outlook. 177

D.8 The database LONG auricle model cross section on transverse plane. 178

D.9 The CT-scanned auricle with thicker cartilage model outlook. 178

D.10 The CT-scanned auricle with thicker cartilage model cross section on transverse plane. 179

List of tables

3.1 Material used in manufacture 32

3.2 Comparison between auricle phantoms 33

3.3 Frequency Response Result 49

3.4 Abaqus Parameters 50

3.5 Abaqus Frequency Response 55

3.6 Elastic 50A curing condition 57

3.7 Phantom models comparison 60

4.1 Volunteer test result statistic analysis 74

5.1 Summary of auricle mesh models in FE 89

5.2 Mesh convergence results 94

5.3 Summary of sinusoidal excitation parameters 107

6.1 Summary of FE simulation results for earable and earphone 122

Nomenclature

Acronyms / Abbreviations

ADC	analogue-to-digital converter
AEEG	ambulatory electroencephalogram
Ag/AgCl	silver/silver-chloride
BCI	Brain-Computer Interfaces
CT	Computed tomography
CT	Computed tomography
ECG	electrocardiography
EEG	electroencephalogram
EOG	Electrooculography
EOG	electrooculography
FEA	Finite Element Analysis
FE	Finite Element
MRI	Magnetic Resonance Imaging
MRI	Magnetic resonance imaging
NI	Neural Interface
PEDOT:PSS	poly(3,4-ethylenedioxythiophene) polystyrene sulfonate
PPG	Photoplethysmography

SNR	signal-to-noise ratio
SWD	Soft wearable devices

Chapter 1

Introduction

1.1 What Is an Earable Device

In our daily lives, the external ear, or auricle, frequently interacts with various objects and technologies. Acoustically, it plays a crucial role in enabling us to localize sound sources. Functionally, it serves as a support point for everyday accessories, such as glasses, earbuds, and headphones, highlighting its structural importance [1].

Building on these anatomical and functional advantages, the auricle has emerged as a promising site for the development of wearable technologies, collectively referred to as "Earables." These devices often incorporate biosensors such as gait sensors, photoplethysmography (PPG) sensors, sweat sensors, and skin electrodes. They provide a range of functionalities, including health monitoring, AI-powered assistance, and medical diagnostics [2].

More recently, researchers have explored the use of Earables as Neural Interfaces (NI) . Conventional neural interface systems typically require full scalp coverage with high-density electrode arrays, commonly 64, 128, or 256 channels, to capture electroencephalography (EEG) signals. These setups are bulky and impractical for everyday or long-term use, limiting their application outside laboratory settings [3]. To address this, the concha region of the auricle has been identified as a viable site for EEG signal acquisition. This has led to the research domain known as Ear-EEG, which focuses on utilising the concha and surrounding auricular areas for neural signal recording. Numerous studies have since investigated how the ear can be used effectively for Brain-Computer Interfaces (BCI) and other neurotechnology applications.

Additionally, the long-standing history of electronic devices worn on the ear, particularly headphones and earphones, demonstrates both technical maturity and user acceptance. Their diverse, ergonomic designs suggest that the ear is not only a functionally promising but also a socially acceptable location for wearable neural interfaces [4].

1.2 Why Study Auricle Mechanics

As earable technologies continue to diversify in function and form, understanding the physical interaction between these devices and the auricle becomes essential to ensure both technical performance and long-term wearer comfort.

Despite the increasing number of proposed Earable devices, most of them primarily focus on EEG signal acquisition and overlook long-term comfort and skin interaction. The auricle consists of soft tissue that is prone to irritation, including blisters and inflammation, especially under continuous mechanical loading or prolonged wear.

To address these concerns, this project proposes a biomechanical approach: beginning with a detailed study of the auricle's mechanical properties, constructing a mechanical model, and designing Earable devices informed by this model. The goal is to ensure both functionality and user comfort. This approach centres on the mechanical response of the auricle, providing a foundation for designing next-generation Earables with improved ergonomics and safety.

1.3 Scope of This Thesis

This research lies at the intersection of multiple disciplines, including biomechanics, neuroscience, electrical engineering, human-centred design, and kinesiology. The primary focus of this report is the creation of a mechanical model of the auricle and the evaluation of its interaction with wearable devices.

Finite Element Analysis (FEA) is used to simulate the auricle's response to external forces, such as those exerted by wearable devices. A significant effort is devoted to identifying suitable material models that mimic the auricle's multilayer structure, including accurate estimation of tissue layer thickness and assigning corresponding mechanical properties.

The contact mechanics between the auricle and wearable devices are also studied, including simulations of loading and surface interaction. Given the complexity of the auricle's geometry and material heterogeneity, data acquisition relies heavily on both experimental measurements

and simulation validation. Structural mechanics, therefore, plays a central role in this research.

Further stages of the project will involve integrating the mechanical findings with electronic and neural components, including the development of a functional Earable prototype capable of recording neural signals and performing signal processing.

1.4 Outline of This Thesis

This thesis is organised into seven chapters, each of which addresses a specific stage in the development, analysis, and evaluation of auricle-based earable technologies. The structure progresses logically from foundational background and literature, through experimental and computational investigations, to the design and assessment of prototype devices. Together, these chapters form a coherent framework that reflects the systematic approach taken throughout the research.

Chapter 1 & 2 – Introduction and Literature Review Chapter 1 presents the background, motivation, and scope of the study. Chapter 2 offers an in-depth literature review, focusing on auricle biomechanics, existing EEG technologies, and prior earable designs. This chapter will later be expanded to include three-dimensional modelling techniques and simulation strategies.

Chapter 3 – Development of the Phantom Auricle Model This chapter describes the creation of a physical auricle model and outlines the experimental methodology used to analyse its mechanical properties. The work presented here is still under development and is intended for future publication.

Chapter 4 – Volunteer Study on Auricle Mechanics This chapter presents preliminary findings from a human study involving volunteers, with the aim of assessing variability in the mechanical response of the auricle across individuals.

Chapter 5 – Finite Element Analysis of the Auricle This chapter details the process of generating a digital auricle model and performing FE simulations to evaluate its structural response under device attachment. The simulation work builds directly on the experimental results obtained from the phantom auricle model.

Chapter 6 – Earable Prototype Analysis This chapter discusses the design of the earable device, with a particular focus on the interaction between its structure and the auricle. It

also outlines plans for integrating sensors and ensuring stable, high-quality neural signal acquisition.

Chapter 7 – Conclusion This chapter summarises the key findings of this project, including the development of a validated auricle mechanics model, and discusses the implications of these findings for earable design. It also highlights opportunities for future work in electrical and neural signal integration.

Together, these chapters present a comprehensive exploration of auricle-based wearable devices, combining mechanical modelling, experimental analysis, and engineering design to inform the development of next-generation earable systems.

Chapter 2

Literature review

The interdisciplinary scope of this project encompasses mechanical analysis, neuroscience, electrical engineering, human factors engineering, and kinesiology. This chapter aims to summarise the development of earable neural interface devices, examine their benefits and applications, and identify the gaps between academic research and real-world implementation.

2.1 Neural Interfaces: Development and Applications

Rehabilitation therapists have used neural interface (NI) systems to restore lost functionality in people with movement impairments for around two decades [5]. The core principle involves the use of neural signals from the patient to control external digital systems. Interest in NI systems increased significantly after the clinical trial of Hochberg [6], in which motor cortex signals were collected and used to control a robotic arm as well as software applications. Over time, the scope of NI systems has expanded beyond rehabilitation, encompassing applications such as controlling digital devices, interacting with virtual environments, and enhancing cognitive functions [7].

NI systems are generally categorized into invasive and non-invasive types [8]. Invasive methods, such as intracortical microelectrode arrays, offer a higher signal-to-noise ratio (SNR) and more spatially focused signal acquisition. These techniques can capture detailed neuronal activity, including action potentials and local field potentials, providing rich information for BCIs. However, these microelectrodes require surgical implantation, which carries risks like

infection and tissue damage [9], and may face limited public acceptance due to their invasive nature.

In contrast, non-invasive methods, such as EEG, are safer and more accessible but typically offer lower SNR and spatial resolution. Despite these limitations, advancements in signal processing and machine learning have improved the performance of non-invasive BMIs, making them increasingly viable for various applications [10].

The choice between invasive and non-invasive NI systems involves a fundamental trade-off between signal fidelity and user safety. Given the growing interest in safer, more accessible alternatives, this section will focus on past and ongoing research in the domain of non-invasive NI systems. In particular, we explore how wearable devices offer a promising platform for non-invasive NI due to their proximity to neural signal sources, user comfort, and discreet integration into daily life.

2.1.1 Neural Signal Background

Understanding neural signals is essential for the design and development of NI systems. Among the various electrophysiological modalities, electroencephalography (EEG) remains the most widely used due to its non-invasiveness and ability to capture real-time brain activity[11]. EEG records electrical potentials generated by neuronal activity in the cerebral cortex, offering insights on cognitive states, sensory processing, and neurological conditions. The information extracted includes oscillatory brain rhythms (e.g., alpha, beta, theta, delta bands as illustrated in Figure 2.1), event-related potentials, and pathological features such as epileptic discharges. Complementary signals such as electrooculography (EOG) and electrocardiography (ECG) also play important roles in neural signal interpretation and system design. EOG tracks eye movements through corneo-retinal potentials and is used in sleep staging, drowsiness detection, and eye-gaze interfaces[12]. ECG measures the electrical activity of the heart, providing context for physiological state monitoring and artefact removal in EEG recordings[13].

The pursuit of neural signal monitoring began as early as the 1970s with the development of ambulatory electroencephalography (AEEG) systems [14]. These early devices enabled continuous EEG recording for up to 24 hours using cassette tapes, representing a pivotal shift toward long-term monitoring outside of clinical settings. AEEG was primarily developed to support seizure diagnosis by providing clinicians with extended neural activity data. This capability laid the foundation for modern wearable neural technologies.

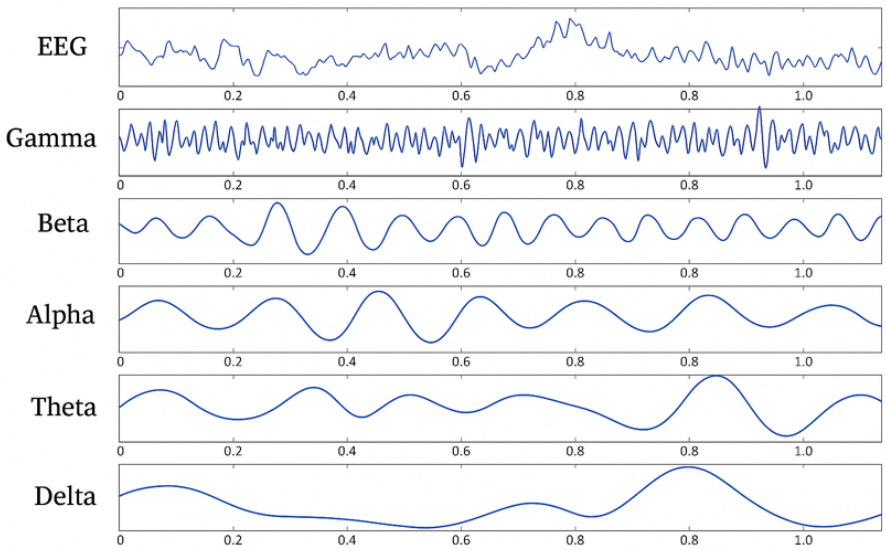


Fig. 2.1 EEG Frequency Bands. Delta (0.5–4 Hz): dominant during deep sleep; Theta (4–8 Hz): associated with drowsiness, meditation, and early sleep stages; Alpha (8–13 Hz): linked to relaxed wakefulness, especially with eyes closed; Beta (13–30 Hz): reflects active thinking, attention, and mental effort; Gamma (30–100 Hz): involved in higher cognitive functions such as perception, memory, and consciousness. Adapted from [11]

In general, an EEG monitoring system is often designed to record and analyse the brain's electrical activity, primarily originating from cortical neurons [15]. As illustrated in Figure 2.2, the system comprises several key components that function collaboratively to capture and process these bioelectrical signals:

- **Electrodes:** Typically made of silver/silver-chloride (Ag/AgCl), these sensors are placed on the scalp to detect voltage fluctuations generated by neuronal activity.
- **Amplifiers:** EEG signals are in the microvolt range and require amplification to increase their magnitude for accurate processing and analysis.
- **Analogue-to-Digital Converters (ADCs):** The amplified analogue signals are converted into digital format for subsequent computational handling.
- **Data Acquisition and Processing Systems:** Digitized signals are transmitted to acquisition systems, often integrated with platforms such as LabVIEW or SIMULINK, for real-time monitoring, storage, and post-processing analysis.

Together, these components form the foundation of EEG systems, enabling the non-invasive observation of neural dynamics. The insights gained from EEG data are instrumental in clinical diagnostics, cognitive neuroscience, and the development of neural interface technologies[16].

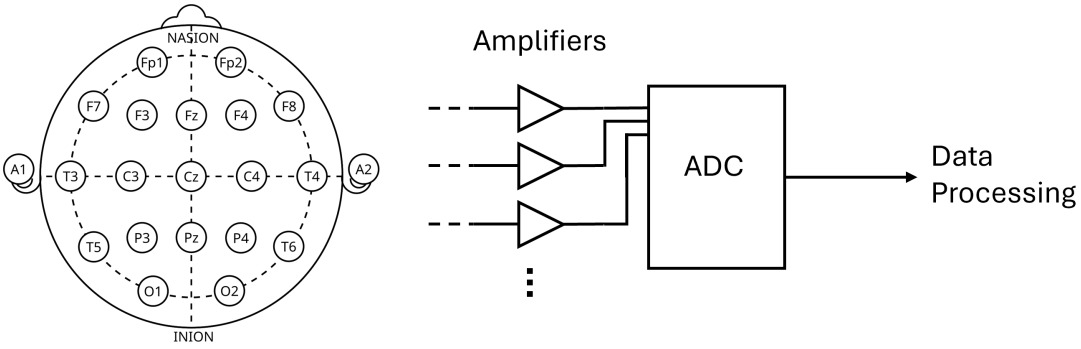


Fig. 2.2 Block diagram of a conventional EEG monitoring system.The diagram illustrates scalp electrode placement according to the international 10–20 system [17], signal amplification and conditioning stages, and subsequent digitisation using a multi-channel analogue-to-digital converter (ADC) prior to data acquisition and processing.

Despite these advances, clinical EEG recordings have historically been limited by time and space constraints for both physicians and patients. These limitations underscored the need for portable and user-friendly EEG systems. Conventional EEG recording systems, such as scalp-mounted array helmets, have facilitated neuroscience research, but are bulky and uncomfortable for everyday use [18]. These systems require firm electrode-skin contact to ensure data quality, which often leads to skin irritation over large contact areas under long term contact. As shown in Figure 2.3, such systems are often intrusive, highlighting the need for more practical and wearable NI alternatives.

Over time, EEG monitoring systems gained widespread adoption in both clinical and research domains for analysing long-duration EEG recordings in naturalistic environments. Modern commercial EEG platforms have since evolved to target applications such as sleep monitoring, mental workload assessment, and attention tracking. Emerging applications also investigate real-time device control using brain signals in non-patient populations. For example, Lin et al. demonstrated an EEG-based control system for piloting an aerial drone [19]. As the goal shifts toward making neural interface systems accessible to the general public, increasing emphasis is placed on portability, comfort, and usability. These demands have catalysed the development of wearable EEG devices, which aim to balance signal fidelity with convenience in daily-life scenarios.



Fig. 2.3 Over scalp EEG recording system.[18] Reflecting the complexity and low social acceptance of scalp EEG devices.

2.1.2 Wearable NI

Wearable technologies are regarded as enabling tools within the framework of Industry 4.0, the current phase of industrial development characterised by the integration of digital-physical systems, automation, and data-driven manufacturing [20]. In this context, wearable devices and sensors have begun to play a pivotal role on the factory floor, enabling real-time assessment, worker safety monitoring, and process optimization [21]. At the same time, advances in immersive and interactive computing environments have created new demands for wearable systems that can serve as intuitive and unobtrusive user interfaces [22]. Within this field, the integration of NI systems into wearable platforms offers significant potential for enhancing communication, control, and information exchange between users and computational devices.

Beyond the potential in the developing market, wearable NI devices provide researchers with tools to study neural activity in naturalistic environments, thereby contributing to the development of more reliable and accessible interfaces. For instance, Gruebler et al. developed a wearable device capable of reading electromyographic signals to classify facial

expressions, demonstrating the synergy between sensor technology and wearable engineering [23]. Similarly, commercial headbands have been introduced to monitor sleep quality and assess user stress and concentration levels based on EEG signals [24, 25].

Building on the fundamental trade-off between signal fidelity and invasiveness outlined in the previous section, wearable non-invasive NI systems must operate under strict physiological and ergonomic constraints. Unlike implanted electrodes, wearable interfaces rely on surface-level signal acquisition, where motion artefacts, variable electrode–skin contact, and limited spatial resolution impose fundamental performance limits. Nevertheless, prior work has shown that these constraints do not preclude effective neural interfacing. For instance, Millán et al. demonstrated that EEG signals could be used to control mobile robots through adaptive learning between the user and the interface [26], while Wolpaw et al. showed that spatial EEG features can be mapped to infer user intent [27]. These studies highlight that, although non-invasive systems operate with reduced signal fidelity, system-level co-adaptation and algorithmic strategies can partially compensate for hardware limitations. Consequently, improving the mechanical and electrical interface between the wearable device and the body becomes a critical lever for enhancing signal quality—particularly for ear-mounted NI devices.

Complementary improvements in wireless data transmission now allow much of the computational load to be offloaded to remote devices, reducing both the size and power requirements of on-body hardware[28]. Nevertheless, non-invasive EEG systems still face notable limitations, such as high skin–electrode impedance and vulnerability to environmental electrical noise. Addressing these constraints remains critical for advancing wearable NI systems toward broader adoption.

Improving the quality of cutaneous electrodes is essential to realising practical NI systems. One approach is the use of conductive polymer coatings, such as poly(3,4-ethylenedioxythiophene) polystyrene sulfonate (PEDOT:PSS) [29]. This material has been enhanced through the addition of flexible substrates and surfactants to improve adhesion and morphology [30]. Dimov et al. developed PEDOT-based coatings incorporating acrylic ester copolymer microparticles, yielding electrodes with impedance levels comparable to commercial alternatives without requiring gels or adhesives [31].

Beyond impedance improvements, PEDOT:PSS coatings also significantly improve the mechanical and chemical interface between electrodes and soft tissue. Their high surface area and gentle mechanical properties reduce inflammation and improve long-term stability of neural recordings[32]. However, electrode design and placement remain challenging. Although head-mounted devices provide good signal coverage, they are cumbersome for

daily use. Therefore, the development of alternative form factors, such as ear-based devices, may offer a more practical solution for continuous neural signal acquisition in daily settings.

2.2 Ear as NI device carrier

As acknowledged by many designers and researchers, the ear is an ideal location for NI attachment. Since the introduction of earphones, ear-based electronic devices have diversified significantly in form and function. This evolution reflects public interest in more comfortable, convenient, and personalized devices. The popularity and commercial success of earphones underscore both the technical maturity of ear-focused designs and their broad public acceptance. Importantly, the ear has also emerged as a prime site for collecting neural signals such as EEG and electrooculography (EOG) . This section introduces the general anatomical structure of the ear and outlines two major advantages of using the ear as a site for NI attachment: physical compatibility and access to meaningful bio-signals.

2.2.1 Ear anatomy

The ear is widely accepted as a structural anchor for personal devices such as earphones, hearing aids, and other wearable technologies. The external ear, or auricle (Figure 2.4), captures and directs sound waves toward the eardrum, enabling auditory perception. The auricle is composed of auricular cartilage overlaid with soft tissue and skin [33]. Its anatomical design determined its unique ability in sound collection and amplification. The cartilage is attached to the skull by ligaments and muscles [34], and its skin is rich in sebaceous glands that secrete sebum, which maintains skin flexibility and moisture balance [35, 36].

The auricle's shape resembles a shell surrounding the entrance to the auditory canal [37]. The helix, forming the outer rim, curves inward and gives the ear its concave geometry. The anti-helix, a convex ridge inside the helix, defines the inner contour. Between them lies the scaphoid fossa, a shallow depression. Additional structures include the tragus, which projects from the front of the ear canal, the lobule (earlobe), composed of soft connective tissue, and Darwin's tubercle, a small projection found in some individuals that reflects a vestigial trait.

To ensure consistent description of anatomical structures and orientations throughout this thesis, Figure 2.5 defines the reference frames and terminology adopted from standard human anatomy [38]. All directions are given with respect to the subject in the anatomical position as depicted standing upright. Consequently, refer to directions toward and away from the

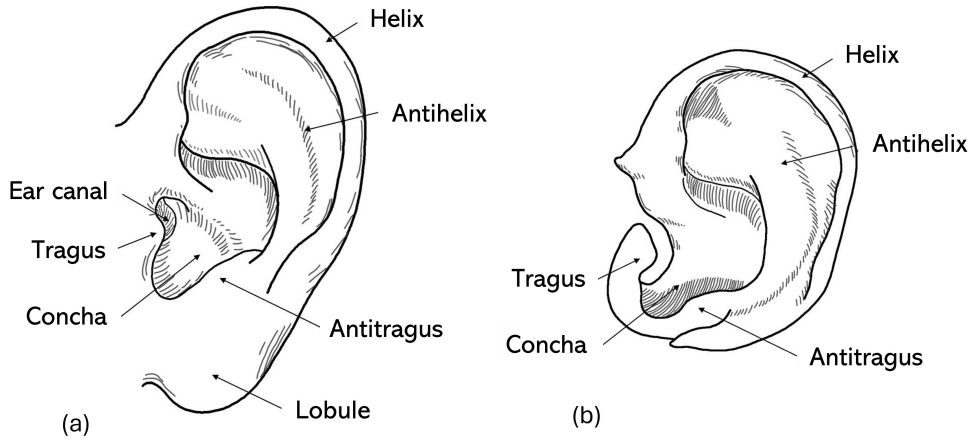


Fig. 2.4 Anatomy of the human auricle. (a) Schematic of the layered skin structure. (b) Cartilaginous framework of the auricle. The figure is adapted and redrawn from [33], with modifications by the author for clarity.

subject's body midline, respectively, "anterior/posterior" indicates the front/back aspects, and "superior/inferior" the upward/downward directions. These conventions are used for all subsequent descriptions of the auricle, device placement, imaging views, and model coordinate reporting unless otherwise stated.

2.2.2 On-Ear device design

The ear, as an exposed and stable facial region, has long been used to support accessories such as earrings and ear cuffs. From a design perspective, the concha is one of the most stable anatomical regions of the auricle. Located below the level of surrounding skin, it forms a natural recess that can securely accommodate devices such as earphones.

An example of practical on-ear sensing is the Cosinuss° One device, adapted for gait detection in a study by Burgos et al. [39]. As shown in Figure 2.6(a), the in-ear sensor captures movement data from a relatively stable point on the body—the head—allowing for more precise gait analysis. This method is especially valuable in real-world settings where photometric gait monitoring is impractical [40]. The improved stability and proximity to the body's centre of mass enable detection of sudden changes in motion, such as falls, making earable gait sensors useful for clinical and caregiver monitoring.

Traditional earphone designs are based primarily on external ear dimensions. However, as Lee et. al. demonstrated [42], optimal earphone design should also consider the shape and

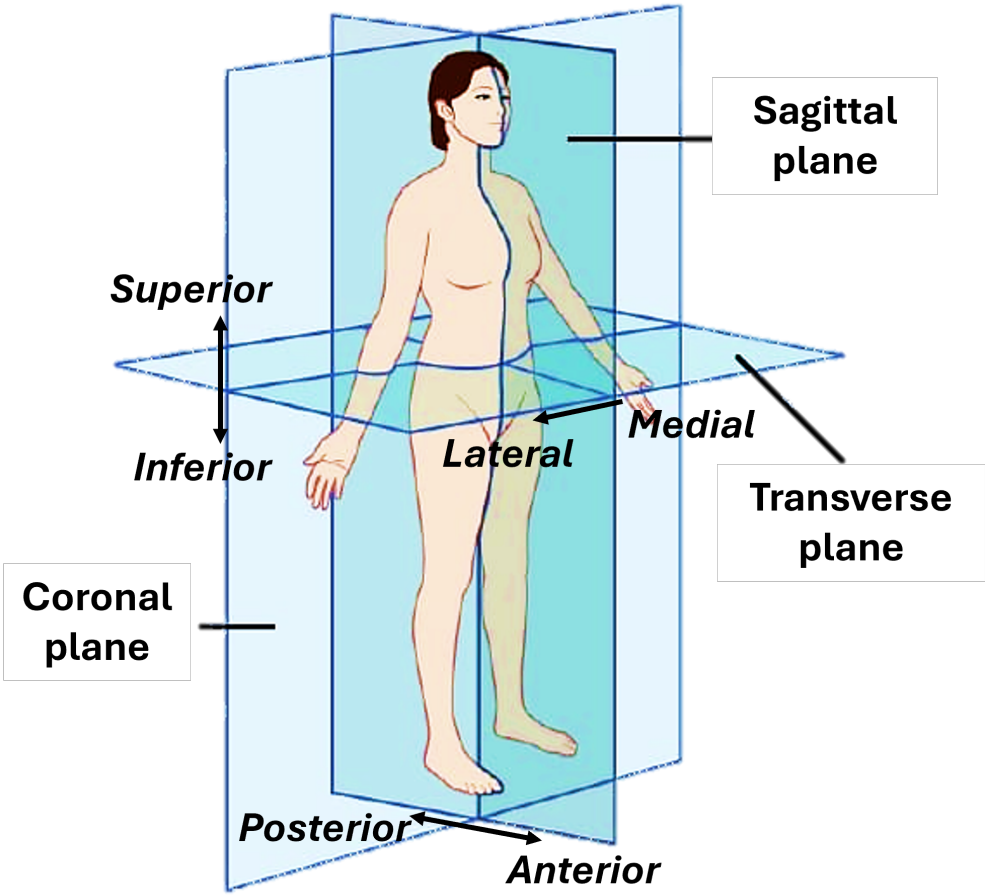
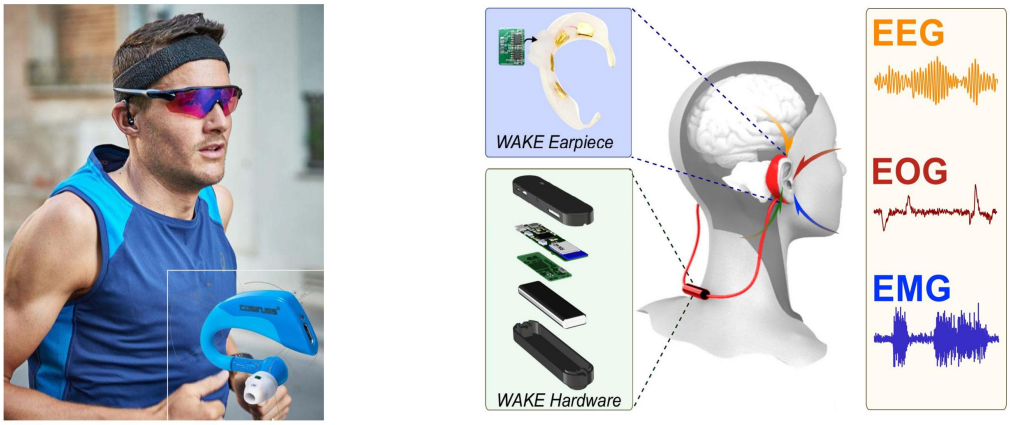


Fig. 2.5 Standard anatomical frames used in this work. The human figure is shown in the anatomical position with the three orthogonal reference planes: sagittal plane (dividing left and right), coronal plane (dividing anterior and posterior), and transverse plane (dividing superior and inferior).

geometry of the auditory canal. In that study, both the outer (pinna and concha) and inner (canal) structures were digitized to create personalized fitting models using 3D imaging.

Figure 2.7 illustrates the conventional ergonomic approach in earphone design, in which the main body of the device is seated within the concha of the auricle and the eartip extends into the auditory canal. Lee further proposed a set of auricular landmarks—such as concha depth, concha width, and canal angle—that can be generalised into ratio-based templates to facilitate mass customisation of earphone geometry.

Earable technology is also expanding into physiological monitoring. For instance, the 'Heartphone' developed by Poh et al. [43] is an intraconcha device designed for heart rate monitoring. Building on this concept, companies such as Plantronics have patented dual-ear



(a) (b)

Fig. 2.6 Ear based devices (a) In-ear accelerometer-based Gait sensor for 'Cosinuss° One'. Reproduced based on the study of Burgos et al.[39] (b) 'WAKE' device illustration reproduced based on the study of Pham et al.[41]

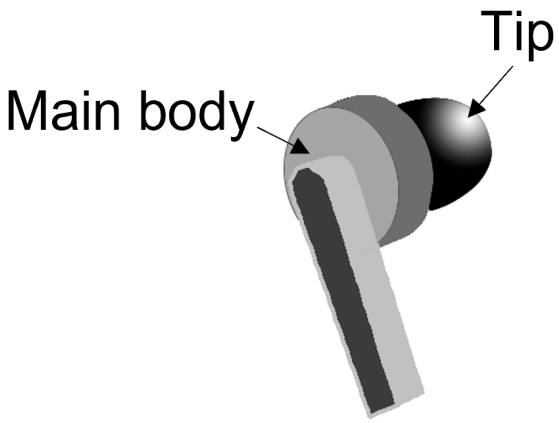


Fig. 2.7 Conventional earphone design, adapted from the Human Factors and Ergonomics Society 2016 Annual Meeting (p. 1054). In this design, the main body is positioned within the auricular concha, while the ear tip extends into the auditory canal.

heart-monitoring systems [44]. Venema et al. [45] demonstrated that these sensors can perform effectively in clinical settings, such as during surgeries, where patients are lying flat. They are also being explored for detecting atrial fibrillation in elderly populations [46].

In addition to health monitoring, user interaction is a growing area of interest. Researchers have explored hands-free control of earphones using tongue gestures. For example, one approach uses tongue movement detection via optical sensing: miniature infrared light emitters and photodiodes are embedded inside the earphone housing, facing the ear canal [47]. This demonstrates the potential of earable devices not just as sensors, but as intuitive interfaces for enhancing daily convenience.

In summary, on-ear device design must balance acoustic performance, structural stability, and long-term wearer comfort. Achieving this balance requires careful consideration of auricular geometry, load distribution, and material selection to minimise pressure hotspots while maintaining secure placement. Advances in ergonomic modelling and customization methods, such as ratio-based templates derived from auricular landmarks, provide a pathway toward designs that accommodate a wide range of users.[48] By integrating these principles, on-ear devices can deliver both functional efficiency and user acceptance, supporting their adoption in everyday and extended-wear applications.

2.2.3 Ear for neural signal collection

The proximity of the ear to the brain makes it a valuable site for biosignal acquisition. Numerous studies have demonstrated the feasibility of collecting EEG signals through ear-based wearable devices. Pham et al. developed a behind-the-ear device, WAKE, designed to detect microsleep episodes and assist users in maintaining alertness [41]. As shown in Figure 2.6b, the system integrates multiple signal modalities, including EEG, EOG, and electromyography (EMG), to enhance detection accuracy.

Research by Mikkelsen et al. has shown that ear-EEG can yield comparable event-related potential (ERP) signals to scalp EEG when the neural source is close to the ear [49]. Additional studies by Kidmose et al. [50] and Kappel et al. [51] further validated the robustness of ear-based EEG acquisition, demonstrating the viability of the auricular region for reliable and non-intrusive EEG monitoring.

Beyond EEG, the auricle has also been explored as a site for collecting other physiological signals. Nguyen et al. and Bui et al. have developed ear-based devices for continuous blood pressure monitoring and sleep stage classification, respectively [52, 53]. These findings reflect a growing research interest in the domain of earable technologies—multi-functional devices that are both wearable and ear-mounted.

In the area of gait detection, accelerometer-based earable devices offer a novel approach to capturing head movements. As the head remains relatively stable during locomotion, sensors

located at the ear can provide useful data on user intent and motion patterns. However, because the auricle is mechanically decoupled from the torso, vibrational transduction is limited. Further investigation is needed to model the relative motion between the auricle and the head or torso, which will enhance the reliability of auricle-based motion sensing systems.

2.2.4 Comfort Considerations for Ear-Based Devices

While many existing earable devices utilize the anatomical features of the auricle for structural support, they often neglect the critical aspect of user comfort. Individual variations in ear shape are significant, yet many prototypes are designed based on a single test subject or average anatomical models. As a result, many proposed devices are cumbersome, poorly fitted, or difficult to wear for extended periods.

There is currently no standardized metric for evaluating the mechanical comfort of ear-worn devices. A systematic study of auricular support properties is needed to inform device design. Such studies would help develop biomechanical models that quantify the load-bearing capacity and pressure distribution of the auricle. These models could in turn guide the design of earable platforms that are both functional and comfortable.

Despite the growing number of ear-based devices developed in recent years, few studies have systematically evaluated the impact of prolonged wear on user comfort. Commercial earphones, for example, have been known to cause skin irritation and even inflammation, often due to poor ergonomic fit or non-personalised designs. Even when ergonomics are considered, integrating sensory systems directly into existing commercial earphones often fails to achieve optimal performance. This is largely due to an incomplete understanding of how these devices mechanically interact with the complex structure of the auricle. These limitations underscore the importance of structural compatibility as a fundamental design criterion in the development of effective and comfortable earable technologies.

A comprehensive comfort assessment framework was proposed by Knight and Baber [54], who identified key factors affecting wearability—such as device size, shape, weight, and load distribution. They demonstrated how imbalances in these attributes could cause physical discomfort over time. Mase et al. further argued that in-ear devices are inherently less obstructive and more discreet compared to other wearable forms, potentially making them more suitable for long-term use [55]. More recently, Wang et al. explored the ergonomic and biometric potential of earable devices, introducing a novel ear-based authentication method based on anatomical and physiological characteristics [56].

2.3 Biomechanical Analysis

Mechanical analysis plays a vital role in the design of comfortable and functional earable devices. To fully realise the potential of such systems, their attachment mechanisms must be carefully engineered to balance stability and long-term comfort. The successful development of these devices depends heavily on the anatomical and mechanical characteristics of the external ear, particularly the auricle, including its shape, tissue composition, and surface features. This chapter establishes a biomechanical framework for evaluating earable wearability, including the development of comfort metrics and comparative analysis with commercial products.

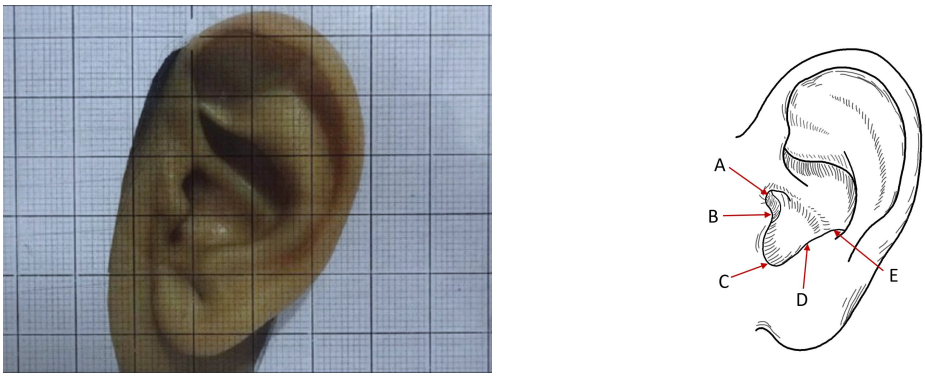
2.3.1 Structural Analysis

A thorough understanding of auricular structure is essential for optimising the mechanical interface between earable devices and the human ear. Due to substantial inter-individual variation in auricle morphology, a personalised approach to device design is often necessary. One practical and non-invasive method for obtaining auricular measurements is photoanthropometry, in which ear photographs are taken against a calibrated grid background to extract two-dimensional geometric parameters [57] (Figure 2.8a).

In-ear devices commonly anchor within the concha—the inner cavity of the auricle—which plays a critical role in retention and comfort. However, variations in conchal anatomy pose design challenges. Ji et al. addressed this issue by defining five key anatomical landmarks around the concha and classifying ear shapes based on their spatial distribution patterns [48] (Figure 2.8b). Similarly, Modabber et al. employed three-dimensional morphological analysis to derive spatial vectors and anatomical profiles suitable for custom-fit wearable technologies [58].

Biomechanical structural analysis often involves evaluating material alignment, contact pressure, and internal stress distribution, methodologies widely applied in musculoskeletal research, such as femoral bone studies [59–61]. Since direct stress measurements *in vivo* are impractical, finite element (FE) simulations are frequently used to model the distribution of mechanical forces in tissues and interfaces [62]. This technique can similarly be used to estimate stress, pressure, and friction between earable devices and auricular skin during real-world use.

Structural modelling of the auricle often begins with medical imaging techniques such as MRI or CT. These modalities provide detailed internal anatomical data, which can be



(a) (b)

Fig. 2.8 Ear structure study (a) Photoanthropometry of auricle structure[57]. (b) Characteristic points around concha of auricle[48]

processed using segmentation methods. One common technique, intensity thresholding, converts grayscale images to binary masks by classifying pixel values above or below a defined threshold, which is useful in separating auricle tissue from surrounding air or ear canal cavities [63].

Alternatively, 3D surface scanning offers a non-invasive means of capturing auricular geometry. For example, Lee et al. used face scans to create custom-fit respiratory masks for paediatric patients [64]. The advantage of this method is its iterative efficiency in achieving subject comfort, especially for live human studies. However, its limitation lies in capturing only surface topography, without insight into internal cartilage structure. In addition, the reconstruction of accurate 3D models requires substantial computational effort and expertise in digital processing workflows.

Another useful tool for biological structure study would be mimicking phantoms, which are physical models designed to replicate the geometry, mechanical properties, and tissue-layer structure of human anatomy. For instance, researchers have developed skin phantoms to model the interaction with dry electrodes across the range of frequencies necessary for biopotential signals, aiding in the characterization of wearable electrodes in electrophysiological monitoring applications [65]. Similarly, corneal phantom models have been fabricated to study the dynamic response of early keratoconus under air puff stimulation, providing insights into corneal biomechanics [66]. A phantom model for human ear can greatly aid the development of earable devices.

2.3.2 Ear Material Analysis

The mechanical behaviour of the auricle is shaped by its composite layers—namely cartilage, connective tissue, and skin. The auricular cartilage serves as the load-bearing framework, while the overlying skin and subcutaneous tissues contribute damping and compliance. Both components jointly determine the response of the ear under external force, which is critical for understanding device fit and stability.

Griffin et al. (2016) evaluated the regional mechanical properties of auricular cartilage through indentation testing, simulating the effects of localised compression. They found notable stiffness variation across different anatomical sites, with the helix exhibiting a lower Young's modulus (1.4 MPa) and the concha showing higher stiffness (2.1 MPa) [67]. These findings highlight the importance of region-specific considerations in earable device design.

Stephen et al. reported even higher values (5.11 MPa) using tensile testing of engineered cartilage samples shaped into standardised dog-bone specimens [68]. Variability in mechanical properties can arise from multiple factors, including donor age, ethnicity, and post-mortem degradation. Similar inconsistencies are noted in skin tissue studies, particularly due to the difficulty of measuring properties *in vivo* [69–71].

To address the limitations of in vitro study, several non-invasive methods have been proposed. Lakhani et al. used vacuum suction techniques to estimate *in vivo* skin stiffness by tracking tissue displacement under negative pressure [72]. Other methods include dynamic indentation testing to evaluate viscoelastic behaviour at shallow depths [73], and force-torque transducer-based tangential loading for shear deformation analysis [74]. Despite their promise, these techniques often encounter limitations such as adhesion artifacts, limited loading capacity, and challenges in extracting absolute modulus values.

In a subsequent study, Griffin et al. (2017) used forearm skin as a surrogate for auricular skin and reported an average Young's modulus of approximately 1.03 MPa [70]. Given the inherent variability and complexity of biological tissues, such proxy measurements should be interpreted with caution. As suggested in other literatures, the stiffness of human skin tissue can vary from 50 kPa to 1.2 MPa depending on skin region and experiment methods [75–77]. Mechanical properties can vary markedly with anatomical location, underlying tissue composition, hydration state, and individual physiological differences. Consequently, while average values offer a useful reference, they cannot fully represent the heterogeneity of auricular tissue mechanics. This underscores the need for direct, site-specific characterisation and appropriate material models to capture the substantial variation observed across individuals and the complex behaviour of soft biological tissues.

2.3.3 Finite Element Analysis

FE Analysis is a computational tool used to model and predict the mechanical response of complex structures under various loading conditions [78]. For mechanical properties of the auricle, FE provides a practical method to simulate stresses, strains, and deformations without invasive procedures. This is particularly advantageous given the anatomical complexity and inter-individual variability of the auricle, which makes standardised experimental testing challenging [79].

By integrating three-dimensional structural models derived from medical imaging or surface scanning, the auricle can be discretized into element mesh that represent components such as the skin, cartilage, and connective tissue. These models can be assigned heterogeneous material properties, such as tissue-specific Young's modulus values obtained via indentation or tensile testing, and subjected to boundary conditions that emulate real-world interactions, including device attachment, compression, and motion [80, 81].

Many studies have successfully applied FE analysis in biomechanics and biomedical engineering to assess soft tissue deformation, contact pressure distribution, and to guide the optimisation of medical and wearable device designs [62]. In facial reconstructive surgery, Chabanas et al. introduced a three dimensional graphic model of the human face with a finite element mathematical model to estimate the biomechanical consequences of tissue ablation and rearrangement [82].

FE methods are particularly valuable in the design of earable devices, enabling detailed simulation of the pressure exerted by the device on the complex auricular surface, assessment of deformation under dynamic loading, and optimization of material properties and geometries to enhance both wearability and stability [83]. For instance, FE simulations have been used effectively in analogous contexts, such as predicting contact pressures, deformation, and resulting comfort in earpieces navigating the geometry of the ear canal [84]. These application helps guide design improvements towards better user experience. This approach underscores the utility of FE analysis in translating anatomical complexity into quantitatively informed design decisions for comfortable, secure, and ergonomic earable systems.

In the context of earables, this method allows researchers to predict areas of high stress concentration that may contribute to discomfort or skin irritation. The study of Benacchio et al. used the FE method to determine the stress concentration induced by insertion of ear plugs in the ear canal [85]. Furthermore, simulations can be iteratively adjusted to explore the effect of different material choices, attachment geometries, and user-specific anatomies.

At present, a key gap in the development of earable devices lies in the absence of a robust, predictive framework that can capture the mechanical behaviour of the auricle under realistic usage conditions. Physical testing alone cannot fully account for the anatomical complexity, variability between individuals, and the range of dynamic loading scenarios encountered during daily wear. FE analysis offers a pathway to address this shortfall by enabling the validation of mechanical assumptions, the systematic refinement of design parameters, and the extrapolation of laboratory findings to real-world contexts.

2.4 Contact Considerations for Wearable Devices

Earable devices remain in prolonged contact with the auricle and adjacent skin. Ensuring comfort, safety, and stable signal acquisition requires a deep understanding of both pressure distribution and mechanical behaviour under dynamic conditions. This section discusses key challenges, including ergonomic fit, pressure sensitivity, and robustness under motion.

2.4.1 Pressure Distribution

Improper ergonomic design can lead to excessive localized pressure, causing user discomfort and potential skin injury. In-ear devices, in particular, are prone to causing inflammation and irritation with long-term wear.

FE simulation is an effective tool to model how a device distributes pressure across skin surfaces. For instance, Lee et al. used FE analysis to optimize the shape of oxygen masks for different facial structures [86]. They built mesh models of both the face and mask to simulate contact pressures and evaluate ergonomic fit. A similar approach could be applied to simulate earable device interaction with auricular geometry.

In addition to computational modelling, user-centred studies provide insight into real-world comfort. Chiu et al. evaluated discomfort associated with various Bluetooth earphones by surveying users with different auricle shapes [87]. Their findings suggest that pressure concentration in specific auricular regions correlates with discomfort and pain, and should be minimized in design.

Beyond mechanical discomfort, poorly fitted earpieces may contribute to skin health issues. Rafidah et al. noted that prolonged friction from ill-fitting earphones can lead to skin irritation and minor trauma [88]. Additionally, unventilated in-ear designs can raise temperature and

humidity within the ear canal, disrupting natural tissue conditions and increasing infection risk [89].

2.4.2 Robustness Under Motion

A crucial design challenge for earable and on-ear sensor systems is maintaining stable device operation during user movement. Everyday activities such as walking, jogging, or speaking introduce mechanical vibrations and motion that can disrupt sensor contact and degrade signal quality, an issue especially detrimental in EEG and other sensitive biosignal measurements [90]. For instance, studies emphasize that motion artifacts in dynamic EEG recordings arise from disturbances at the skin–electrode interface, connecting cables, and acquisition circuitry, compromising signal fidelity in portable and wearable contexts [91, 92].

Stability under motion is particularly important for sports-oriented earphones, where users frequently report that devices fail to remain securely in place during intense activity. As suggested by Choi et. al.(2022), factors such as sweat and earwax can diminish skin friction, complicating retention and forcing designers to strike a delicate balance between wearer comfort and device stability [92].

Motion induced artefacts present a major challenge for sensor based earable systems. In an earphone based eye gesture control study, Manabe et al. showed that everyday head and body movements led to false inputs and unstable baselines [93]. While conductive elastomer materials such as Ag rubber can enhance signal reliability, improvements at the material level alone do not fully resolve motion artefacts. As a result, careful mechanical design is required to limit motion induced disturbances in ear mounted wearable devices.

Mechanical improvements such as custom moulded earpieces and soft conformal interfaces can substantially enhance stability by maintaining consistent contact and reducing slippage. Studies on in ear EEG systems have shown that custom fit designs provide better comfort, improved electrode skin contact, and greater resistance to motion induced signal degradation when compared with generic designs [94]. Similarly, research on wearable electrodes demonstrates that optimised geometry and attachment strategies, including dual electrode configurations and conformal electronics, can markedly improve robustness to motion artefacts during dynamic activities such as running or jumping [95].

For earable EEG systems, more studies are needed in the mechanical analysis and design required to ensure a stable electrode–skin interface during motion. Although advances in electrode materials have been considerable, far less attention has been devoted to the structural and biomechanical factors that drive motion-induced artefacts. Progress in this area

will depend on integrating mechanical modelling, ergonomic form factor optimisation, and motion-decoupling strategies, which are key elements for achieving comfortable, high-fidelity, and robust wearable neural interfaces.

2.4.3 Material for Wearable Devices

A complete test procedure is required for selecting materials suitable for earable device design. In the field of soft wearable devices (SWDs), materials are typically evaluated based on their flexibility, adaptability, and lightness [96].

Dávila-Vilchis and her research team proposed a structured framework for wearable device development, integrating medical, therapeutic, and engineering perspectives to guide the selection of soft materials [97]. This framework is divided into four key phases. The first involves identifying user needs and existing problems, along with reviewing related solutions in the literature. The second phase focuses on establishing project requirements and generating initial design concepts. In the third phase, selected concepts are refined and validated through simulations or theoretical models. Finally, the fourth phase includes user testing to assess real-world performance. Each phase contributes to refining the material selection process, ensuring the device meets functional, ergonomic, and clinical standards.

In a review on wearable systems for Parkinson's disease, Almahadin et al. highlighted the importance of user comfort and material acceptability. Patients expressed preferences regarding different materials, such as cloth, metal, and leather, and noted concerns about skin comfort, including whether materials would increase humidity or cause stickiness and discomfort during prolonged use [98].

Hence, the design of Earable devices must prioritize biocompatible, breathable, and skin-friendly materials, especially given the sensitivity of the auricle and surrounding areas. The material must also support secure contact without causing irritation, maintain performance under motion, and be suitable for long-term, daily wear. These requirements will guide material testing and selection in the development process of the Earable platform.

2.5 Summary of Literature and Research Gap

This chapter has reviewed the interdisciplinary foundations, design considerations, and biomechanical principles relevant to the development of earable neural interface (NI) devices. It explored the anatomical advantages of the ear for biosignal acquisition, especially for EEG,

EOG, and other physiological signals, highlighting its potential as a stable, non-invasive, and user-accepted platform.

Current advances in wearable technology demonstrate growing interest in integrating sensing systems into ear-mounted devices. Studies have shown promising results in ear-EEG performance, gait detection, cardiovascular monitoring, and even user interaction through in-ear gesture control. However, many existing solutions lack systematic attention to long-term comfort, structural compatibility, and robustness under motion.

The mechanical structure and material properties of the auricle vary significantly among individuals. While prior research has begun exploring auricle morphology and material characterisation, there remains a lack of comprehensive models that link biomechanical analysis, material choice, and user comfort metrics into a cohesive design framework. Furthermore, few studies evaluate how device–tissue interactions affect comfort, stability, and signal quality in real-world, dynamic settings. In particular, there is a clear gap in mechanical analysis and motion-decoupling design for earable EEG systems, where ensuring a stable electrode–skin interface under motion is critical to reducing artifacts. Addressing this requires integrating mechanical modelling, ergonomic optimisation, and structural innovation into the design process alongside material selection.

In summary, although significant progress has been made in earable technology, there remains a clear gap in a unified design methodology that couples personalisation, biomechanical modelling, material analysis, and comfort testing with a predictive, physics-based design loop. To address this, this thesis incorporate realistic model FE simulation of the auricle to quantify deformation, contact pressure distribution, and dynamic response under wearing and activity conditions. These FE outputs can be used to iterate device geometry, placement, and material choices prior to prototyping, and then be cross-validated against impedance, fit, and comfort measurements. This project therefore proposes a structured, simulation-in-the-loop platform for developing versatile, comfortable, and sensor-integrated earable systems.

Chapter 3

Mechanical Study with Auricle Phantom Model

3.1 Introduction

Accurately assessing the mechanical properties of the human auricle poses significant challenges. While *in vivo* experiments offer the most reliable biomechanical data, the auricle's soft tissue complexity, individual anatomical variability, and the lack of standardised test procedures make it difficult to perform such assessments. Additionally, the auricle's superficial location and variable skin and cartilage composition further complicate accurate measurement.

To overcome these limitations, this study began by constructing a physical phantom model of the human auricle, a replica with known geometry and selected material properties. Phantom models are widely used in biomedical engineering for situations where *in vivo* testing is impractical or ethically restricted, such as ultrasonic imaging, cardiovascular simulations, and musculoskeletal loading studies. In this context, the auricle phantom serves as a controllable and repeatable proxy to explore auricular mechanics under a variety of loading conditions.

The phantom model was designed to replicate key structural features of the human auricle using a medical image processed ear-shaped construct. Its fabrication employed a combination of 3D printing and silicone gel moulding. These techniques offer the precision needed to replicate anatomical structures, as well as the cost effective construction of models.

Once fabricated, the phantom was subjected to mechanical testing to evaluate its structural behaviour under static and dynamic loading. These experiments aimed to characterise

stiffness, deformation patterns, and vibration properties. This phase of testing also served to refine methodologies and hardware setups in preparation for later *in vivo* studies on human subjects.

Understanding the auricle's mechanical behaviour is particularly relevant to the development of earable technologies, where accurate skin-device contact, long-term comfort, and vibration stability are critical. The outcomes of this phantom-based study therefore not only validate experimental techniques but also provide a physical model for examining interaction between wearable biomedical devices and auricle structure.

Objectives

The primary objectives of this chapter are as follows:

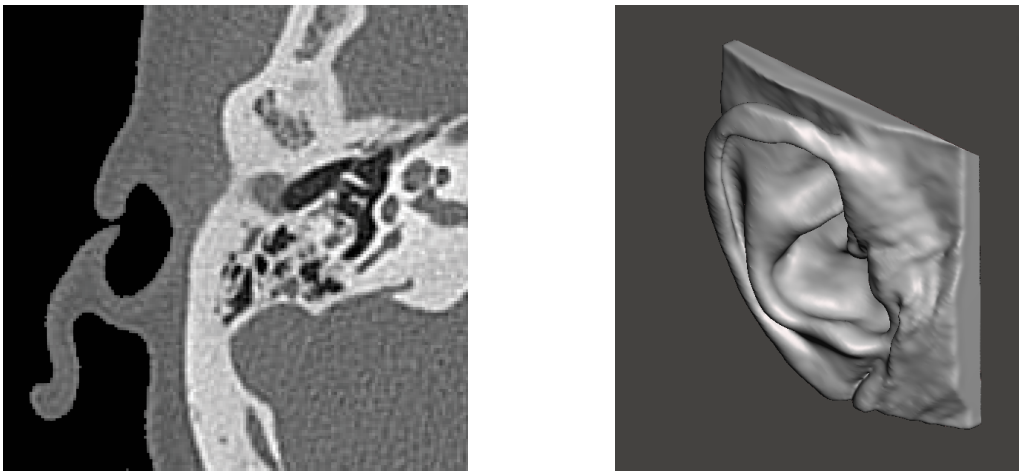
- Construct auricle phantom models from medical imaging data.
- Design and implement loading protocols to assess the mechanical behaviour of auricle phantoms.
- Quantify deformation characteristics of the auricle phantom under static and dynamic loads.
- Build and validate a finite element model to simulate auricular mechanics.
- Compare experimental results with simulations to assess predictive accuracy and limitations.
- Refine phantom fabrication techniques to better approximate *in vivo* auricle properties.

3.2 Phantom Model Construction

This section describes the construction process of a phantom model of the auricle. The auricle geometry was derived from a medical image and generated into a 3D model. A secondary inner layer was incorporated to replicate the cartilage of the auricle, allowing the model to mimic the internal structure and mechanical behaviour of the human auricle. The resulting 3D model was modified to enhance its manufacturability for phantom models.

3.2.1 Medical Image Processing

The phantom model was initially developed from a medical image of a cadaver ear. A computed tomography (CT) scan of the head, including the external ear, was acquired for cochlear researches by Hrncirik et al. [99]. The data acquisition and scanning were performed by certified professionals. Figure 3.1(a) illustrates the original CT scan, showing the anatomical structure of the head and ear. The auricle was segmented from the scan using Amira* software, employing intensity thresholding to isolate the external ear structures, as shown in Figure 3.1(b).



(a) (b)

Fig. 3.1 Auricle model acquisition techniques: (a) micro-CT scanned image including the ear section; (b) segmentation result of the ear and its surroundings.

The original segmented auricle model retained the full anatomical detail of the external ear, which posed significant challenges for phantom fabrication. In particular, the overall structure was too thin, with deep troughs and sharp edges that made it difficult for silicone gel to fill the mould uniformly and demould cleanly. To address these issues, the model was simplified using mesh editing software (Meshmixer 3.5; Autodesk, CA). The modifications included increasing the overall thickness of the auricle, reducing curvature and slope angles, and removing non-essential anatomical features such as the tragus and ear canal. The resulting simplified model is shown in Figure 3.2.

To more accurately replicate the auricle's internal architecture, it was necessary to include a model of the auricular cartilage. However, standard CT imaging lacks sufficient soft tissue contrast to clearly differentiate cartilage from surrounding tissue. While magnetic resonance imaging (MRI) offers better soft tissue contrast, it typically does not provide sufficient resolution to capture the thin cartilage layer of the auricle. Based on anatomical literature

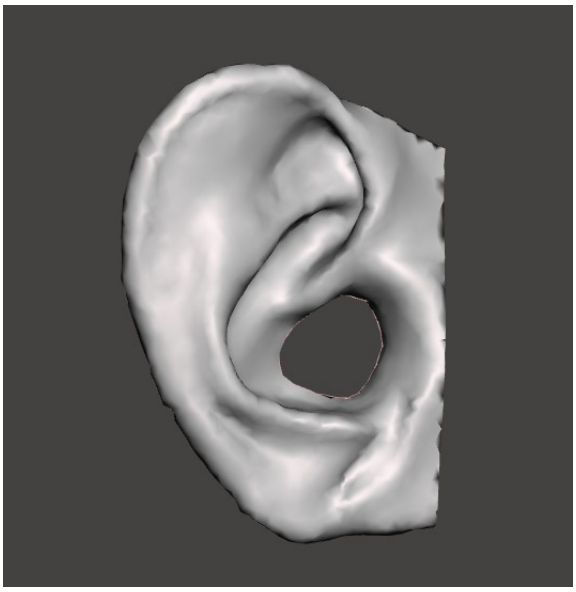


Fig. 3.2 Simplified auricle model edited and rendered with Meshmixer

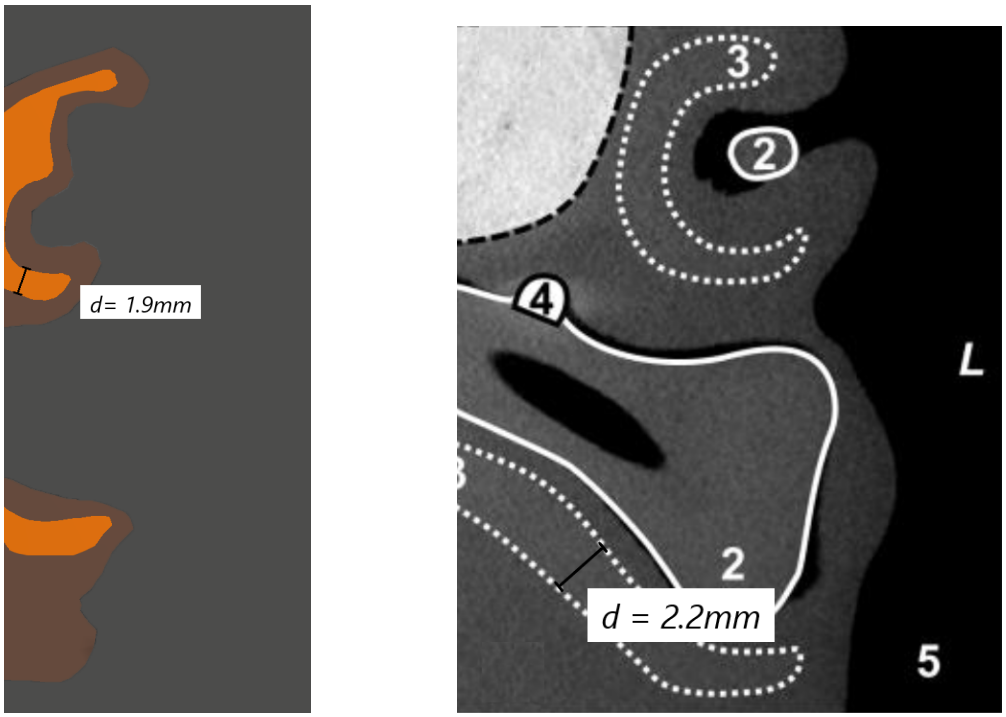
[33], auricular cartilage is known to span the helix, antihelix, and concha, but is absent in the lobule, which was shown in Figure 2.4. Using this anatomical guidance, the cartilage was estimated by applying the *Hollow* function in Meshmixer to generate a uniformly contracted inner layer from the outer auricle model. The lobule portion was subsequently truncated to reflect the absence of cartilage in that region. Cross-sections of the final model are shown in Figure 3.3(a).

This structural approximation is consistent with the methodology used by Benacchio et al., who constructed an artificial ear with a similarly layered cartilage geometry for in-ear device testing [85]. Their cross-sectional representation, aligned in the similar anatomical plane, is reproduced in Figure 3.3(b) for comparison.

With the simplified geometry and layered structure defined, the next step was to physically realise the auricle phantom using appropriate manufacturing techniques.

3.2.2 Phantom Manufacture

Following the completion of the digital model, a physical phantom was fabricated using a combination of 3D printing and injection moulding techniques. The inner cartilage core was first printed with a Formlabs 3B printer (Form 3B; Formlabs, USA), utilising a soft and elastic photopolymer resin (Elastic 50A Resin; Formlabs, USA). As shown in Figure 3.4(a), a three-piece mould box was designed using Fusion 360 (Autodesk, USA), based on a negative



(a) (b)

Fig. 3.3 Comparison of auricle cross-sections. (a) Cross-section of the FE auricle model after generating the cartilage layer. (b) Anatomical reference cross-section adapted from Benacchio et al. [85], illustrating measured cartilage thickness.

extrusion of the simplified auricle geometry. This three-piece configuration was selected to accommodate the complex curvature of the auricle, while also facilitating demoulding without damaging the delicate structure. To ensure precise alignment between mould sections during assembly, integrated shafts and pin-holes were included in the mould design.

To replicate the mechanical characteristics of subcutaneous fat and skin tissue on the auricle's exterior, a silicone gel was selected for significantly lower stiffness than the 3D-printed cartilage material. According to Griffin's study, the Young's modulus of human auricular cartilage typically ranges from 1.4 MPa to 2.1 MPa [67], while the modulus of human skin generally falls between 0.05 MPa and 1.2 MPa [100]. This difference in tissue property highlights the need for a dual-material approach to replicate both layers of auricular tissue.

The phantom model was constructed as a two-layer structure to replicate auricular anatomy, with a soft external skin layer enveloping a more rigid internal cartilage core. The cartilage was 3D printed and the silicone gel for casting are mixed for the preparation of phantom construction. During assembly, the cartilage core was suspended centrally within the mould

cavity, leaving a uniform gap between the core and the surrounding mould walls. This cavity was then filled with a two compound silicone (Silastic 3481 RTV Silicone Moulding Rubber; East Coast Fibreglass Supplies, UK) by injection with a 10 ml syringe to form the outer skin layer. Prior to casting, the silicone gel was degassed under vacuum for 10 minutes to eliminate entrapped air bubbles. The filled mould was subsequently left to cure overnight at room temperature.

Initial fabrication trials revealed a consistent challenge: the silicone gel, when injected from the top, tended to flow unevenly, causing displacement of the cartilage core and resulting in asymmetric skin layer thickness. To resolve this, the injection port was relocated to the bottom of the mould box. This adjustment allowed silicone to rise upwards more uniformly, significantly reducing bubble entrapment and lateral shifting of the cartilage during curing. As a result, casting precision and overall geometric fidelity were improved. The final manufactured phantom, shown in Figure 3.4(b, right), features a pink-tinted silicone outer layer to improve contrast for imaging and to facilitate optical tracking of external markers in subsequent experiments.

While modifying the injection strategy addressed global flow and alignment issues, further improvements were required to ensure consistent local bonding and mechanical stability within the phantom. To this end, several design modifications were applied to the cartilage component, as shown in Figure 3.4(b, left). Circular holes were introduced throughout the core to promote even flow of silicone and reduce the likelihood of trapped air pockets. In addition, wedge shaped features were added along the interface to increase the contact surface area between the cartilage and skin layers, thereby improving interlayer adhesion. Anchoring holes at the base allowed the model to be fixed securely using alignment pins, which proved useful both during casting and in subsequent experimental tests.

Although these fabrication and design choices improved reproducibility and mechanical robustness, the phantom geometry remained a simplified representation of the human auricle. As mentioned in Section 3.1, certain anatomical components, such as the tragus and deeper portions of the ear canal, were excluded due to limitations in the source imaging data and to simplify the fabrication process. These features were considered to have minimal influence on the mechanical response of the auricle's outer geometry and were therefore omitted in this prototype. A more anatomically detailed phantom was developed at a later stage to support extended investigations.

To characterise the mechanical properties of the phantom materials, uniaxial tensile tests were performed on both cured silicone gel and 3D-printed cartilage specimens. The experiments were conducted using an Instron universal testing machine (Model 5584; Instron, USA)



(a) (b)

Fig. 3.4 Combined method result. (a) Assembly of the mould box with the cartilage layer mounted on the middle part (b) Relative size compared to a GBP pound coin of manufactured auricle phantom, left is the 3D printed cartilage, right is the final phantom

equipped with a 10 N load cell, which enabled precise measurement of force and displacement. Standardised dog-bone specimens were prepared following conventional protocols, with a gauge section of 1.6 mm $\times$ 2.0 mm in cross-section and 12.0 mm in height, and overall specimen dimensions of 40.0 mm $\times$ 10.0 mm $\times$ 1.6 mm. The primary objective was to establish stress–strain relationships and extract elastic parameters relevant to the modelling of auricle mechanics.

The test results are presented in Figure 3.5, with the experimental data fitted using a first-order Ogden hyperelastic model. Alternative hyperelastic formulations were evaluated during preliminary analysis; however, the Ogden model was found to provide the most effective balance between fitting accuracy, parameter parsimony, and numerical stability across the relevant strain range[101]. It was therefore adopted for subsequent material characterisation. The strain energy density function for the one-term Ogden model is expressed as

$$W = \frac{\mu}{\alpha}\left(\lambda_1^{\alpha} + \lambda_2^{\alpha} + \lambda_3^{\alpha} - 3\right), \tag{3.1}$$

where λ_i are the principal stretch ratios, α is a dimensionless parameter governing strain stiffening, and μ is a material scaling parameter with units of Pa. It is noted that different normalisations of the Ogden strain-energy function exist in the literature. The present form is retained for consistency with the experimental fitting procedure used in this work. Under this parameterisation, μ does not directly correspond to the small-strain shear modulus. By comparison with the standard Ogden formulation, the initial shear modulus is given by

$$G_0 = \frac{\alpha}{2}\mu. \tag{3.2}$$

For isotropic linear elasticity, the small-strain Young's modulus is related to the shear modulus by $E_0 = 2G_0(1+\nu)$. For nearly incompressible materials ($\nu \approx 0.5$), this yields

$$E_0 \approx \frac{3\alpha}{2}\mu. \tag{3.3}$$

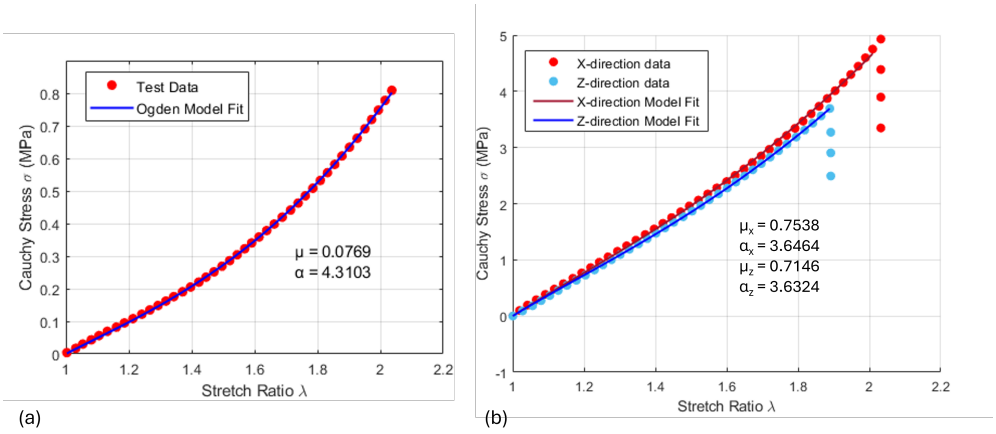


Fig. 3.5 Tensile testing of auricle phantom materials: (a) moulded Silastic 3481 dog-bone specimen; (b) two 3D-printed Elastic 50A specimens, one printed flat on the platform (x-direction) and the other printed vertically (z-direction). μ in both plot have the unit of MPa

Material	Effective Young's Modulus	Volume in model	Weight Used in production
Silicone gel	3.35 MPa	8.8 mL	10.56 g
Elastic SLA	0.42 MPa	9.28 mL	9.81 g

Table 3.1 Materials used in the manufacturing of the auricle phantom

At small strains, the estimated Young's modulus was approximately 0.42 MPa for Silastic 3481 and 3.35 MPa for Elastic 50A. These values represent about twice the stiffness reported for native auricular cartilage and skin; however, this discrepancy is considered acceptable within the context of this study. The phantom model is primarily intended as a platform for developing and validating experimental methods to assess auricle deformation under external loading. As such, the trade-offs in material selection and geometric simplification are justified by the need for structural robustness, repeatability, and practical manufacturability.

Studies relating to additive manufacture had revealed that the printing orientation can effect material stiffness [102]. To evaluate the influence of print orientation on mechanical performance, additional Elastic 50A specimens were fabricated in two build directions: the

x-direction (dog-bone axis parallel to the build platform) and the z-direction (dog-bone axis perpendicular to the build platform). As illustrated in Figure 3.5(b), the x-direction print exhibited slightly higher stiffness and ultimate strength, consistent with stronger inter-layer bonding when tensile loading is aligned with the build plane. Conversely, the z-direction prints, loaded perpendicular to the layer stacking, demonstrated reduced strength due to weaker interlayer adhesion. These results confirm a degree of anisotropy inherent to stereolithographic 3D printing, but the variations remained within tolerances acceptable for the intended phantom application.

The Silastic 3481 silicone specimens exhibited highly compliant and stretchable behaviour, consistent with the mechanical profile of skin-like soft tissues. In contrast, the Elastic 50A resin displayed greater stiffness and reduced extensibility, aligning with expectations for a cartilage-mimicking analogue. A summary of the effective linear material properties used in the phantom model and their usage in volume and grams are provided in Table 3.1.

To contextualise the design choices of the auricle phantom developed in this work, a comparison is made with the artificial ear phantom reported by Benacchio et al..[85] While both phantoms aim to reproduce aspects of human ear mechanics, they were developed for different primary objectives. Table 3.2 summarises the key differences between the two phantoms in terms of material stiffness, intended utility, anatomical regions included, and fabrication cost, highlighting the complementary nature of the two approaches.

Aspect	**This work (Auricle phantom)**	**Benacchio et al. (2018)**
Targeted mechanics	Global auricle stiffness and low-frequency dynamic response (soft silicone, $E \sim 0.4$ MPa).	Local ear canal compliance during insertion (multi-material silicone).
Primary purpose	Mechanical characterisation, FE validation, and device–ear interaction studies.	Ultrasound-based measurement of ear canal wall displacement.
Anatomy included	External ear (auricle only).	Full ear geometry including ear canal.
Fabrication	Low-cost, modular moulding; suited for iterative testing.	Higher complexity due to multi-material and imaging constraints.

Table 3.2 Comparison between the auricle phantom developed in this work and the artificial ear phantom reported by Benacchio et al. (2018).

3.3 Static Loading Response

Upon completing the fabrication of the phantom model, the next objective was to examine its mechanical behaviour under controlled loading. The most immediate method for characterising the auricle's response was through direct mechanical stretching. This experiment involved applying a static load to the auricle phantom and observing the resulting deformation. The experiment aimed to characterise the structural behaviour of the auricle by quantifying its deformation under a gradually increasing static force.

3.3.1 Experiment Method

As introduced earlier, these tensile experiments were designed to reproduce the type of mechanical deformation experienced by the auricle under external force, thereby providing insight into the structural response of the phantom model. The same Instron test system used in Section 3.2 with the 10 N load cell was employed to ensure consistency across material assessments. This mechanical testing platform, characterising base material behaviour and simulating auricle shape deformation, ensured that the phantom construction reflected both material and structural fidelity.

To securely fix the auricle phantom during testing, a custom base was designed and 3D-printed using a hard Grey Pro resin (Formlabs, USA). This base incorporated alignment pins that ensured consistent and stable attachment of the phantom to the lower grip of the Instron machine. The upper grip was connected to the tip of the auricle via a flexible string, creating a pulling mechanism that mimics real-world external traction forces, as illustrated in Figure 3.6(a).

A key assumption underlying the test setup is that, in the human body, the auricle is anchored to the skull, the structure with significantly greater rigidity compared to the soft auricular tissue. Therefore, for mechanical testing purposes, it is assumed that deformation occurs exclusively in the auricular structure. To replicate this natural constraint, the phantom was mounted onto a rigid 3D-printed base connected to the Instron rig, serving as a non-deforming boundary condition throughout the duration of the test.

In order to monitor displacement and track structural deformation, the experiment was recorded using a camera system (PL-B776F; Pixelink, Canada). Figures 3.6(b) and (c) show the experimental pictures for both lateral and anterior pulling tests. The experimental rig was designed to accommodate the phantom securely and reproducibly across different test conditions.

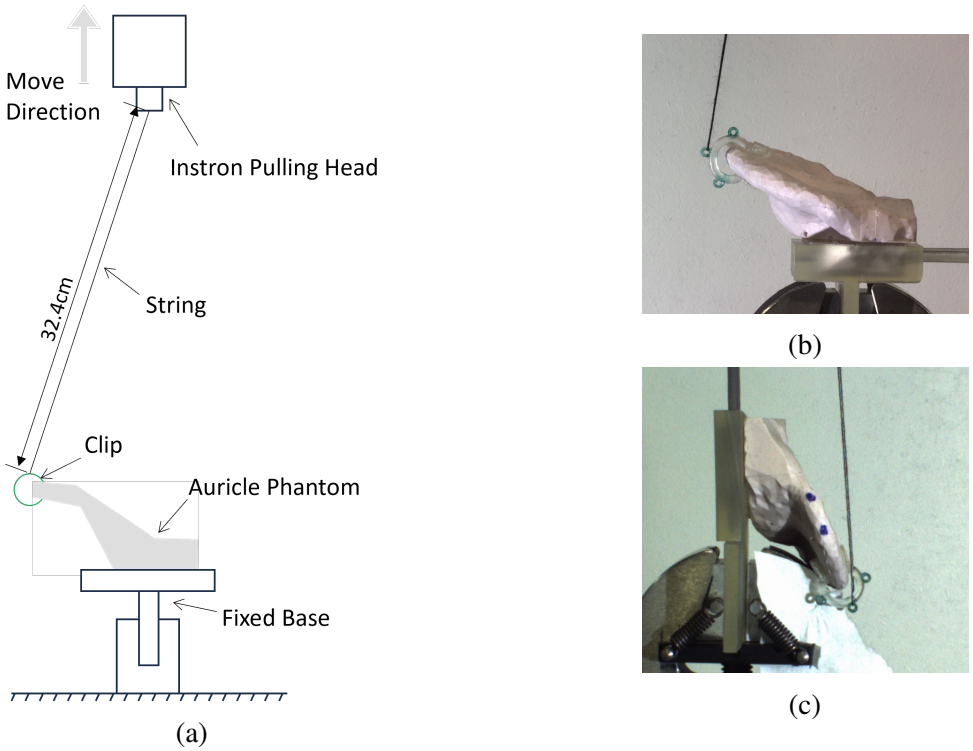


Fig. 3.6 Static loading setup for auricle pulling experiment. (a) Overall sketch of the experiment setup (b) picture for auricle phantom loaded at lateral pulling position (c) picture for auricle phantom loaded at anterior pulling position

A 3D-printed clip was fabricated using a clear, rigid resin (Clear V4 Resin; Formlabs, USA) to attach the pulling string to the auricle phantom. The clip was engineered with multiple functional features. First, soft inner padding layers were applied to enhance surface grip and prevent slippage or localised deformation at the point of contact with the auricle. Second, ring-shaped extensions were incorporated into the design to serve dual functions: as anchor points for the string, and as visual tracking markers for the camera system. These rings were coloured green to ensure high contrast against the phantom's pink exterior, facilitating accurate displacement tracking through image processing.

To process the captured images, a custom image-analysis script was implemented in MATLAB (R2022b; MathWorks, Inc.). The tracking workflow is summarised in Figure 3.7. First, colour filtering was applied to isolate the green attachment rings (Figure 3.7, step 2). The filtered output was then processed using a circular fitting algorithm, with the detected ring contours shown in blue (Figure 3.7, step 3). From the position of the 3 fitted circle, the midpoint between the two clip pads, which is a point located in the middle layer of the phantom, was extracted and marked in red. This point represents the effective clip attachment

and pulling location, and its trajectory was used for subsequent mechanical analysis of auricle deformation. The analysis considers only in-plane motion and neglects displacement along the superior–inferior axis, as a limitation of the photometric tracking approach. Because the camera captured motion from a single viewpoint, out-of-plane (three-dimensional) displacement of the clip could not be resolved.

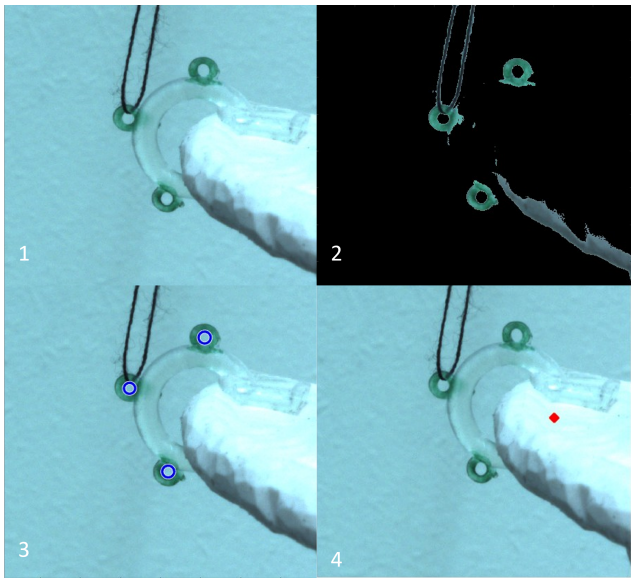


Fig. 3.7 Workflow for image-based recognition of the clip pulling point. (1) Raw experimental image. (2) Colour-filtered image isolating the green attachment rings. (3) Circular fitting of the ring contour (blue) with the clip pads identified. (4) Extraction of the pulling point (red dot), used for trajectory tracking in the mechanical analysis.

Each test began by mounting the auricle phantom onto the rig and attach the string to connect the moving head and the clip. The setup was adjusted by tensioning the string until taut. The measured string length without slack was 32.4 cm for the lateral pulling position and 36.7 cm for the anterior pulling. The load cell was then zeroed to establish a consistent baseline. The Instron head was programmed to displace vertically at a constant speed of 2 mm/min. During the test, images were captured every 2 seconds, and pulling continued until the displacement exceeded the predefined thresholds, 12 mm for lateral pulling and 15 mm for anterior pulling. Each test condition was repeated three times on each of two independently manufactured phantoms produced using the same fabrication method.

An important consideration in the experimental design was the elasticity of the pulling string. Because the string stretches under load, its elongation could introduce systematic error into displacement measurements by contributing additional deformation not attributable

to the auricle phantom. To correct for this, a separate calibration test was conducted to characterise the string's force–elongation behaviour. The string was looped in a double-stranded configuration, enhancing its tensile capacity but also doubling the force required to achieve a given strain. The resulting force–elongation curve is shown in Figure 3.8. The calibration data revealed that the string exhibited approximately 2% strain at 2 N of applied force. This calibration curve was then used to correct the displacement measurements by accounting for string elongation, ensuring that the recorded values accurately reflected the auricle phantom's true deformation under static loading.

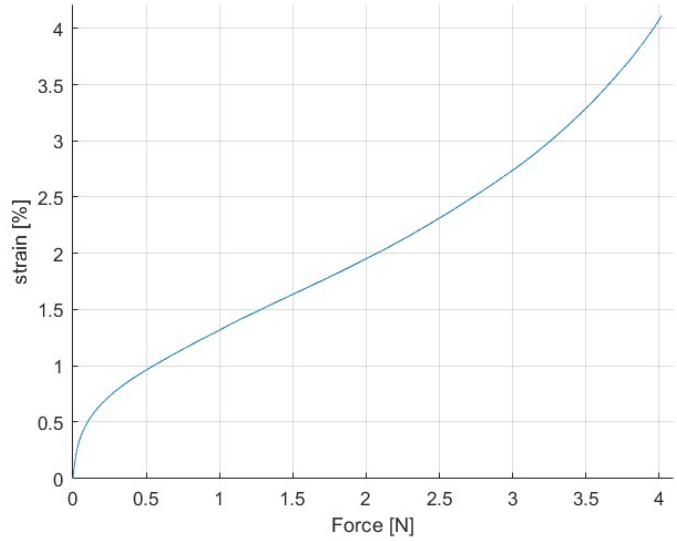


Fig. 3.8 The Strain and force relationship of string used in experiment.

3.3.2 Result And Discussion

Following the completion of the static pulling experiments, the captured image sequences were processed to extract the deformation trajectories of the auricle phantom. This analysis aimed to visualise and quantify the structural response under both lateral and anterior pulling conditions. Colour-based tracking algorithms were applied to isolate the motion of the green ring marker affixed to the clip at the auricle tip, ensuring consistent detection across frames for accurate trajectory extraction. The measured displacements were obtained from pixel-based image coordinates and converted to physical lengths using a calibrated scale. As a result, the dominant source of experimental uncertainty arises from systematic measurement error associated with pixel resolution and image scaling, which was estimated to contribute less than 2% uncertainty to the reported displacement measurements.

Figures 3.9(a) and (b) show the tracked motion paths of the auricle tip for the lateral and anterior pulling configurations, respectively. These trajectories provide direct visual insight into the direction and extent of deformation throughout the loading process. The motion paths reveal differences in displacement behaviour across directions and highlight the spatial nature of auricle deflection under tensile load.



(a) (b)

Fig. 3.9 Image processing result of (a) Inferior view of the auricle model and (b) Posterior view of the auricle model.

The result analysis was then pursued using two different representation methods to interpret the auricle's mechanical behaviour: the deformation angle and the anterior direction displacement. Each approach provides complementary perspectives on the deformation characteristics, allowing for a more comprehensive understanding of the phantom's structural response.

To enable quantitative comparison using deformation angle, a fixed anatomical reference point R was selected near the base of the concha, an area close to the rigid support and assumed to remain undeformed during loading. This point served as a baseline for measuring relative displacement, as illustrated in Figure 3.10. A deformation angle, denoted as θ, was defined as the angle between the horizontal plane and a line connecting this fixed base point to the tracked pulling point on the auricle tip. As external load increased, the auricle experienced progressive bending, which was captured as an increase in angle θ. This approach provided a single interpretable scalar parameter to represent the complex deformation in a simplified yet meaningful manner.

Figure 3.10 also illustrates how the deformation angle θ evolves in response to applied force, increasing from its initial state at F_0 to its final value at F_n. This angular representation enables the mechanical response of the auricle to be quantified and compared across different

loading directions. By expressing deformation in this angular form, the study facilitates more intuitive interpretation and lays a foundation for comparisons with digital simulation models and future *in vivo* testing.

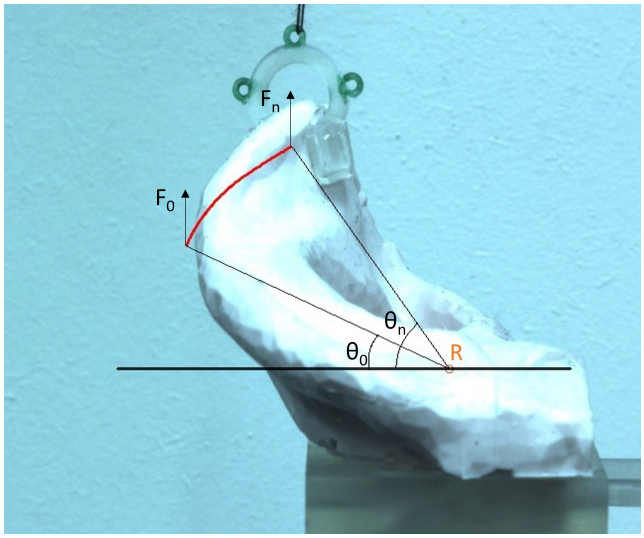
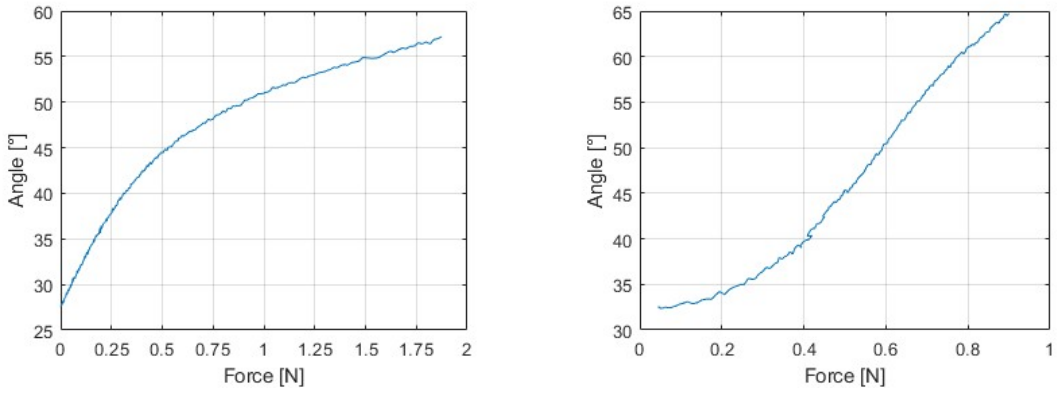


Fig. 3.10 Illustration of measuring the deformation as the angle change under different load

Figures 3.11(a) and (b) present the relationship between applied force and angle θ for the lateral and anterior pulling configurations, respectively. The deformation angle data revealed a distinct variation in mechanical response based on the direction of applied load. Specifically, the anterior pulling condition required considerably less force to achieve an equivalent deformation angle compared to the lateral pulling scenario, suggesting a pronounced directional dependence in the auricle's structural stiffness. This result highlights the anisotropic mechanical behaviour of the auricle, which is particularly relevant for earable device design and attachment mechanisms.

It is important to note that the deformation angle data is subject to certain limitations arising from the photometric capturing setup. Since the angle θ is measured based on two-dimensional projections of auricle movement, only the bending profile visible from a superior or inferior view can be precisely quantified. Additionally, the bending angle is not uniform along the length of the auricle, meaning that θ represents an averaged bending approximation rather than a full spatial deformation profile. Despite these limitations, this measurement approach remains a valuable analytical tool, especially in validating that the anterior pulling direction achieves greater efficiency with lower applied force.

The second representation method involved calculating the displacement in the anterior direction. As shown in Figure 3.12, this was done by mapping the photometrically extracted



(a) (b)

Fig. 3.11 Applied force and deformation relationship (a) Deformed angle of lateral pulling with force applied (b) Deformed angle of anterior pulling with force applied

trajectory to a coordinate system and directly measuring the displacement of the auricle tip with respect to the anterior direction of the auricle. These values were then plotted against the applied force recorded by the 10 N Instron load cell. The resulting force–displacement relationship is presented in Figure 3.13, capturing how the auricle phantom responds to increasing load in terms of anterior translation.

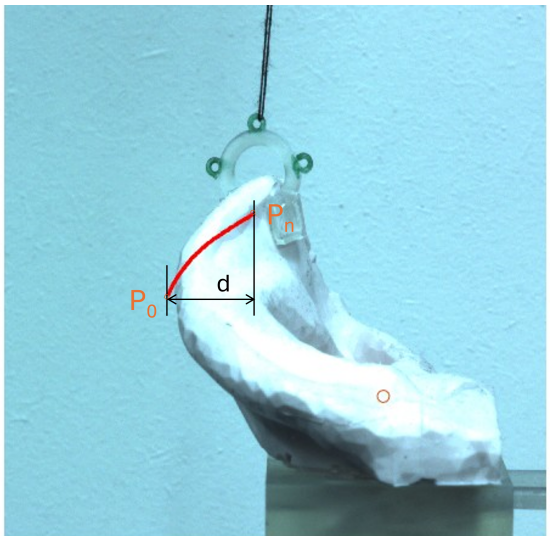
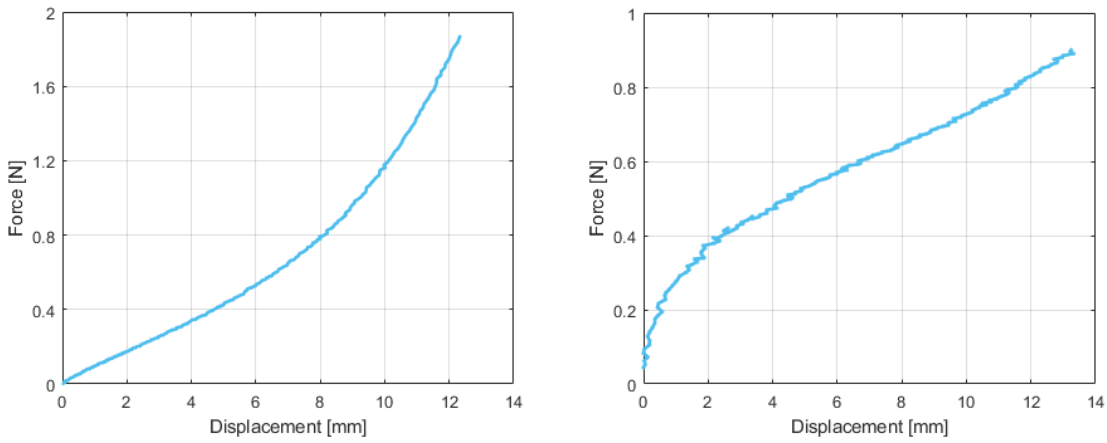


Fig. 3.12 Illustration of measuring the deformation as the displacement along the anterior direction of the auricle

The results demonstrated that in the lateral pulling configuration, the required force increased steeply once the displacement exceeded approximately 8 mm. This trend suggests a nonlinear



(a) (b)

Fig. 3.13 Applied force and displacement in anterior direction relationship for (a) lateral pulling position and (b) anterior pulling position.

stiffening behaviour, likely caused by geometric resistance and material stretch. In contrast, the anterior pulling configuration exhibited a more gradual and steady increase in force over displacement, indicating a more compliant response in that direction.

Both the deformation angle and anterior displacement analyses were derived from a combination of photometric tracking and precision force measurements. These two approaches offer complementary insights into the mechanical response of the auricle phantom, with one capturing rotational bending characteristics and the other quantifying linear displacement under load. Together, they contribute to a robust experimental framework that can be adapted for future *in vivo* validation. Additionally, the successful implementation of these techniques reinforces their potential utility in clinical or wearable device contexts, where non-invasive and repeatable measurement protocols are essential.

3.4 Dynamic Loading Response

While the static experiments provided critical insight into the auricle's structural deformation, a comprehensive characterisation of its dynamic behaviour is essential for understanding how mechanical vibrations impact neural signal acquisition in ear-EEG systems. Earable devices function as neural interfaces that rely on stable skin-electrode contact. However, mechanical vibrations, such as those encountered during walking or talking, can displace electrodes, resulting in signal artefacts or loss. Therefore, analysing the auricle's vibration

characteristics is vital for predicting its susceptibility to mechanical interference and for informing the design of robust electrode placements.

To further explore these dynamic considerations, two complementary experiments were developed to evaluate the vibrational behaviour of the auricle phantom: (1) a load release test to determine the system's natural frequency and damping characteristics, and (2) a sinusoidal base excitation test to evaluate frequency response, amplitude gain, and phase shift.

3.4.1 Experiment Method

The load release test, shown schematically in Figure 3.14(a), was adapted from the static tensile setup. A downward displacement of 15 mm was applied to the auricle phantom using a taut string fixed to the Instron testing machine. To simulate sudden load removal and initiate free vibration, the string was ignited and burnt through to provide a sudden release of load. Blue tracking dots were applied to the phantom surface to facilitate image analysis. This approach enabled a clean impulse excitation without physical interference during vibration.

The resulting motion of the phantom was recorded using a Sony ZV-1 camera in high-speed mode (1000 fps). Figure 3.14(b) shows still frames capturing motion before and after string release. Image processing was applied to track the blue markers on the phantom and green markers on the clip, allowing derivation of displacement-time curves and extraction of dynamic parameters such as natural frequency and damping ratio.

The second experiment used a hydraulic Instron machine to provide controlled sinusoidal vibration to the auricle base, as shown in Figure 3.15(a). Vibrational input frequencies up to 8 Hz and displacements of 2 mm were tested. Coloured tracking markers were placed on both the rig and the auricle tip. These were recorded using the same high-speed video system, enabling extraction of the input motion (rig) and the corresponding output displacement (auricle tip). Figures 3.15(b) and (c) display the configurations for vertical and lateral vibration modes. These data were used to compute frequency-dependent gain and phase relationships, thereby mapping the auricle phantom's frequency response function.

3.4.2 Result Of Load Release Test

Following the cut-release test, the displacement trajectories of the tracked markers on the auricle phantom were analysed to determine the dynamic properties of the system. As shown in Figure 3.16(a) and (c), all tracking points displayed a trajectory of characteristic damped oscillations. While there were differences in amplitude and initial phase among the markers,

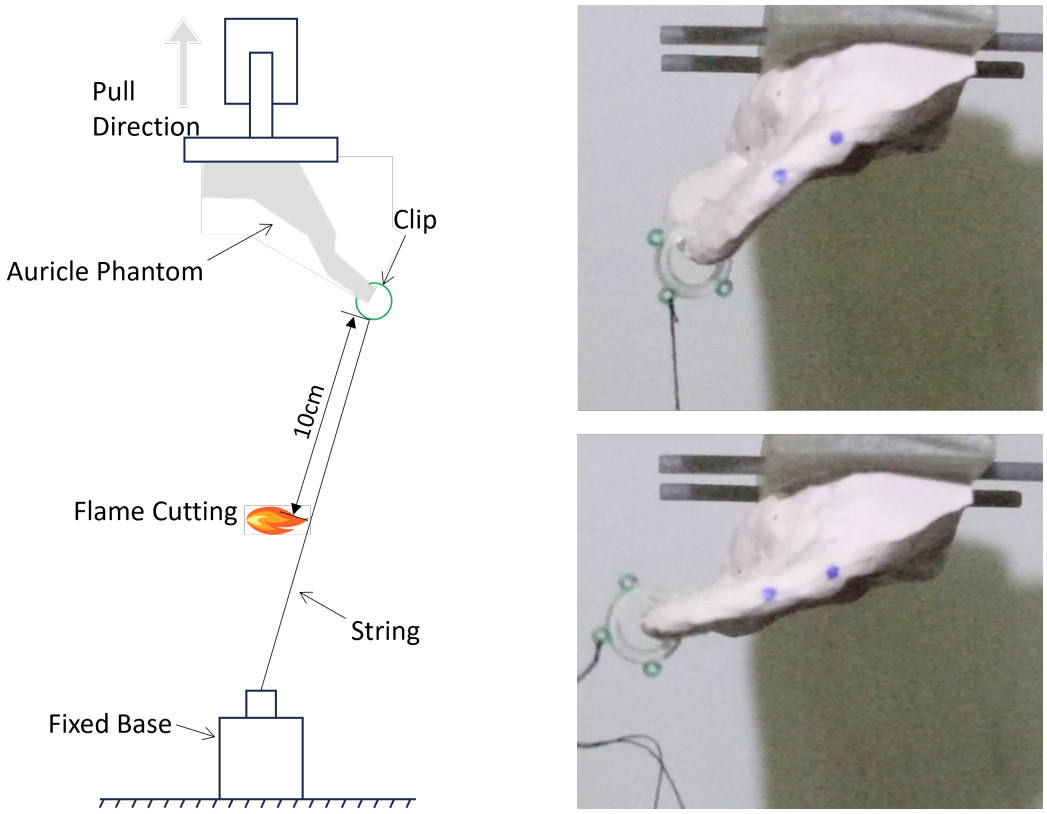


Fig. 3.14 (a) Cut release experiment schematic (b) Screenshots from video capturing cut release experiment

their decay profiles were consistent, as shown in Figure 3.16(b) and (d), suggesting a uniform damping behaviour throughout the structure.

To characterise the response, the z-displacement of the cyan-tracked marker was fit with a damped sinusoid,

$$x(t) = A\,\sin\!\left(2\pi f_d\, t + \phi\right) e^{-\delta t}, \tag{3.4}$$

with fitted parameters $A = 2.506$, $f_d = 49.05$ Hz, $\phi = 2.142$ rad, and $\delta = 48.12$ s^{-1} (Figure 3.17). Here f_d is the *damped* natural frequency and δ is the exponential decay rate. ϕ is the phase difference.

From the decay rate, the time constant is

$$\tau = \frac{1}{\delta} = \frac{1}{48.12} \approx 0.021 \text{ s}.$$

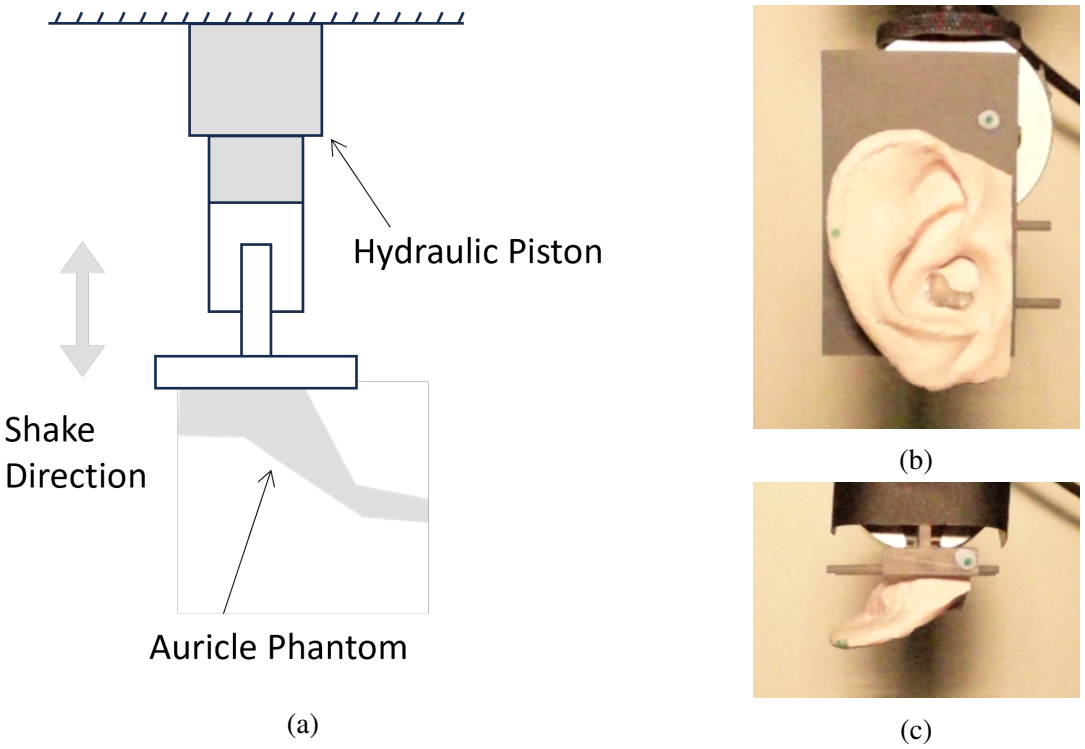


Fig. 3.15 Setup of the dynamic test of frequency response

The angular damped frequency is $\omega_d = 2\pi f_d = 308.19\ \mathrm{rad\,s^{-1}}$. For a linear Single-Degree-of-Freedom (SDOF) oscillator,

$$\omega_d = \omega_n\sqrt{1-\zeta^2}, \qquad \delta = \zeta\,\omega_n, \tag{3.5}$$

so that

$$\omega_n = \sqrt{\delta^2+\omega_d^2} \approx \sqrt{48.12^2+308.19^2} = 311.92\ \mathrm{rad\,s^{-1}},$$

and the (undamped) natural frequency is

$$f_n = \frac{\omega_n}{2\pi} \approx 49.64\ \mathrm{Hz}.$$

The damping ratio is

$$\zeta = \frac{\delta}{\omega_n} = \frac{48.12}{311.92} \approx 0.15.$$

This value indicates that the auricle phantom behaves as an underdamped system, which is characterised by oscillations that gradually decay over time.

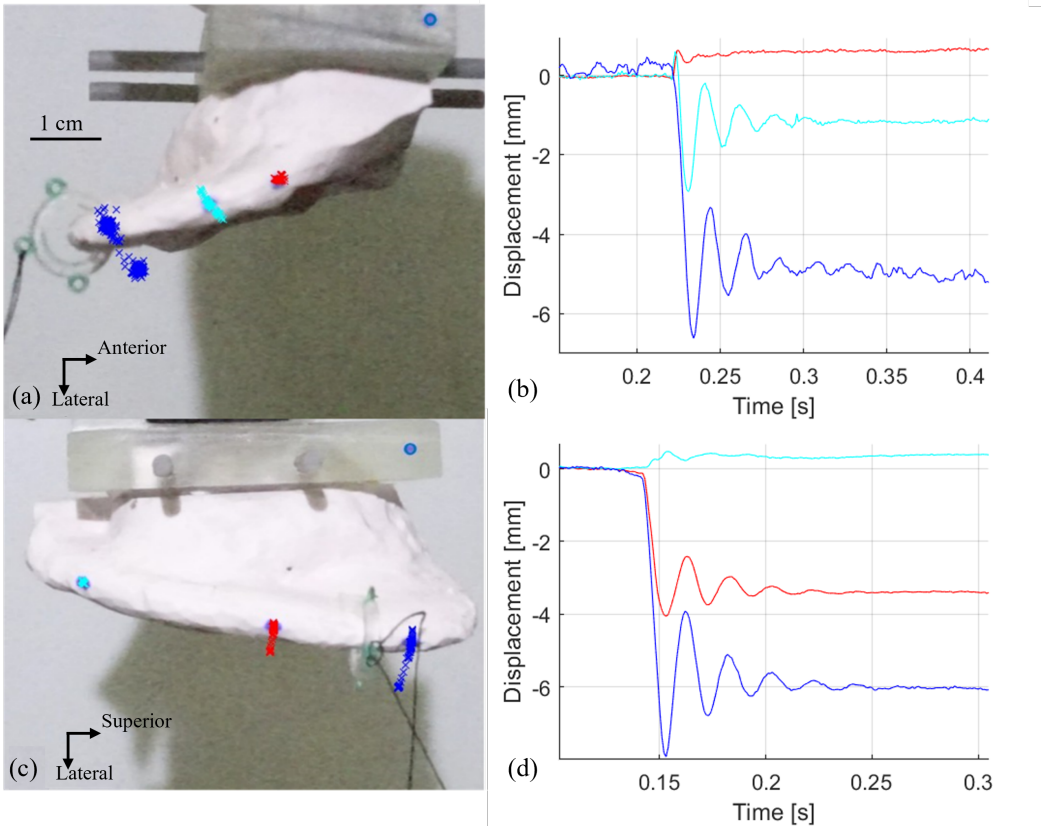


Fig. 3.16 Results of the cut-release experiment captured from two viewing angles: image analysis of (a) the superior view of the auricle and (c) the posterior view of the auricle. The displacement of marker points in the lateral direction was plot over time, with curve colours corresponding to the respective marker colours (b) of the superior view and (d) of the posterior view.

To further interpret the system's mechanical behaviour in the frequency domain, the auricle was modelled as a classical second-order damped oscillator, as illustrated in Figure 3.18(a). This model is widely used to describe dynamic systems that exhibit both inertia and energy dissipation, such as soft tissue responding to mechanical excitation. In this context, the auricle's response to external vibration can be viewed as a mass–spring–damper system, where:

- the mass represents the effective mass of the auricle structure,
- the spring simulates tissue stiffness (elasticity), and
- the damper captures internal energy loss through tissue viscosity.

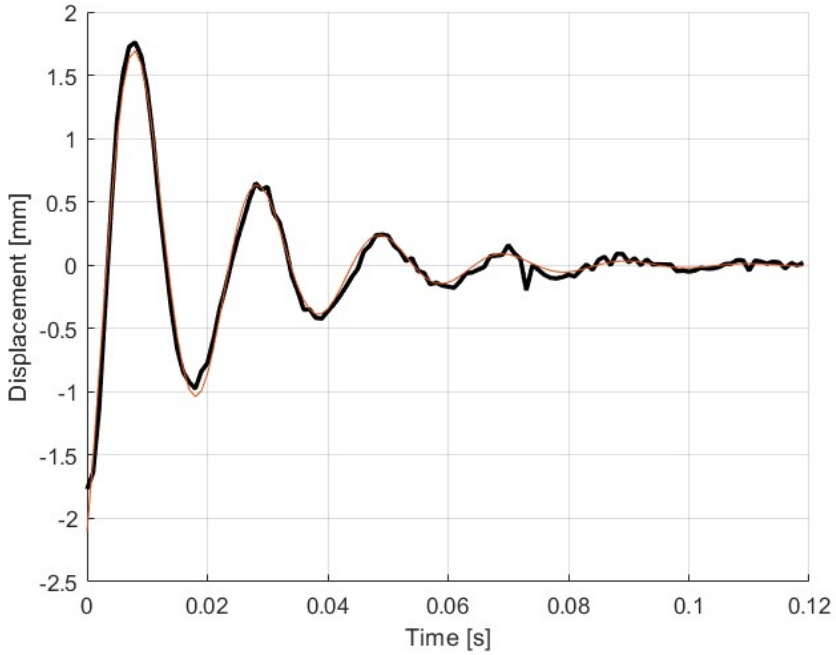


Fig. 3.17 Damped-sinusoid fit to the z-displacement of the tracked marker. The fit parameters are $f_d = 49.05$ Hz and $\delta = 48.12\ \mathrm{s}^{-1}$.

Using this model, the relationship between an imposed oscillatory input (e.g., skull vibration) and the auricle's output displacement can be characterised using a frequency response function, which describes how amplitude (gain) and phase shift vary with frequency.

$$H_{(f)} = \left(\frac{1 + (2\zeta f/f_n)^2}{\left[1 - (f/f_n)^2\right]^2 + (2\zeta f/f_n)^2} \right)^{\frac{1}{2}} \tag{3.6}$$

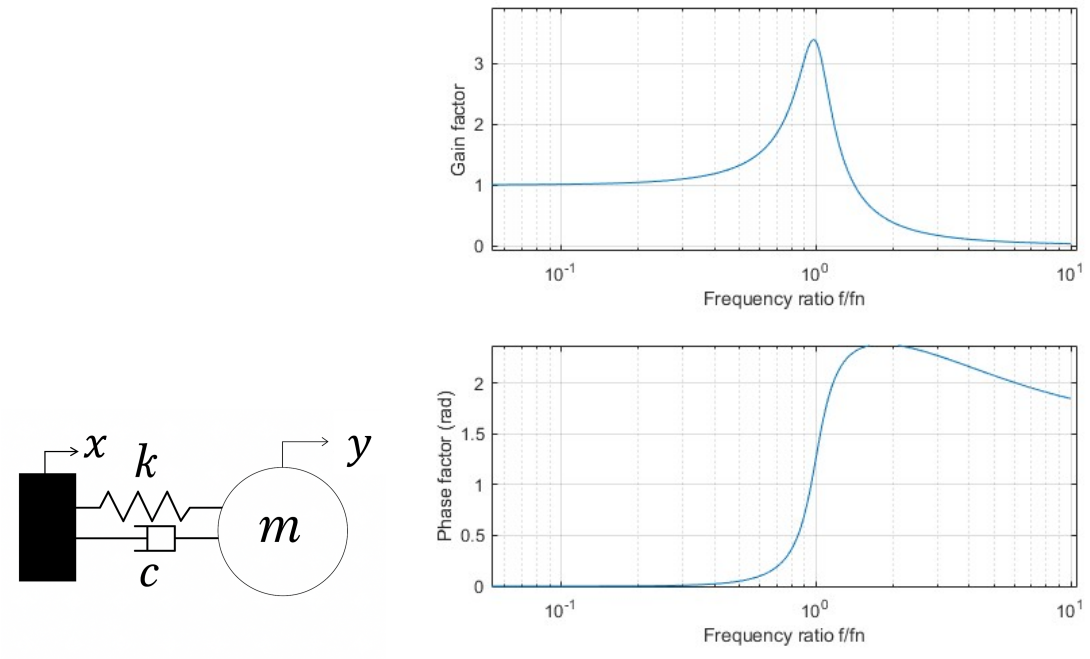
$$\Phi_{(f)} = \left(\frac{2\zeta\,(f/f_n)^3}{1 - (f/f_n)^2 + (2\zeta f/f_n)^2} \right)^{\frac{1}{2}} \tag{3.7}$$

where:

- $H(f)$ is amplitude gain as a function of frequency f.
- $\Phi(f)$ is phase shift as a function of frequency f.
- f is input frequency (Hz).

- f_n is natural frequency of the system (Hz).
- ζ is damping ratio (dimensionless).

Figure 3.18(b) presents the resulting gain and phase curves generated using the measured natural frequency and damping ratio. These curves represent the auricle phantom's expected vibrational response across a range of input frequencies as a proportion to the natural frequency of the auricle phantom model, ranging around 1 Hz to 500 Hz, which are particularly relevant to real-world disturbances encountered in wearable EEG scenarios (e.g., motion-induced noise) and lower range for human audible frequency.



(a) (b)

Fig. 3.18 (a) Illustration for a second-order damped oscillator, with x as the displacement of input frequency signal and y as the displacement of output frequency signal. (b) Calculated gain and phase factor with respect to the vibration frequency for the experiment phantom model.

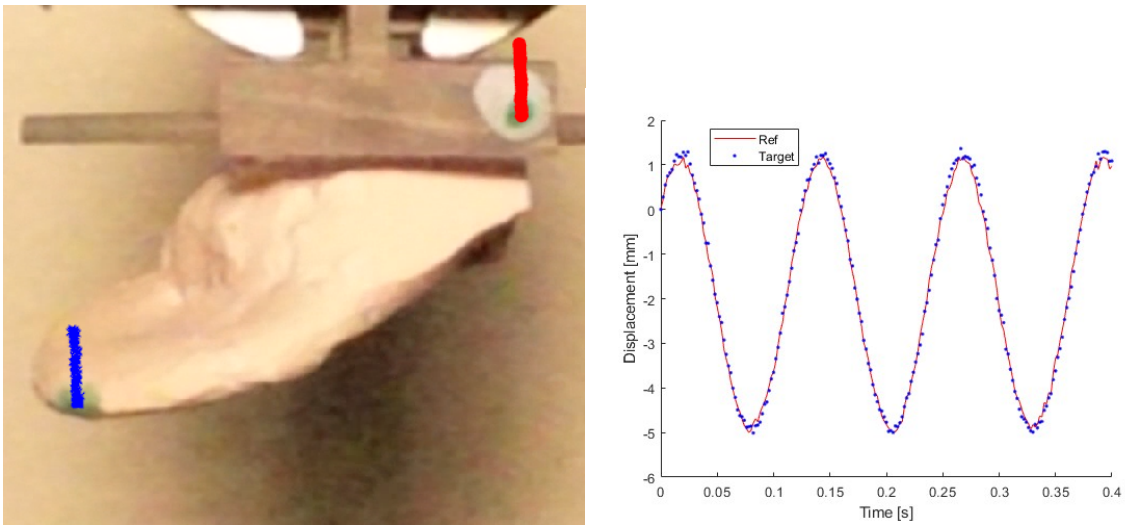
3.4.3 Result Of Vibration Response Test

The vibration response of the auricle phantom was quantitatively assessed using high-speed video recordings from the sinusoidal base excitation experiments. A custom MATLAB script

was employed to track the motion of two key points: the auricle tip (target) and the rigid mounting base (reference). These tracking points represented the system's output and input, respectively. Figure 3.19(a) illustrates the selected points, with the auricle tip shown in blue and the base in red, overlaid on a representative video frame.

For each test frequency, the lateral direction displacement of both points was extracted on a frame-by-frame basis with MATLAB. As shown in Figure 3.19(b), the resulting displacement profiles closely followed sinusoidal patterns. These waveforms were then fitted with sinusoidal functions to determine their amplitudes and temporal phase relationships.

From the fitted curves, the vibration gain, defined as the amplitude ratio between the auricle tip and the base, was calculated. The phase shift was also determined by quantifying the temporal offset between the two sine waves. Across the tested frequency range, the observed phase shifts were minimal, indicating nearly synchronous motion between the base and the auricle tip.



(a) (b)

Fig. 3.19 (a) Tracked points on the phantom (blue: auricle tip) and reference base (red) as captured from high-speed video during sinusoidal excitation. These points represent the output and input of the system, respectively. (b) Displacement curves for both tracked points in the lateral direction. This data was used to calculate the system's gain and phase shift at each excitation frequency.

Table 3.3 summarises the measured gain values for vertical and lateral vibration configurations across tested frequencies from 2 Hz to 8 Hz. The gain is defined as the percentage increase

of the amplitude of auricle tip motion to that of the base platform, with values greater than 0 indicating amplification of displacement through the soft tissue structure.

Frequency (Hz)	Vertical Vibration	Lateral Vibration
2	0.25%	0.41%
4	0.68%	1.10%
6	0.63%	1.79%
8	1.06%	3.59%

Table 3.3 Measured vibration gain of the auricle phantom model at low input frequencies.

As shown in figure 3.18, the gain gradually increases with frequency, indicating a frequency-dependent amplification consistent with the system's low stiffness and underdamped behaviour. In particular, the gain in the lateral direction at 8 Hz reached 3.59%, higher than that of the vertical configuration. This suggests that the auricle structure is more responsive to lateral vibration at low frequencies, which aligns with findings from the static test results.

From theoretical modelling of the auricle as a second-order damped system (with natural frequency $f_n = 49.64$ Hz and damping ratio $\zeta = 0.156$), the expected gain and phase shift at 8 Hz were calculated as:

$$\frac{f}{f_n} = \frac{8}{49.64} \approx 0.16, \quad H(8\text{ Hz}) \approx 1.03, \quad \Phi(8\text{ Hz}) \approx 0.0013$$

The close match between the theoretical gain (1.03 which is 3%) and the experimental value (3.59%) supports the validity of the simplified dynamic model used in earlier sections. However, it should be noted that the current test setup is limited to a maximum input frequency of 8 Hz, which is well below the natural frequency of the auricle phantom. As such, this low-frequency range only captures the initial linear portion of the frequency response curve.

To fully characterise the dynamic behaviour, particularly near resonance range, future work should incorporate extended vibration testing across a broader frequency spectrum. This will allow for more accurate modelling of vibrational artefacts in ear-EEG systems and inform the design of stable, low-noise earable devices.

3.5 Digital Simulation Approaches

One of the main objective of the earable project is to construct a predictive digital model of the auricle for earable design and evaluation. The scope of mechanical experiments has captured the basic response of the auricle structure and given us ideas of the design specification. But

it is restricted by laboratory equipment limitations and test sample constraints. To expand the horizons of understanding the mechanical properties of the auricle, the same phantom model is now employed for finite element (FE) analysis in computational simulation. This recreated model is referred to as the digital phantom model.

The model was validated with the same setups of experiment in the mechanical test setups to analyse if the simulation results agree with the experimental results.

3.5.1 FE Simulation Of Mechanical tests

A key goal of this study is to develop a predictive digital model of the auricle to support earable device design and evaluation. While mechanical experiments have provided foundational insights into auricular deformation and vibrational response, they are inherently constrained by physical limitations, such as equipment capabilities, sample variability, and repeatability concerns. To overcome these limitations and generalise findings beyond the laboratory context, finite element (FE) analysis was employed to create a digital counterpart to the phantom model, referred to as the digital phantom model. This construction of the phantom model is also a demonstration before the construction of realistic auricle model for modelling actual human auricle interaction.

Before constructing the simulation, it was necessary to establish unit consistency within the Abaqus FE software, which operates in a unitless framework. All quantities were converted using a millimetre–gram–second (mm–g–s) base unit system. Table 3.4 summarises the conversion scheme used to ensure coherence across length, mass, force, and derived quantities.

	Unit used	SI unit equivalent
Length	mm	10^{-3}m
Mass	g	10^{-3}kg
Density	gmm^{-3}	$10^{6}kgm^{-3}$
Force	$gmms^{-2}$	$10^{-6}kgms^{-2}$ [N]
Pressure	$gmm^{-1}s^{-2}$	$kgm^{-1}s^{-2}$ [Pa]
Acceleration	mms^{-2}	$10^{-3}ms^{-2}$
Moment of Inertia	mm^4	$10^{-12}m^4$

Table 3.4 Unit conversion scheme used in Abaqus simulations.

To ensure that the digital simulation reflected the physical phantom model accurately, all simulation conditions, geometry, boundary constraints, mesh refinement, and loading procedures, were designed to match those used in physical experiments. The resulting model

was used to predict structural stiffness, deformation patterns, and dynamic properties, which were then validated against experimental measurements.

3.5.2 Simulation Setup

To replicate the conditions of the physical experiments, the auricle's double-layer geometry, consisting of an inner cartilage core and an outer skin layer, was imported into Abaqus for finite element analysis. The model geometry was derived directly from the phantom ear design, ensuring consistency between the experimental and numerical setups. Material properties were assigned to match those of the phantom constituents: the inner cartilage analogue was represented by 3D-printed Elastic 50A resin, while the outer skin layer was modelled using Silastic 3481 silicone. Both layers were meshed using tetrahedral solid elements, providing adequate representation of the complex auricular geometry while maintaining computational efficiency.

Although both cartilage and skin exhibit nonlinear, hyperelastic behaviour in reality, they were approximated in this study as isotropic linear elastic solids. The cartilage layer was assigned a Young's modulus of $E = 3.35$ MPa with Poisson's ratio $\nu = 0.40$, while the skin layer was assigned $E = 0.42$ MPa with $\nu = 0.45$. This simplification was adopted intentionally to streamline the initial modelling process and to isolate the influence of structural geometry and boundary conditions on the deformation response.

Under the small to moderate deformation regime examined here, the linear elastic formulation provides a reasonable approximation of the first-order force–displacement relationship and global deformation pattern of the auricle. While this assumption precludes accurate representation of large-strain nonlinearities and time-dependent viscoelastic effects, it is sufficient for the present objective, which is to validate the overall simulation framework and assess its consistency with controlled experimental measurements. The emphasis at this stage is therefore on capturing relative deformation trends and load transfer rather than achieving full constitutive fidelity. More advanced hyperelastic and viscoelastic material formulations will be introduced in later sections to improve physiological realism.

Boundary conditions and loading protocols were selected to closely replicate the experimental setup. The auricle base was fully constrained in all degrees of freedom to represent fixation to the skull and the mechanical clamping used during testing. External loading was applied at the lateral helix rim via a reference point coupled to a small surface patch, replicating the clip-and-string arrangement used in experiments. This configuration enabled controlled application of displacement or force while recording reaction forces and resulting deformations.

The simulation procedures were divided into two steps to mirror the experimental protocols:

- **Static loading tests:** quasi-static anterior pulling of the helix tip at a controlled rate to evaluate force–displacement behaviour and effective auricle stiffness.
- **Dynamic release tests:** free oscillation of the auricle following release, used to estimate the first-mode natural frequency and compare with vibration measurements from the phantom experiments.

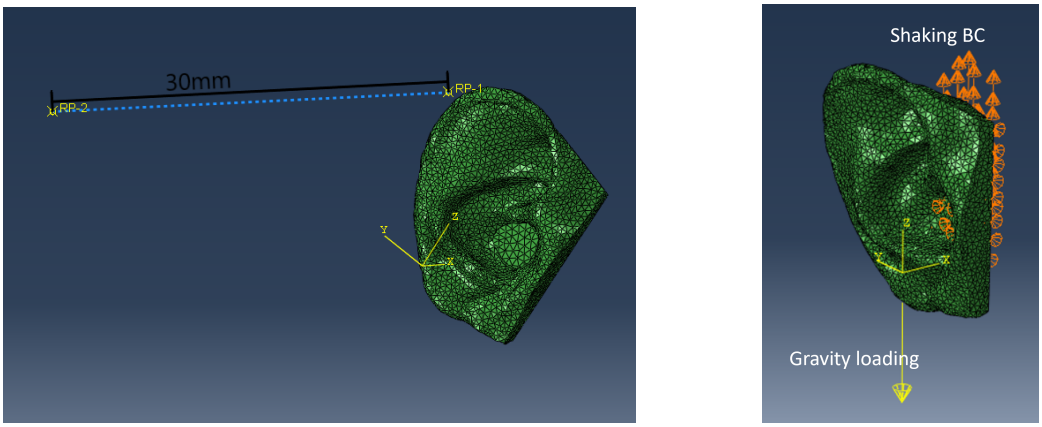
Together, this simulation setup provided a consistent basis for comparison with experimental results, ensuring that observed differences could be attributed primarily to material modelling assumptions rather than inconsistencies in geometry, boundary conditions, or loading protocols.

Static Loading Simulation

The static test setup is illustrated in Figure 3.20(a). To emulate the static tensile tests, a Static Step was defined in Abaqus. The rear surface of the model was fixed, representing the skull attachment in the physical setup. An offset reference point was defined where the clip applied force in the real-world test. A 30 cm virtual string (matching experimental dimensions) was modelled via a connector element, applying a linear displacement boundary condition at the string's end to simulate the pulling action of the Instron machine. This induced a rotational and tensile force at the attachment site, mirroring the experimental loading mechanism.

Dynamic Load-Release Simulation

In the dynamic load release simulation, a second analysis step was performed immediately following the static loading phase, as illustrated in Figure 3.20(a). In this subsequent dynamic step, the displacement constraint applied in the static test was removed, allowing the structure to oscillate freely as it returned toward its equilibrium position. This setup mimics the load release experiment conducted on the physical phantom and captures the transient vibrational behaviour of the model. By analysing the resulting oscillatory motion, key dynamic parameters, such as natural frequency and damping ratio, were extracted to characterise the auricle's dynamic response.



(a) (b)

Fig. 3.20 The FE simulation setup for verifying the experimental results. (a) Replication of the static loading setup, also the same setup for load release dynamic test. (b) Replication of the frequency response setup.

Base Excitation Simulation

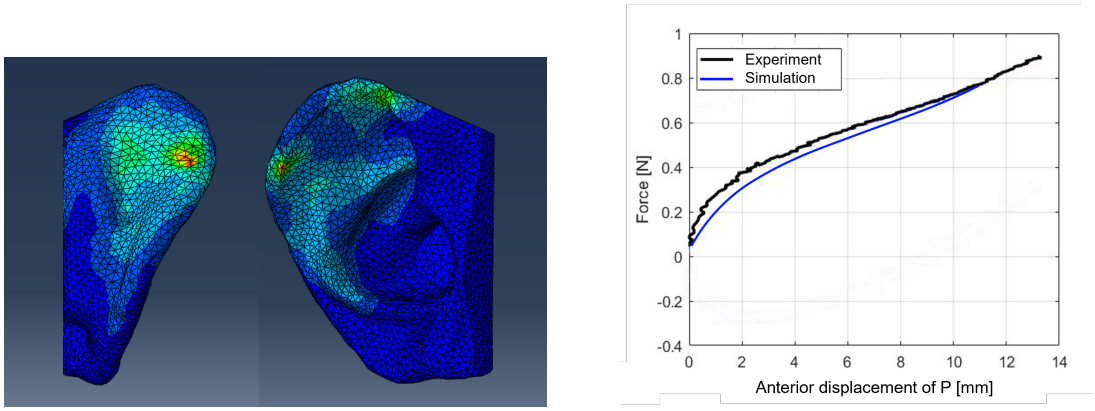
To replicate the second dynamic test, the sinusoidal base vibration, the auricle base was assigned a periodic displacement boundary condition as shown in Figure 3.20(b). The model was excited along the x-axis at the same frequencies (2–8 Hz) and amplitudes (2 mm) as in the physical experiment. Motion tracking was implemented at the auricle tip to derive gain and phase relationships. These digital results were then compared to their experimental counterparts for validation.

3.5.3 Simulation Result And Comparison

Figure 3.21(a) presents the von Mises stress distribution of the auricle model under static loading conditions. This simulation replicates the experimental configuration, including the fixed rear surface resembling the solid rig that the auricle phantom was attached on, and the offset point where force was applied corresponding to the clip attachment in the mechanical tests.

To compare the simulation result with the experiment, the anterior pulling simulation and the experiment data are plotted in Figure 3.21(b). The simulation showed a great agreement with the data collected in the experiment.

The dynamic behaviour of the model, following load release, was analysed using displacement tracking and curve fitting. Figure 3.22 illustrates the damped sinusoidal response. The



(a) (b)

Fig. 3.21 FE simulation results of the static loading test. (a) Von Mises stress distribution under static deformation. (b) Comparison of the static response from the simulation with the experimental response, showing the applied force as a function of displacement.

best-fit function to Eq. 3.4 is given by:

$$f(t) = -8.474 \times \sin(2\pi \times 48.1 \times t - 4.9485)e^{-63.12t}$$

From this fit, the model's natural frequency was determined to be 48.1 Hz, with a decay time constant of:

$$\tau = \frac{1}{63.12} = 0.0158 \text{ s}$$

This result shows good agreement with experimental observations, though the simulation's natural frequency is slightly lower than the experimentally measured 49.05 Hz. This discrepancy is likely due to variations in phantom fabrication, especially differences in thickness and material distribution. Since the natural frequency of an elastic 3D structure scales with geometric factors such as cross-sectional thickness cubed, even minor manufacturing variances can produce substantial frequency shifts.

To further validate the model, frequency response tests were simulated using sinusoidal base excitation, and results were compared with both the physical phantom and theoretical predictions. Table 3.5 summarises the gain values extracted from simulation, experiment, and predicted second-order system calculations.

The simulation model produced lower gain values than those observed experimentally. This discrepancy may be explained by mechanical imperfections in the experimental setup, such as imperfect piston motion, where the actuator's displacement and velocity deviate from

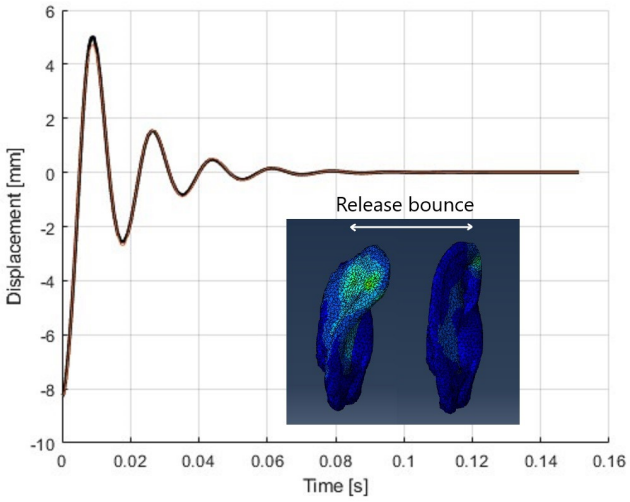


Fig. 3.22 The load release simulation with the model, fitted to a damped sinusoidal function

Frequency (Hz)	Simulation Gain	Theoretical Gain	Experimental Gain
2	0.12%	0.12%	0.41%
4	0.43%	0.50%	1.10%
6	0.96%	1.12%	1.79%
8	1.73%	2.91%	3.59%

Table 3.5 Comparison of frequency response gain from FE simulation, theoretical model, and experimental phantom tests.

the intended smooth sinusoidal waveform, or variations introduced during material curing, neither of which were present in the idealised simulation. Furthermore, the sinusoidal excitation in the physical test was limited by the performance of the vibration equipment, leading to deviations from the ideal input profile which was used in the simulation.

Despite these differences, the overall trends between simulation, theory, and experiment remain consistent. The simulation successfully captured the general mechanical behaviour of the auricle phantom, validating the digital model as a reliable tool for further investigation and design evaluation. Future improvements will involve refining material models to include hyperelastic behaviour and integrating more anatomically accurate geometries to support clinical translation.

3.6 Improved Phantom Model and Experimental Refinement

Based on the findings from earlier sections in this chapter, the simplified phantom model, while effective for developing experimental protocols, exhibited key limitations in biomechanical realism. In particular, its simplified geometry and relatively stiff cartilage material limited its ability to replicate the deformation behaviour of the human auricle. To address these shortcomings, a new realistic phantom model was developed with enhanced anatomical fidelity and material refinement.

3.6.1 Improved Construction Process

The realistic phantom was created using a high-resolution auricle scan, retaining full anatomical details including the tragus, antihelix, and cymba conchae. The ear canal contributes little to the mechanical response of the auricle so it is not included in the realistic model. In contrast to the simplified phantom, the features like helix and antihelix have greater curves and slopes angle and distinct shape. As a result, both the skin and cartilage layers were thinner and more representative of actual auricular anatomy. However, this also introduced fragility during demoulding due to the delicate structure.

To mitigate this, a water-soluble mould box was fabricated using polyvinyl alcohol (PVA), which dissolves in water (see Figure 3.23 (a)). This allowed for a non-destructive demoulding process, preserving the integrity of the phantom's thin features. The resulting realistic phantom is shown in Figure 3.23 (b).

In pursuit of more realistic auricular phantoms, two softer silicone gels were evaluated for the skin layer to better approximate the compliance of human tissue. These materials, clear Ecoflex™ 00-30 and pink Mold Max™ 10 (Smooth-On Inc., USA), were selected based on their mechanical softness and mouldability. The internal cartilage core continued to be fabricated using Elastic 50A resin (Formlabs, USA), though the UV curing protocol was modified to fine-tune its mechanical response.

In addition to testing the silicone and fully cured cartilage analogues, a dedicated study was conducted to evaluate the influence of curing duration on the mechanical performance of Elastic 50A resin. Samples were cured under UV light for 0, 5, 10, and 20 minutes, and their tensile behaviour was subsequently compared. The specimens were prepared as standardised dog-bone samples with the same geometry described in Section 3.2.2 (gauge section:



(a) (b)

Fig. 3.23 Construction of Realistic Phantom Model (a) The mould box which are printed with PVA. (b) Moulded auricle phantoms with two different silicone gel materials

1.6 mm × 2.0 mm, height: 12.0 mm; overall dimensions: 40.0 mm × 10.0 mm × 1.6 mm). All tests were performed using the same Instron platform described previously, ensuring direct comparability of results. As summarised in Table 3.6, a 5-minute cure reduced stiffness by approximately one-third relative to a fully cured specimen (20 minutes) while maintaining adequate tensile strength for structural stability. This intermediate curing condition was therefore selected for phantom fabrication, as it produced cartilage-like stiffness values that were more consistent with those reported in the literature and aligned with the design objectives of the auricle model.

Feature	**Not Cured**	**5-min UV cure**	**10-min UV cure**	**20-min UV cure**
Effective Young's Modulus	1.8 MPa	2.4 MPa	3.32 MPa	3.40 MPa
Ultimate Tensile Strength	0.7 MPa	2.1 MPa	2.62 MPa	3.22 MPa
Elongation at break	0.54	1.13	1.35	1.58

Table 3.6 Comparison of different curing condition for the cartilage material Elastic 50A with tensile test.

The improved two-layer phantom models, fabricated using these adjusted materials and curing protocols, are shown in Figure 3.24. Visually and mechanically, these new phantoms presented a more compliant, skin-like response compared to the earlier simplified version.

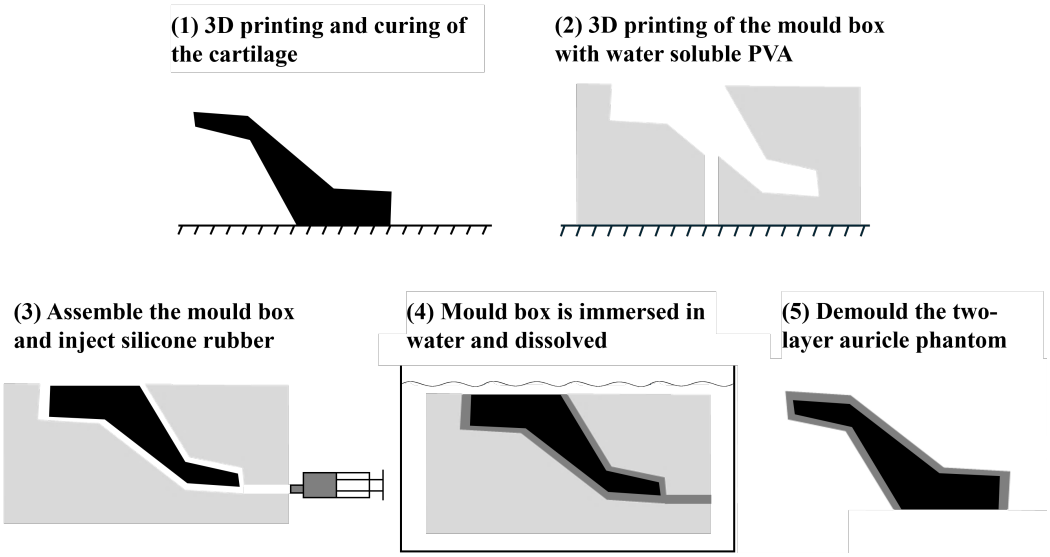


Fig. 3.24 Step-by-step construction process of the auricle phantom model

However, comparative tests revealed that the Ecoflex™ 00-30-based model exhibited excessive damping behaviour, deviating from the dynamic response of actual auricular tissue. As a result, this material was excluded from further experiments. The Mold Max™ 10-based phantom, which offered a better match to physiological damping characteristics, was retained for continued testing. More details on Phantom model production is included in Appendix A.

3.6.2 Experimental Refinement

To evaluate whether the realistic phantom more accurately represents auricle behaviour, the static and dynamic loading experiments described earlier were repeated with refinements to the experimental setup. As shown in Figure 3.25, the static loading test was repositioned to apply traction at a 15° anterior angle. This adjustment was chosen to align with the setup used in the volunteer study described in Chapter 4, thereby improving physiological relevance and enabling more direct comparison between phantom and *in vivo* results.

Tracking markers were again applied to the auricle surface, and deformation analysis followed the same image-processing pipeline established previously (see Section 3.3). This ensured methodological consistency across different phantom iterations and facilitated quantitative comparison of displacement trajectories.



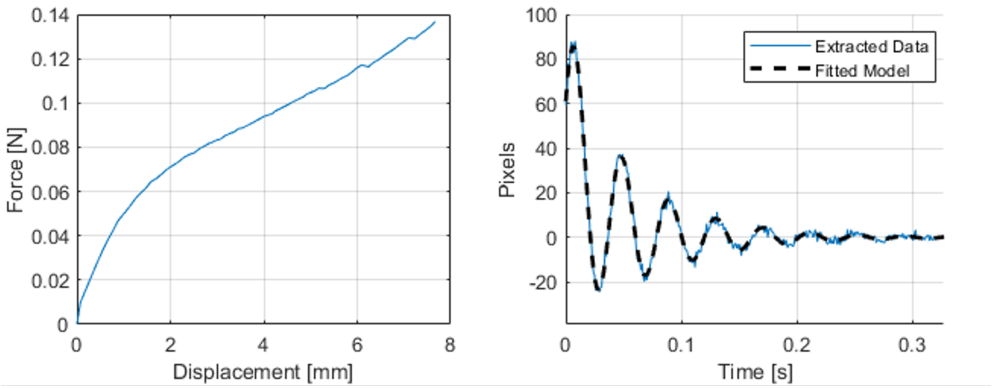
Fig. 3.25 Refined static loading experiment on the realistic auricle phantom, applying traction at a 15° anterior angle to replicate the volunteer testing protocol.

3.6.3 Static and Dynamic Results

The deformation trajectories and vibration responses obtained from the realistic phantom exhibited closer agreement with trends observed in human subject testing (see Chapter 4). Figure 3.26(a) shows the static displacement response processed using the same tracking method described in Section 3.3, while Figure 3.26(b) presents the dynamic behaviour of the phantom, with displacement data fitted to the damped sinusoidal model defined in Eq. 3.4.

Compared with the earlier simplified phantom, the realistic phantom demonstrated reduced stiffness, greater compliance, and damping behaviour more representative of physiological tissue. In static loading tests, the force required to achieve comparable displacements was significantly lower. This reflects both the thinner profile of the realistic phantom and the use of softer silicone and cartilage-mimicking materials in its layered construction. These refinements brought the phantom's mechanical properties into closer correspondence with those of the actual human auricle.

In dynamic testing, the realistic phantom exhibited a first-mode natural frequency of 24.63 Hz, substantially lower than that of the simplified model. This value falls within the range of natural frequencies measured in human auricles (see Chapter 4), further supporting the improved biomechanical fidelity of the refined phantom model.



(a) (b)

Fig. 3.26 Mechanical testing of the realistic auricle phantom. (a) Static loading: displacement of the tracked point in the vertical direction plotted against applied force. (b) Dynamic response: free vibration of the tracked point following release, with displacement fitted to a damped sinusoidal model.

3.6.4 Summary of improvements

Table 3.7 provides a summary comparison between the simplified and realistic phantoms, highlighting key differences in geometry, materials, and mechanical performance.

Feature	**Simplified Phantom**	**Realistic Phantom**
Cartilage Material	Elastic 50A (fully cured)	Elastic 50A (5-min UV cure)
Skin Material	Silicone Gel Silastic 3481	Mold Max™ 10 (Smooth-On Inc., USA)
Geometry	Simplified	Anatomically accurate
Demoulding Method	Rigid mould (manual)	PVA mould (water-soluble)
Stiffness	Overestimated	Aligned with human data
Experimental Fidelity	Moderate	High (matches volunteer data)

Table 3.7 Comparison of simplified and realistic auricle phantom models

The improvements presented in this section significantly enhance the phantom's ability to simulate real auricular mechanics. This advancement strengthens the foundation for *in vivo* validation and supports the clinical relevance of future experiments involving wearable neural interfaces.

3.7 Conclusions

This chapter presented a comprehensive methodology for characterising the mechanical behaviour of the human auricle through a combination of physical phantom experiments and FE simulations. By integrating static and dynamic loading tests with image-based deformation tracking, the study established reproducible and interpretable metrics for assessing auricular mechanics. In particular, the introduction of the deformation angle parameter, θ, enabled consistent comparison across loading directions, while dynamic load–release experiments quantified the auricle's natural frequency and damping properties. These findings are directly relevant to understanding vibration-induced artefacts in ear-mounted EEG systems and other auricle-mounted devices.

The mechanical tests developed in this study serve as a baseline for future *in vivo* investigations of auricular biomechanics. The static tests established appropriate loading configurations and reliable deformation metrics, while the dynamic tests revealed resonant behaviour and damping characteristics that are essential for predicting device stability. Although the detailed measurement of deformation angles used in the phantom tests could not be directly implemented in subsequent volunteer studies, these results nonetheless provided a quantitative linkage between external loading and structural deformation.

To complement the experimental programme, an FE model of the auricle was developed using the same geometry and material definitions as the phantom. The primary purpose of this digital phantom was methodological validation: confirming that the simulation setup, boundary conditions, and analysis procedures could replicate the observed behaviour and characteristics in experiments. The model successfully reproduced both static deformation and dynamic response trends, thereby validating the simulation framework. For simplicity, linear elastic properties and relatively coarse meshes were adopted for computational efficiency. However, this demonstration successfully established the basis for more advanced FE models incorporating nonlinear viscoelastic material models, refined meshes, and subject-specific morphologies.

The simplified phantom proved to be valuable as an initial test platform but exhibited higher stiffness than native auricular tissue. To address this discrepancy, a more anatomically and mechanically refined phantom was subsequently developed, featuring softer skin-mimicking materials, improved cartilage geometry, and advanced moulding techniques. This realistic phantom produced deformation responses more consistent with human data and provides an important intermediate step between simplified test structures and full *in vivo* validation.

In summary, this chapter established a feasible testing and modelling pipeline for auricle mechanics, combining experimental validation with digital simulation. The framework fills a methodological gap in the characterisation of ear–device interactions and lays the groundwork for future research. Building on this work, subsequent studies can extend toward *in vivo* validation, patient-specific modelling, and the optimisation of earable neural interfaces for stable, comfortable, and high-fidelity biosignal acquisition.

Chapter 4

Human Auricle Study and Biomechanical Modelling

4.1 Introduction

In the previous chapter, the mechanical behaviour of the auricle was investigated using synthetic phantom models, enabling controlled evaluation of deformation and vibrational response under static and dynamic loading. While these models provide valuable baseline data, they cannot fully capture the anatomical variability and biological complexity of the human ear. The mechanical characterisation of *in vivo* auricles remains largely unexplored in the literature, despite its relevance to clinical applications, ergonomics, and the design of ear-mounted devices.

This chapter addresses that gap by presenting a methodology for *in vivo* measurement of auricle mechanics. The approach builds on the phantom model testing framework, adapting the experimental system to safely and accurately assess human subjects under both static and dynamic loading conditions. Particular emphasis is placed on developing procedures that can be applied consistently across individuals, while accommodating the wide variation in auricle size, shape, and stiffness.

The aim is to establish a reliable measurement protocol capable of capturing the key mechanical parameters of the auricle under realistic conditions. These parameters will be used to compare the mechanical behaviour of the human auricle with that of the phantom models, assess inter-individual variability, and examine their implications for the interaction between wearable devices and the ear. In addition, this chapter includes a system-modelling analysis

that interprets the observed deformation behaviour using a simplified beam theory based mechanical framework.

4.2 Human Subject Experiment Design

4.2.1 Method development

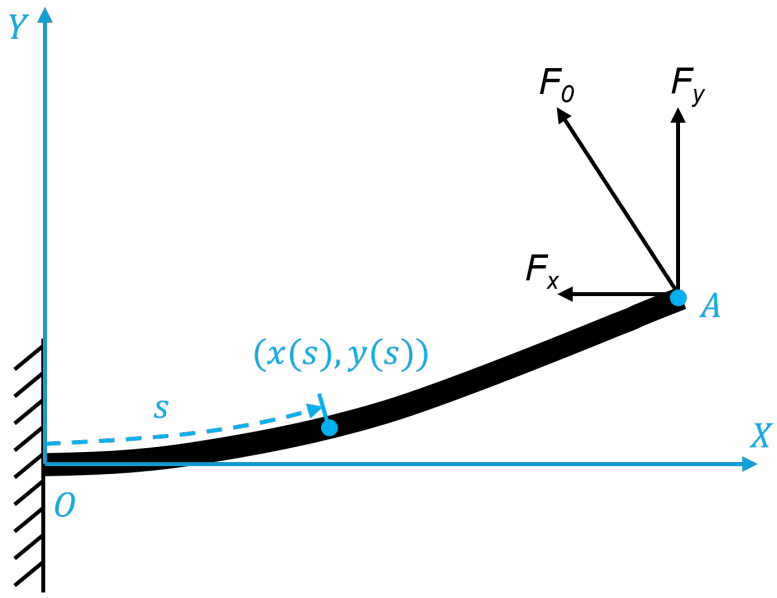
As established in Chapter 3, static testing of the auricle can be evaluated through either the deformation angle or the displacement of the auricle tip. However, when transitioning to human subjects, practical constraints limit the feasibility of certain measurement approaches. Specifically, obtaining superior or inferior views of the human auricle, which are required for accurate angular measurements, is challenging in a clinical or laboratory environment. In contrast, lateral views are more readily accessible and compatible with standard camera setups. This view was also discussed in Chapter 2 (Figure 2.8), where the auricle was positioned against a grid background. Therefore, the deformation-angle method was ruled out, and a displacement-based analysis was adopted for human testing.

For dynamic testing, ethical and safety considerations prevented the application of continuous sinusoidal vibrations to participants' heads, as used in the phantom model experiments. Instead, the dynamic properties of the human auricle were evaluated using the impulse response test. This approach avoids continuous stimulation while still enabling the assessment of natural frequency and damping characteristics.

To adapt the experimental setup for *in vivo* conditions, key modifications were made to both the clip interface and the measurement apparatus. Based on the baseline experiment developed in Chapter 3, anterior pulling was selected over lateral pulling, as it requires significantly less force to achieve comparable deformation. This choice prioritises participant comfort by reducing the pressure exerted by the clip on the ear.

4.2.2 Beam Model Consideration

To guide the experimental design, a simplified cantilever beam model was considered to simulate the auricle's bending behaviour under load, as shown in Figure **??**. In this model, the auricle is idealised as a homogeneous elastic beam, fixed at one end and subjected to an angled point load at the free end. This setup falls within the framework of large-deflection



[Beam-end loading]A straight beam subjected to beam-end loading

beam theory, which extends classical Euler–Bernoulli theory to accommodate geometrical nonlinearities [103].

The bending behaviour follows the classical moment–curvature relationship:

$$EI\kappa = M, \tag{4.1}$$

where E is the Young's modulus, I is the second moment of area, κ is the beam curvature, and M is the bending moment.

Considering the case of large deformation, the bending moment at any point along the arc length s is given by:

$$EI\frac{d\theta}{ds} = M(s) = F_y[x(L) - x(s)] + F_x[y(L) - y(s)], \tag{4.2}$$

where F_x and F_y are the horizontal and vertical components of the applied force, and $x(s)$ and $y(s)$ define the coordinates of the deformed beam along its arc length, as illustrated in Figure **??**. The terms $x(L)$ and $y(L)$ correspond to the coordinates at the free end of the beam. This can be generalised into the following system:

$$\begin{aligned} &\text{Differential equation:} && \frac{d^2\theta}{ds^2} = -\frac{F_y}{EI}\cos\theta(s) - \frac{F_x}{EI}\sin\theta(s), \\ &\text{Boundary conditions:} && \theta(0) = 0, \quad \frac{d\theta}{ds}(L) = 0. \end{aligned}$$

The full geometrically nonlinear formulation and boundary value problem (BVP) used to describe large deflections are provided in Appendix B. In brief, solving for the rotation field $\theta(s)$ and integrating the resulting geometric relations yields the spatial deformation of the beam, which serves as a first-order approximation of auricular bending under applied forces [103].

A MATLAB implementation based on this formulation was used to simulate the beam response under representative auricular parameters ($E = 0.8$ MPa, length 10 cm, width 1 cm, and end load 0.12 N). These values are not exact anatomical measures but were selected to provide a tractable yet physiologically relevant estimate of auricular mechanics within the simplified beam framework.

The resulting deformation was analysed by plotting the horizontal displacement of the beam's free end as a function of the angle at which the external force was applied, while keeping the force magnitude constant. To enable comparison across different loading directions, the displacement was expressed as a normalised measure: the tip deflection in the beam's length axis divided by the original beam length. This *normalised displacement* represents the relative strain-like deformation of the structure, independent of its absolute size.

The bending angle was defined as the angle between the applied force vector and the perpendicular axis of the beam. In this configuration, the applied angle directly governs how effectively the force generates bending moments relative to axial loading. As shown in Figure 4.1, the normalised horizontal displacement reached a maximum when the force was applied at approximately 77°. Within a range of $\pm 5^\circ$ around this orientation, the change in normalised displacement remained within 2%, indicating low sensitivity to small deviations in pulling direction.

These findings suggest that an applied load angle of around 72–82° yields the most stable and reproducible deformation behaviour, with minimal local variance in displacement relative to force angle. With the beam under simulation set to comparable parameter with auricle dimension and properties, the overall structural bending of the auricle can be assume to have similar profile as the beam. This orientation was therefore selected as the experimental pulling direction for subsequent auricle loading tests, ensuring consistency and physiological relevance.

4.2.3 Experimental Setup

The complete experimental setup for *in vivo* auricle testing is shown in Figure 4.2(a). Participants were seated comfortably in a stable chair, with their head stabilised using a modified

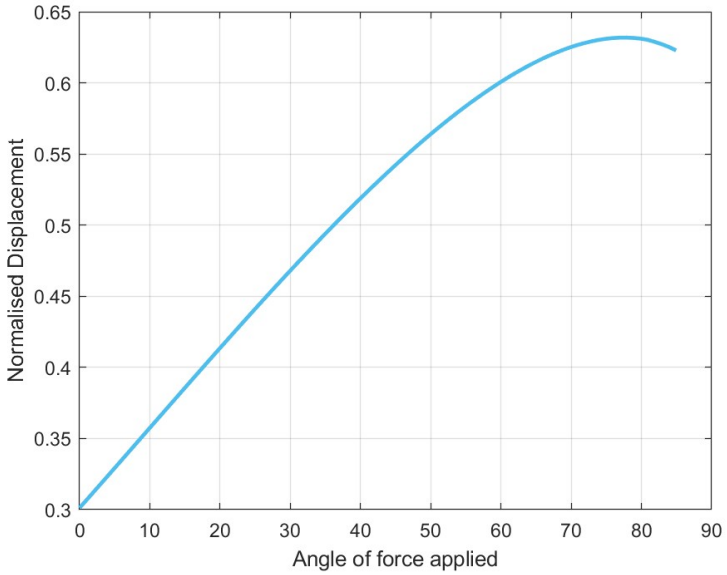
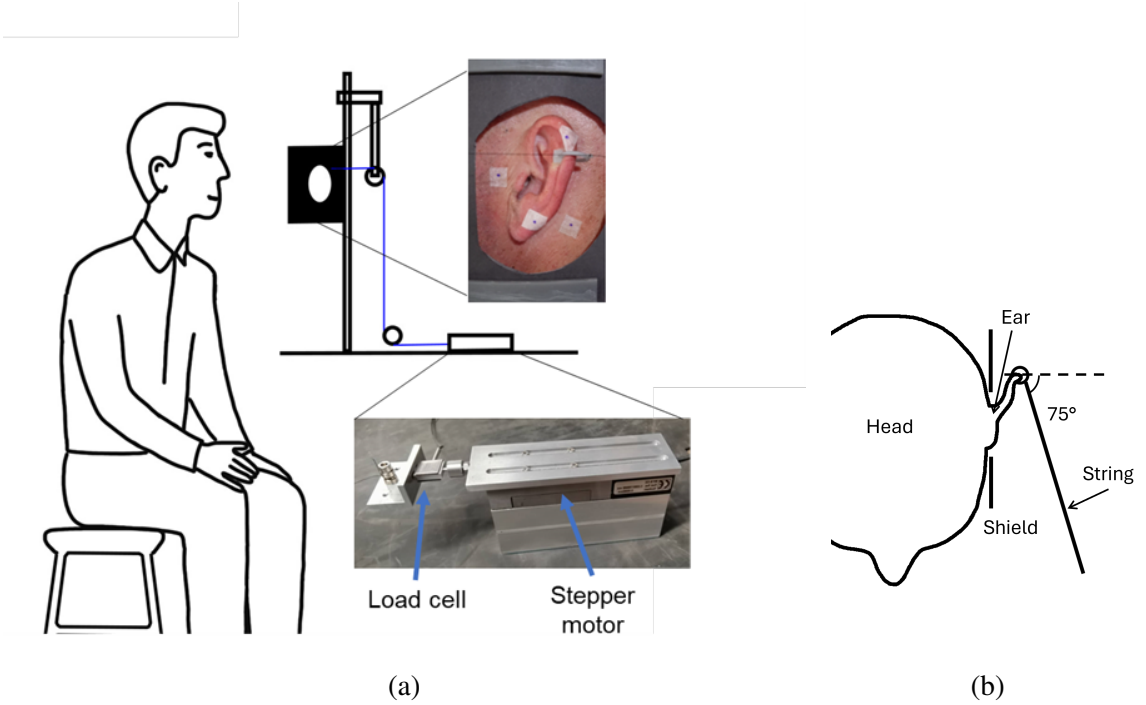


Fig. 4.1 Effect of pulling angle on beam deformation. The horizontal axis shows the angle of applied force relative to the beam length, while the vertical axis shows the normalised tip displacement (tip deflection in the length axis divided by the beam's original length). Maximum displacement occurs near 77°.

chin rest to minimise involuntary motion during testing. A 3D-printed adjustable shielding frame with a black coloured paper cover was positioned above the face, leaving the auricle exposed through an elliptical aperture. This design served two key purposes: (1) it concealed facial features to maintain participant anonymity in captured images, and (2) it provided a consistent photometric reference for spatial calibration of image data, enabling conversion from pixel to physical units.

The tip of the auricle was fixed with a 3D printed clip and connected to a string, which passed through a series of pulleys before reaching the motor assembly. As illustrated in Figure 4.2(b), the string was aligned to pull at an angle of approximately 75°, determined from prior beam model analysis to maximise effective anterior displacement while maintaining repeatability.

The motor assembly of the experimental apparatus is shown in Figure 4.3. The system comprised a stepper motor with an integrated linear stage (Miniature Steel Motorised Linear Stage, Newport Corporation, USA; 0.1 μm step resolution; 25 mm travel range), driven by a motor controller unit (SMC100PP, Newport Corporation). A precision load cell (Model GSMTM-4.5N, Interface Force Measurement Ltd., UK) was installed at the terminal end of the string to continuously monitor tensile force during auricle deformation. The load



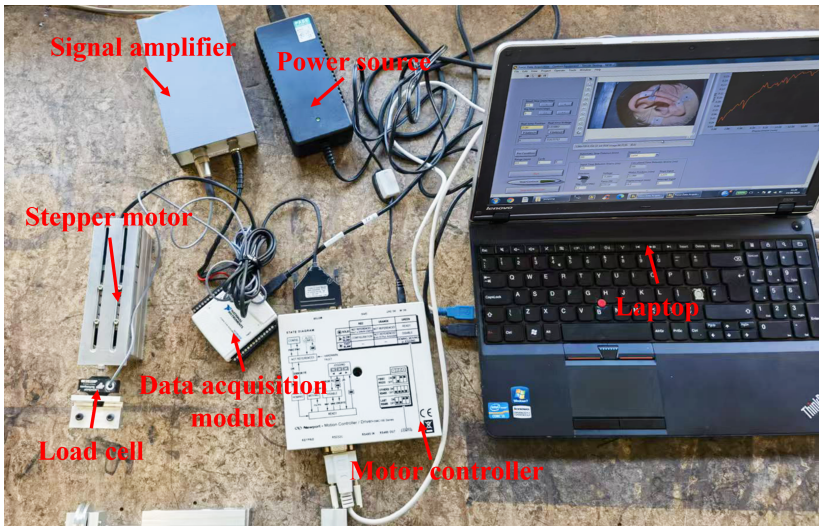
(a) (b)

Fig. 4.2 (a) Volunteer test configuration with facial shielding and auricle exposed. Blue tracking markers are applied to the auricle surface, and the string is routed through a pulley system. (b) Superior view of the pulling direction, confirming the pulling angle was set to approximately 75° relative to the sagittal plane.

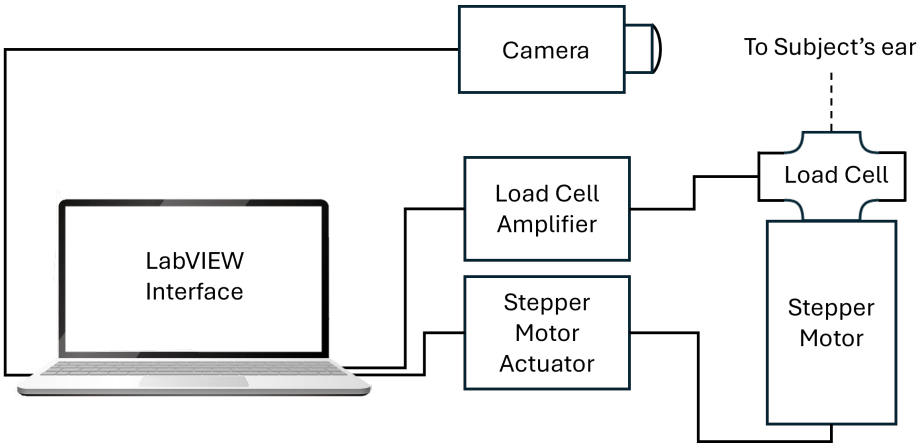
cell signal was amplified via a customised signal amplifier (1000× gain, Department of Engineering, University of Cambridge) and digitised using a data acquisition module (USB-6002; National Instruments, USA).

The force calibration of the load cell was performed using standard weights ranging from 25 g to 200 g. For each weight increment, the corresponding voltage output was recorded. A linear regression model was fitted to the calibration data to generate a scale factor and bias offset, which were used for real-time conversion during experiments.

Auricle deformation was captured using a Sony ZV-1 camera (Sony Europe BV, UK) positioned orthogonally to the subject's head. The camera was selected for its compact form factor, 4K recording capability, and high frame rate (up to 1000 fps), which were critical for dynamic analysis. Blue circular markers were applied to strips of surgical tape and fixed to anatomically consistent regions of the auricle. These markers helped achieve automated image-based tracking by providing strong colour contrast against human skin.



(a)



(b)

Fig. 4.3 (a) Photo of the experimental equipment in the laboratory (b) Apparatus schematic of the measurement unit.

All components were synchronised and controlled through a custom LabVIEW GUI program developed in-house. The program allowed the operator to:

- Control the stepper motor at a defined speed (0.5 mm/s),
- Read and calibrate force data in real time from the amplified load cell signal,
- Trigger camera image capture at defined intervals,
- Visualise the live force-displacement curve during testing.

A total of 31 volunteers were recruited for this study, aged between 18 and 40 years. The study was approved by the Research Ethics Committee of the Department of Engineering, University of Cambridge, and all participants provided written informed consent (see Appendix C). For each subject, auricle dimensions were measured using a photometric method. A reference ruler of known length was placed in the same plane as the auricle to ensure calibration accuracy (Figure 4.4). The auricle length was defined as the maximum vertical distance, typically measured from the superior helix to the lobule, while the auricle width was defined as the maximum horizontal distance measured perpendicular to the length axis. These definitions ensured consistency across all participants and enabled direct comparison with established anatomical reference data.

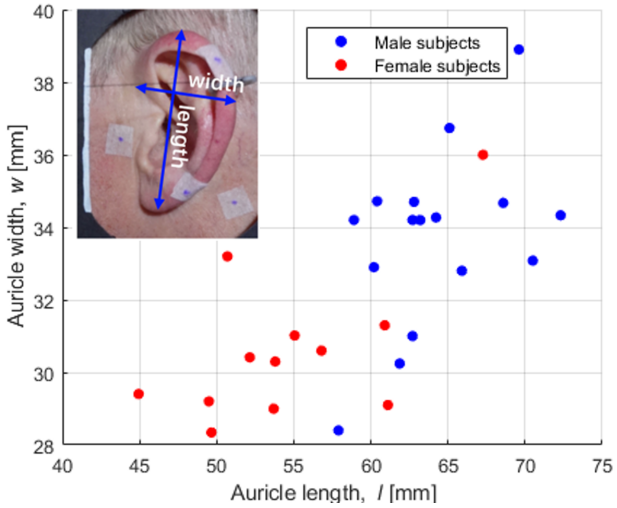


Fig. 4.4 Photometric measurement of auricle dimensions. Auricle length was defined as the maximum vertical distance from the superior helix to the lobule, and width as the maximum horizontal distance perpendicular to the length. Pixel distances were converted into physical measurements using a reference scale positioned in the same imaging plane.

4.3 Static Loading Response

4.3.1 Data Collection Procedure

To initiate each trial, the experimental rig was first configured to ensure repeatable loading conditions. The stepper motor was returned to its baseline position, allowing the attached string to be manually adjusted until it was taut and aligned with the pulley system. The top

pulley was then positioned to match the predefined anterior pulling axis, approximately 75 degrees relative to the sagittal plane of the head.

Once the system alignment was visually verified and the auricle clip secured comfortably on the participant's ear, the data acquisition system was launched via a custom LabVIEW interface. This program controlled the stepper motor to apply anterior traction at a constant speed of 0.5 $\mathrm{mm\,s^{-1}}$. This quasi-static loading rate was selected based on preliminary phantom trials, balancing the need to minimise viscoelastic effects in soft tissue while maintaining participant comfort and sufficient temporal resolution for image capture.

As traction was applied, the auricle underwent anterior deformation in response to the increasing load. Pulling continued until the lateral displacement of the auricle tip reached approximately 25% of the individual's auricle width. This threshold was empirically determined during pilot testing to provide sufficient mechanical insight while remaining well tolerated by all participants. It also ensured that deformation was evaluated at a consistent relative level across individuals with varying ear sizes.

For each participant, the experiment was repeated three times to assess intra-subject consistency and potential variability arising from clip positioning or subtle head movements. Between trials, the auricle was allowed to return to its resting state, and the clip was carefully repositioned to maintain consistency. During each test, images were captured from the lateral view. The full data collection process for each participant typically lasted between 30 and 40 minutes.

All force data recorded by the load cell, together with time-stamped image sequences, were saved and indexed using anonymised subject identification codes for subsequent processing and analysis.

4.3.2 Data Processing and Analysis

Following data collection, the acquired image sequences were processed using a custom MATLAB script developed to quantify auricle deformation with sub-pixel precision. The script performed automated tracking of colour-coded markers applied to predefined anatomical regions on the participant's head and ear. These markers were created using surgical tape coloured with a blue dye, selected to contrast sharply against human skin tones under the lighting conditions used, thereby facilitating reliable segmentation through colour thresholding.

Each experimental condition was repeated three times for every participant, as described in the experimental protocol. The resulting force–displacement and displacement–time traces were compared to assess repeatability across trials. Variations in displacement between repetitions were small, typically within 0.5 mm, corresponding to approximately 5% of the median displacement. Force measurements exhibited slightly higher variability, with differences of up to 0.01 N, equivalent to approximately 10% of the median applied load. Given this level of variability, the median dataset was selected for subsequent data presentation and analysis, as it provides a robust and representative description of auricle behaviour while minimising sensitivity to experimental noise and marker-tracking uncertainty.

To isolate auricle motion from general head movement or postural drift, the markers were divided into two categories: reference markers and deformable-region markers. Reference markers were affixed to relatively immobile regions of the skull, specifically the mastoid process and the zygomatic arch, chosen for their structural rigidity and minimal motion relative to auricle deformation.

Deformable-region markers were applied to the lateral margin of the auricle helix, near the superior and inferior portions of the helix rim. These locations were selected based on their involvement in the deformation path during anterior pulling, as established in phantom model trials.

Each frame in the image sequence was analysed to extract the two-dimensional coordinates of all markers. A noise-reduction filter was applied to eliminate erroneous detections caused by lighting glare or minor skin features, and marker trajectories were tracked using a centroid-matching algorithm.

Auricle-specific deformation was calculated by expressing the displacement of each auricle marker relative to the average displacement of the reference markers in the same frame. This differential approach corrected for residual head motion, such as slight sliding or chin movement, that could occur despite the use of a chin rest. The resulting displacement represented the net anterior motion of the auricle under applied load.

To enable meaningful cross-participant comparison, displacement data were normalised by the auricle width w, defined as the maximum horizontal span of the ear measured photogrammetrically using a planar calibration reference.

The processed and normalised data were grouped by self-identified gender for exploratory analysis. As shown in Figure 4.5, average applied load is plotted against normalised displacement for male and female participants, illustrating both inter-individual variability and potential gender-related differences in auricle mechanical stiffness.

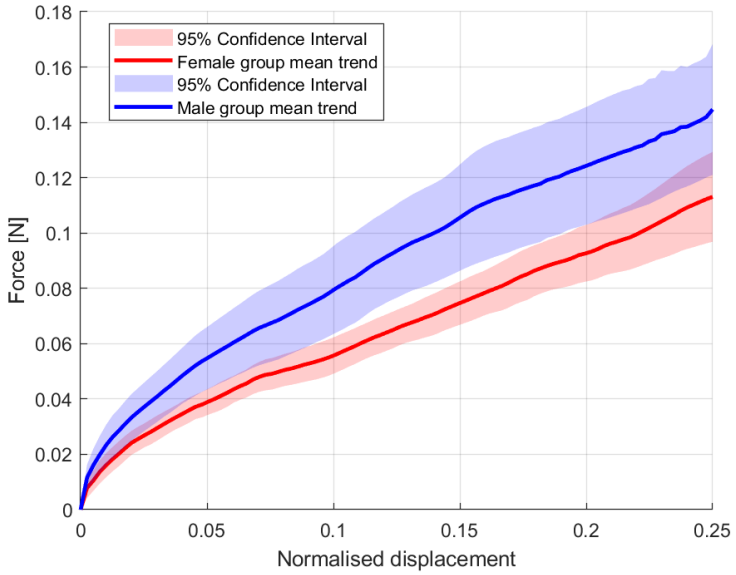


Fig. 4.5 Volunteer static test result: The average measured load of male and female is plotted with the normalised displacement, which is the displacement of the marker point divided by the auricle width.

4.3.3 Statistic Summary and Discussions

To evaluate potential sex-based differences in auricular morphology and mechanical response, several key parameters were analysed: auricle length, auricle width, and effective stiffness derived from static loading experiments, along with natural frequency and damping constant obtained from dynamic impulse testing. A summary of the statistical outcomes is provided in Table 4.1. Between group comparisons were conducted using two-sample independent t-tests under a 95% confidence level. The null hypothesis for each test stated that there was no statistically significant difference between male and female participant groups

Auricle dimensions were significantly larger in male participants, with average lengths of 64.2 mm $\pm$ 4.23 and widths of 33.7 mm $\pm$ 2.45, compared to 54.6 mm $\pm$ 6.13 and 30.7mm $\pm$ 2.13 for females. These differences were statistically significant with p-values of 2.3×10^{-5} and 9.7×10^{-4}, respectively.

To characterise mechanical behaviour, an effective stiffness parameter was introduced. This parameter was defined as the load measured at 25% normalised displacement divided by the corresponding absolute displacement, yielding a stiffness value in units of Nm^{-1}. Across the entire participant group, the mean effective stiffness was 16.3 Nm^{-1} $\pm$ 5.18. Notably, females demonstrated slightly higher stiffness (18.3 Nm^{-1} $\pm$ 4.51) than males (14.7 Nm^{-1} $\pm$

Parameters	Subject group	N	Mean	SD	t-statistics
Length [mm]	All	28	60.1	6.96	$p = 2.3 \times 10^{-5}$
	Male	16	64.2	4.23	
	Female	12	54.6	6.13	
Width [mm]	All	28	32.4	2.75	$p = 9.7 \times 10^{-4}$
	Male	16	33.7	2.45	
	Female	12	30.7	2.13	
Effective stiffness [Nm^{-1}]	All	28	16.3	5.18	$p = 0.069$
	Male	16	14.7	5.25	
	Female	12	18.3	4.51	
Natural frequency (f) [Hz]	All	28	20.6	3.7	$p = 0.0023$
	Male	16	19.1	3.25	
	Female	12	23.7	3.95	
Damping constant (τ) [ms]	All	28	29.3	8.0	$p = 0.039$
	Male	16	33.2	8.0	
	Female	12	24.9	5.2	

Table 4.1 Volunteer test result statistics. Statistical analysis of volunteer test results included t-tests on all measured parameters, with the null hypothesis stating that there is no difference between male and female groups. At a 0.05 confidence level, significant differences were found between the male and female groups in terms of auricle width, length, and damping constant.

5.25), which was not statistically significant at the 0.05 level ($p = 0.069$). Nonetheless, this trend may point to subtle sex-related differences in auricular compliance, motivating further investigation with an expanded sample size.

4.4 Dynamic Loading Response

The dynamic mechanical behaviour of the auricle was investigated through a free-vibration experiment following static loading. This procedure was designed to elicit natural oscillatory motion of the auricle in response to a sudden release, enabling quantification of key dynamic parameters such as natural frequency and damping constant. In this context, the term *natural frequency* refers to the dominant vibrational mode of the auricle as a mechanical structure following impulse release. Under small deformation conditions, the auricle response can be approximated as a lightly damped vibratory system, such that the extracted frequency reflects the global coupling between auricular stiffness and effective mass, rather than localised tissue motion.

4.4.1 Dynamic Data Collection

High-speed video acquisition was employed to capture the auricle's motion immediately after release. Recordings were performed using the same camera system utilised for the static tests, configured in high-frame-rate mode at 1000 frames per second (fps). This sampling rate was selected to ensure temporal resolution sufficient to resolve high-frequency vibrations, typically in the range of 10–30 Hz, as observed in phantom and pilot studies.

The auricle was marked with coloured tracking points, as described previously. Upon reaching the target deflection, a rapid, force-free release was achieved by severing the pre-tensioned string using a controlled flame. This method was adapted from the dynamic impulse experiment described in Chapter 3.4. The flame was applied at a distance of approximately 10 cm from the participant and directed away from the body to avoid discomfort or awareness. This approach minimised mechanical noise that could otherwise be introduced by manual or mechanical detachment mechanisms, thereby initiating free oscillation of the auricle toward its equilibrium position. The resulting motion was recorded for approximately 2 seconds upon release, providing sufficient duration to capture multiple oscillation cycles and their decay.

4.4.2 Data Processing and Modelling

The recorded high-speed video sequences were analysed using a MATLAB script adapted from the static tracking pipeline. Marker trajectories were extracted frame-by-frame, and displacement curves were fitted using a damped sinusoidal model:

$$f(t) = A \cdot \sin(2\pi f t + \phi) e^{-\lambda t} + C \cdot e^{-\tau t} \tag{4.3}$$

This expression consists of two distinct components:

- **Oscillatory damping term:**

$$A \cdot \sin(2\pi f t + \phi) \cdot e^{-\lambda t} \tag{4.4}$$

  models the elastic response of the auricle immediately after release, where:

  - A is the initial oscillation amplitude [mm]
  - f is the natural frequency of oscillation [Hz]

  - ϕ is the phase offset [rad], dependent on initial conditions
  - λ is the dynamic damping coefficient [s^{-1}], reflecting the rate of amplitude decay due to internal tissue friction and air resistance

- **Viscoelastic relaxation term:**

$$C \cdot e^{-\tau t} \tag{4.5}$$

  accounts for slower viscoelastic drift observed in some participants, where:

  - C is the magnitude of the viscoelastic decay [mm]
  - τ is the viscoelastic damping constant [s^{-1}], describing the exponential decay associated with time-dependent tissue relaxation

Although the fitted function includes both an oscillatory damping term and a viscoelastic decay component, the primary focus of this study lies in characterising the auricle's dynamic elastic behaviour, specifically its natural frequency and dynamic damping coefficient. The viscoelastic term was incorporated solely to improve the precision of curve fitting and to account for slow, time-dependent tissue relaxation. Under the small-amplitude, short-duration oscillations induced by the impulse-release protocol, the auricle response is dominated by elastic restoring forces and inertial effects, allowing the system to be approximated as a lightly damped vibratory structure. The extracted oscillation frequency therefore represents an effective natural frequency of the auricle, while higher-order modes, non-linear effects, and long-timescale viscoelastic behaviour are assumed to contribute negligibly and are not explicitly modelled.

For illustrative purposes, one participant's displacement trace was fitted with the following function as shown in Figure 4.6:

$$f(t) = 9.67 \cdot \sin(2\pi \cdot 19.8 \cdot t - 1.60) \cdot e^{-30.2t} - 2.24 \cdot e^{-4.56t},$$

where the oscillatory term captures the primary vibrational response with a natural frequency of 19.8 Hz and damping coefficient of $\lambda = 30.2\ s^{-1}$, while the additional exponential decay term with $\tau = 4.56\ s^{-1}$ accounts for residual viscoelastic relaxation.

A viscoelastic component was incorporated into the analysis framework to enable reliable extraction of two key parameters from the dynamic displacement traces: the oscillation frequency and the damping constant. These parameters were selected because they capture the essential vibrational characteristics of the auricle and were the only measures carried forward for subsequent statistical analysis.

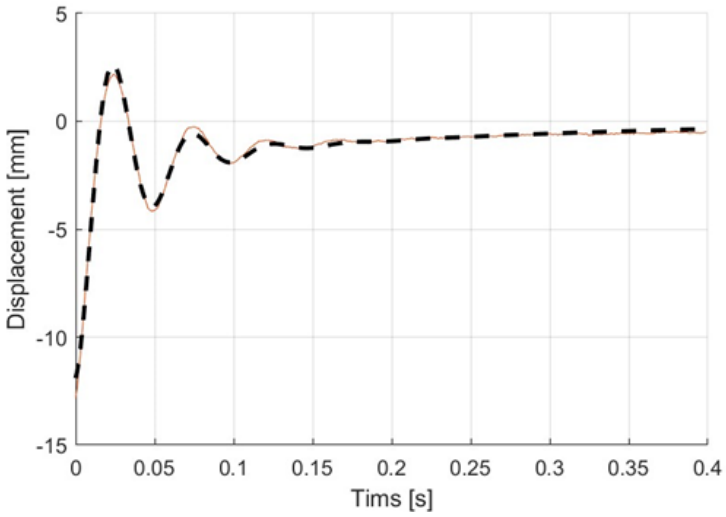


Fig. 4.6 Processed dynamic result of the high frame rate video with marker displacement as a function of time. The oscillation is fitted with a damping sinusoidal function.

The statistical outcomes are summarised in Table 4.1. Dynamic testing revealed clear sex-based distinctions. The natural frequency of auricular vibration was significantly higher in females (23.7 ± 3.95 Hz) compared to males (19.1 ± 3.25 Hz), with $p = 0.0023$. This finding indicates that female participants exhibited a higher-band vibrational response. In addition, the damping constant, τ which representing the temporal decay constant of oscillation, was significantly shorter in females (24.9 ± 5.2 ms) than in males (33.2 ± 8.0 ms), with $p = 0.039$.

Taken together with the static loading results, these findings demonstrate that sex-based anatomical differences influence not only auricular morphology but also its mechanical behaviour across both static and dynamic regimes. This has direct implications for the design of ear-mounted devices, where vibrational stability and tissue coupling may vary systematically between male and female users.

4.5 Analysis Of Auricle Mechanics

4.5.1 Correlation with Geometric Properties

To investigate the influence of auricular geometry on mechanical behaviour, both static and dynamic response parameters were evaluated with respect to two primary anatomical features: auricle length and width. This analysis aimed to determine whether variations in external

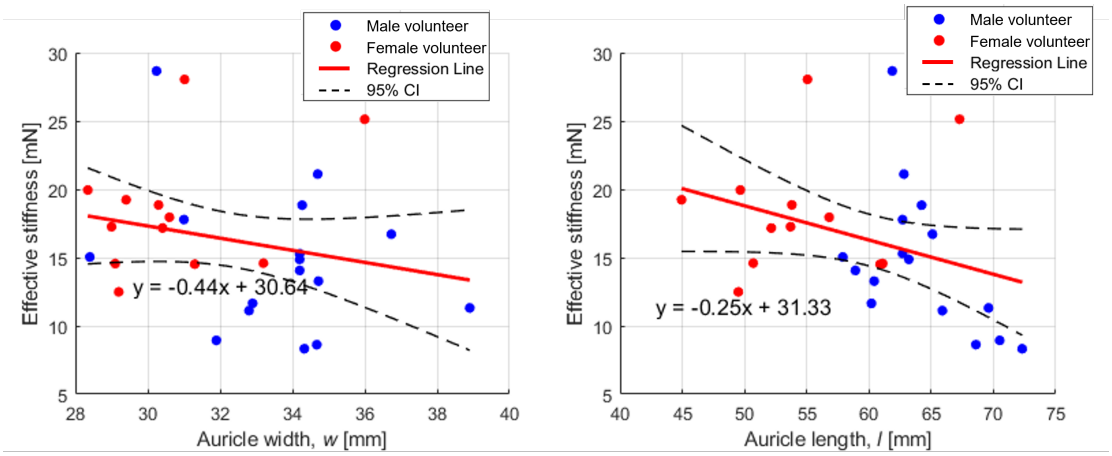


Fig. 4.7 Measured effective stiffness from static auricle tests as a function of (a) auricle width and (b) auricle length. Linear regression lines with 95% confidence intervals are plotted as dashed bands. The R^2 values for each fit is: (a) 0.05 and (b) 0.11, indicating negligible correlation.

auricular dimensions correspond to consistent trends in stiffness or vibrational properties across the population.

Figures 4.7 and 4.8 present scatter plots of effective stiffness (from static loading tests) and natural frequency (from dynamic tests) as functions of auricle width and length. Linear regression lines with 95% confidence intervals are included to indicate the general direction and strength of any observable correlations.

The results in Figure 4.8 indicate an inverse relationship between auricle size and natural frequency: participants with longer or wider auricles tend to exhibit lower vibrational frequencies. The regression for length with natural frequeny has the highest R^2 value (0.3012). This trend is consistent with theoretical expectations, as larger structures generally oscillate more slowly due to increased effective mass and compliance.

In contrast, no significant correlation was found between auricle size and stiffness (Figure 4.7). This suggests that stiffness is influenced less by gross geometric scaling and more by subject-specific factors such as cartilage density, skin elasticity, or internal anatomical variation. These findings support the hypothesis that auricle geometry plays a more dominant role in determining dynamic rather than static mechanical properties.

To interpret the observed dynamic trends, the natural frequency is treated as a system-level mechanical descriptor reflecting the coupled effects of auricular stiffness, effective mass distribution, and boundary constraints at the base of the ear. In this study, the extracted

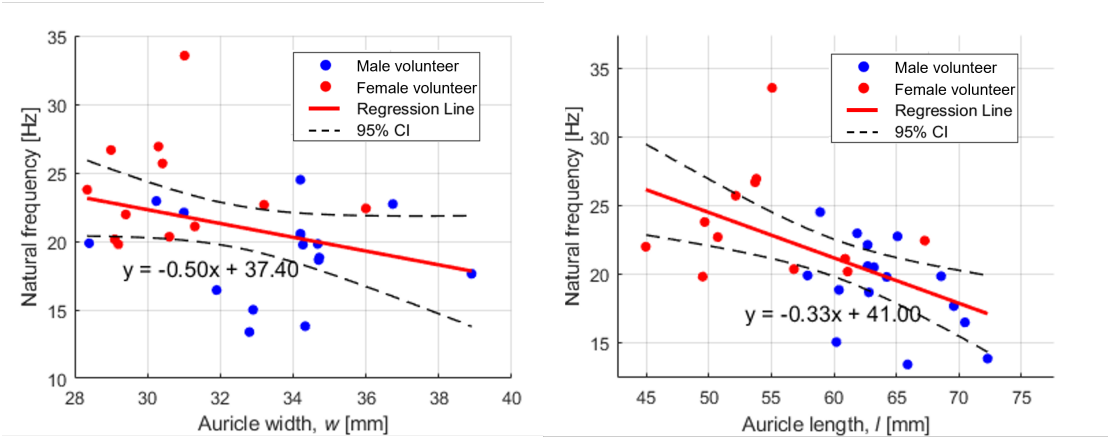


Fig. 4.8 Natural frequency calculated from dynamic auricle tests as a function of (a) auricle width and (b) auricle length. Linear regression fits with 95% confidence intervals are shown as dashed regions. The R^2 values for width and length correlations are 0.11 and 0.30, respectively, indicating a moderate inverse relationship with length.

frequency represents a dominant global vibrational mode of the auricle rather than a local tissue resonance. Unlike static stiffness, which characterises resistance to quasi-static deformation, natural frequency captures the auricle's response to dynamic perturbation and therefore provides complementary insight into its mechanical behaviour. This interpretation motivates the use of an idealised mechanical model to relate measured stiffness, geometry, and frequency.

4.5.2 Beam Model Analysis

To further interpret the auricle's mechanical behaviour, an idealised beam model was employed, consistent with the cantilever framework introduced in Figure **??**. The purpose of this analysis was to determine whether the deformation trends observed experimentally could be rationalised using established mechanical principles of elastic beam theory.

In this simplified representation, the auricle is modelled as a cantilever beam of length L, fixed at its base and subjected to a point load F at the free end, corresponding to anterior pulling. According to Euler–Bernoulli beam theory, the tip deflection δ in the load direction is expressed as

$$\delta = \frac{FL^3}{3EI} \tag{4.6}$$

where E is the Young's modulus of the material and I is the second moment of area of the beam cross-section. This formulation shows that tip displacement scales linearly with applied force but is strongly influenced by geometric factors, particularly the cubic dependence on length (L^3).

Although the auricle is a curved, anisotropic, and multilayered soft-tissue structure rather than a homogeneous elastic beam, this approximation provides a first-order framework for qualitative interpretation. In particular, the cantilever model captures how auricle compliance depends both on material stiffness (E) and on morphological variation (L and cross-sectional geometry), offering a mechanical basis for the inter-subject variability observed in volunteer tests.

This beam theory model suggests that stiffness is directly proportional to the product of the material modulus and the second moment of area, and inversely proportional to the cube of the beam length:

$$k = \frac{F}{\delta} = \frac{3EI}{L^3} \tag{4.7}$$

In our experiments, we observed that stiffness k was invariant with respect to geometric parameters such as auricle length and width. This empirical observation implies a compensating relationship between I and L, specifically:

$$I \propto L^3 \tag{4.8}$$

For a rectangular cross-section, the second moment of area is expressed as:

$$I = \frac{bd^3}{12} \tag{4.9}$$

Assuming that the length and width of the auricle scales linearly with each other, which implies $b \propto L$, we can then derive:

$$bd^3 \propto L^3 \Rightarrow d \propto L^{\frac{2}{3}} \tag{4.10}$$

This derivation suggests a non-linear scaling of auricle thickness with respect to its length, potentially explaining the observed stiffness uniformity across varying auricle sizes.

To understand the auricle dynamic behaviour, the model was then extended to the natural frequency f_n of a cantilever beam with one end fixed [104]. This dynamic response of

deflection at the end of the beam can be written as:

$$f_n = \frac{1.875^2}{2\pi L^2}\sqrt{\frac{EI}{\rho A}} \tag{4.11}$$

where ρ is the material density and $A = bd$ is the cross-sectional area of the beam.

Substituting $EI = \frac{kL^3}{3}$, the frequency expression becomes:

$$f_n \propto \frac{1}{L^2\sqrt{A}}\sqrt{EI} \propto \sqrt{\frac{1}{LA}k} \tag{4.12}$$

If $A \propto L^{5/3}$ as derived above, then:

$$f_n \propto L^{-4/3}\sqrt{k} \tag{4.13}$$

Next, the relationship between measured stiffness and natural frequency was examined. As shown in Figure 4.9(a), a scatter plot of the measured natural frequencies against auricle stiffness values is presented, along with a fitted curve following the theoretical scaling law $f_n \propto \sqrt{k}$. This visualisation confirms the expected trend derived from classical beam dynamics, where higher stiffness corresponds to increased natural frequency.

In addition, Figure 4.9(b) illustrates the regression model derived in function 4.13, which incorporates both geometric and mechanical parameters. Specifically, the model predicts a scaling of the form $f_n \propto L^{-4/3}\sqrt{k}$, combining auricle length and stiffness into a unified descriptor of vibrational behaviour.This combined descriptor integrates geometric and mechanical contributions to auricle vibration. The improved R^2 value (from 0.476 to 0.529) demonstrates that including auricle length enhances predictive power and aligns with the theoretical scaling law for cantilevered beam systems.

Together, these findings demonstrate that while auricle stiffness appears independent of geometric size, the natural frequency is governed by a combination of geometry and stiffness, following a mechanical scaling law consistent with beam theory. This supports the validity of using simplified mechanical analogues to predict auricular dynamics.

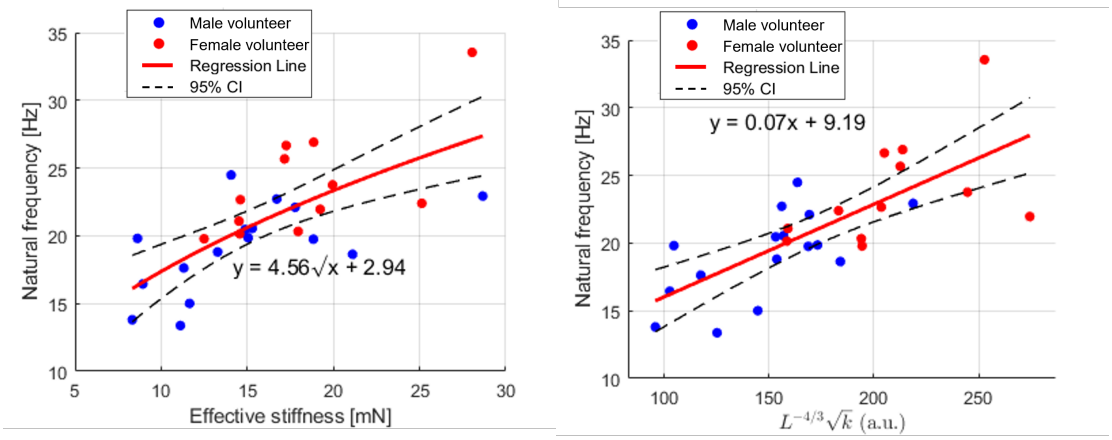


Fig. 4.9 (a) Relationship between measured auricle stiffness and its natural frequency, with a fitted curve based on the theoretical model $f_n \propto \sqrt{k}$, with $R^2 = 0.47$ (b) Regression model using the composite parameter $f_n \propto L^{-4/3}\sqrt{k}$ showing improved correlation with $R^2 = 0.53$

4.6 Conclusions

This study introduced and validated a novel, non-invasive experimental methodology for the *in vivo* characterisation of human auricle mechanical properties. By combining static loading and dynamic release tests with photometric tracking, load-cell force measurement, and high-speed imaging, this protocol enabled the precise quantification of auricular stiffness and vibrational behaviour across variant participants.

The static test provided insight into the auricle's compliance under anteriorly applied loads. A consistent pulling angle of approximately 75 degrees, identified through beam model simulations, ensured high repeatability and reduced experimental variability. By normalising displacement measurements with respect to auricle width, the results were comparable across individuals of differing ear sizes. Effective stiffness was derived at a fixed deformation threshold (25% of auricle width), and showed no statistically significant dependence on sex, despite observed geometric differences in auricle length and width between male and female participants.

Dynamic loading via an impulse-release method allowed for the extraction of key vibrational parameters, particularly the natural frequency and damping constant. The use of a high-speed camera at 1000 fps and tailored MATLAB fitting scripts enabled accurate reconstruction of the damped oscillatory motion. Although a viscoelastic decay component was included in the fitting model to enhance curve accuracy, the primary focus of analysis remained on the

dynamic oscillation characteristics. To simplify the development of FE model, the effect of viscoelasticity was neglected. Future study should try to include this aspect of tissue behaviour to further complete the model.

Correlation analysis and beam-theory based modelling revealed a weak inverse relationship between auricle size (length and width) and its natural frequency, supporting the hypothesis that larger auricles exhibit slower vibrational responses due to increased structural mass and compliance. Notably, auricle stiffness did not exhibit strong dependence on geometric parameters, suggesting that intrinsic material properties and gender, rather than size, play dominant roles in determining static mechanical behaviour.

The relationship between stiffness and natural frequency was further explored through a dimensional analysis using an idealised beam model, which demonstrated that frequency scales with the square root of stiffness and inversely with auricle geometry. The experimental results had demonstrated that the stiffness and natural frequency largely followed this theoretical prediction $f_n \propto L^{-4/3}\sqrt{k}$, with $R^2 = 0.53$, Suggesting that auricle mechanics can be modelled through mechanical measurements and correlated with the geometry of the auricle.

Taken together, these findings contribute a validated framework for auricle mechanical characterisation that is both experimentally practical and analytically grounded. This framework provides an essential foundation for future research and engineering applications, including data for developing FE models of human auricles and the design of earables, where understanding ear tissue dynamics is critical for comfort, performance, and signal fidelity.

Chapter 5

Auricle Computational Modelling and Geometric Matching

5.1 Introduction

The external ear, or auricle, presents a complex anatomical structure that plays a crucial role in the design of wearable and biomedical devices, particularly in combination with sensoring technologies that require stable contact with the skin for sensing or stimulation. Understanding and accurately modelling the mechanical response of the auricle under various loads becomes essential for ensuring device stability, comfort, and performance, which will greatly advance the development of earable devices.

Building on the phantom-based methodology in Chapter 3, which established auricle mechanical experiment procedure and simulation validation for auricle meshes, and the *in vivo* mechanical characterisation reported in Chapter 4, this chapter develops computational auricle models that emphasise both anatomical realism and mechanical fidelity. We investigate two complementary modelling sources: (i) the high-resolution CT dataset previously used for phantom construction, and (ii) an open-source auricle database curated to capture broader inter-subject variability across male and female populations.

These digital auricle models are used to conduct FE simulations, incorporating both linear elastic and hyperelastic (Ogden) material models. Through parametric analysis, the mechanical behaviour of the auricle under both static and dynamic loading, similar to the setup in the previous chapters, is explored in detail. The simulations are calibrated using experimental

data from human subjects and phantom models, enabling identification of material properties that produce physiologically consistent outcomes.

By simulating auricle deformation and vibrational behaviour under realistic boundary conditions, and validating these models against empirical observations, this work establishes a robust computational foundation for future auricle-based device development. In addition, this chapter investigates the interaction between auricle morphology and mechanical response, offering insights into design adaptation for user-specific anatomical variation.

5.2 Auricle Model Construction

5.2.1 Auricle Mesh Generation

To accurately represent the mechanical behaviour of the auricle in FE simulations, it is essential to construct surface meshes that capture both realistic anatomical features and population-level morphological variability. This section outlines the procedures used to generate auricle meshes from two primary sources: (1) a refined, subject-specific model based on a previously constructed phantom auricle, and (2) a set of anatomically valid auricle geometries extracted from a publicly available 3D scan database. These meshes form the geometric foundation for the subsequent simulation and parameter studies presented in this chapter.

1. Phantom-Based Auricle Mesh Refinement

The first mesh was developed by refining the phantom auricle model described in Chapter 3. While the original phantom provided a simplified approximation of auricular geometry suitable for initial validation, it lacked sufficient anatomical fidelity for realistic simulation of auricular mechanics.

To enhance anatomical fidelity in the auricle model, the same CT scan of a cadaveric external ear previously utilised was revisited [99]. The original scan used a Nikon XT 225 ST micro-CT scanner (Nikon Metrology, Tring, UK), which yielded a voxel resolution of 27 µm. The acquired scans were reconstructed and segmented using Stradview software (version 7.0; University of Cambridge; [105]). Following segmentation, the resulting surface model was further refined through manual post-processing in Meshmixer (Autodesk, USA), as shown in Figure 5.1. The refinement workflow included the following key steps:

- **Surface smoothing and curvature preservation** to eliminate segmentation artefacts while retaining detailed anatomical contours critical for mechanical fidelity.
- **Adaptive remeshing** to ensure uniform mesh density and improve element quality for finite element analysis.
- **Layered thickness modelling** to generate distinct skin and cartilage layers using a combination of planar cutting and hollowing operations based on anatomical proportions.

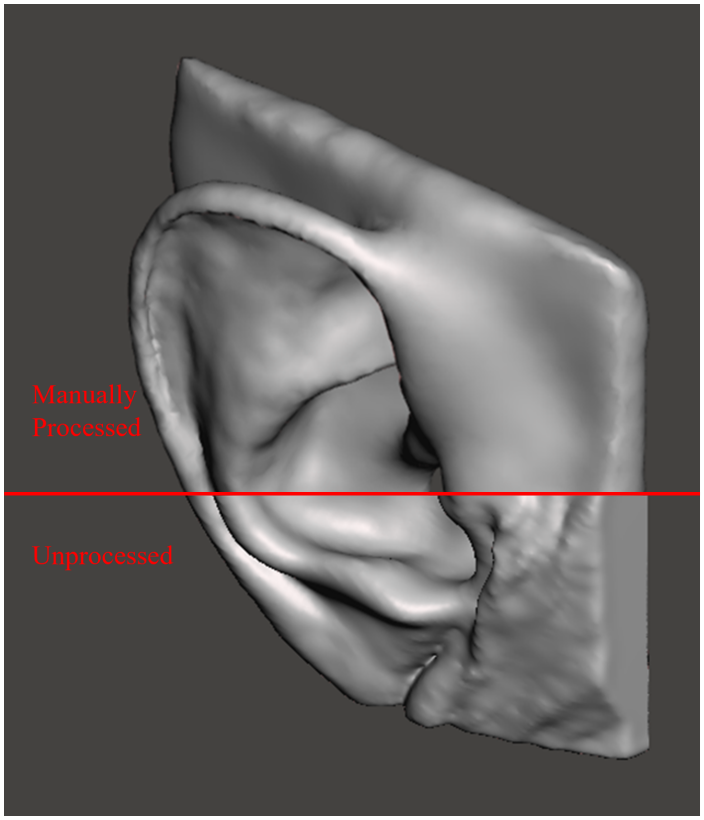


Fig. 5.1 CT-derived auricle mesh before and after manual post-processing in Meshmixer. Above the red line: processed model after surface refinement, adaptive remeshing, and separation into a skin shell and cartilage core via controlled offsets. Below the red line: the unprocessed triangulation from segmentation, showing rugged texture and irregular surface.

The resulting auricle model was constructed as a two-layer structure: an external skin envelope and an internal elastic cartilage core. The division between these layers was implemented using a hollowing function as previously described in Chapter 3.2, which applied a user-defined offset to the external mesh surface and generate a shell. The thickness

of the skin layer was determined by this offset, and the residual internal volume was assigned to the cartilage domain. This approach enabled control over the thickness distribution while maintaining the overall morphology.

To evaluate anatomical realism, the cartilage and skin layers of the model were compared against cadaveric cross-sections adapted from the Visible Human Project [106], courtesy of the U.S. National Library of Medicine. As illustrated in Figure 5.2, the cartilage layer generated from subtracting the hollow 0.65 mm and 0.75 mm auricle surface are consistent with measurements from human anatomical cross-sections, which has a thickness of around 0.45 ± 0.10 mm, supporting the validity of the layered structural representation. To preserve adequate skin volume while matching the observed cartilage thickness, we adopted a hollow distance of 0.75 mm for subsequent model generation.

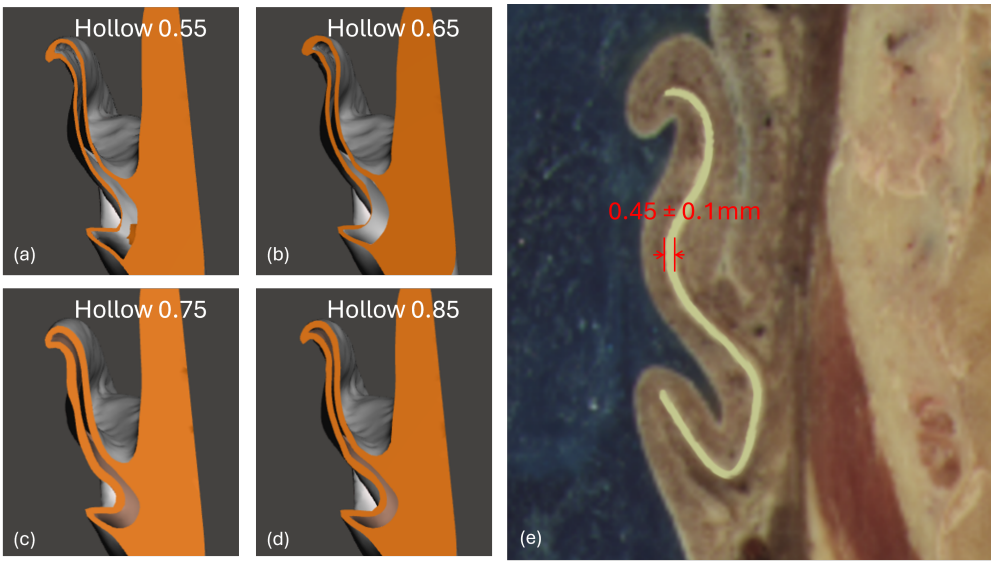


Fig. 5.2 Anatomical validation of the layered auricle model. (a)–(d) Cross-sections of the FE model generated with inward offset ("hollow") distances of 0.55, 0.65, 0.75, and 0.85 mm, respectively. (e) Cadaveric cross-section adapted from the Visible Human Project [106], indicating a cartilage thickness of $\approx 0.45 \pm 0.10$ mm. Cartilage layers produced with 0.65–0.75 mm hollows (b,c) closely match the anatomical reference while maintaining sufficient skin volume.

For preparation of finite element analyses, the layered auricle geometry was remeshed at multiple target resolutions in MeshLab [107] to improve element regularity and aspect ratios while removing residual artefacts from hollowing layer. Each mesh variant was exported in STL format and converted to Abaqus input files via Gmsh [108], preserving topology and

layer correspondence. The resulting CT-derived model constitutes the baseline geometry for all validation studies and parameter-sensitivity analyses presented in this chapter.

2. Geometry-Diverse Auricle Meshes from 3D Scan Database

To investigate how auricular mechanics are influenced by geometric variation, a second set of surface meshes was derived from the *WiDESPREaD* (Wideband Directivity Simulation Platform for Realistic Acoustic Devices) database [109]. This publicly available dataset includes high-resolution 3D scans of 86 adult human heads, originally collected for research in acoustic transmission and sound localisation. Each subject was scanned using a dual-system approach: a Kinect 3D scanner (Microsoft, USA) was employed to capture the overall head geometry, while the auricular region was imaged using an Artec Space Spider handheld scanner (Artec 3D, Luxembourg). The latter system offers a spatial resolution of up to 50 μm, providing highly detailed reconstructions of auricular morphology suitable for biomechanical simulation and morphological analysis.

From this dataset, three auricle meshes were selected to represent distinct morphological profiles, referred to hereafter as the *Long*, *Short*, and *Thick* auricle models. These meshes were chosen based on dimensional characteristics that span the range of auricle size and shape observed in the volunteer population.

Each model followed a standardised preparation pipeline:

- **Region isolation**, in which the auricle was manually segmented from the full head geometry using Fusion 360.
- **Surface cleaning and denoising** to correct scan artefacts and reconstruct regions with missing anatomical detail, especially around the lobule, back of the auricle, and antihelix.
- **Triangulation and remeshing** using MeshLab to ensure uniform surface quality compatible with finite element meshing standards.
- **Layered thickness modelling** employing the same hollowing strategy used for the CT-derived model, allowing consistent definition of skin and cartilage regions based on anatomical reference data.

The resulting meshes were each remeshed at varying resolutions and exported in STL format before being processed into Abaqus input files using Gmsh. These geometrically diverse

models enable simulation-based studies of how morphological variation affects auricle mechanical behaviour.

Summary of Mesh Dataset

Table 5.1 summarises the origin, resolution, and intended use of each auricle mesh. The CT-derived model, offering higher surface resolution, serves as the simulation baseline for model validation. In contrast, the *WiDESPREaD*-based models represent the anatomical diversity and support geometry-dependent analysis.

Model Name	Source	Dimensions (W×H) [mm]	Scan Resolution
CT Baseline	Clinical CT scan + manual refinement	32.8 × 59.7	27 µm
Long model	*WiDESPREaD* 3D scan dataset	32.6 × 67.7	50 µm
Short model	*WiDESPREaD* 3D scan dataset	33.1 × 52.7	50 µm
Thick model	*WiDESPREaD* 3D scan dataset	34.4 × 61.4	50 µm

Table 5.1 Summary of auricle mesh models used in finite element simulations. Each model is characterised by its source, physical dimensions (width × height, in mm), and scan resolution. The CT-derived baseline model serves as a high-fidelity anatomical reference, while the remaining models represent shape variations extracted from the *WiDESPREaD* database.

To visually compare these mesh geometries with experimental measurements, their respective auricle lengths and widths were plotted against the volunteer dataset, as shown in Figure 5.3. This highlights the range of anatomical representation provided by the selected models and supports their relevance for population based mechanical analysis.

5.2.2 Auricle Simulation Demonstration

To provide an initial verification of the finite element (FE) auricle model, a demonstration simulation was performed replicating the loading and boundary conditions used in the *in vivo* volunteer study. The purpose of this exercise was not to finalise material definitions or mesh strategies, but rather to assess whether the model is capable of reproducing experimentally observed mechanical behaviour in a representative loading case. This baseline comparison establishes confidence in the model framework, upon which more detailed parametric studies, including mesh density, constitutive law selection, and sensitivity to morphological variability,

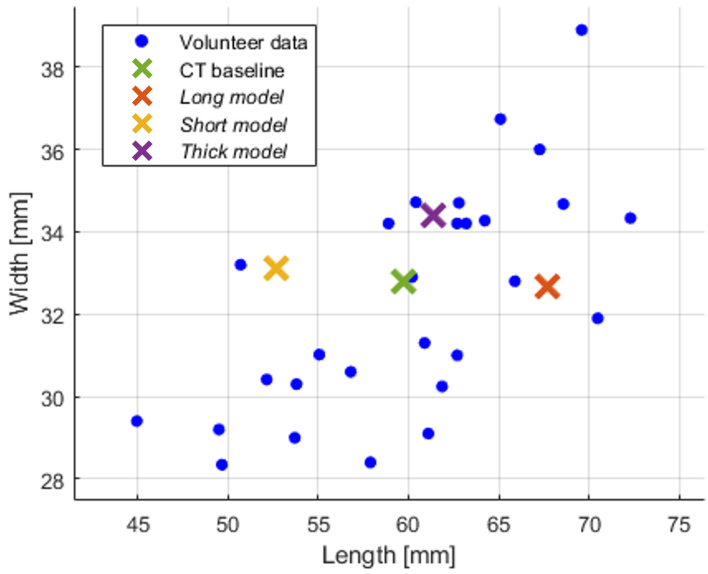


Fig. 5.3 Comparison of auricle model dimensions with volunteer data from Chapter 4. The selected meshes (Long, Short, Thick, and CT-derived) span the measured range of auricle width and length in the population.

which will be systematically explored later in this chapter. The geometry used here was the CT-derived auricle mesh, with an average element edge length of 0.8 mm.

All finite element simulations were performed locally on a workstation equipped with an Intel® Core™ i9-10900K CPU operating at 3.70 GHz. The system is configured with 64 GB of RAM and runs a 64-bit Windows operating system. Abaqus/Standard was executed using a shared-memory parallel setup with 8 CPU cores allocated per job. This computational environment provided sufficient memory and processing capability for both high-resolution mesh analyses and dynamic simulations, ensuring reliable performance for the convergence studies and parametric sweeps conducted in this work.

Boundary Conditions and Constraints

The auricle was represented as a two-layer structure comprising an outer skin layer and an underlying stiffer cartilage core. Preliminary simulations indicated that, in order to reproduce the volunteer experimental data, the cartilage had to be assigned a lower effective stiffness than values typically reported in the literature, which range between 1.4 MPa and 2.1 MPa [67]. For the skin, previously reported Young's modulus values span from 50 kPa to 1.4 MPa [77].

As discussed in Chapter 2, this discrepancy may arise because dissected post-mortem tissue often loses its original elasticity, leading to higher apparent stiffness in cadaveric measurements compared with living tissue. To illustrate this effect in a simple demonstration analysis, each layer was therefore assigned reduced linear elastic material properties within the reported ranges: the skin with Young's modulus $E = 0.12$ MPa and Poisson's ratio $\nu = 0.48$, and the cartilage with $E = 1.0$ MPa and $\nu = 0.45$. Both layers were meshed with C3D4 tetrahedral elements. This choice of properties avoids the computational burden associated with highly incompressible formulations, while retaining sufficient accuracy to capture the key mechanical behaviour of the auricle.

The base of the auricle was constrained to reflect cranial fixation and rigidity of skull bones. Nodes at the conchae base were fixed in all translational degrees of freedom, consistent with the stabilisation provided by a chin rest and head support during the volunteer experiments.

Anterior loading was applied at the lateral tip of the helix, oriented 75° from the sagittal plane to replicate the 'clip and string' loading protocol used in experiments illustrated in Figure 4.2(b). The applied force was introduced via a reference point coupled to a small surface patch on the helix rim, allowing both controlled load application and displacement readout.

Modelling Assumptions

The simulation comprised two sequential analysis steps: a static step followed by a dynamic step. The static step represented the quasi-static pulling process, during which inertial and damping effects were assumed negligible owing to the low loading rate of 0.5 mm/s. The skin and cartilage layers were coupled using a *tie* constraint, enforcing full displacement compatibility at their interface. Contact interactions between tissue surfaces were not modelled, and the auricle was assumed to deform freely without self-contact within the applied deformation range.

For this initial demonstration, both the skin and cartilage layers were modelled as linear elastic, nearly incompressible solids. This material assumption neglects the well-documented nonlinear and viscoelastic behaviour of auricular tissue; however, it was adopted intentionally to reduce computational complexity and to establish a transparent baseline for model validation. Under the small to moderate strain levels examined in this study, the linear elastic approximation captures the first-order stiffness response governing auricle deformation and dynamic behaviour.

The primary objective of this modelling stage was to validate the simulation workflow and assess its ability to reproduce experimentally measured force–displacement and vibration characteristics, rather than to achieve full physiological fidelity. More advanced constitutive descriptions, including hyperelastic and viscoelastic material models, together with mesh refinement and contact modelling, are introduced in later sections to improve predictive accuracy and anatomical realism.

Simulation Results and Comparison

Figure 5.4 shows the simulated auricle deformation under anterior tensile loading. Maximal displacement occurred at the helix tip, with bending along the anterior–posterior axis, in line with both mechanical expectation and observed experimental deformation profiles.

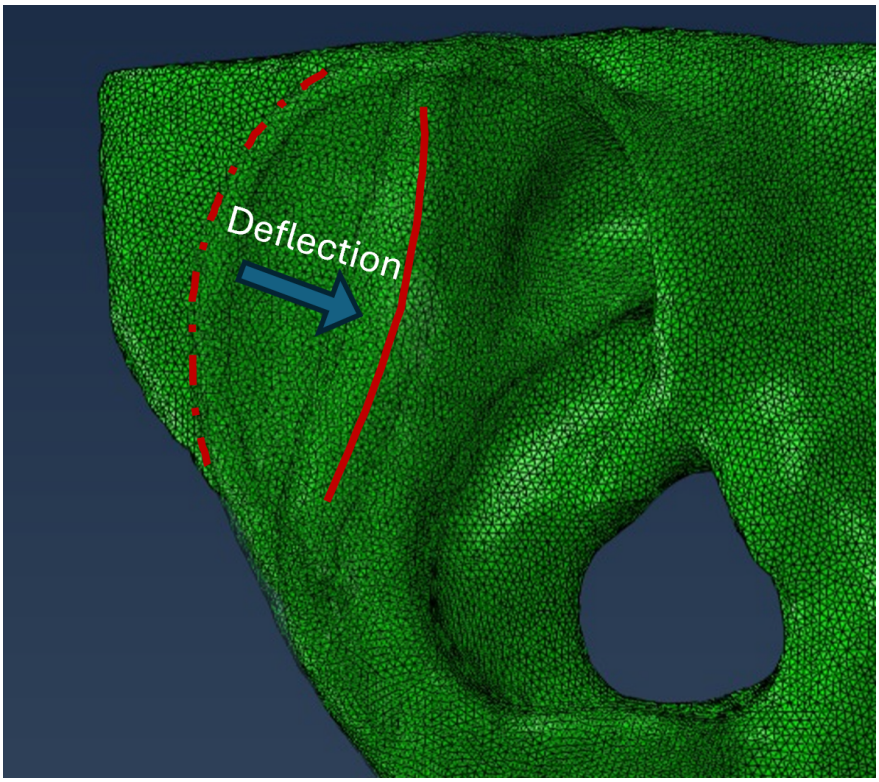


Fig. 5.4 Demonstration simulation of auricle deformation under anterior pulling. The deformation pattern shows bending along the anterior–posterior axis with maximal displacement at the helix tip, consistent with volunteer experiment observations. Parameters used here (material properties, mesh density) are preliminary and will be refined in subsequent sections.

Quantitative comparison was performed by evaluating the effective stiffness from the applied force F and the resulting displacement δ, which was the same normalised displacement as

described in Chapter 4.3 of 0.25, at the clip reference point:

$$k = \frac{F}{\delta}.$$

The computed stiffness of 10.4 Nm^{-1} falls within one standard deviation of the average measured stiffness across volunteers, supporting the model's predictive capability. A dynamic release simulation further predicted a first-mode natural frequency of 26.8 Hz, within two standard deviations of experimental values.

These findings confirm that, even with simplified material laws and preliminary meshing, the FE model captures the static compliance and vibrational response of the auricle. This demonstration provides confidence in the underlying modelling framework, while recognising that the parameters applied here are provisional. A conclusive study of mesh refinement, constitutive model selection, and parameter sensitivity will follow in later sections of this chapter.

5.2.3 Auricle Mesh Verification

To confirm the numerical reliability and accuracy of the simulation outcomes, a mesh convergence study was performed on the CT-derived auricle model. The objective was to determine an optimal mesh density that ensures stable mechanical output, specifically, displacement, stiffness, and natural frequency, under standardised loading.

Methodology

Five auricle surface meshes were created using isotropic remeshing in MeshLab, targeting average element lengths of 1.2, 1.0, 0.8, 0.6, and 0.4 mm. The corresponding node counts ranged from approximately 11,500 to 100,600. These meshes were exported in STL format and converted to Abaqus-readable input files (.inp) via Gmsh. All simulations were run in Abaqus/Standard under identical boundary conditions and material properties as outlined in the previous section.

The following metrics were extracted from each simulation:

- Maximum displacement at the helix tip
- Reaction force at the loading point
- Effective stiffness (computed as $k = F/\delta$)

- First-mode natural frequency (via modal analysis)

Results and Analysis

Results from the convergence study are summarised in Table 5.2. As the mesh was refined, both stiffness and natural frequency asymptotically approached stable values, with less than 2% variation observed between the two finest resolutions. Based on these findings, a 0.6 mm element size (approx. 43,800 nodes) was selected as the standard for balancing computational cost with accuracy in the subsequent simulations.

Element Length [mm]	**Node Count**	**Computation Time [min]**	**Effective Stiffness [Nm^{-1}]**	**Natural Frequency [Hz]**
1.2	11,500	24	13.91	29.34
1.0	16,400	43	12.36	27.94
0.8	24,800	92	10.84	26.44
0.6	43,800	280	10.31	25.69
0.4	100,600	1470	10.12	25.25

Table 5.2 Mesh convergence results for auricle simulation under static loading.

The results in Table 5.2 indicate that both displacement and natural frequency values converge with mesh refinement. Specifically, both natural frequency and effective stiffness stabilised with element lengths below 0.6 mm, with a change of less than 2% observed between the 0.6 mm and 0.4 mm meshes. These results suggesting numerical convergence in the dynamic response below mesh element length of 0.8 mm.

Discussion and Mesh Selection

While finer meshes offered marginal improvements in accuracy, they incurred substantial increases in computation time. In particular, the 0.4 mm mesh required over 900 minutes of runtime, more than 5 times the duration of the 0.6 mm mesh, despite offering minimal additional accuracy.

Based on this trade-off between computational cost and numerical precision, the 0.6 mm mesh was selected for all subsequent simulations. This resolution provided a reliable approximation of mechanical behaviour while maintaining feasible computation times for large-scale parametric and dynamic studies.

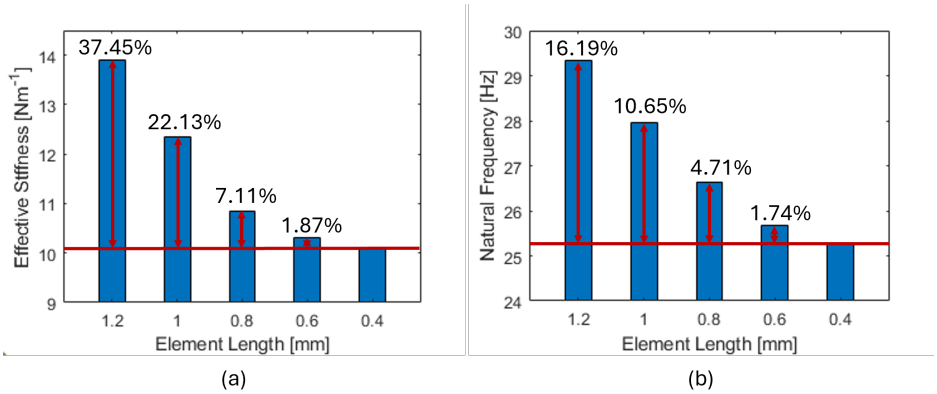


Fig. 5.5 Mesh convergence analysis of the auricle finite element model. The plots show the variation in (a) effective stiffness and (b) natural frequency as functions of the average element edge length. Numerical results correspond to the data summarised in Table 5.2. Each value is expressed as a percentage difference relative to the reference solution obtained with the finest mesh (element length = 0.4 mm).

5.3 Parameter Study

To understand the sensitivity of auricle mechanics to material properties, a parametric study was conducted using both linear elastic and hyperelastic material models. These studies aimed to evaluate how varying material stiffness affects key mechanical responses such as static stiffness and natural frequency. The outcomes guided the selection of suitable constitutive models and parameter ranges for later simulations involving morphological variation.

5.3.1 Linear Material Study

As a baseline analysis, the auricle model was simulated with linearly elastic properties for both skin and cartilage layers. The Young's modulus (E) of each tissue type was varied independently. The Poisson's ratio (ν) of skin layer was kept constant at 0.495 to reflect the near-incompressibility of soft tissue.

Simulation Setup

- Skin modulus range: E_{skin} = 0.06 – 0.16 MPa
- Cartilage modulus range: $E_{\text{cartilage}}$ = 0.6 – 1.6 MPa

- Poisson's ratio: Skin $\nu = 0.495$, Cartilage $\nu = 0.45$ (fixed for all tests)
- Outputs: effective stiffness k, natural frequency f_n

Results and Observations

To evaluate the sensitivity of auricular mechanical response to changes in skin stiffness, a series of simulations were conducted in which the Young's modulus of the skin layer (E_{skin}) was varied while maintaining fixed values for the cartilage modulus ($E_{\text{cartilage}}$). The effective stiffness and the first-mode natural frequency of the auricle were extracted for each parameter combination. Representative results for three different values of $E_{\text{cartilage}}$ are shown in Figure 5.6.

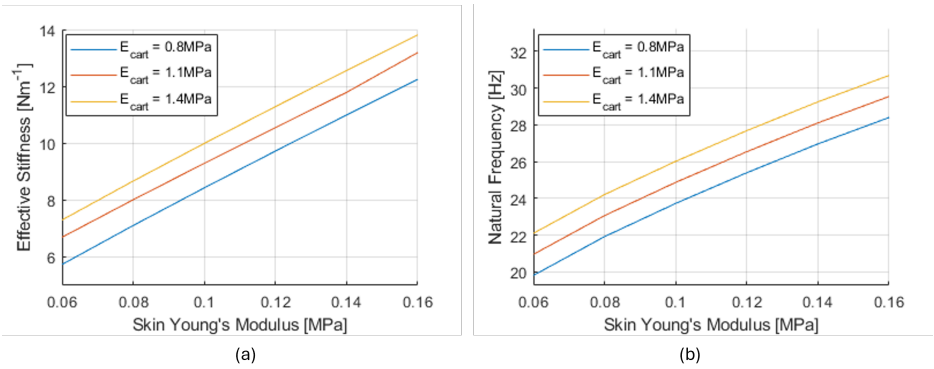


Fig. 5.6 Contour plots of auricle stiffness and natural frequency under a linear elastic material model, with varying skin modulus and fixed cartilage modulus at three levels.

As expected, both the effective stiffness and the natural frequency increased monotonically with increasing values of E_{skin} and $E_{\text{cartilage}}$. The influence of the skin modulus was notably greater than that of the cartilage, which can be attributed to the larger volume fraction and surface coverage of the skin layer, as well as its greater contribution to resisting global deformation. Structurally, this behaviour reflects the mechanics of a sandwich composite system, in which the outer layers primarily govern bending stiffness because bending stress varies linearly with the distance from the neutral axis [110].

While the observed trends align with mechanical expectations, significant deviations from the experimental data were identified. In particular, the simulated stiffness and natural frequency values, especially at the lowest tested combinations of material moduli, remained markedly higher than those recorded in the *in vivo* volunteer experiments. As illustrated in Figure 5.7, the parameter sweep using a linear elastic model matches with the edge of the experimental

data range; however, it failed to reproduce results at the lower end frequency and higher end of stiffness spectrum. This limitation highlights the inadequacy of the linear elastic assumption in accurately representing the mechanical behaviour of auricular soft tissue.

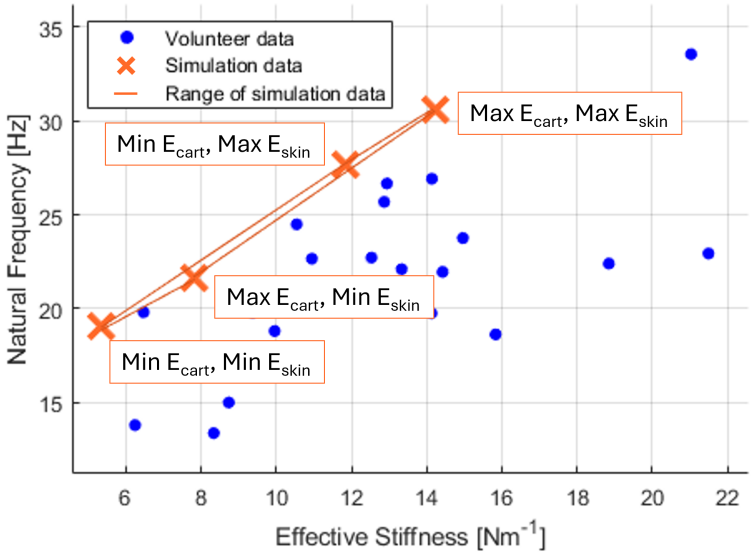


Fig. 5.7 Simulation result plot together with volunteer data. The range of the simulation data is illustrated as a parallelogram with four limit simulation data.

Furthermore, previous experimental studies have demonstrated that auricular tissue exhibits strain-dependent stiffening, a hallmark of hyperelastic or non-linear material behaviour. These findings underscore the limitations of linear elasticity in modelling auricular mechanics and motivate the implementation of a hyperelastic constitutive model, which is explored in the subsequent section.

5.3.2 Hyperelastic Material Study — Ogden Model

To more accurately capture auricle behaviour under large deformations, a first-order Ogden hyperelastic model was employed. This model captures non-linear stiffening through strain-energy potential functions governed by shear modulus μ_i and stiffening parameter α_i, as defined below:

$$W = \sum_{i=1}^{N} \frac{\mu_i}{\alpha_i} \left(\lambda_1^{\alpha_i} + \lambda_2^{\alpha_i} + \lambda_3^{\alpha_i} - 3\right) + D_1 (J-1)^2 \tag{5.1}$$

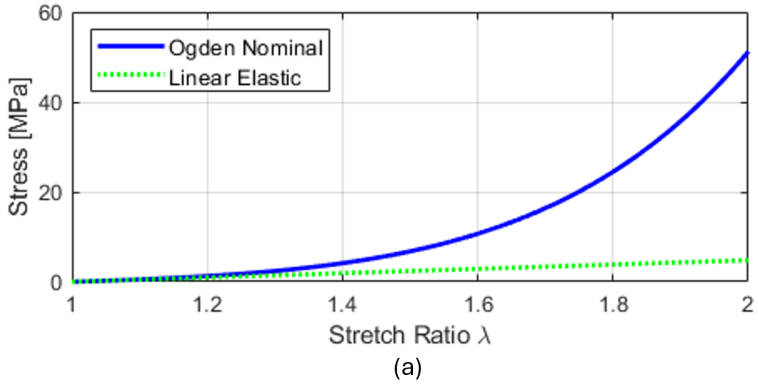
This expression defines the strain energy density function W for the Ogden hyperelastic material model of order N, where:

- μ_i are the shear modulus parameters for the i-th term.
- α_i are the nonlinear material parameters describing the stiffening response of the material.
- $\lambda_1, \lambda_2, \lambda_3$ are the principal stretch ratios along the three principal material directions.
- $J = \lambda_1 \lambda_2 \lambda_3$ is the determinant of the deformation gradient, representing the local volume change.
- D_1 is the penalty parameter controlling material compressibility. It is related to the bulk modulus K by $K = 2/D_1$.

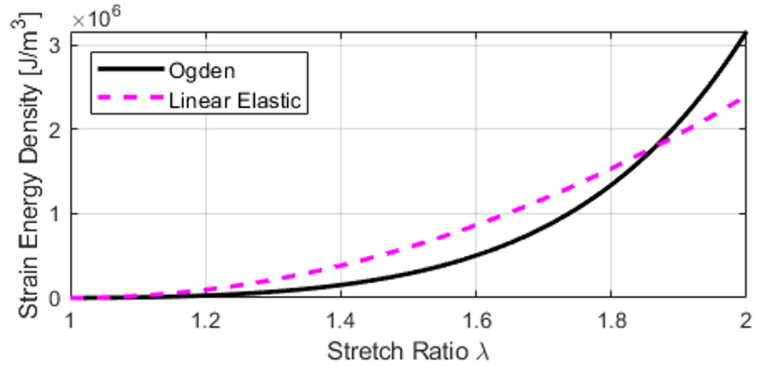
The first term accounts for the deviatoric (shape-changing) part of the deformation, while the second term enforces volumetric constraints. For biological tissues like skin, which are nearly incompressible, the Ogden model provides a suitable framework for capturing their nonlinear, strain-dependent response.

Stress–Strain Behaviour Comparison

Figure 5.8 compares the stress–stretch response of a linear elastic material and a one-term Ogden hyperelastic material under uniaxial extension up to 100% strain. The Ogden model, commonly used to represent nonlinear soft biological tissues, is parameterised here with $\mu = 0.4$ MPa and $\alpha = 8$. For comparison, a linear elastic material is defined using an equivalent Young's modulus computed as $E_{\text{equiv}} = \frac{3}{2}\alpha\mu = 4.8$ MPa, following the small-strain approximation derived from the Ogden formulation [101]. The bottom subplot presents the corresponding strain energy densities, further highlighting the nonlinear strain stiffening effect captured by the Ogden model. This behaviour is critical for replicating the auricle's mechanical response: a compliant regime at small deformations ensures comfort and flexibility, while the increased stiffness at large strains enhances resistance to deformation, thereby modulating the natural frequencies of the earable–auricle system.



(a)



(b)

Fig. 5.8 Comparison of material responses under uniaxial extension up to strain ratio of 2. (a) Stress–stretch curve showing the nonlinear response of a one-term Ogden hyperelastic material with $\mu = 0.4$ MPa and $\alpha = 8$ compared to a linear elastic material with equivalent Young's modulus $E_{\text{equiv}} = 4.8$ MPa. (b) Corresponding strain energy density. The Ogden model captures the characteristic stiffening at large strains observed in soft biological tissues.

Bulk Modulus Consideration

In the compressible Ogden hyperelastic formulation, the parameter D controls volumetric compressibility: smaller D corresponds to a higher bulk modulus, helping enforce near-incompressibility[111].

In the limit of small strains, one can relate D to the bulk modulus K via $K = 2/D$ and then use classical small-strain elasticity relations[112]

$$K = \frac{2\mu(1+\nu)}{3(1-2\nu)}.$$

Rearrangement yields

$$\nu = \frac{3K - 2\mu}{2(3K + \mu)}.$$

Substituting $K = 2/D$ gives

$$\nu = \frac{6/D - 2\mu}{2(6/D + \mu)}.$$

This relation provides a rough estimate of the effective Poisson's ratio in the small-strain regime, highlights the coupling between the shear modulus μ and D in governing the volumetric response. To visualise this relationship, a sensitivity plot (Figure 5.9) illustrates how decreasing D increases incompressibility. In this study, values of D were selected to achieve effective Poisson's ratios of $\nu = 0.495$ for the skin layer and $\nu = 0.46$ for the cartilage layer, consistent with physiological values.

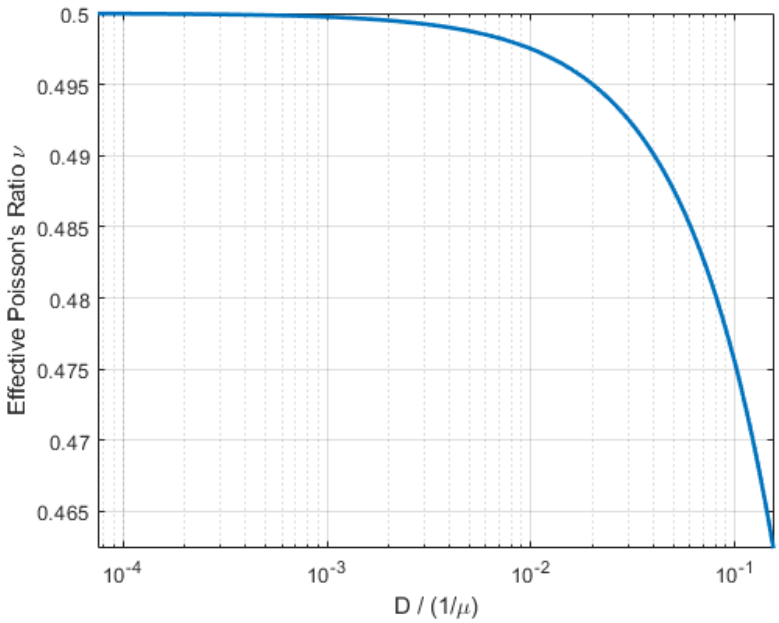


Fig. 5.9 Effect of D on Poisson's Ratio ν in Ogden Model. The x-axis is plotted as the dimensionless ratio $D/(\frac{1}{\mu})$. A smaller D value corresponds to a higher degree of incompressibility, approaching the theoretical limit of $\nu = 0.5$.

Simulation Setup

To investigate the influence of hyperelastic parameters on auricle mechanics, a parametric sweep was conducted across a range of plausible material values for both skin and cartilage layers. The tested ranges were:

- Skin shear modulus: $\mu_{\text{skin}} = 20 – 60$ kPa
- Skin stiffening parameter: $\alpha_{\text{skin}} = 12 – 20$
- Cartilage shear modulus: $\mu_{\text{cartilage}} = 0.2 – 0.6$ MPa
- Cartilage stiffening parameter: $\alpha_{\text{cartilage}} = 2 – 5$
- Effective Poisson's ratio: $\nu_{\text{skin}} = 0.495$, $\nu_{\text{cartilage}} = 0.46$

For each combination of parameters, two key output metrics were extracted from simulation results: the effective auricle stiffness k, calculated under a prescribed static deformation corresponding to 0.25 normalised displacement, as defined in the linear model experiments. And the natural frequency f_n of the auricle structure calculated with damped oscillation.

Simulation Strategy for Frequency Estimation

Given the nonlinear and nearly incompressible nature of Ogden material models, convergence difficulties were encountered during dynamic simulations involving abrupt or large-scale deformation. To address this, the simulation strategy was split into two distinct stages:

1. A static analysis with a large prescribed deformation was performed to estimate effective stiffness.
2. A subsequent dynamic frequency extraction was carried out with a smaller displacement amplitude of 8 mm, which is less than one-third of the original static deformation, to ensure stability and prevent excessive mesh distortion.

This two-stage approach enabled stable and consistent extraction of dynamic response characteristics across a wide hyperelastic parameter space.

Simulation Results

The auricle stiffness and corresponding natural frequencies were calculated for all tested combinations. Figures 5.10 and 5.11 summarise the parametric influence of skin and cartilage Ogden parameters.

The simulation envelope was compared to experimentally obtained volunteer test data, as shown in Figure 5.12. Among all variables, μ, the shear modulus, exerted the most significant

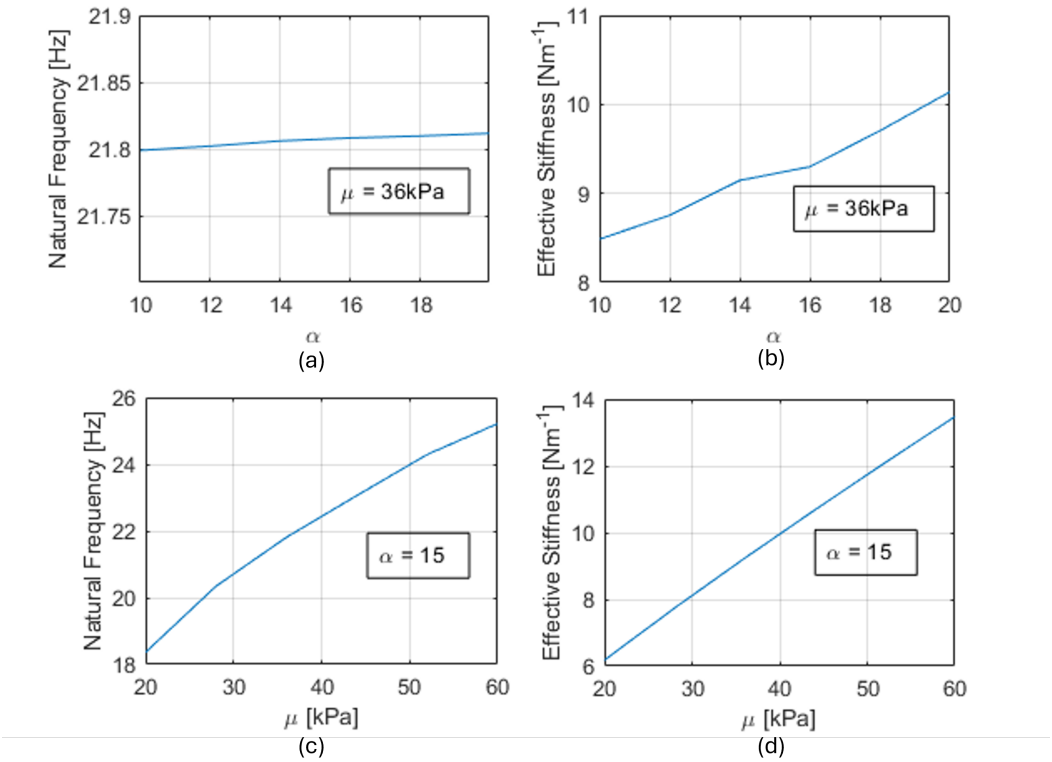


Fig. 5.10 Effect of skin hyperelastic parameters μ_{skin} and α_{skin} on simulated auricle mechanics. Cartilage properties were held constant at $\mu = 0.4$ MPa, $\alpha = 3.0$. (a) and (b): Variation of α_{skin} on effective stiffness and natural frequency, respectively. (c) and (d): Influence of μ_{skin} on stiffness and frequency.

influence on auricle mechanical response. For the skin layer, increasing μ_{skin} led to consistent and substantial increases in both stiffness and frequency. Changes in α_{skin} also increased stiffness, but did not significantly alter frequency. This trend is consistent with the physical interpretation that frequency, being assessed under small displacement in the dynamic step, is less sensitive to strain-stiffening effects governed by α.

Similarly, for the cartilage layer, changes in $\mu_{\text{cartilage}}$ affected both stiffness and natural frequency, although the sensitivity was less than that observed for the skin layer. This is likely due to the smaller volume and lower deformation strain experienced by the cartilage core relative to the outer skin layer. Conversely, changes in $\alpha_{\text{cartilage}}$ had minimal effect on both mechanical metrics, reinforcing the notion that stiffening parameters primarily manifest under larger strain regimes not dominant in this study.

These findings underscore the critical role of nonlinear hyperelastic formulations, particularly the inclusion of shear modulus, in accurately capturing auricle behaviour. The derived

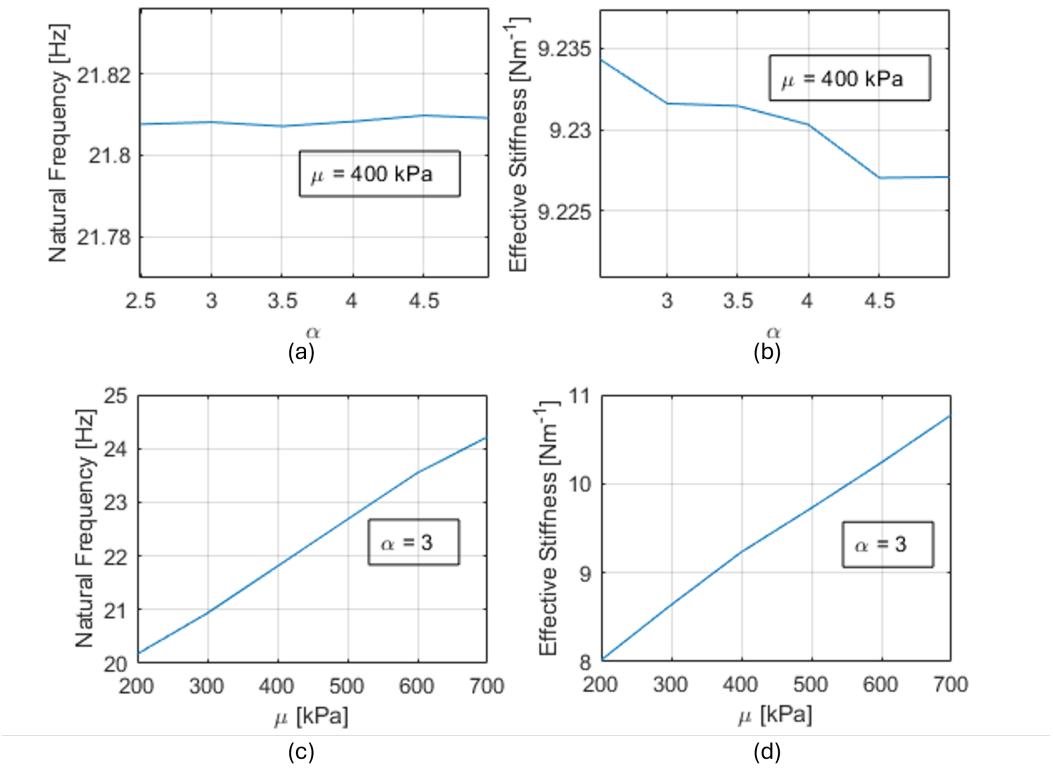


Fig. 5.11 Effect of cartilage hyperelastic parameters $\mu_{\text{cartilage}}$ and $\alpha_{\text{cartilage}}$ on simulated auricle mechanics. Skin parameters were fixed at $\mu = 36$ kPa, $\alpha = 15.0$. (a) and (b): Variation of $\alpha_{\text{cartilage}}$ on stiffness and natural frequency. (c) and (d): Influence of $\mu_{\text{cartilage}}$ on stiffness and frequency.

simulation dataset also enables future surrogate modelling efforts, where auricle mechanics could be estimated from experimentally derived μ values or anatomical estimations.

Summary

This parametric study demonstrates that:

- Linear elasticity fails to capture nonlinear tissue behaviour, especially strain-dependent stiffening.
- The Ogden model better matches experimental data across both stiffness and vibrational metrics.
- Skin shear modulus has a greater impact than cartilage in shaping auricle mechanics under both static and dynamic conditions.

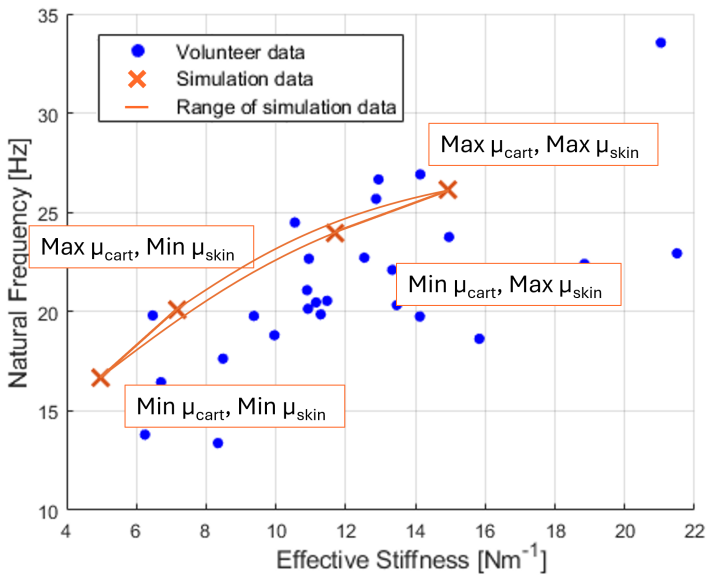


Fig. 5.12 Comparison of Ogden model simulation range with experimental volunteer data. Simulation envelope spans the range of μ values. α variation does not produce significant shifts, hence the parallelogram bounding only μ extremes is shown.

These results justify the use of Ogden hyperelastic material formulations in future auricle simulations involving population-scale variation and device interaction.

5.3.3 Geometric Variation and Morphological Impact

Building on the validated Ogden material model, the influence of anatomical variability was then investigated by simulating three additional auricle meshes from the *WiDESPREaD* dataset: the *Long*, *Short*, and *Thick* auricle geometries. Each mesh was simulated using identical range of Ogden parameters to identify the effect of geometry. Additionally, the baseline CT-scanned mesh was modified to include a thicker cartilage layer mesh, further exploring how auricle anatomy structure influences mechanical outcomes.

Figure 5.13 presents stiffness and natural frequency results for each configuration in comparison with the baseline model overlaying the volunteer test data. A distorted polygram is illustrated to demonstrate the range of mechanical result from different Ogden material parameter.

As shown in Figure 5.13(a), the *Short* models generally exhibited higher natural frequencies than the baseline model, consistent with their reduced geometric dimensions. The *Thick*

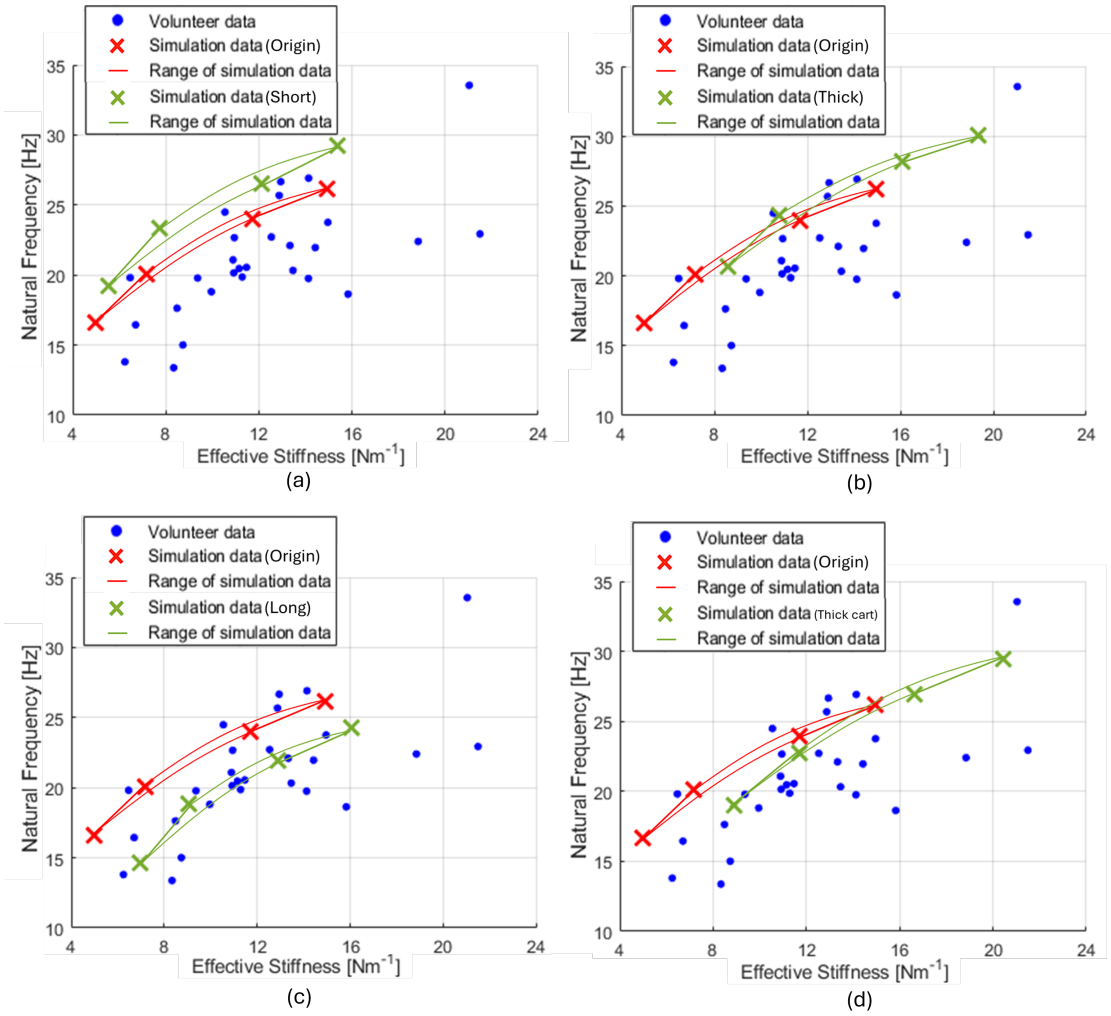


Fig. 5.13 Mechanical response (effective stiffness and natural frequency) of auricle models with varied geometries. All simulations used identical material and boundary settings. (a) Baseline vs. shorter ear; (b) baseline vs. thicker auricle; (c) baseline vs. longer ear; (d) baseline vs. thicker cartilage layer. "Origin" refers to the baseline model.

model demonstrated both higher stiffness and frequency, attributed to its increased cross-sectional area. The *Long* model, despite showing slightly higher stiffness, exhibited a reduced natural frequency due to its altered mass distribution and larger deformation modes.

Notably, increasing the cartilage thickness relative to the baseline model led to a clear rise in both effective stiffness and natural frequency. However, the increase in stiffness was more substantial than that of frequency, indicating a stronger sensitivity of the auricular structural response to changes in cartilage geometry. This suggests that local cartilage thickening serves as an effective strategy for modulating the mechanical behaviour of the auricle. Importantly,

such adjustments allow for more accurate replication of *in vivo* deformation behaviour while preserving anatomical realism, offering a computationally efficient alternative to acquiring and processing more auricle models.

Summary and Discussion

These comparative simulations reveal that auricle morphology significantly affects mechanical behaviour. Even with identical material properties, different auricle meshes produced markedly different mechanical response ranges. Importantly, the range of responses simulated was well aligned with the volunteer test results, reinforcing the representativeness of the human subject experiments for population-level variability.

Among the models studied, cartilage thickness emerged as a particularly effective parameter for modulating mechanical response. It allows significant alteration of stiffness and frequency characteristics without changing the external auricle geometry. Although the baseline model incorporated cartilage thickness estimated from anatomical references, the true geometry and layering remain uncertain. This highlights a key limitation in current modelling approaches and motivates future work toward more accurate strategies, such as imaging-based cartilage segmentation, to better replicate auricle mechanics in simulation.

5.4 Auricle Model Verification

To establish the validity of the auricle FE model for practical application in wearable device development, further investigations were conducted focusing on system-level vibrational behaviour and contact interaction with external loads. The following sections present analyses of stress distribution, deformation characteristics, and device interaction under realistic loading scenarios.

5.4.1 System Vibration Study

The dynamic component of the anterior pulling experiment revealed the natural vibration frequency of the ear tip in the lateral direction. However, a broader characterisation of auricular dynamics was necessary to evaluate the model's behaviour across multiple excitation directions and frequencies. In this study, a systematic vibration analysis was performed on the CT-scanned auricle finite element model, defined by Ogden hyperelastic parameters $\mu_{\text{cartilage}} = 0.4$ MPa, $\alpha_{\text{cartilage}} = 3.0$, $\mu_{\text{skin}} = 36$ kPa, and $\alpha_{\text{skin}} = 15.0$.

Table 5.3 summarises the sinusoidal excitations applied in the simulations, including the frequency range, vibration direction (lateral), and input amplitude. The excitation frequencies were selected based on the system's previously identified natural frequency, denoted f_n, which was determined to be 21.8 Hz for the baseline model. The full frequency sweep spanned from $\frac{f_n}{10} = 2.18$ Hz to $10f_n = 218$ Hz, thereby covering sub-resonant, resonant, and super-resonant dynamic conditions.

Direction	Frequency range (Hz)	Input amplitude
Lateral	2.18–218	2.0 mm

Table 5.3 Summary of sinusoidal excitation parameters used in the dynamic response study. Frequencies range from $\frac{f_n}{10}$ to $10f_n$, where $f_n = 21.8$ Hz is the natural frequency of the baseline model.

The system's response was summarised as a Bode diagram (Figure 5.14). The solid black curves represent the analytical single-degree-of-freedom (SDOF) prediction, based on the natural frequency f_n and damping ratio ζ, using the standard expressions for amplitude gain $H(f)$ and phase $\Phi(f)$, as defined in Equations (3.6) and (3.7), and illustrated in Figure 3.18 back in chapter 3.

In comparison, the red curves in Figure 5.14 represent the FE simulation results for the full auricle model, evaluated under identical boundary conditions and excitation amplitudes. This allows direct comparison between the simplified analytical model and the full-geometry simulation, highlighting deviations due to geometric and material complexity.

Recalling the definitions from Eq. (3.6) and (3.7), the analytical forms of the gain and phase functions are

$$H_{(f)} = \left(\frac{1 + (2\zeta f/f_n)^2}{\left[1 - (f/f_n)^2\right]^2 + (2\zeta f/f_n)^2} \right)^{\frac{1}{2}} \tag{3.6}$$

$$\Phi_{(f)} = \left(\frac{2\zeta\,(f/f_n)^3}{1 - (f/f_n)^2 + (2\zeta f/f_n)^2} \right)^{\frac{1}{2}} \tag{3.7}$$

These expressions capture the frequency-dependent response of the idealised SDOF system, enabling direct comparison between the simplified analytical model and the numerically simulated full-geometry FE results.

Agreement between the two confirms that, despite the complexity of auricular geometry and heterogeneous material properties, the dominant vibrational mode of the auricle can be approximated by an equivalent linear oscillator with parameters identified experimentally.

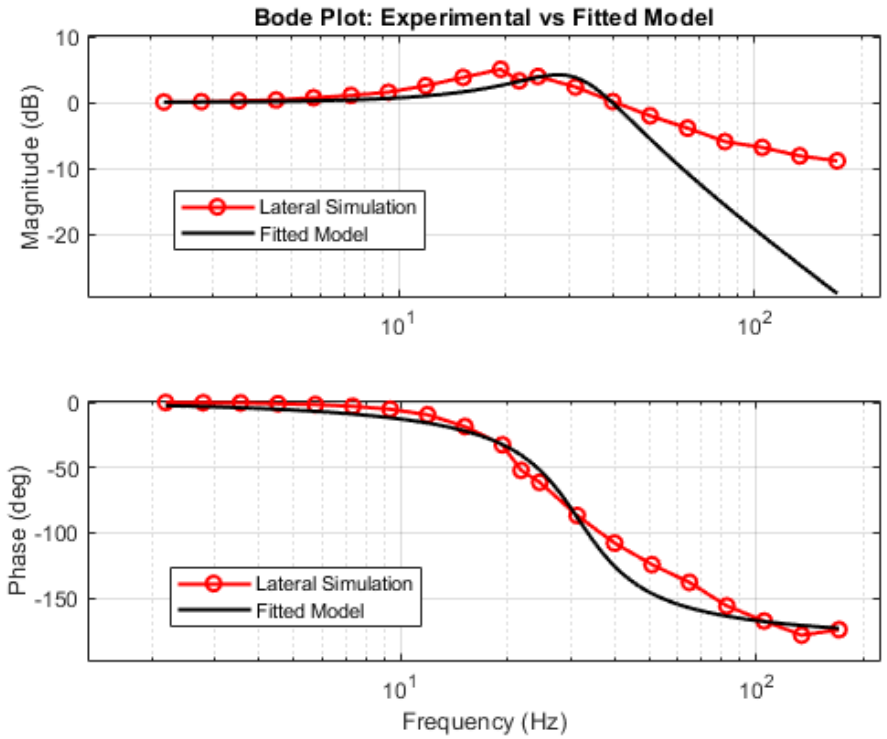


Fig. 5.14 System vibration characterisation of the auricle model. Solid black lines: SDOF linear prediction using (f_n, ζ). Red lines with circles: FE harmonic response for lateral excitations. Shaded regions mark frequency bands with noticeable modal coupling.

At low frequencies ($f \ll f_n$) region plotted in Figure 5.14, the FE response follows the SDOF prediction closely, indicating that the first mode dominates the displacement field. As frequency increases, deviations emerge in both gain and phase due to (i) modal coupling with higher modes, (ii) geometric features that induce non-uniform stiffness across the auricle structure, and (iii) displacement deflection in other axes. Although the auricle is a geometrically complex, multi-degree-of-freedom system, the SDOF approximation largely captures its global vibration behaviour and provides an accessible framework for interpretation. It should be noted, however, that the choice of input amplitude may influence the detailed response and therefore requires further validation in future work. Overall, this frequency-response scan provides practical guidance on (a) bandwidths where the auricle behaves quasi-rigidly (favourable for stable sensor contact) and (b) resonant bands where small input oscillations can produce amplified motion and potential electrode drift.

5.4.2 Earable Interaction

With the auricle model exhibiting realistic physical properties, its interaction with other components in contact mechanics was subsequently evaluated. Finite element (FE) simulations were conducted using custom earable prototypes designed for neural and biometric signal acquisition. The device geometry was modelled in Fusion 360 by subtracting the simplified auricle surface from a pipe-like structure to ensure a conformal interface between the prototype and the auricle model. The design concept was inspired by recent ear-clip earphones that clasp over the auricle by engaging the antitragus and helix regions. The designated electrode attachment sites were positioned anterior to the helix toward the facial direction, within the conchal cavity, and posterior to the auricle near the mastoid region. For simplicity, the flexible eutectogel electrode pads were not included at this stage of modelling.

To test the robustness of the model in capturing device–auricle interaction, both the overall device mass and its distribution were varied to reflect realistic packaging constraints, such as battery placement, electronic layout, and housing design. The baseline prototype is assigned with a linear elastic model that is slightly stiffer than the cartilage material ($E = 2$ MPa and $\nu = 0.4$). It had a total mass of 13.35 g (corresponding to a volume of 8.90 cm^3, assuming a density of 1.50 g/cm^3). To examine the effect of mass distribution, two additional weights of 5.00 g each were assigned either to the anterior or posterior region of the device, mimicking alternative component placements. These scenarios allowed assessment of how shifts in centre of mass influence local pressure distribution and device stability during dynamic loading.

Three representative mass configurations were considered:

1. **Posterior-biased mass**, with an additional 5 g applied toward the mastoid side.
2. **Anterior-biased mass**, with an additional 5 g applied toward the facial side.
3. **Balanced distribution**, baseline device with no additional test weights.

To represent the redistributed component mass, point masses were implemented in Abaqus as *inertia points* rigidly coupled to designated nodes on the device shell at either the anterior or posterior regions (Figure 5.15). This ensured that the extra weight contributed to the overall gravitational load and altered the device's centre of mass without introducing artificial stiffness to the structure. The baseline device mass was defined through its material density, while the test weights were added as concentrated masses to capture realistic packaging scenarios.

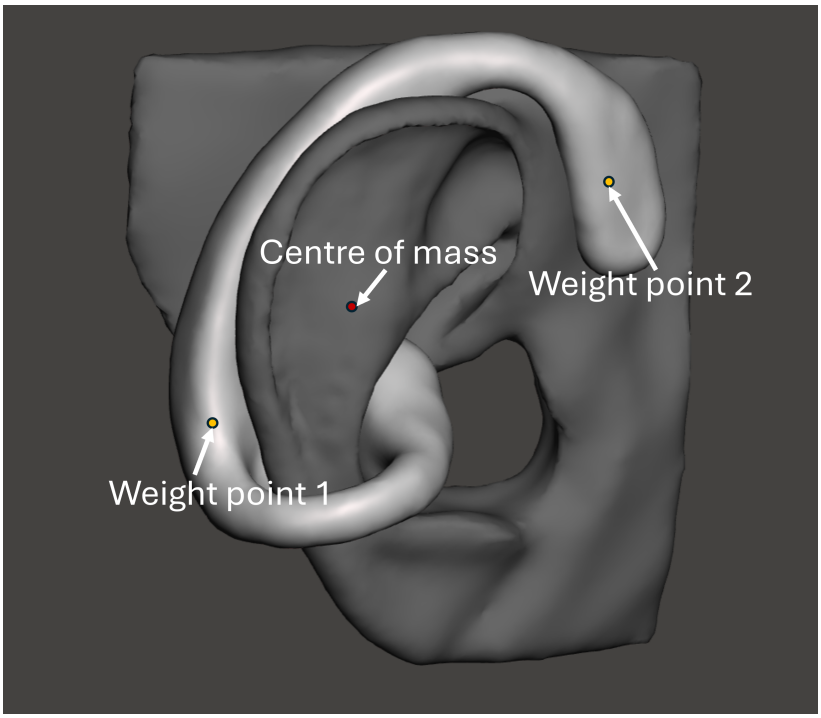


Fig. 5.15 Earable prototype fitted to the CT-derived auricle model. The baseline design (13.35 g) was evaluated together with configurations including two 5 g test masses placed at posterior (weight point 1) and anterior (weight point 2) positions, simulating alternative component layouts. The highlighted centre of mass and added mass points were used in FE simulations to analyse weight distribution effects.

All simulations were conducted under a static general step with gravity applied in the superior–inferior direction ($-z$ axis) to replicate device self-weight acting on the auricle. The auricle model was constrained at its base to represent fixation to the skull, with translational degrees of freedom restricted at the root of the helix and along the posterior conchal attachment. Contact between the device and auricle was defined using an exponential pressure–overclosure law (*Surface Behavior, pressure-overclosure=EXPONENTIAL, 0.05, 0.1). This formulation allows the contact pressure to increase smoothly as surfaces approach one another, providing a more physiologically realistic interaction than a perfectly rigid "hard" contact. However, exponential contact control is computationally demanding, as the nonlinear contact stiffness significantly increases solver effort, leading to longer simulation times compared with simpler hard-contact definitions. More detailed FEA setup can be found in Appendix E.

Von Mises stress distribution within the auricle tissue layers was extracted as the primary metric from this analysis to evaluate deformation patterns and identify regions of concentrated

pressure. The stress values were obtained from the nodal outputs of the tetrahedral mesh. The auricle model was evenly meshed with an element size of 0.6 mm. In such a mesh, the number of elements roughly scales with the cube of the inverse element size, while the number of surface nodes scales with its square. Therefore, the total node count can be used as an approximate indicator of the model's geometric resolution and the surface area subjected to pressure.

These analyses provided a consistent framework for comparing how anterior-, posterior-, and balanced mass distributions influence auricle deformation, stress concentrations, and pressure profiles under static gravitational loading.

5.4.3 Simulation Results for Earable Interaction

Figure 5.16 presents the results of the static FE analysis for the balanced mass configuration (no additional weight). The stress maps for the other two mass distributions did not exhibit any visible differences. Stress concentrations were consistently observed in the concha and helix root regions, the mastoid-facing surface, and along the facial-side helix.

In addition to mapping qualitative stress distributions, quantitative comparisons were conducted using two metrics: the peak von Mises stress and the surface area of the auricle experiencing stresses greater than 300 Pa. To estimate the pressure applied by the earable to the auricle, a load equivalent to a weight of 5 g distributed over an area of 1 cm^2 can be approximated as 500 Pa. The threshold of 300 Pa was adopted as a comfort-onset criterion, representing a conservative estimate that remains well below known pain thresholds. This level was selected to identify regions where the user may begin to perceive local pressure. In facial and cranial ergonomics, discomfort thresholds have been reported to vary across locations and often fall within a few hundred Pascals in sensitive regions [113], while pressure pain thresholds in musculoskeletal and skin tissues typically exceed 100 kPa according to algometry studies [114]. The grouped-bar histograms in Figure 5.17 allow direct comparison of different mass-distribution scenarios in terms of both stress magnitude and the spatial extent of loading.

The differences among the three weight distributions were unexpectedly small, despite the substantial change in overall mass from 13.35 g to 18.35 g (an increase of approximately 37%). This may be explained by the omission of nodes experiencing stresses below 300 Pa in the plotted data, as well as by the large contact area between the auricle and the device, which effectively distributed the applied load across the interface. Nevertheless, it remains evident that the posterior weight distribution (weight point 1) produced a larger increase in the

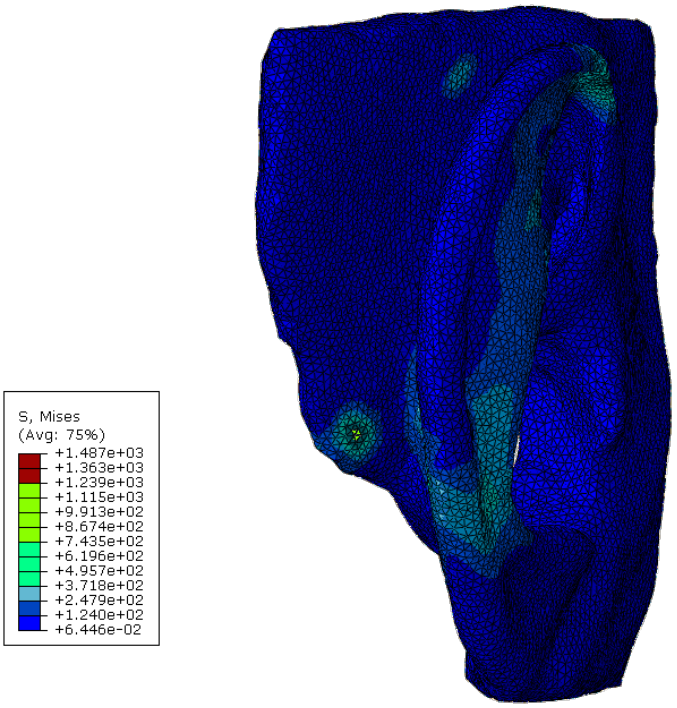


Fig. 5.16 Von Mises stress map of the auricle for the earable with no additional mass. Stress hotspots are evident around the mastoid region and helix root, with intensity varying according to the distribution of device weight. The stress maps for the other two mass configurations do not show any visible differences.

number of nodes above the 300 Pa threshold compared with the anterior weight distribution (weight point 2).

These results highlight the utility of the model for evaluating earable design performance. An anterior mass bias generated more localised stress peaks, particularly around the helix region, which may compromise comfort. In contrast, a posterior mass bias redistributed stresses more evenly across the auricle surface but induced greater overall deformation. The balanced configuration reduced extreme values but did not fully eliminate stress concentrations. Overall, these findings emphasise the need to optimise both total device weight and its mass distribution to achieve mechanical stability while maintaining user comfort.

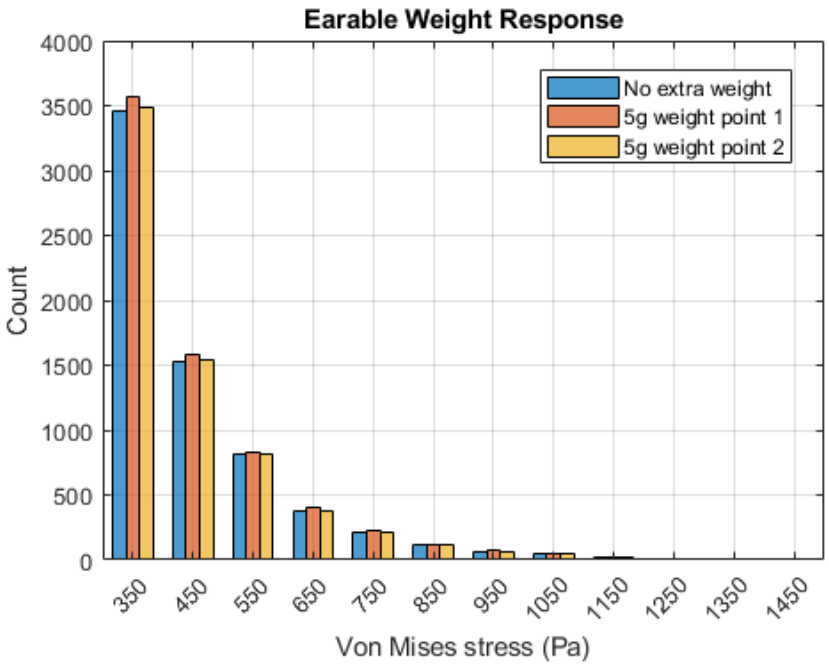


Fig. 5.17 Quantitative comparison of auricle loading under different mass distributions. Grouped-bar histograms compare anterior-biased, posterior-biased, and balanced configurations in terms of peak von Mises stress and the mesh elements surface subjected to stresses above selected thresholds. Each histogram bin is labelled by its mid-point value (e.g., the interval 300–400 Pa is represented by 350 Pa), following standard practice in statistical data presentation to denote the central tendency of each bin range.

5.5 Discussion and Conclusion

This chapter presented FE models of the human auricle that integrate anatomically accurate geometry from CT and large-scale 3D scan datasets with nonlinear hyperelastic material formulations. The model was experimentally validated and subsequently applied to study auricle behaviour under different loading, motion, and device–interaction scenarios relevant to earable systems.

The first set of findings concerned material modelling. Linear elastic formulations were insufficient to reproduce the full range of deformations observed in experiments. In contrast, the Ogden hyperelastic model demonstrated good agreement with measured stiffness and vibration responses, as confirmed by comparison of multiple auricle models with volunteer test data. Parameter sweeps highlighted that the shear modulus of skin and cartilage is the primary factor influencing stiffness.

Validation with experimental data provided further confidence in the model. Quasi-static and dynamic tests on volunteers closely matched the model's predictions in both force–displacement response and natural frequency range. The frequency response of the baseline model indicated a sensitive band in the range of 20–30 Hz, consistent with measured vibration behaviour.

Geometry was also shown to play an important role. Morphological variations such as auricle length, width, and cartilage thickness significantly influenced stiffness and resonance. This emphasises that geometry must be considered when designing devices intended for diverse user populations.

Simulations of earable prototypes demonstrated the value of the auricle model in evaluating the interaction between the device and the tissue. Regions of elevated stress were consistently observed in the concha and helix, particularly under concentrated loading conditions. The mass distribution of the device only slightly influenced both the localised stress concentrations and the global pressure distribution across the auricle. In particular, the simulations showed that applying mass at point 2 induced less pronounced mechanical impact compared to point 1, suggesting that shifting the device's weight anteriorly may help mitigate user discomfort. These findings provide practical design guidance for balancing comfort, mechanical stability, and packaging constraints in the development of earable systems.

However, there are limitations. The present model employs isotropic, homogeneous material properties and idealised support conditions. In reality, auricular tissue exhibits anisotropy and viscoelasticity, while surrounding skin and muscle outside the modelling domain can further affect motion. Expanded validation across a broader subject pool and greater anatomical variation will be essential. Future work should also incorporate advanced constitutive models and explore long-term loading and dynamic conditions representative of real-world use.

In conclusion, the FE model developed here provides a validated and adaptable framework for studying auricle mechanics in the context of earable device design. It captures both geometry- and material-dependent behaviour and enables systematic evaluation of how design choices affect comfort, stability, and motion artefacts. These results establish a foundation for future electromechanical simulations of motion-robust neural interfaces and more complex analyses of device–auricle interaction.

Chapter 6

Earable Prototype Evaluation and Device Decoupling Analysis

6.1 Introduction

Building on the anatomically and mechanically validated auricle model established in the previous chapters, this chapter examines how different ear-mounted devices interact with the auricle under conditions representative of daily use. Earable devices are a class of wearable technologies designed to interface with the external ear for applications in biosignal acquisition (e.g., EEG, EMG), motion sensing (e.g., head tracking), and user interaction (e.g., audio control). Their placement on the auricle leverages a stable and accessible anatomical site, enabling continuous and unobtrusive data capture in everyday life. Compared to conventional head-mounted or scalp-worn systems, earables offer advantages in form factor, social acceptance, and integration into familiar accessories such as headphones or hearing aids.

Despite these benefits, the auricle presents distinct engineering challenges. Its soft-tissue composition, compliant attachment to the skull, and susceptibility to deformation from facial motion and environmental vibration introduce variability in device contact and stability. Motion artefacts arising from gait or head movements can compromise sensor reliability and user comfort. While earable technologies have been widely studied in terms of electronics and signal processing, systematic investigation of the contact mechanics between devices and the auricle has been rare. This gap limits our understanding of how physical interface design affects comfort, stability, and performance.

The aim of this chapter is therefore to evaluate the physical interface between earable devices and the auricle using a combined experimental and computational approach, thereby validating the use of auricle FE modelling as a tool for studying device–human interaction. Two representative device designs are considered:

1. **Personalised Earable** – a custom-fit prototype designed to conform closely to the wearer's auricular geometry (Figure 5.15).
2. **Commercial Earphone** – a standard in-ear audio device without motion-stabilising features.

The Earable prototype model was copied from Chapter 5.4.2, which was already meshed to C3D4 elements with average element length of 0.8 mm. The commercial earphone model was downloaded and recaptured in Fusion 360 to create a mesh with element length of 0.8 mm. Static and dynamic FEAs are performed to characterise contact pressure distribution and vibration response. To further validate the usefulness of the auricle model in comparing earable device design, sample gait trajectory was measured with an IMU mounting device, which provide reference data for evaluating device stability during locomotion comparable to daily life. The focus is placed on contact mechanics at the auricle–device interface, as pressure distribution is directly linked to perceived comfort and the likelihood of motion artefacts. The simulation setup followed the general structure of that included in Chapter 5.4.2 for consistancy. The chapter is structured into three sections: mechanical decoupling under controlled conditions, real-world vibration induced by gait, and skin–electrode impedance under physiological loads.

6.2 Device Coupling and Pressure Distribution under Controlled Vibration

6.2.1 Objective

This study aims to characterise the device fit, static conformity, and mechanical robustness under simple harmonic conditions. The investigation combines FE simulations and experimental validation to assess the devices under three representative conditions:

1. **Static loading**: Evaluating local stress and pressure distribution at the auricle–device interface to determine conformity and fitting.

2. **Sinusoidal vibration**: Simulating periodic excitations such as gait-induced oscillations or environmental sources.

The primary goal is to compare the earable and earphone models in terms of mechanical coupling, contact pressure distribution, and robustness against motion artefacts.

6.2.2 Static FE Analysis

A static FE analysis was first conducted to evaluate how different device geometries interact with the auricle. Both the earable prototype and the commercial earphone were modelled using the same linear elastic material to ensure a fair comparison under identical mechanical assumptions. Figure 6.1 illustrates the earable device, which is the same model used in Chapter 5.4, and the chosen commercial earphone. The earable model used has a weight of 13.35 g and the earphone model weight 11.55 g, assuming the same material density used for simulation. The commercial earphone was selected due to its multi-contact design, which includes structural components distributed in the concha bowl, behind the helix rim, and in front of the tragus. This geometry allows the device to rest on multiple regions of the auricle, thereby spreading its weight across several contact zones.

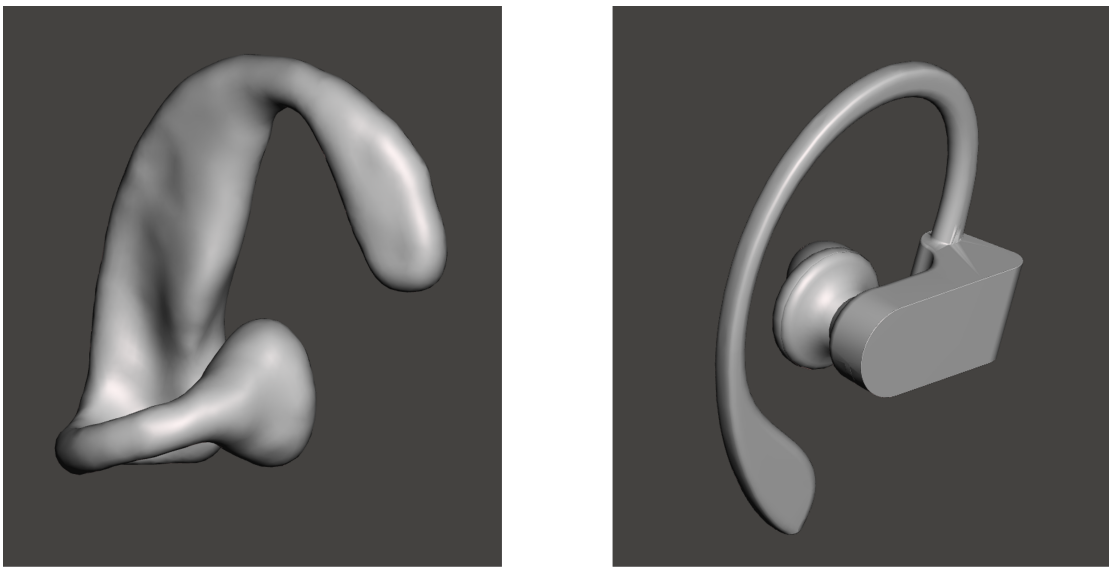


Fig. 6.1 Display of (a)the earable model and (b)) the earphone model.

However, as a mass-produced product, the earphone is not tailored to individual auricle anatomy. When placed on a personalised auricle model, this mismatch can lead to uneven

pressure distribution and localised stress concentrations due to poor conformity. In contrast, the earable prototype was designed to fit the auricle contour more closely, improving surface contact and mechanical coupling.

The FEA setup was improved based on the contact experiment in Chapter 5.4.2, where the earable device was set to be in contact with the auricle model. With the commercial earphone, the model was first assembled to the auricle through a series of displacement boundary condition (Detailed in Appendix E). After the earphone reached the designed contact position with the auricle model, the contact analysis was initiated with a similar setup as the earable model.

In this analysis, the focus was placed on contact pressure (`CPRESS` in Abaqus) rather than von Mises stress, since the pressure at the skin–device interface is more directly related to user comfort and potential discomfort during prolonged wear. The pressure values are stored at the surface nodes of the finite element mesh, and the number of surface elements can be approximated from the total node count, assuming each node is shared by multiple connected elements. For simplicity in subsequent analyses, the number of nodes was therefore used directly as an indicator of the contact area and the overall pressure distribution on the auricle model.

As shown in Figure 6.2, the results revealed distinct differences between the two designs. The earable model exhibited a more uniform pressure distribution across the concha and antihelix, suggesting that its anatomical fit helps to spread load more evenly. In contrast, the earphone model produced higher localised pressures, particularly at the helix root and ear canal entrance. These concentrated regions of loading indicate an increased risk of user discomfort and highlight the advantages of the earable design in distributing contact forces while maintaining anchoring stability.

6.2.3 Dynamic FE Sinusoidal Vibration Analysis

To investigate dynamic transmission characteristics, sinusoidal base excitations of 2 and 4 Hz with amplitudes of 5 mm were applied at the skull–auricle interface for both the earable and earphone models. Two principal simulation outcomes were analysed: (i) device and auricle displacements, and (ii) the evolution of pressure distribution across the auricle–device contact interface.

The simulations were initialised using a restart from the final step of the preceding static contact study, ensuring that realistic pre-stressed contact conditions were preserved. Both contact model was set with an implicit dynamic step. Displacement boundary conditions

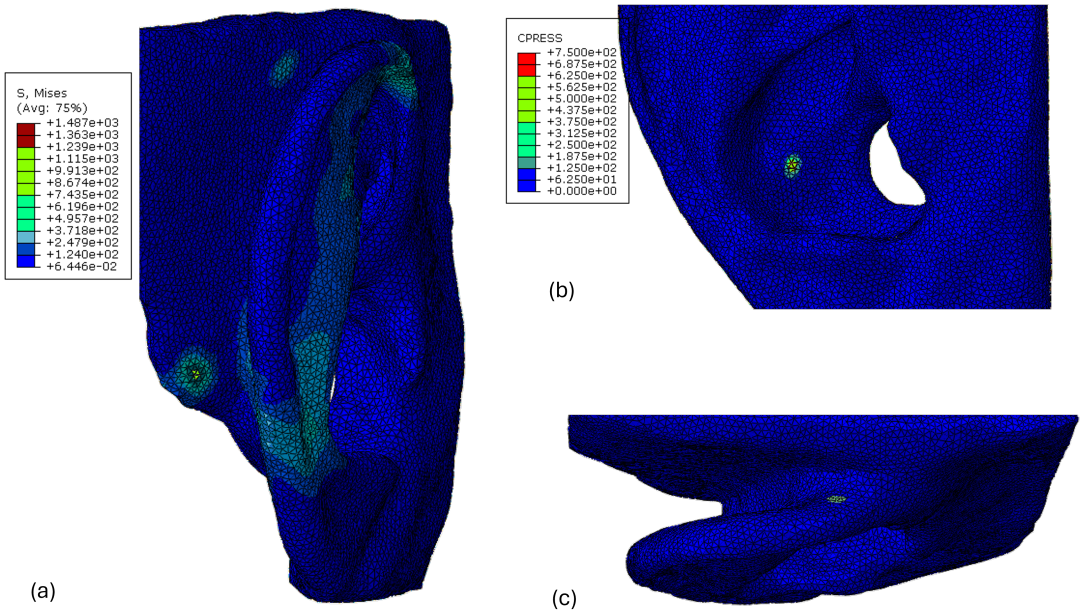


Fig. 6.2 FE static analysis of auricle–device interaction. Contact pressure (CPRESS) distribution is shown on the auricle surface for (a) the earable model, demonstrating uniform loading across the concha and antihelix, and (b, c) the earphone model, where localised high pressures occur at the helix root and concha.

were applied at the base of the auricle to reproduce skull-driven harmonic oscillations. This configuration allowed the devices to vibrate in conjunction with auricle motion, replicating the physiological excitation pathway.

To demonstrate the result of the vibration, the auricle base was driven at 4 Hz. The time-sequenced contact pressure field was outputted. Figure 6.3 depicts the vibration trajectories of both the auricle base and the devices under the sinusoidal excitation implied by the BCs, illustrating their relative synchronisation and displacement patterns. The waveform of the auricle base is tied to the excitation source which means its waveform is the BC waveform. The device displacement shows irregular decouple at the first two cycles and reached equilibrium in the following cycles. To compare the difference in applied pressure from the device to the auricle, the number of finite elements exceeding a threshold of 20 Pa was recorded, as shown in Figure 6.4.

The complete simulation outcomes are summarised in Table 6.1. The table reports results from both static loading and dynamic sinusoidal vibration analyses at 2 Hz and 4 Hz for the earable device and the commercial earphone. For each condition, maximum and average

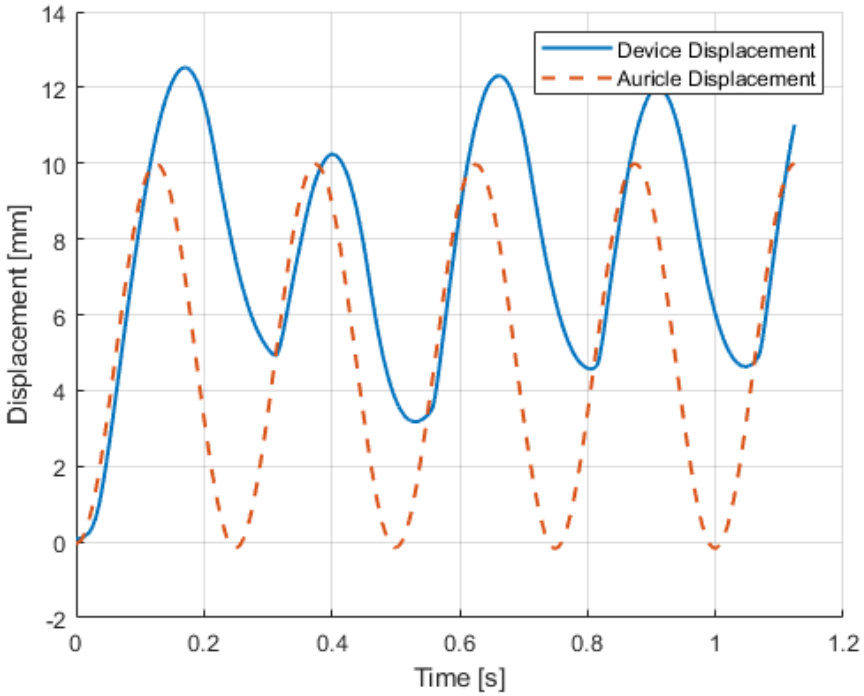


Fig. 6.3 Vibration trajectories of auricle and devices under harmonic excitation, demonstrating relative motion coupling.

contact pressure (CPRESS) values are provided, together with the number of elements exceeding thresholds of 20 Pa and 500 Pa. Human cutaneous pressure sensing thresholds typically lie in the low-Pascal to tens-of-Pascals range, depending strongly on the skin region, probe geometry, and contact area [115, 116]. Hence the 20 Pa threshold was used to refer to the area that can feel the contact. The 500 Pa was chosen as the comfort threshold with the same reasoning as in Chapter 5.4.2, which is a conservative estimation [113]. Entries denoted as "N/A" indicate cases where the device became completely decoupled from the auricle during vibration, as illustrated in Figure 6.5.

The tabulated results highlight several key differences between the two device types. First, under static conditions, the earable already demonstrated a substantially larger number of contact nodes above 20 Pa (659) compared to the earphone (73), reflecting its broader area of engagement with the auricle. Despite this wider contact area, the earable maintained relatively low peak loading, with only 42 nodes above 500 Pa, compared to 4 nodes for the earphone.

Under dynamic vibration at 2 Hz, both devices showed an increase in maximum pressure and number of loaded nodes. The earable exhibited a lower maximum pressure (3.15 kPa)

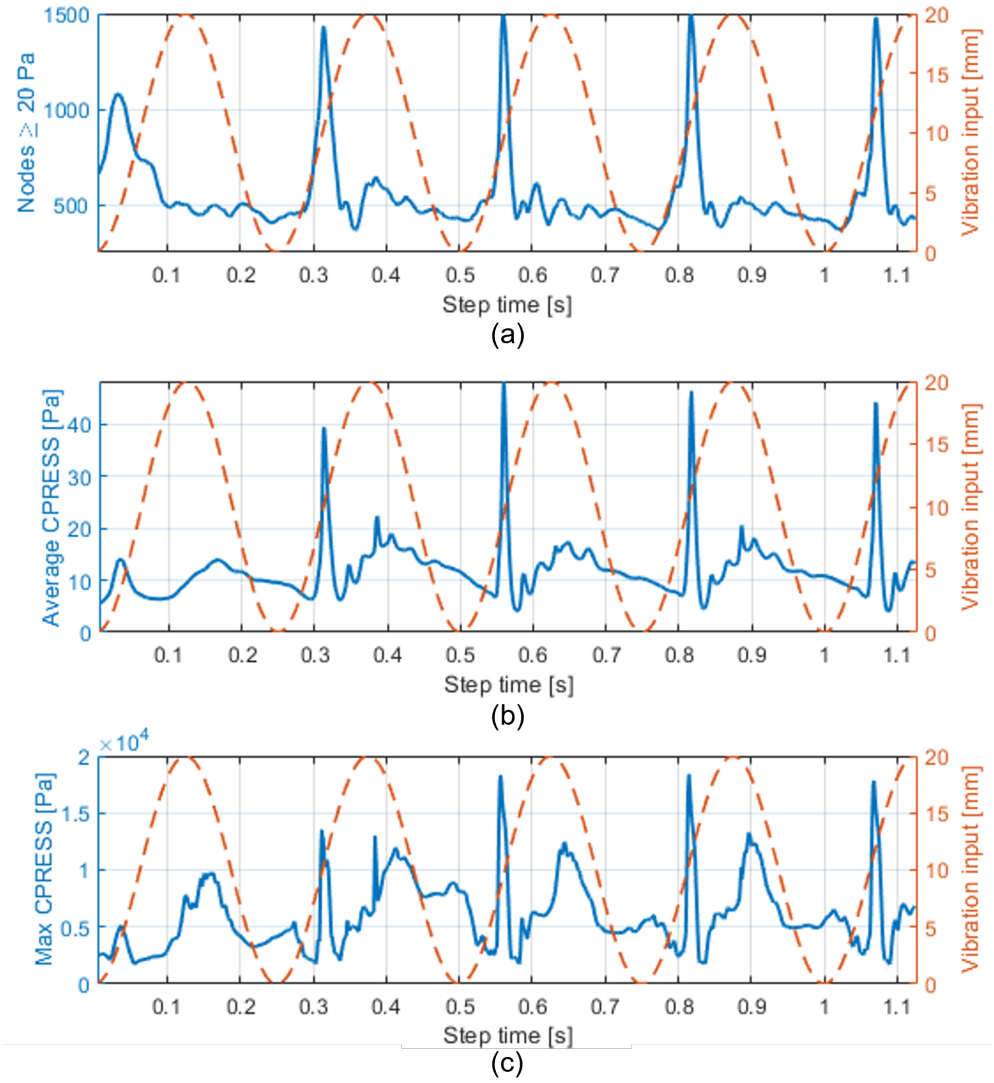


Fig. 6.4 Simulation results of contact pressure response during sinusoidal excitation of the earable–auricle system. (a) Time history of the number of contact (slave) nodes experiencing a normal contact pressure (CPRESS) exceeding the specified threshold (left y-axis), overlaid with the normalised input displacement waveform $y = -\cos(2\pi ft) + 1$ (right y-axis). (b) Average CPRESS across all contact nodes as a function of time. (c) Maximum CPRESS recorded among all contact nodes.

and more elements above 20 Pa (746), yet the increase in high-pressure nodes above 500 Pa was modest (from 42 to 52). In contrast, the earphone, showing a higher maximum pressure at 5.37 kPa, concentrated its load into fewer elements, increasing from 4 to 30 nodes above

		Static	2 Hz	4 Hz
Earable Device	Max CPRESS [kPa]	2.38	3.15	18.33
	Average CPRESS [Pa]	5.54	5.88	48.33
	Max Nodes $>$ 20 Pa	659	746	1496
	Max Nodes $>$ 500 Pa	42	52	440
Earphone	Max CPRESS [kPa]	0.71	5.37	N/A
	Average CPRESS [Pa]	3.74	13.49	N/A
	Max Nodes $>$ 20 Pa	73	154	N/A
	Max Nodes $>$ 500 Pa	4	30	N/A

Table 6.1 Summary of FE simulation results for earable and earphone models under static and dynamic sinusoidal vibration (2 Hz and 4 Hz). N/A denotes conditions where the device was completely decoupled from the auricle.

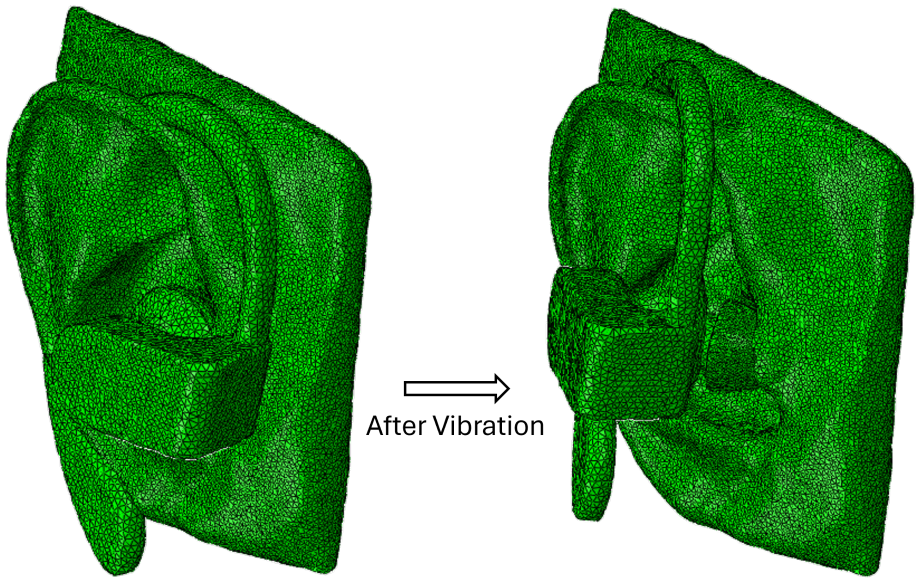


Fig. 6.5 The earphone model decoupled after having a 4 Hz vibration with amplitude of 5 mm. As illustrated, the earphone speaker part is fully detached from the auricle conchae.

500 Pa. This pattern suggests that the earphone relies on more localised contact points, which increases the risk of pressure hotspots and unstable coupling.

At 4 Hz, differences between the two devices became more pronounced. The earable remained mechanically coupled to the auricle, as shown in Figure 6.3, where both the device and the auricle exhibited vibration with noticeable phase and amplitude differences. However, this came with a higher peak contact pressure (18.33 kPa) and an increased number of high-pressure nodes (440). In contrast, the earphone lost all effective contact with the auricle, as

reflected by the "N/A" values recorded—indicating complete mechanical decoupling. This result confirms that the commercial earphone lacks sufficient conformal fit to maintain stable contact under dynamic loading.

Overall, the findings demonstrate that the earable prototype maintains contact more reliably and distributes pressure more evenly across the auricle. While the earable does experience higher peak pressures at elevated frequencies, its broader contact area helps prevent localised overloading and detachment. The commercial earphone, by comparison, concentrates stress in fewer regions and is more prone to decoupling. These results highlight the superior dynamic stability and comfort potential of the earable design.

6.3 *In Vivo* Gait Analysis and FE Validation

6.3.1 Objective

This study extends the sinusoidal vibration work into realistic motion. While the previous section focused on controlled sinusoidal excitations to probe the mechanical coupling of devices to the auricle, real-world motion introduces more complex dynamics. To investigate this, a gait analysis study was conducted, combining experimental IMU recordings and dynamic FE simulations to assess device stability during walking. Gait-induced vibrations and head oscillations can introduce motion artefacts that compromise the quality of biosignal acquisition, particularly for devices mounted on compliant, soft-tissue structures such as the auricle. This study combines experimental gait measurements and FE simulations: first, by quantifying artefacts through IMU recordings, and second, by applying experimentally measured head trajectories as boundary conditions in FE models to replicate and further analyse device–auricle decoupling behaviour.

6.3.2 Experimental System Setup

The experimental system comprised a custom-designed earable prototype equipped with a compact 9-axis inertial measurement unit (IMU; LSM9DS1, SparkFun). An identical IMU was embedded in a head-mounted reference module positioned on the subject's head to capture skull-coupled motion. Both IMUs were interfaced with an Arduino-based microcontroller and synchronised via I^2C communication. A schematic of the setup is shown in Figure 6.6.

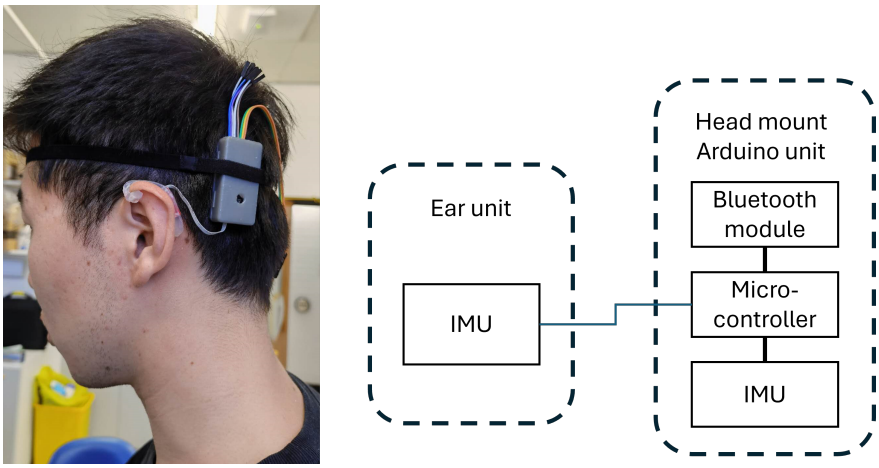


Fig. 6.6 Schematic of the gait analysis setup. The auricle-mounted earable and the head-mounted reference module (grey box) each contain IMUs. Data acquisition is synchronised through an Arduino microcontroller and powered by a portable battery carried by the subject.

The auricle-mounted unit was connected to the head module via a lightweight, flexible cable to minimise mechanical interference. Power and data acquisition were supplied by an on-body power bank and DAC system carried in the subject's pocket. The overall system maintained a lightweight, low-profile form factor to minimise inertial loading and preserve natural head and ear motion characteristics.

6.3.3 Protocol and Data Acquisition

A single-subject walking trial was conducted in a 20 m indoor hallway under controlled conditions. Before data collection, the subject wore the auricle-mounted earable prototype and performed a two-step calibration routine:

- **Stance phase:** standing still for 10 s to record gravitational orientation.
- **Forward-bending phase:** bending forward for 10 s to establish anterior–posterior axis alignment.

Following calibration, the subject walked naturally along the corridor at a constant, comfortable pace. IMU data were streamed in real time, with both auricle- and forehead-mounted units recording tri-axial accelerations synchronously at 200 Hz. The trial was repeated several times to ensure repeatability. No intentional facial or head movements were introduced, and the test environment was kept free of external disturbances.

Raw IMU outputs were processed to align local sensor axes with anatomical directions. A transformation matrix, derived from the calibration phases, was applied to rotate acceleration vectors into a common upright reference frame:

- x-axis: anterior–posterior (forward–backward),
- y-axis: medial–lateral (left–right),
- z-axis: superior–inferior (up–down).

Figure 6.7 compares the time-aligned, calibrated accelerometer signals from both IMUs. Differences in amplitude and frequency content are particularly evident in the lateral and superior axes, reflecting the auricle's compliant motion relative to the skull.

These acceleration data were then integrated to reconstruct 3D displacement trajectories for both the head and the auricle. The forehead IMU trajectory, representing true skull motion, was subsequently used to define boundary conditions in the FE simulations. In this way, experimental gait data directly informed the computational model, enabling a closed-loop validation framework.

6.3.4 FE Simulation with IMU-derived Boundary Conditions

To explore the dynamic response of the auricle–device system under gait-induced motion, a finite element simulation was performed using the CT-derived auricle model with the attached device prototype.

The simulation was conducted in Abaqus/Standard using an explicit dynamic step with moderate dissipation settings. Material properties for the skin and cartilage were assigned according to the validated Ogden hyperelastic parameters described in Chapter 6. To replicate *in vivo* conditions, the simulation was initialised as a restart from the previous static contact step, ensuring realistic pre-stressed contact between the device and auricle.

The experimentally measured head accelerations were decomposed into three orthogonal directions and assigned as tabular amplitude inputs in Abaqus. These inputs drove the auricle base with the recorded skull trajectory, while the auricle itself experienced its natural inertial response. In effect, the auricle–device model was subjected to the same dynamic boundary conditions captured during gait.

The FEA results were post-processed to quantify the coupling between the device and the auricle. Specifically, the number of surface elements experiencing contact pressures

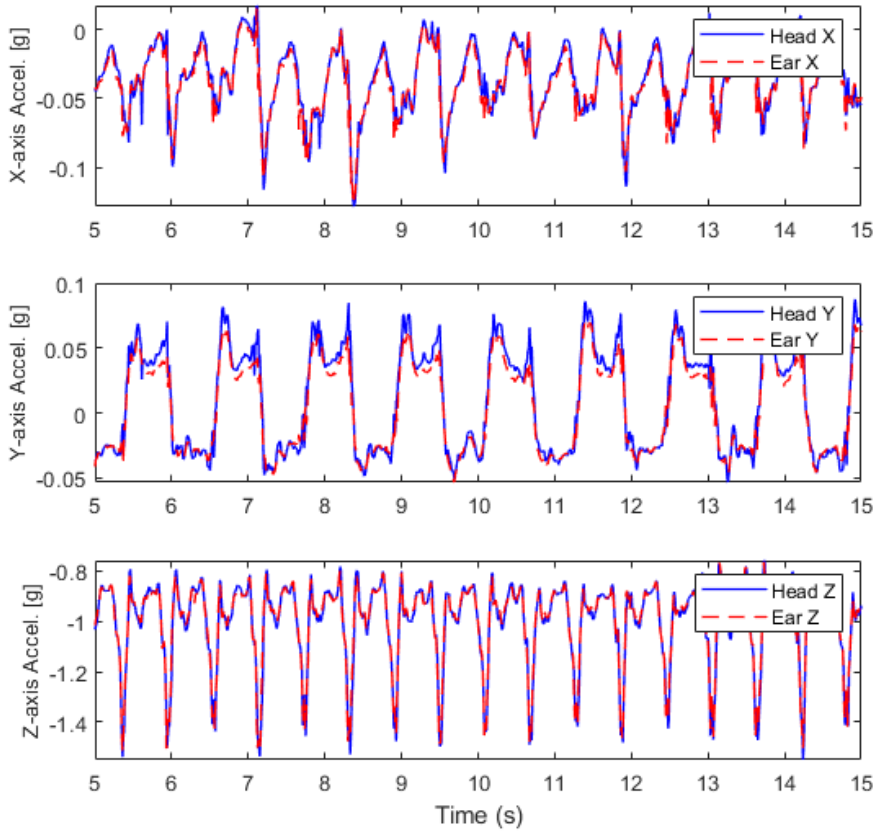


Fig. 6.7 Time-domain comparison of acceleration data recorded at the forehead (head-mounted IMU) and behind the ear (auricle-mounted earable). Data are rotated into a common anatomical reference frame, where the x-axis corresponds to the anterior–posterior (forward–backward) direction, the y-axis to the medial–lateral (left–right) direction, and the z-axis to the superior–inferior (up–down) direction.

exceeding 20 Pa and 500 Pa were extracted and plotted as a function of time (Figure 6.8). This procedure enabled the simulation to reproduce and extend the experimental observations, offering insight into the conditions under which the earable may begin to decouple from the auricle.

In Figure 6.8(c), the average contact force exerted by the earable was estimated by multiplying the average pressure by the number of nodes with non-zero `CPRESS` values (indicating contact) and by the average surface area per element, which was approximated in MeshLab as 0.24 mm^2. The resultant contact force varied within a narrow range of approximately

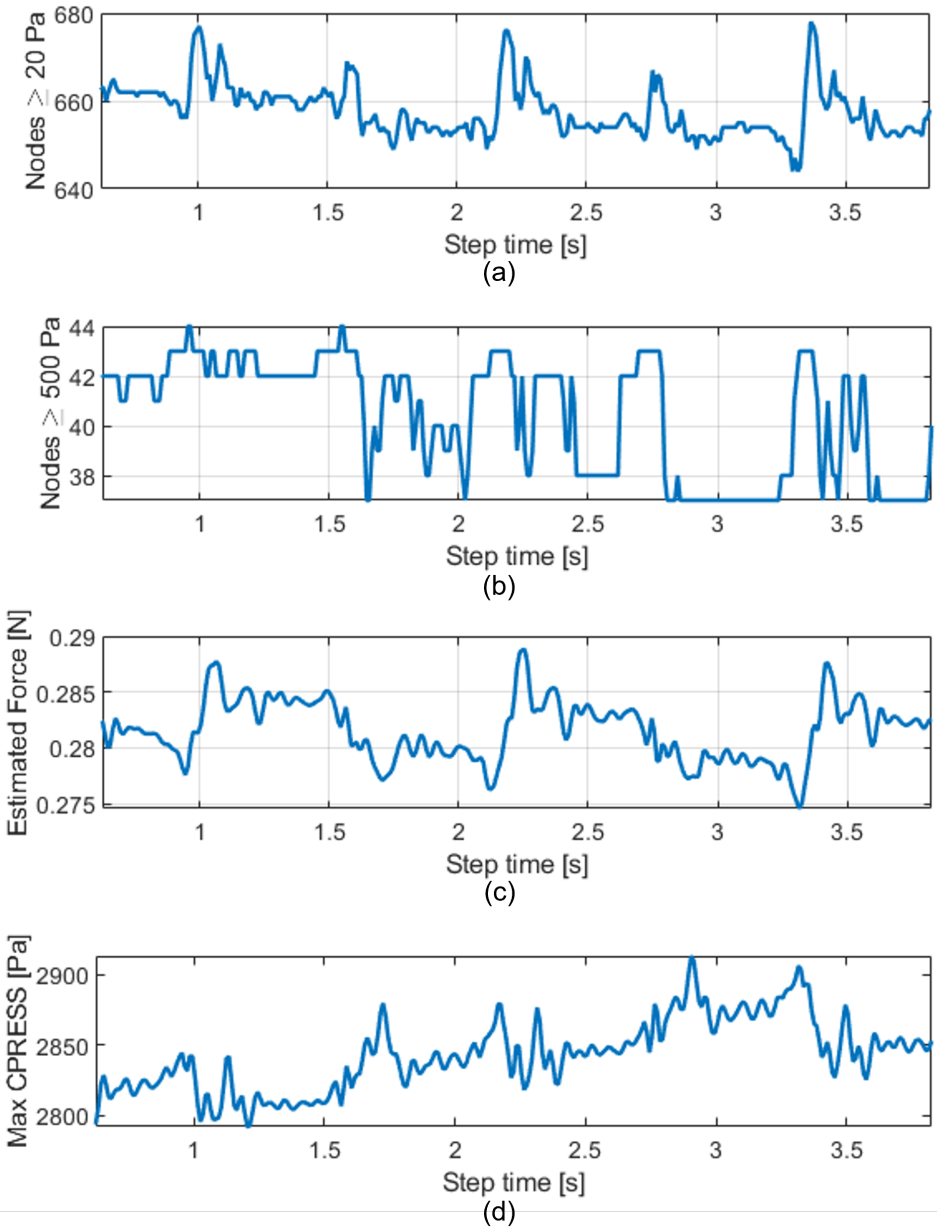


Fig. 6.8 Gait-driven FE simulation results for the earable prototype. (a) Node count with CPRESS > 20 Pa. (b) Node count with CPRESS > 500 Pa. (c) Estimated total force applied from the device to the earable surface (d) Maximum CPRESS during contact. All plots show time series behaviour over a representative gait cycle.

0.015 N, corresponding to about 5% of the total applied pressure, indicating a stable and well-coupled interface between the device and the auricle.

6.3.5 Results and Key Findings

The combined experiment and simulation framework demonstrated that the auricle-mounted earable exhibits measurable yet modest deviations from skull-coupled motion during gait (as shown in Figure 6.7, where only small differences appear between the two traces). The variation in node count and average contact pressure is comparable to the difference observed between the 2 Hz vibration experiment and the static loading condition, as reported in Table 6.1 in Section 6.2. Finite element simulations driven by experimentally measured IMU trajectories produced detailed pressure-distribution maps that could not be directly obtained *in vivo*. While the *in vivo* measurements provided realistic motion trajectories, the simulations further confirmed that gait motion does not induce significant decoupling of the earable device from the head.

These results demonstrate that the contact condition under gait-induced motion can be effectively analysed using finite element analysis (FEA). The characteristic gait frequency, typically between 1.5 and 2 Hz, corresponds closely to the 2 Hz sinusoidal excitation used in the controlled experiment. This underscores the capability of the developed auricle mechanical model to accurately capture and validate earable–skin interaction and decoupling behaviour under realistic dynamic conditions.

6.4 Earable Electrode Study

6.4.1 Introduction

Beyond mechanical stability, many earable applications rely on high-quality skin–electrode contact to acquire biosignals such as EEG. This section investigates the mechanical–electrical coupling at the electrode–skin interface using a combined experimental, analytical, and FE-based approach.

6.4.2 Contact Characterisation of Soft Electrodes

To evaluate the performance of auricle-mounted electrodes for earable devices, a comprehensive investigation was conducted into their mechanical and electrical interactions with the skin. A soft, conformable electrode based on PEDOT:PSS eutectogel was tested under controlled compression to characterise its contact behaviour [117]. This material has previously been demonstrated to be a promising candidate for future earable applications. The

primary objective was to determine how the applied normal force influences the contact area and the resulting skin–electrode impedance, both of which are critical to ensuring reliable signal acquisition in neural interface systems.

As illustrated in Figure 6.9, a motorised test rig was developed to press the soft electrode against a flat, transparent acrylic substrate, thereby simulating a rigid auricle-backed surface. A load cell measured the applied normal force, while a high-resolution camera positioned beneath the acrylic captured the evolving contact profile. The core components of the setup, which are the stepper motor and load cell, were adapted from the previous mechanical experiments on the human auricle (see Chapter 4.2.3). Image-processing techniques were employed to quantify the contact radius and area across a range of applied forces (Figure 6.10).

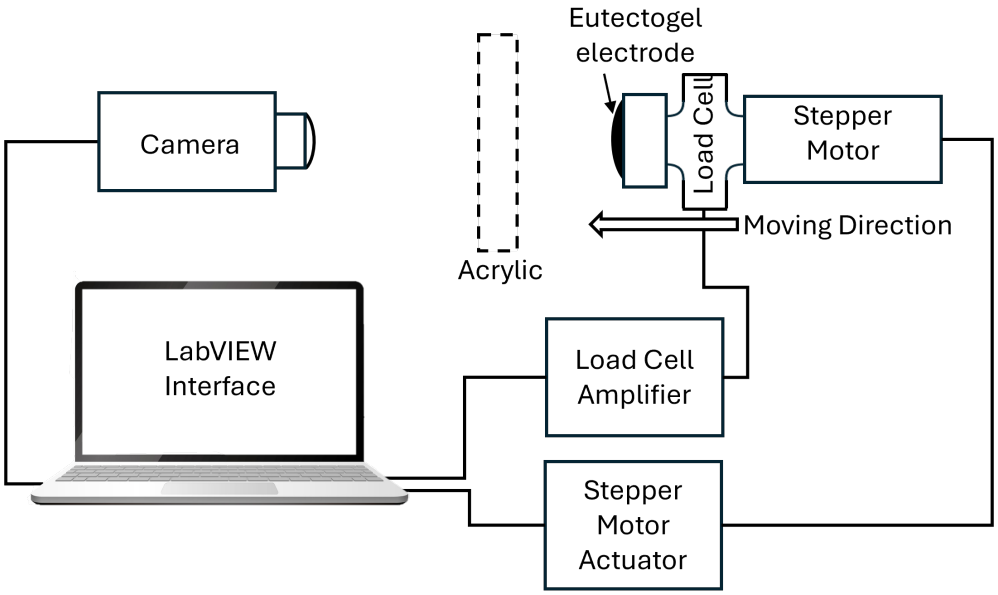


Fig. 6.9 Schematic of the electrode–acrylic contact experiment. The motorised actuator applied controlled compressive forces to the soft eutectogel electrode, while a load cell measured the normal load and a camera captured the contact area through the transparent acrylic.

To standardise the mechanical model, a side-view photograph of the eutectogel profile was taken, as shown in Figure 6.11(a). This profile image was digitised and processed to estimate the geometric dimensions of the electrode. During fabrication, the electrode base radius was constrained to 10 mm. Based on pixel calibration of the side-view image, the electrode geometry was approximated as a truncated spherical cap with a parent-sphere radius of 9.7 mm. This simplified representation enabled analytical modelling of its contact mechanics.

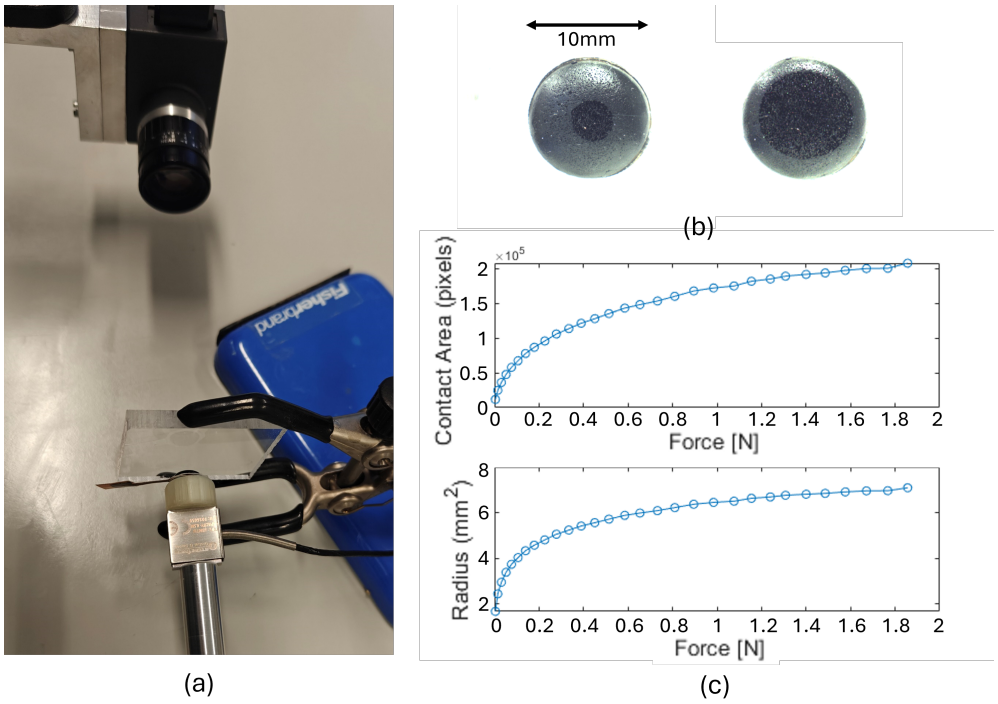


Fig. 6.10 Experimental setup and results for the electrode–acrylic contact study. (a) Photo of motorised mechanical test rig. (b) Representative camera images showing the evolution of the contact region with increasing load. (c) Quantified contact area and equivalent contact radius as a function of applied normal force.

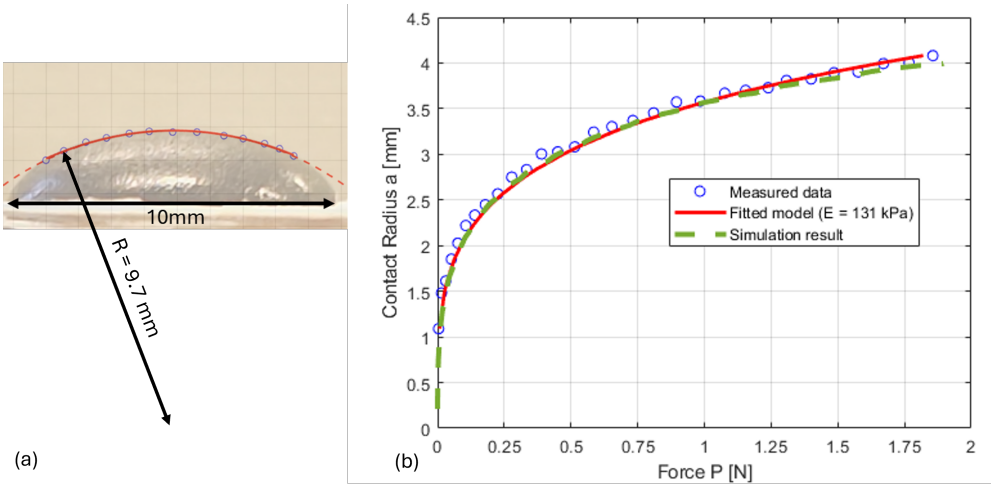


Fig. 6.11 Characterisation of the eutectogel electrode. (a) Side-view image used to extract the profile geometry, approximated as a truncated spherical cap. (b) Comparison of experimental force–contact radius data with analytical prediction from the Winkler foundation model and validation using FE simulations with Ogden hyperelastic parameters.

The analytical model is derived from the classical Winkler foundation, which assumes that the local contact pressure is proportional to the local normal deflection:

$$p(x,y) = k\,w(x,y), \tag{6.1}$$

where p is the contact pressure, w is the indentation (normal surface deflection), and k is the foundation modulus (spring stiffness per unit area) [118, 119]. For an axisymmetric contact of radius a, the resultant force is obtained by integrating the pressure distribution over the contact area:

$$F(a) = \iint_{A(a)} p\,dA = \int_0^a 2\pi r\,p(r)\,dr. \tag{6.2}$$

The spherical-cap geometry defines the undeformed profile as

$$\phi(r) = \sqrt{R^2 - r^2},$$

where R is the parent-sphere radius and $R - \phi(r)$ measures the sag at radial coordinate r. If the undeformed apex thickness is h_0, the local through-thickness of the gel becomes

$$t(r) = h_0 - \big(R - \phi(r)\big), \tag{6.3}$$

and the indentation relative to the contact edge is

$$w(r) = \phi(r) - \phi(a), \qquad 0 \le r \le a, \tag{6.4}$$

which satisfies $w(a) = 0$. Substituting these relations into the Winkler assumption yields the local pressure distribution:

$$p(r) = \frac{E}{t(r)}\big[\phi(r) - \phi(a)\big] = \frac{E}{h_0 - \big(R - \sqrt{R^2 - r^2}\big)}\left[\sqrt{R^2 - r^2} - \sqrt{R^2 - a^2}\right], \tag{6.5}$$

where E is the effective small-strain Young's modulus.

Inserting (6.5) into (6.2) gives the final load–contact-radius relation:

$$F(a) = 2\pi E \int_0^a r\,\frac{\sqrt{R^2 - r^2} - \sqrt{R^2 - a^2}}{h_0 - \big(R - \sqrt{R^2 - r^2}\big)}\,dr, \tag{6.6}$$

which predicts the force as a function of the measured or prescribed contact radius.

As a limiting case, if the gel thickness is uniform ($t(r) \equiv t_0$) and the indentation is approximately constant ($w(r) \approx \delta$), then $k(r) \to k = E/t_0$ and the expression reduces to

$$F \approx \pi k a^2 \delta = \pi \frac{E}{t_0} a^2 \delta, \tag{6.7}$$

the standard Winkler result for a flat, uniform foundation compressed by a rigid flat punch. The generalised formulation in (6.6) therefore extends this classical model to account for the spherical-cap geometry and nonuniform thickness of the eutectogel electrode.

The fitted effective modulus obtained from the Winkler-based contact model was $E_w \approx$ 131 kPa, consistent with expectations for soft polymeric gels [117]. To incorporate this modulus into the finite element (FE) simulations, the equivalent shear modulus μ for a one-term Ogden hyperelastic material was derived.

For the one-term Ogden model, the small-strain shear modulus satisfies $G \simeq \mu$, and the corresponding linearised Young's modulus is

$$E_{\text{lin}} \approx 2\mu(1+\nu), \tag{6.8}$$

where ν is the Poisson's ratio. Since the eutectogel electrode is fairly compressible, we assume $\nu \approx 0.35$. Substituting $E_{\text{lin}} = E_w = 131{,}000$ Pa gives

$$\mu = \frac{E_w}{2(1+\nu)} = \frac{131{,}000}{2 \times 1.35} \approx 48{,}500 \text{ Pa}.$$

Thus, the Ogden parameters used in the FE model were updated to $\mu \approx 4.85 \times 10^4$ Pa, $\alpha = 2.0$, and $D = 4 \times 10^{-5}$ Pa^{-1}. With these parameters, the FE simulations reproduced the experimental force–contact radius relationship and contact area evolution with good agreement across the tested range, as shown in Figure 6.11(b).

This demonstrates that the Ogden model, parameterised from the effective modulus identified in the Winkler foundation fit, provides a consistent and robust description of the electrode's mechanical response. Minor discrepancies between model and experiment can be attributed to finite-strain stiffening effects, geometric idealisations in the Winkler approximation, and small nonuniformities in the gel material. Overall, the combination of experimental measurements, Winkler foundation modelling, and FE simulations validates the use of the Ogden hyperelastic formulation for this class of soft, conformable electrodes.

6.4.3 Skin Impedance Measurement and Pressure Dependence

To assess the electrode's performance under realistic anatomical conditions, an *in vivo* impedance study was conducted. The soft eutectogel electrode was positioned anterior to the tragus, an anatomically appropriate site for earable sensor placement. A commercial pre-gelled reference electrode (Ambu Neuroline 720) was affixed to the zygomatic arch to form a two-electrode configuration. Both electrodes were connected to a precision impedance analyser (Sciospec ISX-3, Sciospec Scientific Instruments GmbH) capable of high-resolution broadband impedance spectroscopy.

Controlled and repeatable normal forces were applied using a custom mechanical rig adapted from the stepper-motor and load-cell apparatus described in Section 4.2.3. During each trial, the actuator advanced the test electrode against the skin until initial contact was detected, at which point the force reading was zeroed. The electrode was then incrementally displaced in five 0.5 mm steps, reaching a total displacement of 2.5 mm. This corresponded to a force range of approximately 0–0.6 N, depending on individual skin compliance. The procedure ensured consistent and repeatable electrode–skin contact while minimising variability arising from manual placement or subject movement (Figure 6.12).

The resulting impedance spectra were used to evaluate the relationship between contact pressure and electrical coupling at the electrode–skin interface. A total of 12 volunteers aged between 18 and 40 years participated in the study. Ethical approval was obtained from the Research Ethics Committee of the Department of Engineering, University of Cambridge, and all participants provided written informed consent (see Appendix C).

Impedance spectra were acquired using an AC sweep from 1 Hz to 1 kHz, a range commonly employed in bioelectrical impedance spectroscopy to probe both resistive and capacitive tissue behaviour [120]. At 50 Hz, which is relevant to EEG systems due to proximity to mains frequency, a consistent reduction in impedance with increasing applied force was observed (Figure 6.13), in line with established practices for evaluating electrode–skin impedance under line-frequency conditions [121].

Across all trials, the overall trend showed a monotonic decrease in electrode–skin impedance with increasing force, eventually reaching a plateau for forces greater than approximately 0.1 N. Below this threshold, impedance exhibited steep gradients on the order of a few mN, which proved difficult to resolve reliably. Even under head fixation and posture control, involuntary micro-movements of the subject introduced fluctuations that masked fine impedance changes at very low loads. Nevertheless, the saturation trend above 0.1 N suggests a strong correlation between applied force, contact radius, and skin–electrode impedance, pointing

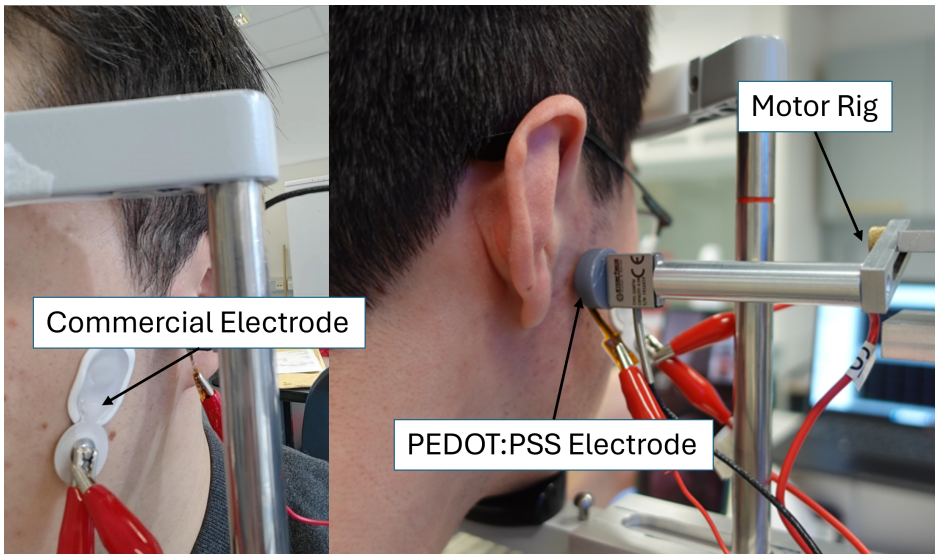


Fig. 6.12 Experimental setup for electrode–skin impedance measurement. The eutectogel electrode was placed anterior to the tragus and the reference electrode on the zygomatic arch. A custom rig applied calibrated normal forces, and impedance spectra were acquired using an AC sweep.

towards a predictable mechanical–electrical relationship that can be further quantified in future studies.

6.4.4 Estimating Contact Radius and Interface Modelling

The impedance measurements established a clear dependence on applied force, but the intermediate variable, the effective contact radius between the electrode and skin, cannot be measured directly *in vivo*. Unlike electrode–acrylic experiments, where the counterface is rigid and well defined, the skin interface is compliant, heterogeneous, and layered. To resolve this complexity, FE simulations were employed to estimate how the soft eutectogel electrode deforms against auricular tissue and how the contact radius evolves with force.

The FE model represented the electrode as a truncated spherical cap in contact with a skin layer, as shown in Figure 6.14. The skin was modelled using Ogden hyperelastic parameters, with a thickness T range of 1.5–2.5 mm to capture anatomical variability across the auricle. Boundary conditions fixed the base of the skin to mimic coupling with the skull, and a frictionless normal contact formulation was applied at the skin-electrode interface to isolate the effects of normal loading. Simulations were conducted over an applied force range of 0.05–1.5 N, consistent with the impedance experiments. The results demonstrated a

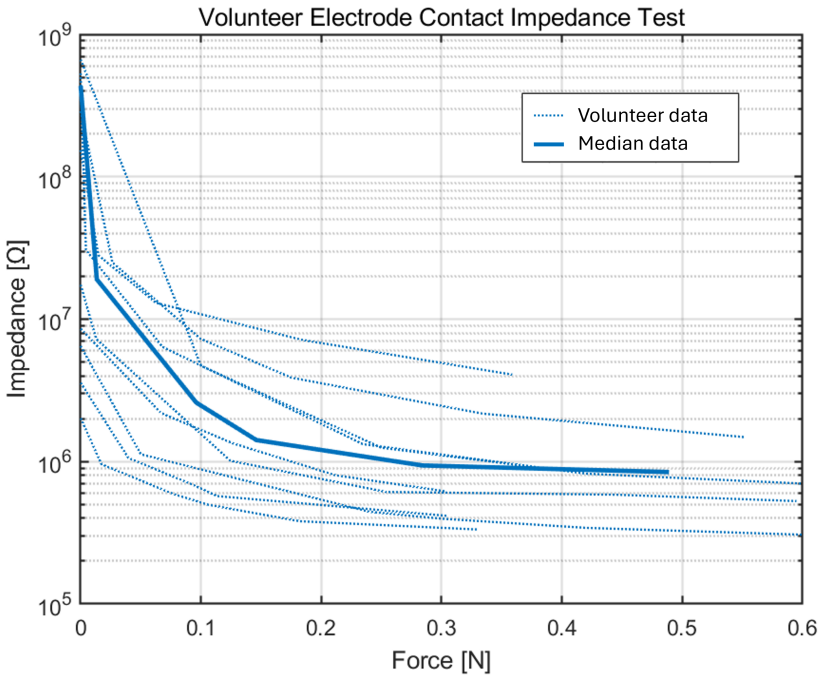


Fig. 6.13 Electrode–skin impedance at 50 Hz as a function of measured applied normal force (0–0.6 N). Thin dotted curves show individual measurements from multiple subjects; the thick solid curve denotes the across-subject median. Impedance generally decreases with increasing force, while between-subject variability remains substantial.

nonlinear yet monotonic increase in contact radius with increasing force, with thinner skin layers producing larger radii under the same load due to reduced compliance (Figure 6.15).

With this relationship, the applied force in the impedance experiments can be replaced by the FE-predicted contact radius. Replotting the data in this form (assuming a representative skin thickness of 2.0 mm) reveals impedance as a direct function of contact radius (Figure 6.16). The curves highlight the mechanical and electrical coupling more explicitly: impedance decreases as the skin and electrode contact area increases.

This behaviour can be understood through the concept of *spreading resistance*. At the electrode-skin interface, electrical current is confined to a finite contact area $A_c \sim \pi r^2$, where r is the effective contact radius. The resistive component of the impedance can be approximated by

$$R \propto \frac{\rho}{A_c}, \tag{6.9}$$

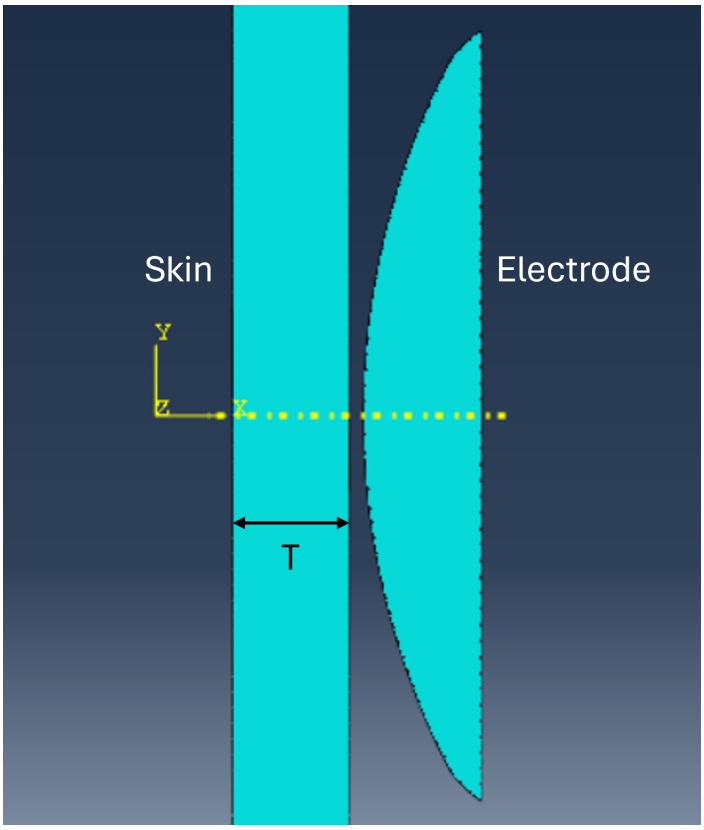


Fig. 6.14 FE analysis of an electrode in contact with a skin layer of thickness $T = 2$ mm.

where ρ is the effective resistivity of the skin–electrode interface. Substituting $A_c \propto r^2$ yields

$$R \propto r^{-2}, \tag{6.10}$$

implying that, on a log–log scale, the theoretical slope of $\log R$ versus $\log r$ should be -2 under the assumption of uniform current density, constant resistivity, and negligible edge effects. This relation follows classical constriction (spreading) resistance theory, commonly used to model current flow through circular contact patches on semi-infinite conducting media [122].

As applied force increases, the contact radius, and hence A_c, increases, leading to a reduction in impedance. The observed plateau in impedance beyond 0.1 N reflects the saturation of the available conductive surface; once most of the potential contact area is engaged, further increases in radius contribute minimally to conductance. In practical terms, controlling applied loads below 0.1 N proved challenging due to involuntary subject micro-movements,

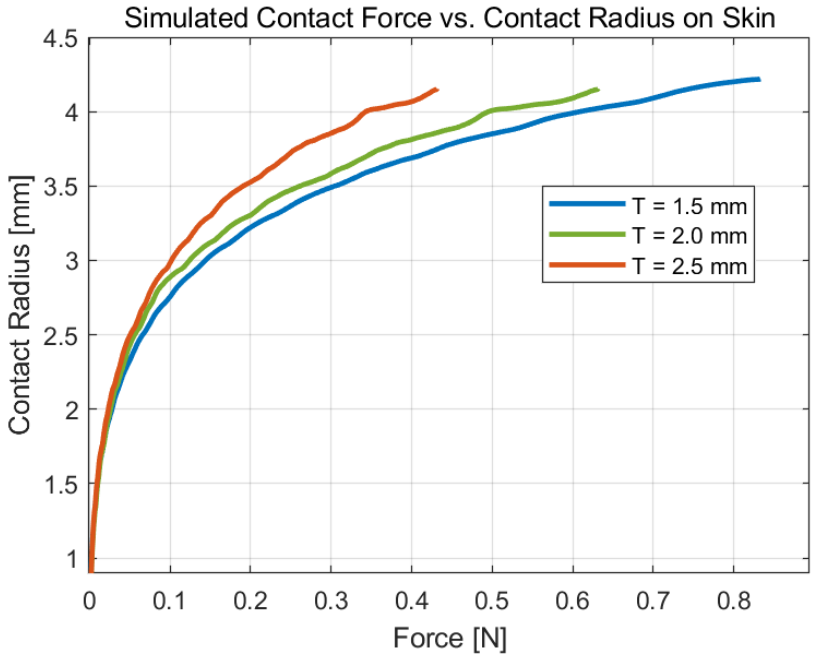


Fig. 6.15 FE simulation of electrode contact with soft skin layers of varying thickness T (1.5–2.5 mm). The contact radius increases with applied force, and thinner skin layers exhibit larger effective radii under the same load, reflecting anatomical variability.

which introduced force fluctuations on the order of millinewtons and obscured fine impedance changes.

Interestingly, the experimentally observed $\log R$–$\log r$ curves exhibit an average slope closer to -3, which is steeper than the idealised -2 prediction. This deviation likely arises from a combination of factors: (i) non-uniform current distribution and partial contact, where the real conductive area grows sublinearly with geometric expansion; (ii) current spreading into deeper tissue layers, which alters the effective current path; (iii) pressure-dependent changes in gel or skin resistivity; and (iv) capacitive effects at the electrode-skin interface that modify the apparent impedance at measurement frequency. These effects collectively steepen the apparent scaling behaviour, producing a stronger than quadratic dependence between impedance and contact radius.

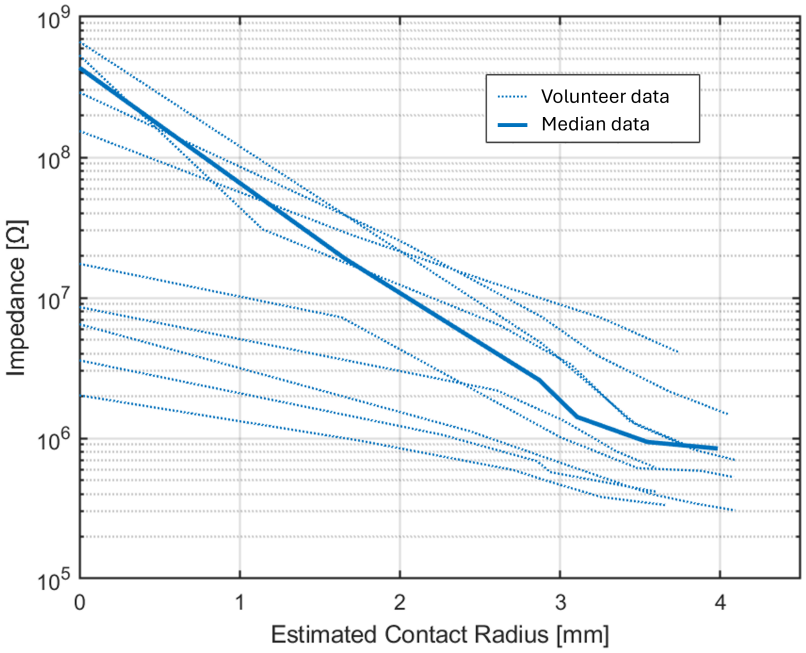


Fig. 6.16 Electrode–skin impedance at 50 Hz plotted against FE-predicted contact radius (assuming a 2.0 mm skin layer). The median data was highlighted as the thick solid line. The inverse relationship reflects the dependence of spreading resistance on contact area, though inter-individual variability remains substantial.

6.5 Results and Discussion

This chapter presented multiple works related to FEA linking mechanical simulation, gait-based dynamics, and electrode–skin impedance to characterise auricle–device interaction. The validated auricle model developed in Chapter 5 enabled consistent evaluation of contact pressure, coupling, bioelectrical performance across designs.

Across static and dynamic conditions, effective coupling depended primarily on device geometry: designs that spread contact show more stable and continuous pressure fields. The Earable prototype also demonstrate good stability in gait induced vibrations. Electrically, both experiments and simulations indicated a practical force threshold (≈ 0.1 N) to achieve low contact impedance; anatomical factors (e.g., tissue stiffness, thickness) modulate how readily this threshold translates into effective contact area.

The key contribution of this chapter is not the immediate derivation of device-specific design rules, but the demonstration that the proposed experimental–computational framework provides a physically grounded and generalisable description of auricle mechanics. By

combining static loading, impulse-release dynamics, and simplified mechanical modelling, this work establishes that auricle behaviour can be captured using a small set of interpretable mechanical parameters, namely effective stiffness and natural frequency, which jointly reflect geometry, material properties, and boundary constraints.

Crucially, the agreement between experimental measurements and idealised beam-based scaling laws demonstrates that the auricle can be treated as a mechanically consistent structure for a wide range of loading and contact scenarios. This validates the use of the developed auricle model as a foundation for broader analyses beyond those presented in this chapter, including detailed contact mechanics, pressure distribution, motion-induced detachment, and device–ear coupling behaviour. As such, the framework developed here serves as an enabling tool for subsequent chapters, rather than a closed set of application-specific conclusions.

Overall, this chapter demonstrates the predictive capability of the auricle model for device interaction and establishes it as a practical, pre-clinical design tool. By enabling digital exploration of geometry, load distribution, and material choices, the platform reduces reliance on volunteer testing in early iterations, shortens development cycles, and supports safer and more ethical study planning.

In practice, the model can allow designers to screen concepts for stable contact, pressure hot-spots, and impedance targets before fabrication, then refine promising candidates with fewer, better focused human trials. As such, it can advance human-centred engineering by linking mechanical fit and bioelectrical performance to concrete design decisions, and provide a foundation for future personalisation and NI signal acquisition that sustain optimal contact in daily use.

Chapter 7

Conclusion

7.1 Summary of Key Findings

This thesis presents a comprehensive investigation into the mechanical and electrical interaction between wearable auricle-mounted devices, which termed *Earables* in this Thesis, and the human external ear. The work integrates experimental studies, finite element (FE) simulations, and prototype testing to address the core challenge of achieving robust mechanical coupling and low-noise biosignal acquisition from the auricle.

Phantom Auricle Modelling

A key methodological foundation was the creation of a physical auricle phantom, designed to replicate the anatomical geometry and mechanical behaviour of the human ear. The phantom enabled controlled mechanical testing under repeatable loading conditions and provided a validated baseline for finite element modelling. Material characterisation revealed that layered construction with distinct skin and cartilage analogues is essential for capturing the auricle's biomechanical properties. This phantom allowed simulation to experiment validation, establishing credibility for further in silico analysis.

Volunteer-Based Mechanical Testing

In vivo tests were conducted on human volunteers to measure auricle deflection and oscillatory behaviour under anterior tensile loading. The results demonstrated subject-specific variability

in auricle stiffness and damping, but also confirmed general trends in mechanical response. These experimental results provided critical benchmarks for FE model validation and were used to infer effective mechanical parameters, such as static stiffness and vibration frequency.

Finite Element Simulation of Auricle Mechanics

A detailed auricle model was constructed from high-resolution CT data and supplemented by mesh datasets representing morphological diversity. Mesh convergence studies established optimal meshing strategies for accurate yet computationally feasible simulations. Using both linear and Ogden hyperelastic models, the simulations replicated mechanical responses observed in experiments, including deformation under tensile loading and free vibration behaviour.

Parametric studies revealed that auricle mechanical properties are highly sensitive to both material parameters and geometric variations, such as auricle length, width, and cartilage thickness. This highlights the importance of subject-specific modelling in wearable device design. The FE model also served as a platform for simulating dynamic interactions with wearable systems under motion, including walking-induced vibration.

Prototype Evaluation and Device Decoupling

Earable prototypes were fabricated and tested under both static and dynamic conditions. A detailed study of skin-electrode contact demonstrated that electrode impedance is strongly modulated by applied pressure and skin geometry. These experiments were supported by contact mechanics simulations that validated pressure–area relationships.

In motion artefact studies, auricle-mounted IMUs revealed characteristic amplification of gait harmonics and asymmetric oscillations due to unilateral leg motion. Frequency-domain analysis showed that soft tissue resonance plays a non-negligible role in artefact propagation. Finite element simulations further confirmed the potential of device tuning to avoid resonant coupling with gait-induced frequencies.

7.2 Limitations

While the results offer significant insights into auricle mechanics and device interaction, several limitations must be acknowledged:

- **Sample size**: Volunteer tests were limited in number, restricting the generalisability of observed inter-subject variability.
- **Simplified modelling assumptions**: FE simulations neglected dynamic contact friction and viscoelastic damping effects, which may become significant in long-term wear or dynamic loading.
- **Device complexity**: The tested earable prototypes represent early-stage designs, and their geometry and materials do not yet fully reflect potential commercial implementations.
- **Sensor bandwidth**: IMU data were sampled at 200 Hz, which is sufficient for gait analysis but may miss higher frequency artefacts in tasks like jaw clenching or speech.

7.3 Future Work

Advanced material and contact modelling. Extend the FE model to include rate dependent viscoelastic behaviour, potential anisotropy in skin/cartilage, and frictional contact with pressure–area evolution. Quantify how these additions shift stiffness, resonance, and artefact transmission under long duration wear.

Population-aware personalisation. Scale *in vivo* testing to a larger, demographically diverse cohort and build statistical shape–mechanics models that map auricular morphology to effective mechanical parameters. Use these models to issue design envelopes and safety margins for population-level fit and comfort.

Design for decoupling (and purposeful coupling). Exploit the observed sensitivity to geometry and materials to explore segmented frames, compliant mechanisms, and tuned mass/stiffness distributions that suppress coupling at gait harmonics. In parallel, investigate purposeful coupling when it benefits sensing (e.g., amplifying low band vibrations while rejecting others).

Closed-loop electro-mechanical validation. Embed real-time EEG/EMG (or impedance tracking) into prototypes to quantify how mechanical design choices (pressure, area, stiffness) translate to signal quality. Use these readouts for automated, simulation-in-the-loop design updates.

Longitudinal comfort and stability. After using FE model to validate design, conduct volunteer study for evaluating fit, pressure hotspots, and electrode–skin impedance over

hours to days, including sweat/temperature effects and repeated donning. Translate findings into practical wear time guidance and adaptive retention strategies.

Toolchain robustness and reproducibility. Package the CT-derived meshing, cartilage layer generation, and analysis scripts into a documented pipeline with versioned meshes and inputs, enabling replication and extension across research groups and product teams.

7.4 Concluding Remarks

This thesis has demonstrated that the auricle is not merely a passive anatomical site but an active mechanical substrate that significantly influences the design and performance of wearable neural interfaces. Through a combination of physical modelling, human subject experiments, and simulation-driven design, a robust framework has been established for understanding and engineering earable systems. The insights gained lay the groundwork for a new generation of auricle-mounted devices that are both biophysically informed and functionally reliable.

References

[1] Changshuo Hu, Qiang Yang, Yang Liu, Tobias Röddiger, Kayla-Jade Butkow, Mathias Ciliberto, Adam Luke Pullin, Jake Stuchbury-Wass, Mahbub Hassan, Cecilia Mascolo, and Dong Ma. A survey of earable technology: Trends, tools, and the road ahead, 2025.

[2] Tobias Röddiger, Christopher Clarke, Paula Breitling, Tim Schneegans, Haibin Zhao, Hans Gellersen, and Michael Beigl. Sensing with earables: A systematic literature review and taxonomy of phenomena. *Proc. ACM Interact. Mob. Wearable Ubiquitous Technol.*, 6(3), September 2022.

[3] Netiwit Kaongoen, Jaehoon Choi, Jinwoo Choi, Haram Kwon, Chaeeun Hwang, Guebin Hwang, Byung Kim, and Sungho Jo. The future of wearable eeg: a review of ear-eeg technology and its applications. *Journal of Neural Engineering*, 20, 10 2023.

[4] Abdul Aziz, Ravi Karkar, Kan Ding, Jay Harvey, and Phuc Nguyen. Earables as medical devices: Opportunities and challenges. In *Adjunct Proceedings of the 2023 ACM International Joint Conference on Pervasive and Ubiquitous Computing & the 2023 ACM International Symposium on Wearable Computing*, UbiComp/ISWC '23 Adjunct, page 339–341, New York, NY, USA, 2023. Association for Computing Machinery.

[5] John P. Donoghue. Bridging the brain to the world: A perspective on neural interface systems. *Neuron*, 60(3):511–521, 2008.

[6] Leigh R Hochberg, Mijail D Serruya, Gerhard M Friehs, Jon A Mukand, Maryam Saleh, Abraham H Caplan, Almut Branner, David Chen, Richard D Penn, and John P Donoghue. Neuronal ensemble control of prosthetic devices by a human with tetraplegia. *Nature*, 442(7099):164–171, 2006.

[7] Caterina Cinel, Davide Valeriani, and Riccardo Poli. Neurotechnologies for human cognitive augmentation: Current state of the art and future prospects. *Frontiers in Human Neuroscience*, 13, 01 2019.

[8] David Steyrl, Reinmar Kobler, and Gernot Müller-Putz. On similarities and differences of invasive and non-invasive electrical brain signals in brain-computer interfacing. *Journal of biomedical science and engineering*, 9:393–398, 06 2016.

[9] Shujhat Khan, Leonie Kallis, Harry Mee, Salim El Hadwe, Damiano Barone, Peter Hutchinson, and Angelos Kolias. Invasive brain–computer interface for communication: A scoping review. *Brain Sciences*, 15(4), 2025.

[10] Ju-Chun Hsieh, Hussein Alawieh, José del R. Millán, and Huiliang Wang. The evolving landscape of non-invasive eeg-brain-computer interfaces: Current trends and future perspectives. *Device*, 2(12):100647, 2024.

[11] Eric R. Kandel, John Koester, Sarah Mack, and Steven Siegelbaum, editors. *Principles of neural science*. New York : McGraw Hill, sixth edition. edition, 2021.

[12] Donnell J. Creel. Chapter 33 - the electrooculogram. In Kerry H. Levin and Patrick Chauvel, editors, *Clinical Neurophysiology: Basis and Technical Aspects*, volume 160 of *Handbook of Clinical Neurology*, pages 495–499. Elsevier, 2019.

[13] Ekta Dahiya, Anubha Kalra, Andrew Lowe, and Gautam Anand. Wearable technology for monitoring electrocardiograms (ecgs) in adults: A scoping review. *Sensors*, 24:1318, 02 2024.

[14] J.R Ives and J.F Woods. 4-channel 24 hour cassette recorder for long-term eeg monitoring of ambulatory patients. *Electroencephalography and Clinical Neurophysiology*, 39(1):88–92, 1975.

[15] Said Abosreea. *Design and Implementation of Electroencephalogram System*. PhD thesis, King Salman International University, 07 2016.

[16] Y. Qin, Y. Zhang, Y. Zhang, S. Liu, and X. Guo. Application and development of eeg acquisition and feedback technology: A review. *Biosensors (Basel)*, 13(10):930, oct 2023.

[17] Herbert H. Jasper. The ten-twenty electrode system of the international federation. *Electroencephalography and Clinical Neurophysiology*, 10:371–375, 1958.

[18] Lau M. Andersen, Robert Oostenveld, Christoph Pfeiffer, Silvia Ruffieux, Veikko Jousmäki, Matti Hämäläinen, Justin F. Schneiderman, and Daniel Lundqvist. Similarities and differences between on-scalp and conventional in-helmet magnetoencephalography recordings. *PLOS ONE*, 12(7):1–19, 07 2017.

[19] Jzau-Sheng Lin and Zi-Yang Jiang. Implementing remote presence using quadcopter control by a non-invasive bci device. *Computer Science and Information Technology*, 3(4):122–126, 2015.

[20] Konstantinos Kotzias, Faiza A. Bukhsh, Jeewanie Jayasinghe Arachchige, Maya Daneva, and Abhishta Abhishta. Industry 4.0 and healthcare: Context, applications, benefits and challenges. *IET Software*, 17(3):195–248, 2023.

[21] Morteza Jalali Alenjareghi, Firdaous Sekkay, Camelia Dadouchi, and Samira Keivanpour. Wearable sensors in industry 4.0: Preventing work-related musculoskeletal disorders. *Sensors International*, 7:100343, 2026.

[22] Rosiane Serrano, Larissa Fortunati, and Daniel Pacheco Lacerda. Wearable technologies in the fashion value ecosystem: a conceptual model. *Innovation Management Review*, 19(2):90–105, 11 2021.

[23] Anna Gruebler and Kenji Suzuki. Design of a wearable device for reading positive expressions from facial emg signals. *IEEE Transactions on Affective Computing*, 5(3):227–237, 2014.

[24] Joong Woo Ahn, Yunseo Ku, and Hee Chan Kim. A novel wearable eeg and ecg recording system for stress assessment. *Sensors*, 19(9), 2019.

[25] Chin-Teng Lin, Chun-Hsiang Chuang, Chih-Sheng Huang, Shu-Fang Tsai, Shao-Wei Lu, Yen-Hsuan Chen, and Li-Wei Ko. Wireless and wearable eeg system for evaluating driver vigilance. *IEEE Transactions on Biomedical Circuits and Systems*, 8(2):165–176, 2014.

[26] Jd.R. Millan, F. Renkens, J. Mourino, and W. Gerstner. Noninvasive brain-actuated control of a mobile robot by human eeg. *IEEE Transactions on Biomedical Engineering*, 51(6):1026–1033, 2004.

[27] Jonathan R Wolpaw, Niels Birbaumer, Dennis J McFarland, Gert Pfurtscheller, and Theresa M Vaughan. Brain-computer interfaces for communication and control. *Clinical Neurophysiology*, 113(6):767–791, 2002.

[28] Belal Heyat, Shaguftah, Yassir Hasan, and Mohd. Maroof Siddiqui. Eeg signals and wireless transfer of eeg signals. 12 2015.

[29] *PEDOT : principles and applications of an intrinsically conductive polymer / Andreas Elschner [and others].* CRC Press, Boca Raton, FL, 2011.

[30] Mei Ying Teo, Nara Kim, Seyoung Kee, Bong Seong Kim, Geunjin Kim, Soonil Hong, Suhyun Jung, and Kwanghee Lee. Highly stretchable and highly conductive pedot:pss/ionic liquid composite transparent electrodes for solution-processed stretchable electronics. *ACS Applied Materials & Interfaces*, 9(1):819–826, 2017. PMID: 27990796.

[31] Ivan B. Dimov, Armin Sautter, Wilfried Lövenich, Christian Neumann, and George G. Malliaras. Adhesive cutaneous conducting polymer electrodes. *Applied Physics Reviews*, 9(2):021401, 2022.

[32] Jing Li, Daize Mo, Jinyuan Hu, Shichao Wang, Jun Gong, Yujing Huang, Zheng Li, Zhen Yuan, and Mengze Xu. Pedot:pss-based bioelectronics for brain monitoring and modulation. *Microsystems & Nanoengineering*, 11(1):87, 2025.

[33] David Fitzpatrick Dale Purves, George J Augustine. *Neuroscience.* Fifth edition, 2012. The External Ear.

[34] Alice Szymanski and Zachary Geiger. Anatomy, head and neck, ear. In *StatPearls*. StatPearls Publishing, Treasure Island (FL), January 2022.

[35] CG Wright. Development of the human external ear. *Journal of the American Academy of Audiology*, 8(6):379–382, 1997.

[36] Tapio Nikkari. Comparative chemistry of sebum. *Journal of Investigative Dermatology*, 62(3):257–267, 1974.

[37] E. N Marieb. *Human anatomy and physiology.* Benjamin Cummings, Menlo Park, CA, 4th edition, 1998. The Outer (External) Ear.

[38] II Dalley, Arthur F. and Anne M. R. Agur. *Moore's Clinically Oriented Anatomy, 9e*. Lippincott Williams Wilkins, a Wolters Kluwer business, 01 2023.

[39] Clara Piris Burgos, Lea Gärtner, Miguel A. González Ballester, Jérôme Noailly, Fabian Stöcker, Martin Schönfelder, Tim Adams, and Simone Tassani. In-ear accelerometer-based sensor for gait classification. *IEEE Sensors Journal*, 20(21):12895–12902, 2020.

[40] Tong-Hun Hwang, Julia Reh, Alfred O. Effenberg, and Holger Blume. Real-time gait analysis using a single head-worn inertial measurement unit. *IEEE Transactions on Consumer Electronics*, 64(2):240–248, 2018.

[41] Nhat Pham, Tuan Dinh, Taeho Kim, Zohreh Raghebi, Nam Bui, Hoang Truong, Tuan Nguyen, Farnoush Banaei-Kashani, Ann Halbower, Thang N. Dinh, Vp Nguyen, and Tam Vu. Detection of microsleep events with a behind-the-ear wearable system. *IEEE Transactions on Mobile Computing*, pages 1–1, 2021.

[42] Wonsup Lee, Hayoung Jung, Ilgeun Bok, Chulwoo Kim, Ochae Kwon, Teukgyu Choi, and Heecheon You. Measurement and application of 3d ear images for earphone design. *Proceedings of the Human Factors and Ergonomics Society Annual Meeting*, 60(1):1053–1057, 2016.

[43] Ming-Zher Poh, Kyunghee Kim, Andrew Goessling, Nicholas Swenson, and Rosalind Picard. Cardiovascular monitoring using earphones and a mobile device. *IEEE Pervasive Computing*, 11(4):18–26, 2012.

[44] Jacobus Cornelis Haartsen. Dual-ear heart rate detection using asymmetry, Sep 2020.

[45] Boudewijn Venema, Hartmut Gehring, Ina Michelsen, Nikolai Blanik, Vladimir Blazek, and Steffen Leonhardt. Robustness, specificity, and reliability of an in-ear pulse oximetric sensor in surgical patients. *IEEE Journal of Biomedical and Health Informatics*, 18(4):1178–1185, 2014.

[46] Thomas Conroy, Jairo Hernandez Guzman, Burr Hall, Gill Tsouri, and Jean-Philippe Couderc. Detection of atrial fibrillation using an earlobe photoplethysmographic sensor. In *2017 Computing in Cardiology (CinC)*, pages 1–4, 2017.

[47] Kazuhiro Taniguchi, Hisashi Kondo, Mami Kurosawa, and Atsushi Nishikawa. Earable tempo: A novel, hands-free input device that uses the movement of the tongue measured with a wearable ear sensor. *Sensors*, 18(3), 2018.

[48] Xiaomin Ji, Zhaohua Zhu, Zhu Gao, Xiaobo Bai, and Gang Hu. Anthropometry and classification of auricular concha for the ergonomic design of earphones. *Human Factors and Ergonomics in Manufacturing & Service Industries*, 28(2):90–99, 2018.

[49] Kaare B. Mikkelsen, Simon L. Kappel, Danilo P. Mandic, and Preben Kidmose. Eeg recorded from the ear: Characterizing the ear-eeg method. *Frontiers in Neuroscience*, 9:438, 2015.

[50] Preben Kidmose, David Looney, Michael Ungstrup, Mike Rank, and Danilo Mandic. A study of evoked potentials from ear-eeg. *IEEE transactions on bio-medical engineering*, 60, May 2013.

[51] Simon L. Kappel, Mike L. Rank, Hans Olaf Toft, Mikael Andersen, and Preben Kidmose. Dry-contact electrode ear-eeg. *IEEE Transactions on Biomedical Engineering*, 66(1):150–158, 2019.

[52] Anh Nguyen, Raghda Alqurashi, Zohreh Raghebi, Farnoush Banaei-kashani, Ann C. Halbower, and Tam Vu. A lightweight and inexpensive in-ear sensing system for automatic whole-night sleep stage monitoring. In *Proceedings of the 14th ACM Conference on Embedded Network Sensor Systems CD-ROM*, SenSys '16, page 230–244, New York, NY, USA, 2016. Association for Computing Machinery.

[53] Nam Bui, Nhat Pham, Jessica Jacqueline Barnitz, Zhanan Zou, Phuc Nguyen, Anh-Hoang Truong, Taeho Kim, Nicholas Farrow, Anh Nguyen, Jianliang Xiao, Robin R. Deterding, Thang N. Dinh, and Tam N. Vu. ebp: A wearable system for frequent and comfortable blood pressure monitoring from user's ear. *The 25th Annual International Conference on Mobile Computing and Networking*, 2019.

[54] James F. Knight, Daniel Deen-Williams, Theodoros N. Arvanitis, Chris Baber, Sofoklis Sotiriou, Stamatina Anastopoulou, and Michael Gargalakos. Assessing the wearability of wearable computers. pages 75–82, 2006.

[55] Alessandro Masè, Michela snd Micarelli and Giacomo Strapazzon. Hearables: New perspectives and pitfalls of in-ear devices for physiological monitoring. a scoping review. *Frontiers in physiology*, 11:568886–568886, Oct 2020. 33178038[pmid].

[56] Zi Wang, Sheng Tan, Linghan Zhang, Yili Ren, Zhi Wang, and Jie Yang. Eardynamic: An ear canal deformation based continuous user authentication using in-ear wearables. *Proc. ACM Interact. Mob. Wearable Ubiquitous Technol.*, 5(1), mar 2021.

[57] Sharanbasappa R. Japatti, Priyanka J. Engineer, B. Manjunatha Reddy, Akash U. Tiwari, Chidambar Y. Siddegowda, and Reshma B. Hammannavar. Anthropometric assessment of the normal adult human ear. *Annals of maxillofacial surgery*, 8(1):42–50, 2018. 29963423[pmid].

[58] Ali Modabber, Helmut Galster, Florian Peters, Stephan Möhlhenrich, Kristian Kniha, Matthias Knobe, Frank Hölzle, and Alireza Ghassemi. Three-dimensional analysis of the ear morphology. *Aesthetic Plastic Surgery*, 42, Dec 2017.

[59] Andrew T. M. Phillips. Structural optimisation: biomechanics of the femur. *Proceedings of the Institution of Civil Engineers - Engineering and Computational Mechanics*, 165(2):147–154, 2012.

[60] Claire Villette and Andrew Phillips. Microscale poroelastic metamodel for efficient mesoscale bone remodelling simulations. *Biomechanics and Modeling in Mechanobiology*, 16:1–15, 12 2017.

[61] Claire Villette, J. Zhang, and Andrew Phillips. Influence of femoral external shape on internal architecture and fracture risk. *Biomechanics and Modeling in Mechanobiology*, 19, 08 2020.

[62] Ahmet Erdemir, Trent M. Guess, Jason Halloran, Srinivas C. Tadepalli, and Tina M. Morrison. Considerations for reporting finite element analysis studies in biomechanics. *Journal of Biomechanics*, 45(4):625–633, 2012.

[63] Dzung L. Pham, Chenyang Xu, and Jerry L. Prince. Current methods in medical image segmentation. *Annual Review of Biomedical Engineering*, 2(1):315–337, 2000. PMID: 11701515.

[64] W. Lee, L Goto, J.F.M. Molenbroek, and R.H.M. Goossens. Anlysis methods of the variation of facial size and shape based on 3d face scan images. *Proceedings of the Human Factors and Ergonomics Society Annual Meeting*, 61(1):1409–1413, 2017.

[65] Krittika Goyal, David A. Borkholder, and Steven W. Day. A biomimetic skin phantom for characterizing wearable electrodes in the low-frequency regime. *Sensors and Actuators A: Physical*, 340:113513, 2022.

[66] Hui Tong, Mingjue Wu, Jianqiang Han, Lin Li, and Haixia Zhang. A novel approach to fabricate early keratoconus phantom models. *Translational Vision Science Technology*, 14(4):18–18, 04 2025.

[67] M. F. Griffin, Y. Premakumar, A. M. Seifalian, M. Szarko, and P. E. M. Butler. Biomechanical characterisation of the human auricular cartilages; implications for tissue engineering. *Annals of Biomedical Engineering*, 44(12):3460–3467, Dec 2016.

[68] Stephen S. Park, Hong-Ryul Jin, David H. Chi, and Ray S. Taylor. Characteristics of tissue-engineered cartilage from human auricular chondrocytes. *Biomaterials*, 25(12):2363–2369, 2004.

[69] Aisling Ní Annaidh, Karine Bruyère, Michel Destrade, Michael D. Gilchrist, and Mélanie Otténio. Characterization of the anisotropic mechanical properties of excised human skin. *Journal of the Mechanical Behavior of Biomedical Materials*, 5(1):139–148, Jan 2012.

[70] M. F. Griffin, B. C. Leung, Y. Premakumar, M. Szarko, and P. E. Butler. Comparison of the mechanical properties of different skin sites for auricular and nasal reconstruction. *Journal of Otolaryngology - Head & Neck Surgery*, 46(1):33, Apr 2017.

[71] C. Jacquemoud, K. Bruyere-Garnier, and M. Coret. Methodology to determine failure characteristics of planar soft tissues using a dynamic tensile test. *Journal of Biomechanics*, 40(2):468–475, Jan 2007.

[72] Piyush Lakhani, Krashn K. Dwivedi, Atul Parashar, and Navin Kumar. Non-invasive in vivo quantification of directional dependent variation in mechanical properties for human skin. *Frontiers in Bioengineering and Biotechnology*, 9:979, 2021.

[73] G. Boyer, H. Zahouani, A. Le Bot, and L. Laquieze. In vivo characterization of viscoelastic properties of human skin using dynamic micro-indentation. pages 4584–4587, 2007.

[74] Matthew D. Parker, Lynette A. Jones, Ian W. Hunter, A. J. Taberner, M. P. Nash, and P. M. F. Nielsen. Multidirectional In Vivo Characterization of Skin Using Wiener Nonlinear Stochastic System Identification Techniques. *Journal of Biomechanical Engineering*, 139(1), 11 2016. 011004.

[75] M.B. Rubin and S.R. Bodner. A three-dimensional nonlinear model for dissipative response of soft tissue. *International Journal of Solids and Structures*, 39(19):5081–5099, 2002.

[76] Seyed Jamaleddin Mostafavi Yazdi and Javad Baqersad. Mechanical modeling and characterization of human skin: A review. *Journal of Biomechanics*, 130:110864, 2022.

[77] S. Diridollou, F. Patat, F. Gens, L. Vaillant, D. Black, J. M. Lagarde, Y. Gall, and M. Berson. In vivo model of the mechanical properties of the human skin under suction. *Skin Research and Technology*, 6(4):214–221, 2000.

[78] Emily J. Rayfield. Finite element analysis and understanding the biomechanics and evolution of living and fossil organisms. *Annual Review of Earth and Planetary Sciences*, 35(Volume 35, 2007):541–576, 2007.

[79] Shady A. Alshewaier, Mohamed Yacin Sikkandar, Ali Ahmed Ali Almakrami, S. Sabarunisha Begum, Ahmad Alassaf, Ibrahim AlMohimeed, S. Meenatchi Sundaram, Dheeraj Poojary, Natteri M. Sudharsan, and Eddie Y. K. Ng. Investigation of customized total knee implant with articular cartilage under loading conditions using finite element analysis. *PLOS ONE*, 20(2):1–27, 02 2025.

[80] Litao Jia, Siyu Liu, Luosha Gu, Xiaomin Liu, Kexin Sun, Feiyang Chu, Jinshi Zeng, Wenshuai Liu, Haiyue Jiang, and Xia Liu. Integrated biomimetic bioprinting of perichondrium with cartilage for auricle reconstruction. *Bioactive Materials*, 48:100–117, 2025.

[81] J. Zhong, S. Chen, Y. Zhao, J. Yin, Y. Wang, H. Gong, X. Zhang, J. Wang, Y. Wu, and W. Huang. Shape optimization of costal cartilage framework fabrication based on finite element analysis for reducing incidence of auricular reconstruction complications. *Frontiers in Bioengineering and Biotechnology*, 9:766599, dec 2021.

[82] Matthieu Chabanas and Yohan Payan. A 3d finite element model of the face for simulation in plastic and maxillo-facial surgery, 2006.

[83] Yang Wenxiu, Haining Wang, and He Renke. Establishment of a finite element model based on craniofacial soft tissue thickness measurements and stress analysis of medical goggles. *Ergonomics*, 65:1–38, 07 2021.

[84] Yan Yan, Yonghong Liu, and Haining Wang. An earphone fit deviation analysis algorithm. *Scientific Reports*, 13(1):1084, jan 2023.

[85] S. Benacchio, Olivier Doutres, Arnaud le troter, Arthur Varoquaux, Eric Wagnac, Virginie Callot, and Franck Sgard. Estimation of the ear canal displacement field due to in-ear device insertion using a registration method on a human-like artificial ear. *Hearing Research*, 365, 06 2018.

[86] Wonsup Lee, Jin-Gyun Kim, Johan Molenbroek, Richard Goossens, Hayoung Jung, and Heecheon You. Contact pressure analysis for wearable product design. 08 2018.

[87] Hsiao-Ping Chiu, Hsin-Yu Chiang, Liu Chien-Hsiou, Ming-Hsu Wang, and Wen-Ko Chiou. Surveying the comfort perception of the ergonomic design of bluetooth earphones. *Work (Reading, Mass.)*, 49, 09 2013.

[88] Mazlan Rafidah, L Saim, A Thomas, R Said, and B Liyab. Ear infection and hearing loss amongst headphone users. *The Malaysian journal of medical sciences : MJMS*, 9:17–22, 07 2002.

[89] Abdullah A. Alarfaj, Lujain M. AlAhmmed, and Sayed Ibrahim Ali. Perception of earbuds side effects among teenager and adults in eastern province of saudi arabia: A cross sectional study. *Clinical Epidemiology and Global Health*, 12:100784, 2021.

[90] Chenyu Tang, Zhenyu Xu, Edoardo Occhipinti, Wentian Yi, Muzi Xu, Sanjeev Kumar, Gurvinder S. Virk, Shuo Gao, and Luigi G. Occhipinti. From brain to movement: Wearables-based motion intention prediction across the human nervous system. *Nano Energy*, 115:108712, 2023.

[91] Alessandra Giangrande, Alberto Botter, Harri Piitulainen, and Giacinto Luigi Cerone. Motion artifacts in dynamic eeg recordings: Experimental observations, electrical modelling, and design considerations. *Sensors*, 24(19), 2024.

[92] J. Y. Choi, S. Jeon, H. Kim, J. Ha, G. S. Jeon, J. Lee, and S. I. Cho. Health-related indicators measured using earable devices: Systematic review. *JMIR mHealth and uHealth*, 10(11):e36696, nov 2022.

[93] Hiroyuki Manabe, Masaaki Fukumoto, and Tohru Yagi. Conductive rubber electrodes for earphone-based eye gesture input interface. volume 19, pages 33–40, 09 2013.

[94] O. Valentin, G. Viallet, A. Delnavaz, G. Cretot-Richert, M. Ducharme, H. Monsarat-Chanon, and J. Voix. Custom-fitted in- and around-the-ear sensors for unobtrusive and on-the-go eeg acquisitions: Development and validation. *Sensors (Basel)*, 21(9):2953, apr 2021.

[95] M. Schmoigl-Tonis, C. Schranz, and G. R. Müller-Putz. Methods for motion artifact reduction in online brain-computer interface experiments: a systematic review. *Frontiers in Human Neuroscience*, 17:1251690, oct 2023.

[96] Hritwick Banerjee, Zion Tsz Ho Tse, and Hongliang Ren. Soft robotics with compliance and adaptation for biomedical applications and forthcoming challenges. *International Journal of Robotics and Automation*, 33(1):69–80, 2018.

[97] Juana-Mariel Dávila-Vilchis, LAZ-Avilés, Juan Carlos Ávila Vilchis, and Adriana H. Vilchis-González. Design methodology for soft wearable devices—the mosar case. *Applied Sciences*, 9(22), 2019.

[98] Ghayth Almahadin, Ahmad Lotfi, Eva Zysk, Francesco Siena, Marie Mc Carthy, and Philip Breedon. Parkinson's disease: current assessment methods and wearable devices for evaluation of movement disorder motor symptoms - a patient and healthcare professional perspective. *BMC Neurology*, 20, 11 2020.

[99] Filip Hrncirik, Iwan V. Roberts, Chloe Swords, Peter J. Christopher, Akil Chhabu, Andrew H. Gee, and Manohar L. Bance. Impact of scala tympani geometry on insertion forces during implantation. *Biosensors*, 12(11), 2022.

[100] F.M. Hendriks, Dirk Brokken, Johan van Eemeren, Cees Oomens, Frank Baaijens, and J Horsten. A numerical-experimental method to characterize the non-linear behaviour of human skin. *Skin research and technology : official journal of International Society for Bioengineering and the Skin (ISBS) [and] International Society for Digital Imaging of Skin (ISDIS) [and] International Society for Skin Imaging (ISSI)*, 9:274–83, 09 2003.

[101] R. W. Ogden. Large deformation isotropic elasticity–on the correlation of theory and experiment for incompressible rubberlike solids. *Proceedings of the Royal Society of London. A. Mathematical and Physical Sciences*, 326(1567):565–584, 1972.

[102] Stephan A. Brinckmann, Jason C. Young, Ray S. Fertig, and Carl P. Frick. Effect of print direction on mechanical properties of 3d printed polymer-derived ceramics and their precursors. *Materials Letters: X*, 17:100179, 2023.

[103] Stephen P. Timoshenko and James M. Gere. *Theory of Elastic Stability*. McGraw-Hill, New York, 2nd edition, 1961.

[104] H. (Haiyan) Hu. *Vibration mechanics : a research-oriented tutorial / Haiyan Hu.* 2022.

[105] Graham M. Treece. Stradview software, version 7.0. University of Cambridge, U.K.; https://mi.eng.cam.ac.uk/Main/StradView (accessed 10 March 2024), 2025.

[106] U.S. National Library of Medicine. The visible human project. https://lhncbc.nlm.nih.gov/project/visible-human-project, 1994. Accessed on 5 June 2024.

[107] Paolo Cignoni, Marco Callieri, Massimiliano Corsini, Matteo Dellepiane, Fabio Ganovelli, and Roberto Scopigno. Meshlab: an open-source mesh processing tool. *Eurographics Italian Chapter Conference*, pages 129–136, 2008.

[108] Christophe Geuzaine and Jean-François Remacle. Gmsh: A 3-d finite element mesh generator with built-in pre- and post-processing facilities. *International Journal for Numerical Methods in Engineering*, 79(11):1309–1331, 2009.

[109] Fabian Brinkmann, Manoj Dinakaran, Robert Pelzer, Peter Grosche, Daniel Voss, and Stefan Weinzierl. A cross-evaluated database of measured and simulated hrtfs including 3d head meshes, anthropometric features, and headphone impulse responses. *Journal of the Audio Engineering Society*, 2019.

[110] Lorna J. Gibson and M. F. Ashby. *Cellular Solids: Structure and Properties*. Cambridge University Press, Cambridge, UK, 2nd edition, 1999. Discusses mechanical behaviour of sandwich beams and cellular solids.

[111] Yin Yao, Shaohua Chen, and Zhuping Huang. A generalized ogden model for the compressibility of rubber-like materials. *Philosophical Transactions of the Royal Society A*, 380(2242):20210320, 2022.

[112] N. H. Scott. The incremental bulk modulus, young's modulus and poisson's ratio in nonlinear isotropic elasticity: physically reasonable response. *arXiv preprint arXiv:2005.04212*, 2020. preprint.

[113] M. Smulders, L.N.M. van Dijk, Y. Song, P. Vink, and T. Huysmans. Dense 3d pressure discomfort threshold (pdt) map of the human head, face and neck: A new method for mapping human sensitivity. *Applied Ergonomics*, 107:103919, 2023.

[114] Jose Humberto Trueba, Francesca Gasparini, and José de Jesús Agustín Flores Cuautle. Pressure pain threshold values obtained through algometers. *Revista Mexicana de Ingenieria Biomedica*, 42(2):132–148, Aug. 2021.

[115] Jian Wu, Yuxing Ma, Xuanyi Ong, Yifeng Zhao, Wei Ng, Peng Zhang, Kai Li, Boon Hoong Yeow, and Benjamin Chee Kee Tee. A skin-inspired tactile sensor for smart prosthetics. *Science Robotics*, 3(19):eaat0429, 2018.

[116] Joel D. Greenspan and Susan L. B. McGillis. Thresholds for the perception of pressure, sharpness, and mechanically evoked cutaneous pain: effects of probe size and repeated testing. *Somatosensory & Motor Research*, 11(6):467–484, 1994.

[117] Ruben Sarabia-Riquelme, Warren C. Schimpf, Danielle L. Kuhn, and Matthew C. Weisenberger. Influence of relative humidity on the structure, swelling and electrical conductivity of pedot:pss fibers. *Synthetic Metals*, 297:117399, 2023.

[118] Miklós Hetényi. *Beams on Elastic Foundation: Theory with Applications in the Fields of Civil and Mechanical Engineering*, volume XVI of *University of Michigan Studies. Scientific Series*. University of Michigan Press, Ann Arbor, 1946.

[119] D. Johnson and R. Johnson. Motivational processes in cooperative, competitive and individualistic learning situations. In C. Ames and R. Ames, editors, *Research on Motivation in Education, Vol. 2*, pages 249–286. Academic Press, New York, 1985.

[120] S. Abasi, J. Smith, and M. Khan. Bioelectrical impedance spectroscopy for monitoring biological tissue properties. *ACS Measurement Science Au*, 2(4):789–800, 2022.

[121] B. C. Fortune, A. Lee, and R. Johnson. Electrode–skin impedance imbalance and its impact on eeg data quality at 50 hz. *Journal of Neural Engineering*, 18(6):066017, 2021.

[122] P. Zhang et al. On the spreading resistance of thin-film contacts. *IEEE Transactions on Electron Devices*, 59(8):1937–1944, 2012.

Appendix A

Fabrication Detail of Realistic Auricle Phantom

To support the development of the finite element (FE) model of the auricle, a physical phantom exhibiting comparable mechanical behaviour to human tissue was fabricated. Such a phantom enables rapid visualisation of deformation modes and contact regions under loading, complementing simulation results. Building upon the initial prototype presented in Chapter 3, further work was undertaken to improve the anatomical realism and structural fidelity of the auricle phantom.

Simplified Phantom Fabrication

The initial auricle phantom was fabricated using a Formlabs Form 3B 3D printer (Formlabs, USA) and a soft, elastic photopolymer resin (Elastic 50A; Formlabs, USA). The skin layer was cast using a two-part silicone compound (Silastic 3481 RTV Silicone Moulding Rubber; East Coast Fibreglass Supplies, UK), mixed at a ratio of 10:1 with its curing agent. The mixture was injected into a mould box as described in Chapter 3. Figure A.1 shows the assembly of an early mould box configuration, clamped together to achieve proper layer alignment and infill.

During this stage, it proved difficult to observe the internal filling process of the silicone layer, often resulting in trapped air and incomplete infill. To address this issue, a later version of the mould box was fabricated from transparent material to improve visibility during injection,

as shown in Figure A.2. This modification allowed real-time observation of the silicone flow and better control of layer thickness and interface uniformity.

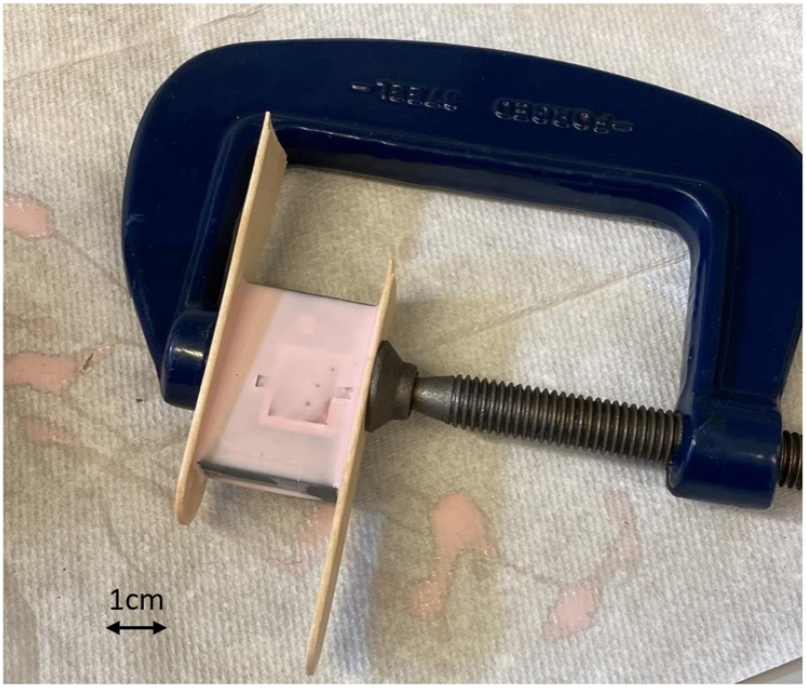


Fig. A.1 Assembly of the initial mould box for the simplified auricle phantom.



Fig. A.2 Transparent mould box used for improved visual control of silicone filling.

Realistic Phantom Fabrication

To produce a more realistic auricle phantom, two softer silicone gels were evaluated for the skin layer to better approximate the compliance of human tissue. These materials, clear Ecoflex^{TM} 00-30 and pink Mold Max^{TM} 10 (Smooth-On Inc., USA), were selected for their low Shore hardness and ease of moulding. The internal cartilage core was again fabricated using Elastic 50A resin, but with a modified UV-curing protocol to achieve more skin-like elasticity.

As the thickness of the skin layer decreased, the use of a rigid mould box led to frequent tearing, as the thin silicone layer adhered more strongly to the surface of the mould than to the inner cartilage structure (Figure A.3). Multiple iterations using inverted silicone moulds were attempted, but these methods still yielded low success rates and recurrent ruptures.

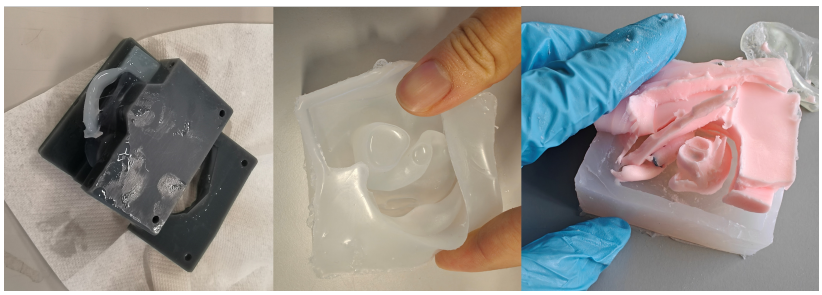


Fig. A.3 Demonstration of failed mould box and ruptured phantoms, with attempts using both Ecoflex^{TM} 00-30 and Mold Max^{TM} 10

To overcome this limitation, a water-soluble mould box was developed using polyvinyl alcohol (PVA), which can be dissolved in water after curing. This approach enabled non-destructive demoulding and preserved delicate auricular features. The resulting phantom, shown in Figure 3.23(b) and discussed in Section 3.6, achieved a more anatomically faithful geometry and realistic mechanical compliance suitable for experimental validation and device–skin contact analysis.

Appendix B

Beam Bending Model for Auricular Deformation

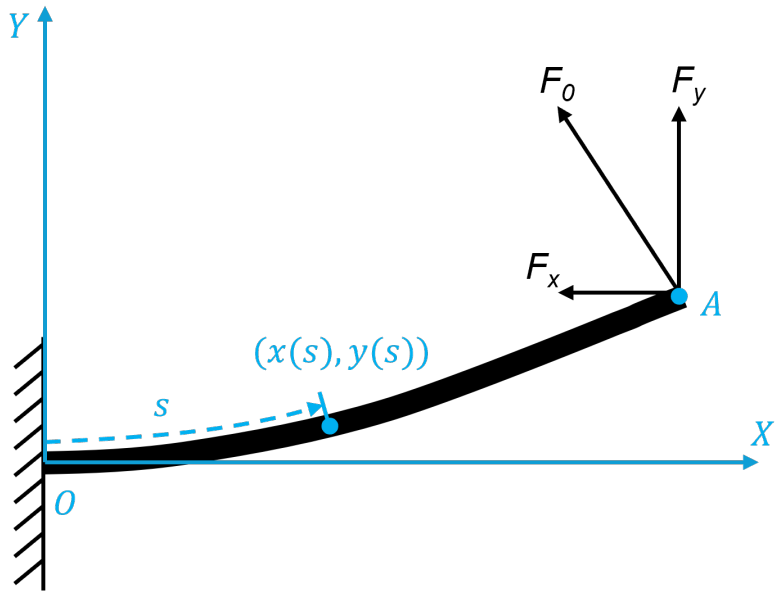


Fig. B.1 A straight beam subjected to end loading.

The governing moment–curvature relationship for a beam is given by:

$$EI\kappa = M$$

where E is the Young's modulus of the material, I is the second moment of area (also referred to as the area moment of inertia), κ is the curvature of the beam, and M is the bending moment. The product EI represents the flexural rigidity of the beam.

Under the assumption of small deflection, the curvature of the beam can be approximated by the second derivative of the transverse displacement $w(x)$ with respect to the axial coordinate x:

$$\kappa = \frac{d\theta}{ds} \approx \frac{d^2w}{dx^2}$$

Here, θ denotes the local rotation angle of the beam's cross-section, and s is the arc length along the deformed beam. The differential relationship between arc length and axial position is:

$$ds = \sqrt{1 + \left(\frac{dw}{dx}\right)^2}\, dx$$

This geometrically nonlinear formulation becomes necessary when the beam experiences large deflections, as may occur during auricular deformation under anterior traction. In the classical Euler–Bernoulli beam theory, shear deformation is neglected and the simplification $M(x) = EI\frac{d^2w}{dx^2}$ is valid only for small displacements. However, for large deflections, this assumption no longer holds, and the full nonlinear form must be retained:

$$M(s) = EI\frac{d\theta}{ds}$$

In the beam-end bending illustrated in Figure D.10, the bending moment at any point along s is given by:

$$EI\frac{d\theta}{ds} = M(s) = F_y[x(L) - x(s)] + F_x[y(L) - y(s)]$$

where F_x and F_y are the horizontal and vertical components of the applied force, and $x(s)$ and $y(s)$ define the coordinates of the deformed beam along its arc length. The terms $x(L)$ and $y(L)$ correspond to the coordinates at the free end of the beam.

Differentiating the above expression yields the following second-order nonlinear differential equation:

$$\frac{d^2\theta}{ds^2} = -\frac{F_y}{EI}\cos\theta(s) - \frac{F_x}{EI}\sin\theta(s)$$

This defines a boundary value problem (BVP) with boundary conditions:

$$\theta(0) = 0 \quad \text{(fixed end)}, \qquad \frac{d\theta}{ds}(L) = 0 \quad \text{(free end)}.$$

The BVP system can thus be expressed as:

$$\begin{aligned} &\text{Differential equation:} \quad \frac{d^2\theta}{ds^2} = -\frac{F_y}{EI}\cos\theta(s) - \frac{F_x}{EI}\sin\theta(s), \\ &\text{Boundary conditions:} \quad \theta(0) = 0, \quad \frac{d\theta}{ds}(L) = 0. \end{aligned}$$

Once $\theta(s)$ is obtained, the spatial configuration of the deformed beam can be reconstructed from the geometric relations:

$$\frac{dx}{ds}(s) = \cos\theta(s), \qquad \frac{dy}{ds}(s) = \sin\theta(s)$$

This modelling framework enables simulation of auricular deformation under experimentally relevant loading conditions. It forms the analytical basis for computational tools developed in this study to optimise loading direction, evaluate structural response, and ensure mechanical consistency across test participants.

Using the BVP system described above, a MATLAB script was developed to simulate the deformation behaviour of a beam under various loading configurations. To approximate the mechanical response of the human auricle, the beam was assigned representative material and geometric properties: a Young's modulus $E = 0.8$ MPa, a cross-sectional width and height of 1 cm, and a total length of 10 cm. A bending force of 0.12 N was applied at the free end of the beam to evaluate displacement and stress distribution. These values are not exact anatomical measures but were selected to provide a tractable yet physiologically relevant estimate of auricular mechanics within the simplified beam framework.

Appendix C

Volunteer Experiment Materials

Volunteer Information Sheet

UNIVERSITY OF CAMBRIDGE
Department of Engineering

29/05/2023

Auricle Mechanics Study – Participant Info

Invitation

Before you decide to take part in this study it is important for you to understand why the research is being done and what it will involve. Please take time to read the following information carefully and discuss it with others if you wish. A member of the team can be contacted if there is anything that is not clear or if you would like more information. Take time to decide whether or not you wish to take part.

Purpose

We are developing an 'Earable' (wearable on ear device) that can house skin electrodes for neural interfacing. This specific application has a high requirement for the mechanical contact between the device and the user's skin. Hence it is important to study the mechanical properties of the human auricle to understand how to design the 'Earable' for better comfort and signal reliability.

We need to collect the mechanical response of human auricles under static and dynamic loading to model the auricle structural properties. With these data, we can construct an auricle model that can be used to facilitate the 'Earable' design.

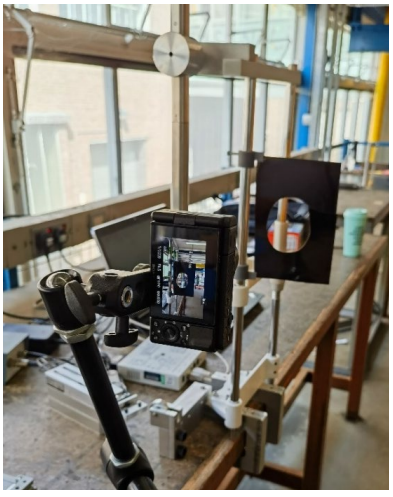
Why have I been chosen?

As an adult age between 18-65, without any auricle or other relevant disorder, you have the ability to provide useful samples.

Do I have to take part?

Taking part is entirely voluntary and refusal or withdrawal will involve no penalty or loss, now or in the future.

What will happen to me if I take part?



You will be sat on a chair in front of a chin rest. You will be asked to put your head on the chin rest at your most comfortable height and position for the rest of the experiment. At least one researcher will be present to run the protocol. The researcher will help to adjust the device to fit your height.

Your ear will be attached to the test device which involves a stepper motor on the desk, a load cell, and a set of trolley systems. A cover will be placed beside your head to make sure your face and other visual identifiable characteristics will not be recorded by the camera system.

Your ear will be tested with 2 sets of experiments, auricle pulling and release tests. The complete session will last approximately 30 minutes.

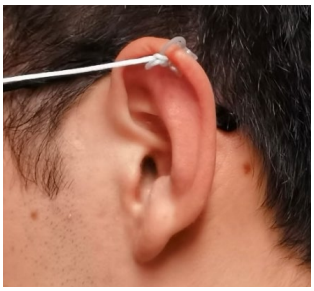
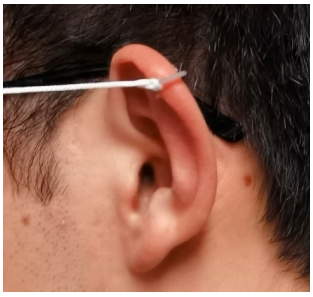
UNIVERSITY OF CAMBRIDGE
Department of Engineering

29/05/2023



Attached herewith is an image depicting the ear clips equipped with soft pads. These clips have been fabricated using 3D printing. The contact end of the clip is covered with elastic and bio-compatible pads. It should be noted that the clip is intentionally designed to possess a degree of flexibility, thereby preventing the application of excessive pressure.

Below, a visual representation illustrates the process by which the device pulls the ear. The device ensures that the range of deformation of the auricle is maintained within a safe and comfortable threshold throughout the procedure.


For safety purposes, it is required that the operator should immediately cease the test if the subject experiences any discomfort. If the stepper motor becomes stuck, the operator must manually stop the pulling and release the ear clip immediately.

The data will be saved with basic information of the test subject without identifiable imformations. These data may need to be uploaded if requested by a potential journal when publishing our work. They will be archived in a secure computer or locked file for 7 years.

Are there possible disadvantages and/or risks in taking part?

The experiment session will use a chin rest which is made of metal to held the participant's head in place. The participants may have allergic response to the alloy used in the chin rest. The mechanism used to test auricle properties may cause discomfort and numbness. You can terminate the experiment at any time during the session.

Will my taking part in this project be kept confidential?

All information you provide as part of the project will be kept strictly confidential. All collected data will be identified only by a code, with personal details kept in a locked file or secure computer with access only by the immediate research team.

More information about the legal basis under which we collect and process your data is found at this link: https://www.information-compliance.admin.cam.ac.uk/data-protection/research-participant-data

Additionally, more general information can be found at this link: https://www.information-compliance.admin.cam.ac.uk/data-protection

UNIVERSITY OF CAMBRIDGE
Department of Engineering

29/05/2023

What will happen to the results of the research project?

Results will be presented at conferences and written up in journals. Results are normally presented in terms of groups of individuals. If any individual data are presented, the data will be totally anonymous, without any means of identifying the individuals involved. There is a chance that the audio and mouth movement data will be reused in future for additional research.

Who is organising and funding the research?

The researchers are all affiliated with the University of Cambridge. Yunpeng Li is completing a PhD funded by the W D Armstrong Trust at the Department of Engineering.

Contact for further information

Yunpeng Li, email at yl804@cam.ac.uk.

UNIVERSITY OF CAMBRIDGE
Department of Engineering

20/01/2025

Electrode Contact Study – Participant Info

Invitation

Before you decide to take part in this study it is important for you to understand why the research is being done and what it will involve. Please take time to read the following information carefully and discuss it with others if you wish. A member of the team can be contacted if there is anything that is not clear or if you would like more information. Take time to decide whether you wish to take part.

Purpose

The electrode contact study is part of the Earable design project. As the Earable device aims to build high performance wearable neural interface, the contact between the skin and electrodes is crucial. This study aims to understand how the electrode-skin impedance would vary with pressure applied on the skin.

The experiment will be using a stepper motor system developed for displacement and force measurement. The stepper motor system will be deployed on a desk with test electrode on its front side. During the test, the skin around the ear of the experimenter will be in contact with the electrode. The electrodes are connected to a potentiostat for impedance measurement.

Why have I been chosen?

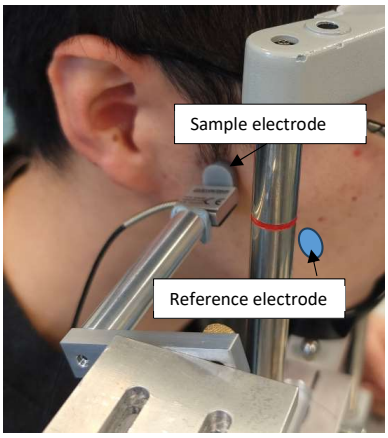
As an adult age between 18-65, without any auricle or other relevant disorder, you have the ability to provide useful samples.

Do I have to take part?

Taking part is entirely voluntary and refusal or withdrawal will involve no penalty or loss, now or in the future.

What will happen to me if I take part?

You will be sitting on a chair in front of the experiment system. As shown on the picture on the right, 2 electrodes will be placed on your head to measure the skin impedance level at different pressure levels. As illustrated on the right, the electrode is placed around the ear.

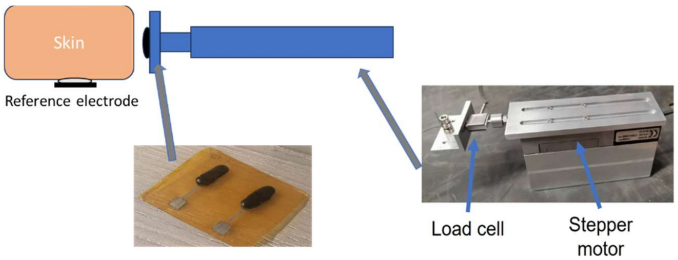


As the experiment starts, you will be asked to sit still on a head rest. During the test, you will be asked to sit on a chin rest and having the zygomatic region (the skin in front of the ear) cleaned for the experiment. A motor with electrode will be adjusted to contact with your skin and start the same test.

UNIVERSITY OF CAMBRIDGE
Department of Engineering

20/01/2025

An Illustration of the system can be seen below.



The stepper motor is controlled by a computer program to push the electrode on the skin with a controlled move. This motor can apply different pressure on the skin to measure the effect of electrode impedance with interface pressure.

For safety purposes, it is required that the operator should immediately cease the test if the subject experiences any discomfort. If the stepper motor becomes stuck, the operator must manually stop the pulling and release stepper motor immediately.

The data will be saved with basic information of the test subject without identifiable imformations. These data may need to be uploaded if requested by a potential journal when publishing our work. They will be archived in a secure computer or locked file for 7 years.

Are there possible disadvantages and/or risks in taking part?

The mechanism used to test auricle properties may cause discomfort and numbness. You can terminate the experiment at any time during the session.

Will my taking part in this project be kept confidential?

All information you provide as part of the project will be kept strictly confidential. All collected data will be identified only by a code, with personal details kept in a locked file or secure computer with access only by the immediate research team.

More information about the legal basis under which we collect and process your data is found at this link: https://www.information-compliance.admin.cam.ac.uk/data-protection/research-participant-data

Additionally, more general information can be found at this link: https://www.information-compliance.admin.cam.ac.uk/data-protection

What will happen to the results of the research project?

Results will be presented at conferences and written up in journals. Results are normally presented in terms of groups of individuals. If any individual data are presented, the data will be totally anonymous, without any means of identifying the individuals involved. There is a chance that the audio and mouth movement data will be reused in future for additional research.

UNIVERSITY OF CAMBRIDGE
Department of Engineering

20/01/2025

Who is organising and funding the research?

The researchers are all affiliated with the University of Cambridge. Yunpeng Li is completing a PhD funded by the W D Armstrong Trust at the Department of Engineering.

Contact for further information

Yunpeng Li, email at yl804@cam.ac.uk.

Volunteer Consent Form

UNIVERSITY OF CAMBRIDGE
Department of Engineering

Consent Form for Auricle Mechanics Study

Please tick the appropriate boxes	**Yes**	**No**
Taking Part		
I have read and understood the project information sheet dated 29/05/2023.	☐	☐
I have been given the opportunity to ask questions about the project.	☐	☐
I agree to take part in the project. Taking part in the project may include being interviewed and recorded (audio or video).	☐	☐
I understand that my taking part is voluntary; I can withdraw from the study at any time and I do not have to give any reasons for why I no longer want to take part.	☐	☐
Use of the information I provide for this project only		
I understand my personal details such as phone number and address will not be revealed to people outside the project.	☐	☐
I understand that my words may be quoted in publications, reports, web pages, and other research outputs.	☐	☐
Use of the information I provide beyond this project		
I agree for the data I provide to be archived in anonymous form in an open data repository for use in further research not related to this project.	☐	☐
I understand that other authenticated researchers will have access to this data only if they agree to preserve the confidentiality of the information as requested in this form.	☐	☐
I understand that other authenticated researchers may use my words in publications, reports, web pages, and other research outputs, only if they agree to preserve the confidentiality of the information as requested in this form.	☐	☐
So we can use the information you provide legally		
I agree to assign the copyright I hold in any materials related to this project to Yunpeng Li.	☐	☐

_____	_____	_____
Name of participant [printed]	Signature	Date
_____	_____	_____
Researcher [printed]	Signature	Date

Project contact details for further information:

Yunpeng Li, Department of Engineering, University of Cambridge, yl804@cam.ac.uk

UNIVERSITY OF CAMBRIDGE
Department of Engineering

Consent Form for Electrode Contact Study

Please tick the appropriate boxes	**Yes**	**No**
Taking Part		
I have read and understood the project information sheet dated 20/01/2025.	☐	☐
I have been given the opportunity to ask questions about the project.	☐	☐
I agree to take part in the project. Taking part in the project may include being interviewed and recorded (audio or video).	☐	☐
I understand that my taking part is voluntary; I can withdraw from the study at any time and I do not have to give any reasons for why I no longer want to take part.	☐	☐
Use of the information I provide for this project only I understand my personal details such as phone number and address will not be revealed to people outside the project.	☐	☐
I understand that my words may be quoted in publications, reports, web pages, and other research outputs.	☐	☐
Use of the information I provide beyond this project I agree for the data I provide to be archived in anonymous form in an open data repository for use in further research not related to this project.	☐	☐
I understand that other authenticated researchers will have access to this data only if they agree to preserve the confidentiality of the information as requested in this form.	☐	☐
I understand that other authenticated researchers may use my words in publications, reports, web pages, and other research outputs, only if they agree to preserve the confidentiality of the information as requested in this form.	☐	☐
So we can use the information you provide legally I agree to assign the copyright I hold in any materials related to this project to Yunpeng Li.	☐	☐

_____		_____	_____
Name of participant	[printed]	Signature	Date
_____		_____	_____
Researcher	[printed]	Signature	Date

Project contact details for further information:

Yunpeng Li, Department of Engineering, University of Cambridge, yl804@cam.ac.uk

Ethics Approval Letter



UNIVERSITY OF CAMBRIDGE
Department of Engineering

Dr Robert Phaal
Chairman of the Ethics
Review Committee

Yunpeng Li

Division C

08 Jun 2023

Dear Yunpeng Li,

Ethical Approval for your Research Project: 'Volunteer Recruitment for Auricle Mechanics Study'

The Department's Research Ethics Committee has considered the documentation you provided in support of your research project in line with recommended procedures concerning ethical approval of research.

I am able to inform you that, with respect to ethical considerations, approval has been given to your project. Please note that this approval is based on the documentation you provided. You must re-submit your application to the Committee should you subsequently make any substantive changes relating to matters reviewed by the Committee.

We are content for this letter to be forwarded to your grant sponsors or to any partner institutions you may be working with if appropriate.

Yours sincerely

[Signature redacted]

Robert Phaal

Department of Engineering
University of Cambridge
Trumpington Street
Cambridge CB2 1PZ
[Email address redacted]

UNIVERSITY OF CAMBRIDGE
Department of Engineering

Dr Robert Phaal
Chairman of the Ethics
Review Committee

Yunpeng Li

Division C

27 Jan 2025

Dear Yunpeng Li,

Ethical Approval for your Research Project: 'Electrode contact experiment for head skin' (application no 583)

The Department's Research Ethics Committee has considered the documentation you provided in support of your research project in line with recommended procedures concerning ethical approval of research.

I am able to inform you that, with respect to ethical considerations, approval has been given to your project. Please note that this approval is based on the documentation you provided. You must re-submit your application to the Committee should you subsequently make any substantive changes relating to matters reviewed by the Committee.

We are content for this letter to be forwarded to your grant sponsors or to any partner institutions you may be working with if appropriate.

Yours sincerely

[Signature redacted]

Robert Phaal

Department of Engineering
University of Cambridge
Trumpington Street
Cambridge CB2 1PZ
[Email address redacted]

Appendix D

Auricle Model Presentation

To present details about the 5 auricle models used in the FEA in Chapter 5, figures on their outlook and intersections are presented in this appendix.

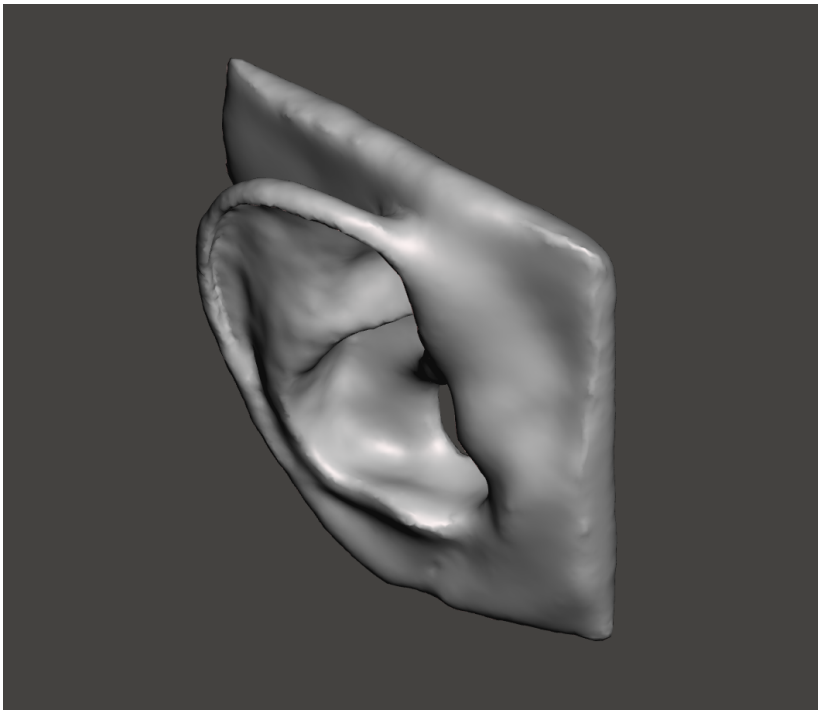


Fig. D.1 The CT-scanned auricle model outlook.

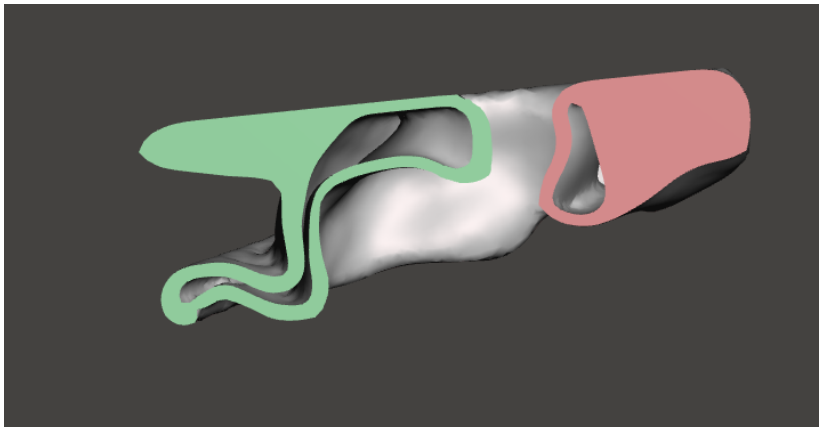


Fig. D.2 The CT-scanned auricle model cross section on transverse plane.

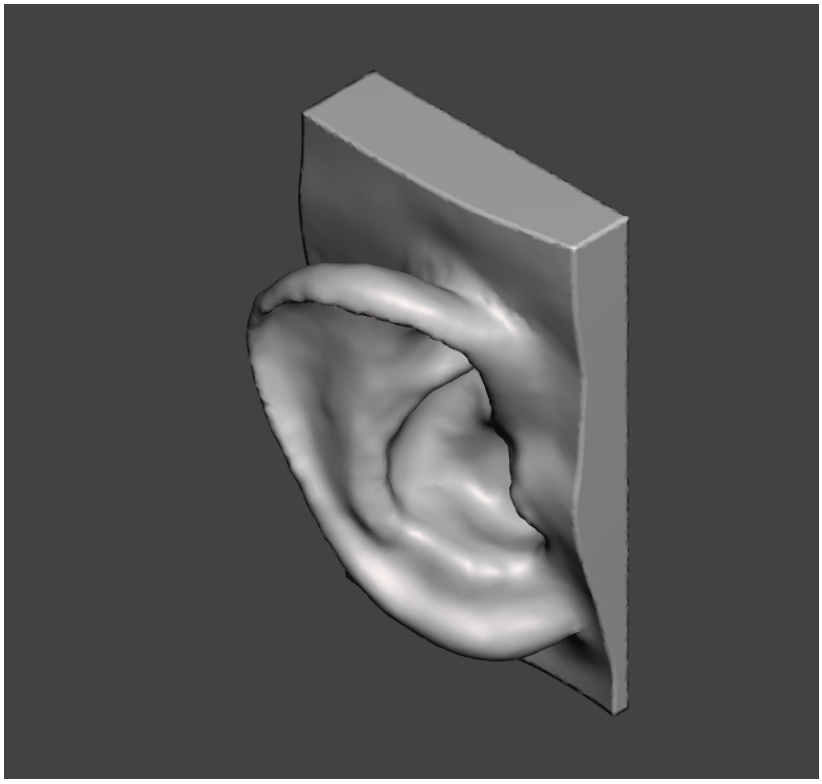


Fig. D.3 The database SHORT auricle model outlook.

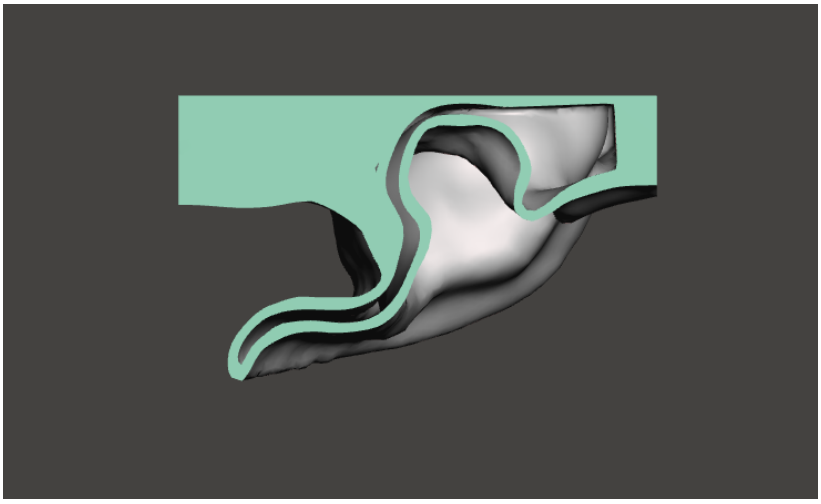


Fig. D.4 The database SHORT auricle model cross section on transverse plane.

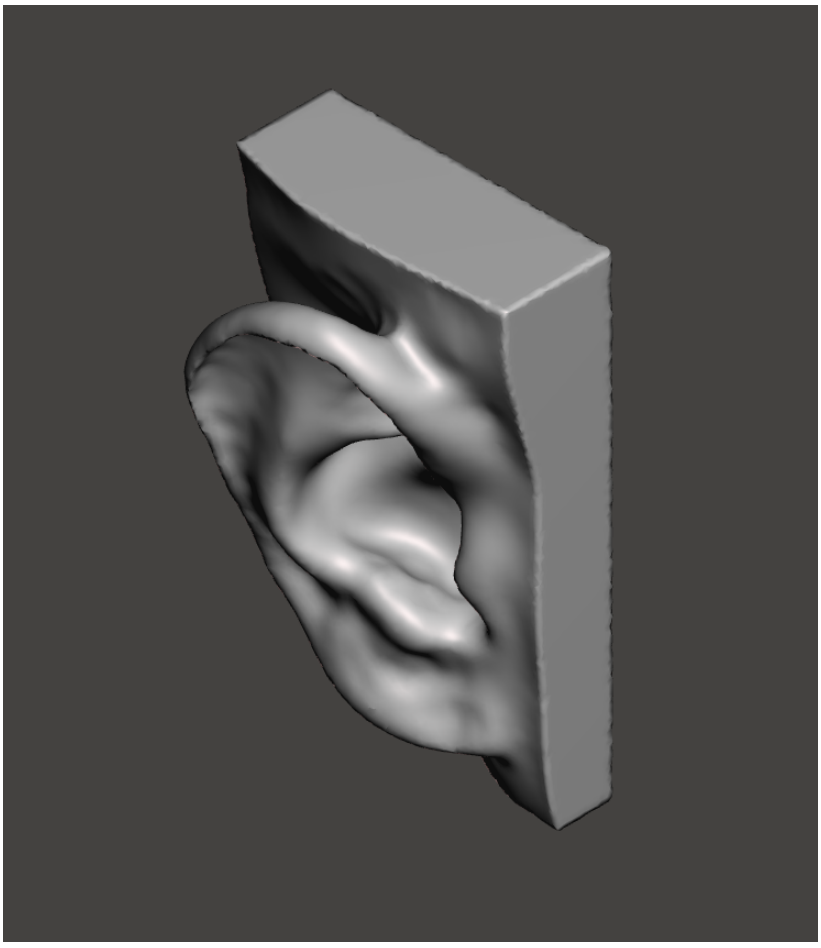


Fig. D.5 The database THICK auricle model outlook.

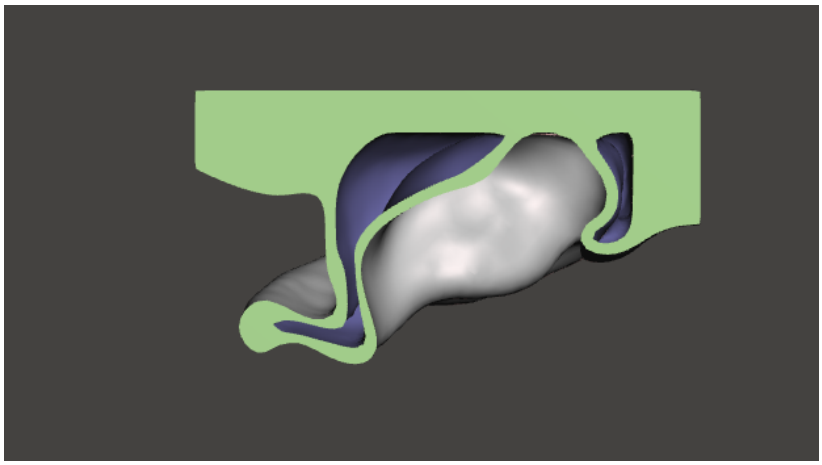


Fig. D.6 The database THICK auricle model cross section on transverse plane.

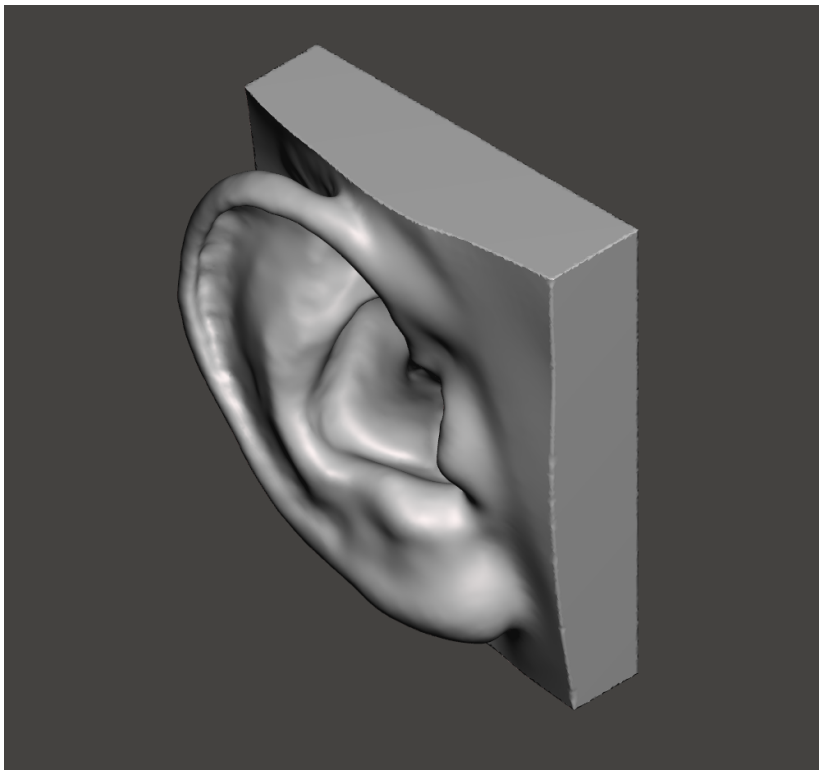


Fig. D.7 The database LONG auricle model outlook.

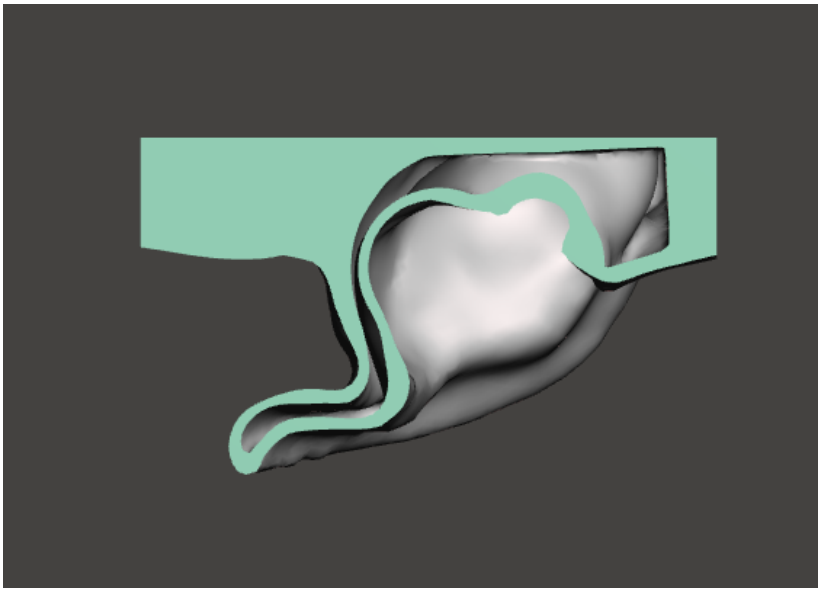


Fig. D.8 The database LONG auricle model cross section on transverse plane.

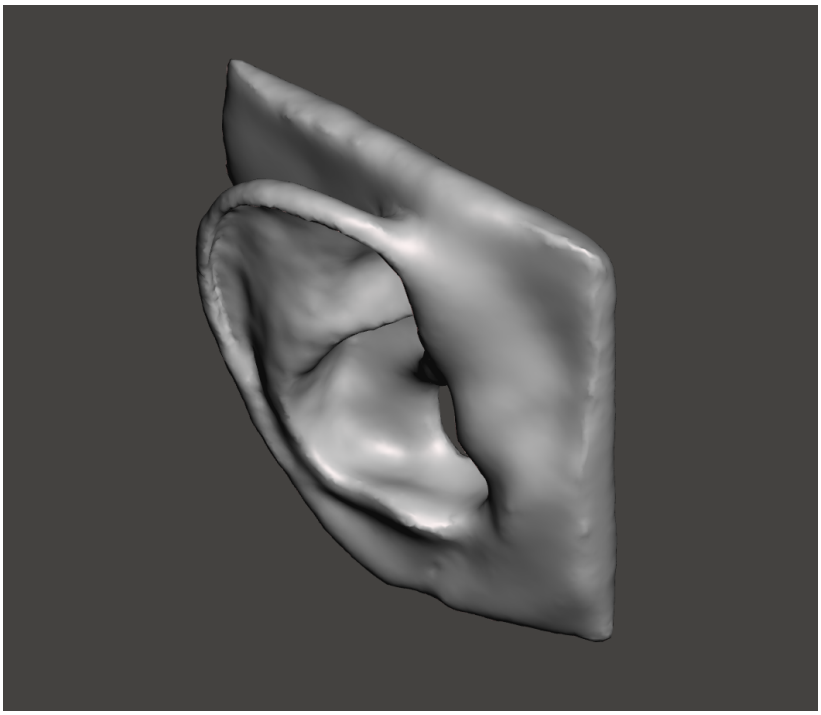


Fig. D.9 The CT-scanned auricle with thicker cartilage model outlook.

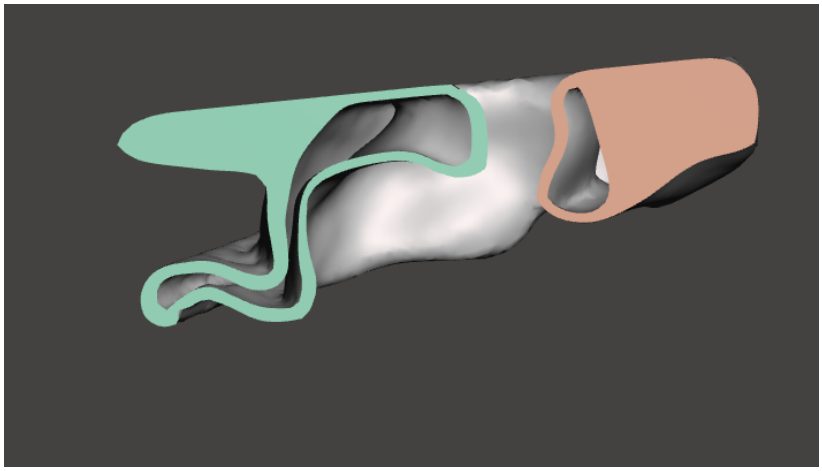


Fig. D.10 The CT-scanned auricle with thicker cartilage model cross section on transverse plane.

Appendix E

Detail FEA Report

FEA setup in Abaqus

The main simulation conducted are listed with their Abaqus .inp file setup lines copied.

Auricle Phantom Mechanics Test (Chapter 3.5)

The following excerpt shows the representative input file used to replicate the mechanical testing procedure applied to the physical auricle phantom. The simulation consisted of a quasi-static step followed by a dynamic step. The static step simulated the controlled displacement loading, while the dynamic step allowed for transient response assessment.

Part of the Abaqus input script is listed below. Minor numerical parameters such as time increments or output frequency were adjusted during different trials, but the overall setup remained the same.

```
** MATERIALS
**
*Material, name=cart
*Damping, alpha=0.004, beta=0.001
*Density
 0.0012,
*Elastic
 3.35e+06, 0.4

*Material, name=skin
```

```
*Damping, alpha=0.004, beta=0.001
*Density
 0.0008,
*Elastic
 420000., 0.45

** ----------------------------------------------------------------
** STEP 1: Static analysis
*Step, name=Step-1, nlgeom=YES, inc=1000000
*Static
0.001, 1., 1e-08, 1.

** Boundary conditions
*Boundary
Base, ENCASTRE
*Boundary
pulling, 1, 1, -13.
pulling, 2, 2
pulling, 3, 3

** Loads
*Dload
, GRAV, 9.8, 1., 0., 0.



** ----------------------------------------------------------------
** STEP 2: Dynamic response
*Step, name=Step-2, nlgeom=YES, inc=1000000
*Dynamic, nohaf
1e-05, 0.5, 1e-11
*Boundary, op=NEW
Base, ENCASTRE
*End Step
```

The static step replicate the pulling process with a boundary condition 'pulling' with fixed displacement. The dynamic step let the auricle spring back to its original position.

Auricle Mechanics Parametric Simulation Demonstration (Chapter 5.2.2)

This simulation was used to evaluate the effect of varying skin and cartilage material parameters on auricle stiffness and natural frequency. A linear elastic model and an Ogden hyperelastic model were compared under identical boundary conditions. The simulation followed the previously stated setup with a static step and a dynamic step. One main difference is that from this simulation, all the mesh element have change to hybrid formation in abaqus.

```
** MATERIALS
**
*Material, name=CARTILAGE
*Damping, alpha=0.006, beta=0.002
*Density
 0.0012,
*Elastic
 1.2e+06, 0.45
*Material, name=SKIN
*Damping, alpha=0.006, beta=0.002
*Density
 0.0008,
*Elastic
160000., 0.465
**
** %Or Ogden model%
**
*Material, name=CARTILAGE
*Damping, alpha=0.01, beta=0.005
*Density
 0.0012,
*Hyperelastic, ogden
400000., 3., 4.1096e-07
*Material, name=SKIN
*Damping, alpha=0.01, beta=0.005
*Density
 0.0008,
*Hyperelastic, ogden
36000., 15., 5.5741e-07
**
** ----------------------------------------------------------------
```

```
**
** STEP: Step-1
**
*Step, name=Step-1, nlgeom=YES, inc=10000
Test Force
*Static
0.02, 1., 1e-05, 1.
**
** Boundary conditions
*Boundary
Base, ENCASTRE
*Boundary
pulling, 1, 1, -6.
pulling, 2, 2, -24
pulling, 3, 3
**
*End Step
** ----------------------------------------------------------------
**
** STEP: Step-2
**
*Step, name=Step-2, nlgeom=YES, inc=10000
*Dynamic,application=TRANSIENT FIDELITY,haftol=0.1
1e-05,0.4,1e-10
**
** BOUNDARY CONDITIONS
**
*Boundary, op=NEW
Base, ENCASTRE
*End Step
```

This input structure was looped across multiple material combinations:

Linear model

- Skin modulus range: $E_{\text{skin}} = 0.06 – 0.16$ MPa
- Cartilage modulus range: $E_{\text{cartilage}} = 0.6 – 1.6$ MPa

- Poisson's ratio: Skin $\nu = 0.495$, Cartilage $\nu = 0.45$ (fixed for all tests)
- Outputs: effective stiffness k, natural frequency f_n

Ogden model

- Skin shear modulus: μ_{skin} = 20 – 60 kPa
- Skin stiffening parameter: α_{skin} = 12 – 20
- Cartilage shear modulus: $\mu_{\text{cartilage}}$ = 0.2 – 0.6 MPa
- Cartilage stiffening parameter: $\alpha_{\text{cartilage}}$ = 2 – 5
- Effective Poisson's ratio: $\nu_{\text{skin}} = 0.495$, $\nu_{\text{cartilage}} = 0.46$

The results are used to extract natural frequency and stiffness curves for comparison with experimental data.

Auricle System Vibration (Chapter 5.4.1)

The vibration analysis simulated the free oscillation behaviour of the auricle under small initial perturbations to extract its natural frequencies. A dynamic implicit step was used and the output are nodel displacements.

```
** ----------------------------------------------------------------
**
** STEP: Vibrate
**
*Step, name=Vibrate, nlgeom=YES, inc=1000
*Dynamic,nohaf
0.0005,5.,1e-07
**
** BOUNDARY CONDITIONS
**
** Name: BC-2 Type: Displacement/Rotation
*Boundary, amplitude=Sin_Amplitude
AURIBASE, 1, 1
AURIBASE, 2, 2
AURIBASE, 3, 3, 5.
```

```
*End Step
```

Listing E.1 Excerpt of the Abaqus input

This setup assigned different frequencies by changing the amplitude texttttSin_Amplitude, which varies between 2.18 Hz to 218 Hz.

Auricle With Earable Interaction (Chapter 5.4.3)

This simulation introduced a mesh body representing the earable device in contact with the auricle. Contact pressure and stress transfer were examined using the `Surface-to-Surface Contact` Interaction formulation in Abaqus.

```
** MATERIALS
**
*Material, name=CARTILAGE
*Damping, alpha=0.01, beta=0.005
*Density
 0.0012,
*Hyperelastic, ogden
400000., 3., 4.1096e-07
*Material, name=PLASTIC
*Damping, alpha=0.003, beta=0.001
*Density
 0.002,
*Elastic
 2e+06, 0.4
*Material, name=SKIN
*Damping, alpha=0.01, beta=0.005
*Density
 0.0008,
*Hyperelastic, ogden
36000., 15., 5.5741e-07
**
** INTERACTION PROPERTIES
**
*Surface Interaction, name=IntProp-1
1.,
*Friction, slip tolerance=0.005
```

```
 0.2,
*Surface Behavior, pressure-overclosure=EXPONENTIAL
0.01, 0.15
**
** BOUNDARY CONDITIONS
**
** Name: BC-1 Type: Symmetry/Antisymmetry/Encastre
*Boundary
AURIBASE, ENCASTRE
**
** INTERACTIONS
**
** Interaction: Int-1
*Contact Pair, interaction=IntProp-1, type=SURFACE TO SURFACE
earablesurf, EARSURF
** ----------------------------------------------------------------
**
** STEP: Step-1
**
*Step, name=Step-1, nlgeom=YES, inc=1000
*Static
0.01, 1., 1e-06, 1.
**
** LOADS
**
** Name: Load-2 Type: Pressure
*Dsload
earablesurf, P, 9e+06
** Name: Load-3 Type: Pressure
*Dsload
extra, P, 1e+06
**
** INTERACTIONS
**
** Interaction: Int-1
*Model Change, type=CONTACT PAIR, remove
earablesurf, EARSURF
*End Step
** ----------------------------------------------------------------
```

```
**
** STEP: contactinitiate
**
*Step, name=contactinitiate, nlgeom=YES, inc=10000
*Static, stabilize=0.002, allsdtol=0.1, continue=NO
1e-05, 1., 1e-08, 0.04
**
** LOADS
**
** Name: Load-2 Type: Pressure
*Dsload
earablesurf, P, 6e+06
** Name: Load-3 Type: Pressure
*Dsload
extra, P, 0.
**
** INTERACTIONS
**
** Interaction: Int-1
*Model Change, type=CONTACT PAIR, add
earablesurf, EARSURF
*End Step
** ----------------------------------------------------------------
**
** STEP: Stablise
**
*Step, name=Stablise, nlgeom=YES, inc=1000
*Static, stabilize=0.001, allsdtol=0.08, continue=NO
1e-05, 1., 1e-08, 0.02
**
** LOADS
**
** Name: Load-2 Type: Pressure
*Dsload
earablesurf, P, 0.
*End Step
** ----------------------------------------------------------------
**
** STEP: DynStablise
```

```
**
*Step, name=DynStablise, nlgeom=YES, inc=10000
*Dynamic,nohaf
0.001,2.,1e-07
**
** BOUNDARY CONDITIONS
**
** Name: BC-1 Type: Symmetry/Antisymmetry/Encastre
*Boundary, op=NEW
** Name: BC-2 Type: Displacement/Rotation
*Boundary, op=NEW
AURIBASE, 1, 1
AURIBASE, 2, 2
AURIBASE, 3, 3
** Name: BC-3 Type: Symmetry/Antisymmetry/Encastre
*Boundary, op=NEW
**
** LOADS
**
** Name: Load-2 Type: Pressure
*Dsload
earablesurf, P, 1e+06
*End Step
```

Listing E.2 Excerpt of the Abaqus input

The contact pair with interaction `Int-1` was defined using the property set `Intprop-1`, which employs an exponential overclosure formulation. This approach reduces computational cost and improves numerical stability, resulting in more consistent contact behaviour. The initial steps of the analysis were used to assemble the device into its designed contact position through geometric transformation and translation. This simulation formed the basis for evaluating comfort and mechanical coupling between the auricle and the earable interface.

Auricle Model Interaction (Chapter 6.2)

The simulation assessed multi-point loading and contact decoupling between the auricle model and the earable and the commercial earphones. The model use a similar vibration step as in Chapter 5.4.1.

```
** ----------------------------------------------------------------
**
** STEP: Vibrate
**
*Step, name=Vibrate, nlgeom=YES, inc=1000
*Dynamic,nohaf
0.0005,5.,1e-07
**
** BOUNDARY CONDITIONS
**
** Name: BC-2 Type: Displacement/Rotation
*Boundary, amplitude=Sin_Amplitude
AURIBASE, 1, 1
AURIBASE, 2, 2
AURIBASE, 3, 3, 5.
*End Step
```

Listing E.3 Excerpt of the Abaqus input

The resulting stress maps CPRESS on nodes are exported for analysis.

Auricle Model Interaction with Gait Input (Chapter 6.3.4)

To simulate realistic dynamic loading, experimental IMU trajectories recorded during walking were converted into time-dependent boundary motion. A dynamic implicit step with prescribed displacement was used. These displacement data are stored in the amplitude `Gait_Amplitude`

```
** ----------------------------------------------------------------
**
** STEP: Gait Vibration
**
*Step, name=Gait Vibrate, nlgeom=YES, inc=1000
*Dynamic,nohaf
0.0005,5.,1e-07
**
** BOUNDARY CONDITIONS
**
** Name: BC-2 Type: Displacement/Rotation
```

```
*Boundary, amplitude=Gait_Amplitude
AURIBASE, 1, 1
AURIBASE, 2, 2
AURIBASE, 3, 3, 5.
*End Step
```

Listing E.4 Excerpt of the Abaqus input

Electrode Contact With Skin (Chapter 6.4.4)

This simulation reproduced the impedance–force relationship by analysing contact pressure between a soft electrode pad and the auricle skin surface. Both the electrode and the skin were modelled as deformable ogden model layers with appropriate material stiffness.

```
** MATERIALS
**
*Material, name=Material-1
*Hyperelastic, ogden
20000., 3., 3.6e-05
*Material, name=Skin
*Hyperelastic, ogden
6000., 15., 1.33e-05
**
** INTERACTION PROPERTIES
**
*Surface Interaction, name=IntProp-1
1.,
*Surface Behavior, pressure-overclosure=HARD
**
** INTERACTIONS
**
** Interaction: Int-1
*Contact Pair, interaction=IntProp-1, type=SURFACE TO SURFACE
s_Surf-1, m_Surf-3
** ----------------------------------------------------------------
**
** STEP: Step-1
**
*Step, name=Step-1, nlgeom=YES, inc=10000
```

```
*Static
0.0001, 1., 1e-07, 0.004
**
** BOUNDARY CONDITIONS
**
** Name: BC-1 Type: Symmetry/Antisymmetry/Encastre
*Boundary
Set-3, ENCASTRE
** Name: BC-2 Type: Displacement/Rotation
*Boundary
Set-2, 1, 1, -1.1
Set-2, 2, 2
Set-2, 3, 3
**
*End Step
```

This setup enabled correlation of contact radius and pressure distribution with impedance measurements, supporting the mechanical–electrical coupling analysis described in Chapter 6.4.

Linear Model and Ogden Model Parametric Scan

This appendix provides the full simulation input corresponding to the parametric studies described in Chapter 5, performed on the auricle mesh using both linear elastic and hyperelastic (Ogden) constitutive models.

Linear Elastic Parametric Scan

Parameters	Cart E	Skin E	Cart Poisson	Skin Poisson	Cart density kgm-3	Skin density	alpha	beta	Natural Frequency	Stiffness
Test1	600000	60000	0.45	0.495	1200	800	0.006	0.002	19.0605216	5.329671854
Test2	800000	60000	0.45	0.495	1200	800	0.006	0.002	19.8028753	5.7369069
Test3	1000000	60000	0.45	0.495	1200	800	0.006	0.002	20.4860424	6.10443442
Test4	1200000	60000	0.45	0.495	1200	800	0.006	0.002	21.1487792	6.783583203
Test5	1400000	60000	0.45	0.495	1200	800	0.006	0.002	21.7353261	7.120668499
Test6	1600000	60000	0.45	0.495	1200	800	0.006	0.002	22.3471625	7.441246536
Test7	600000	80000	0.45	0.495	1200	800	0.006	0.002	21.1771868	6.648667173
Test8	800000	80000	0.45	0.495	1200	800	0.006	0.002	21.915169	7.106229652
Test9	1000000	80000	0.45	0.495	1200	800	0.006	0.002	22.5698286	7.519207721
Test10	1200000	80000	0.45	0.495	1200	800	0.006	0.002	23.1811351	7.899720191
Test11	1400000	80000	0.45	0.495	1200	800	0.006	0.002	23.747792	8.255407762
Test12	1600000	80000	0.45	0.495	1200	800	0.006	0.002	24.1263944	8.679532312
Test13	600000	100000	0.45	0.495	1200	800	0.006	0.002	23.0107996	7.930547421
Test14	800000	100000	0.45	0.495	1200	800	0.006	0.002	23.7237309	8.430719765
Test15	1000000	100000	0.45	0.495	1200	800	0.006	0.002	24.398872	8.88278707
Test16	1200000	100000	0.45	0.495	1200	800	0.006	0.002	24.9775549	9.299393301
Test17	1400000	100000	0.45	0.495	1200	800	0.006	0.002	25.5344756	9.688565261
Test18	1600000	100000	0.45	0.495	1200	800	0.006	0.002	26.3128297	10.12527456
Test19	600000	120000	0.45	0.495	1200	800	0.006	0.002	24.7000315	9.187256038
Test20	800000	120000	0.45	0.495	1200	800	0.006	0.002	25.3956702	9.724446837
Test21	1000000	120000	0.45	0.495	1200	800	0.006	0.002	26.0039708	10.210779
Test22	1200000	120000	0.45	0.495	1200	800	0.006	0.002	26.6544556	10.65934371
Test23	1400000	120000	0.45	0.495	1200	800	0.006	0.002	27.2003449	11.07845047
Test24	1600000	120000	0.45	0.495	1200	800	0.006	0.002	28.0118799	11.62126872
Test25	600000	140000	0.45	0.495	1200	800	0.006	0.002	26.2248525	10.42565562
Test26	800000	140000	0.45	0.495	1200	800	0.006	0.002	26.9651418	10.99567487
Test27	1000000	140000	0.45	0.495	1200	800	0.006	0.002	27.4392355	11.51253905
Test28	1200000	140000	0.45	0.495	1200	800	0.006	0.002	28.148918	11.98976406
Test29	1400000	140000	0.45	0.495	1200	800	0.006	0.002	28.7194883	12.4359011
Test30	1600000	140000	0.45	0.495	1200	800	0.006	0.002	29.2375234	12.97532346
Test31	600000	160000	0.45	0.495	1200	800	0.006	0.002	27.6955109	11.8251758
Test32	800000	160000	0.45	0.495	1200	800	0.006	0.002	28.4031824	12.24967469
Test33	1000000	160000	0.45	0.495	1200	800	0.006	0.002	28.9916358	12.79411724
Test34	1200000	160000	0.45	0.495	1200	800	0.006	0.002	29.5718566	13.29733435
Test35	1400000	160000	0.45	0.495	1200	800	0.006	0.002	30.0958455	13.76810395
Test36	1600000	160000	0.45	0.495	1200	800	0.006	0.002	30.5553521	14.21245935

Hyperelastic Ogden Parametric Scan

Parameters	Cart mu	Cart a	Cart D	Skin mu	Skin a	Skin D	Cart density kgm-3	Skin density	alpha	beta	Natural Frequency	Stiffness
Test1	600000	3	2.74E-07	20000	15	1.00E-06	1200	800	0.01	0.005	20.10178368	7.179967851
Test2	600000	3	2.74E-07	28000	15	7.17E-07	1200	800	0.01	0.005	21.50809005	9.142599175
Test3	600000	3	2.74E-07	36000	15	5.57E-07	1200	800	0.01	0.005	22.86021484	10.54676386
Test4	600000	3	2.74E-07	44000	15	4.56E-07	1200	800	0.01	0.005	24.19435828	11.88207088
Test5	600000	3	2.74E-07	52000	15	3.86E-07	1200	800	0.01	0.005	25.15200941	13.75572673
Test6	600000	3	2.74E-07	60000	15	3.34E-07	1200	800	0.01	0.005	26.16929857	14.93877336
Test7	400000	3	4.11E-07	20000	15	1.00E-06	1200	800	0.01	0.005	18.36181967	6.177076862
Test8	400000	3	4.1096E-07	28000	15	7.17E-07	1200	800	0.01	0.005	20.34270149	7.739504038
Test9	400000	3	4.11E-07	36000	15	5.57E-07	1200	800	0.01	0.005	21.80809005	9.231599175
Test10	400000	3	4.1096E-07	44000	15	4.56E-07	1200	800	0.01	0.005	23.06021484	10.67706386
Test11	400000	3	4.11E-07	52000	15	3.86E-07	1200	800	0.01	0.005	24.29135828	12.08907088
Test12	400000	3	4.1096E-07	60000	15	3.34E-07	1200	800	0.01	0.005	25.21500941	13.47572673
Test13	200000	3	8.22E-07	20000	15	1.00E-06	1200	800	0.01	0.005	16.64498197	4.979592512
Test14	200000	3	8.22E-07	28000	15	7.17E-07	1200	800	0.01	0.005	17.42748172	5.478593522
Test15	200000	3	8.22E-07	36000	15	5.57E-07	1200	800	0.01	0.005	18.62472346	6.177076862
Test16	200000	3	8.22E-07	44000	15	4.56E-07	1200	800	0.01	0.005	20.42570219	7.739504038
Test17	200000	3	8.22E-07	52000	15	3.86E-07	1200	800	0.01	0.005	22.18014462	9.231599175
Test18	200000	3	8.22E-07	60000	15	3.34E-07	1200	800	0.01	0.005	23.98655378	11.71231019
Test19	400000	2	4.11E-07	36000	15	5.57E-07	1200	800	0.01	0.005	21.80760576	9.234453312
Test20	400000	2.5	4.1096E-07	36000	15	5.57E-07	1200	800	0.01	0.005	21.80809005	9.231599174
Test21	400000	3.5	4.11E-07	36000	15	5.57E-07	1200	800	0.01	0.005	21.80709004	9.231452116
Test22	400000	4	4.1096E-07	36000	15	5.57E-07	1200	800	0.01	0.005	21.8082601	9.230298159
Test23	400000	4.5	4.11E-07	36000	15	5.57E-07	1200	800	0.01	0.005	21.809736	9.227025992
Test24	400000	5	4.1096E-07	36000	15	5.57E-07	1200	800	0.01	0.005	21.80907131	9.227080686
Test25	400000	3	4.11E-07	36000	10	5.57E-07	1200	800	0.01	0.005	21.79894477	8.485347093
Test26	400000	3	4.1096E-07	36000	12	5.57E-07	1200	800	0.01	0.005	21.80234624	8.752815139
Test27	400000	3	4.11E-07	36000	14	5.57E-07	1200	800	0.01	0.005	21.80661456	9.145211513
Test28	400000	3	4.1096E-07	36000	16	5.57E-07	1200	800	0.01	0.005	21.80813746	9.298159235
Test29	400000	3	4.11E-07	36000	18	5.57E-07	1200	800	0.01	0.005	21.80976324	9.702599125
Test30	400000	3	4.1096E-07	36000	20	5.57E-07	1200	800	0.01	0.005	21.81170746	10.14043654